CEFET/RJ
DIRETORIA DE PESQUISA E PÓS-GRADUAÇÃO

SYNERGISTIC USE OF PIEZOELECTRIC MATERIALS AND SHAPE MEMORY ALLOYS FOR ENERGY HARVESTING: EXPERIMENTAL AND NUMERICAL ANALYSES

Arthur Adeodato

DSc thesis presented to the Post-Graduation Program of Mechanical Engineering and Materials Technology, Centro Federal de Educação Tecnológica Celso Suckow da Fonseca, CEFET/RJ, as a requirement to obtain doctor degree in Mechanical Engineering and Materials Technology.

Advisor: Pedro Manuel Calas Lopes Pacheco
Advisor: Luciana Loureiro da Silva Monteiro

Rio de Janeiro
May 2022

SYNERGISTIC USE OF PIEZOELECTRIC MATERIALS AND SHAPE MEMORY ALLOYS FOR ENERGY HARVESTING: EXPERIMENTAL AND NUMERICAL ANALYSES

DSc thesis presented to the Post-Graduation Program of Mechanical Engineering and Materials Technology, Centro Federal de Educação Tecnológica Celso Suckow da Fonseca, CEFET/RJ, as a requirement to obtain doctor degree in Mechanical Engineering and Materials Technology.

Arthur Adeodato

Examiners:

Professor D.Sc. Pedro Manuel Calas Lopes Pacheco (Centro Federal de Educação Tecnológica Celso Sukow da Fonseca - CEFET/RJ) (Advisor)

Professor D.Sc. Luciana Loureiro da Silva Monteiro (Centro Federal de Educação Tecnológica Celso Sukow da Fonseca - CEFET/RJ) (Advisor)

Professor D.Sc. Ricardo Alexandre Amar de Aguiar (Centro Federal de Educação Tecnológica Celso Sukow da Fonseca - CEFET/RJ)

Professor D.Sc. Marcelo Amorim Savi (Universidade Federal do Rio de Janeiro - COPPE/UFRJ)

Professor DSc. Aline Souza de Paula (Universidade de Brasília - UnB)

Professor DSc. Carlos de Marqui Júnior (Escola de Engenharia de São Carlos - EESC USP)

Rio de Janeiro

May 2022

Ficha catalográfica elaborada pela Biblioteca Central do CEFET/RJ

A232 Adeodato, Arthur
Synergistic use of piezoelectric materials and shape memory alloysfor energy harvesting: experimental and numerical analyses / Arthur Adeodato. — 2022.
158f. : il. color. , enc.

Tese (Doutorado) Centro Federal de Educação Tecnológica Celso Suckow da Fonseca, 2022.
Bibliografia : f. 137-158
Orientador: Pedro Manuel Calas Lopes Pacheco
Coorientadora: Luciana Loureiro da Silva Monteiro

1. Geração de energia. 2. Energia – Fontes alternativas. 3. Ligas com memória de forma. 4. Método dos elementos finitos. I. Pacheco, Pedro Manuel Calas Lopes (Orient.). II. Monteiro, Luciana Loureiro da Silva. (Coorient.) III. Título.

CDD 621.3121

Elaborada pela bibliotecária Tania Mello – CRB/7 nº 5507/04

DEDICATION

This work is dedicated to my father and grandmother. Responsible to provide all material and emotional conditions to my human being development.

ACKNOWLEDGMENT

I would like to first thank my mentors professors: Pedro Manuel Calas Lopes Pacheco and Luciana Loureiro da Silva Monteiro for wisdom and knowledge transmitted all over my academic trajectory. Would like also to thank professor Marcelo Amorim Savi from UFRJ for all contributions in this thesis development. Also thank all CEFET/RJ workers that contributed to keep the institution facilities in order and harmony. And PPEMM post graduation program for doctoral scholarship.

Second, thank for all friends and coworkes in LACTM (CEFET/RJ) and Mecanon (UFRJ) laboratories. In special, for Brenno Tavares Duarte, that worked side by side with me since master until doctor degree providing an essential experimental assistance for development of this thesis. Also for Daniel de Macedo Barreto Netto and Luã Guedes Costa to assisted me with program language learning. And Lucas Lisboa Vignolli, that developed the constitutive model in this thesis together with me.

Thanks everyone who in some way participated to my journey and helped with simple details that made all difference.

ABSTRACT

SYNERGISTIC USE OF PIEZOELECTRIC MATERIALS AND SHAPE MEMORY ALLOYS FOR ENERGY HARVESTING: EXPERIMENTAL AND NUMERICAL ANALYSES

The seeks for clean and renewable methods to obtain electrical energy is a global demand and experienced continued growth in the last two decades. Besides that, mechanical vibrations are considered a relevant kinetic energy resource and it is present in most environments. Piezoelectric materials arise as an alternative to convert mechanical vibrations into electrical power through the direct piezoelectric effect. Traditional piezoelectric harvesters present narrow bandwidth with great performance when external forcing frequency matches with the harvester's natural frequency, and therefore, the harvester operates in resonance conditions. However, environmental vibration sources can vary their frequency in a wide range promoting a significant drop in the harvester performance. Based on that, nonlinear dynamical responses have been explored as an alternative to increase piezoelectric energy harvesters' operational range. In addition, shape memory alloys (SMAs) present nonlinear thermomechanical coupling and the intrinsic characteristic to change mechanical properties due to solid phase transformation induced by either temperature and mechanical fields. This work investigates the synergistic use of piezoelectric materials and the nonlinear constitutive behavior of shape memory alloys with the aim to provide adaptability characteristics and increase the harvester's operational range. A constitutive model with assumed kinetic phase transformation is developed to describe the SMA constitutive behavior in dynamical conditions. An experimental apparatus is built to characterize the dynamical behavior of a SMA-piezoelectric energy harvester and evaluate the harvester in operational conditions. The analyses consider the influence of SMA phase transformation induced by temperature and mechanical load separately and evaluate the frequency response of the SMA-piezoelectric harvester in different conditions of use. Afterward, a good theoretical-experimental correlation is obtained. Results reveal that the addition of a SMA element in a piezoelectric energy harvester is able to alter its frequency response and increase the operational range via thermal and mechanical stimulus.

Keywords: Energy Harvesting, Piezoelectric Materials, Shape Memory Alloys, Experimental Analysis, Numerical Simulations.

RESUMO

USO SINÉRGICO DE MATERIAIS PIEZOELÉTRICOS E LIGAS COM MEMÓRIA DE FORMA PARA COLHEITA DE ENERGIA: ANÁLISE EXPERIMENTAL E NUMÉRICA

A busca por métodos de obtenção de energia elétrica de forma não poluente é uma demanda global que apresenta contínuo aumento nas últimas duas décadas. Junto a isso, vibrações mecânicas são consideradas uma fonte vasta de energia cinética e presente em muitos cenários. Materiais piezoeléctricos surgem como uma alternativa de converter vibrações mecânicas em energia elétrica devido ao efeito piezoeléctrico direto. Coletores piezoelétricos tradicionais apresentam largura de banda estreita e máximo desempenho quando a frequência de forçamento coincide com a frequência natural do coletor e, portanto, o coletor opera na condição de ressonância. No entanto, fontes de vibrações no ambiente podem ter sua frequência variada em uma ampla faixa promovendo uma queda significativa no desempenho do coletor. Com base nisso, respostas dinâmicas não lineares têm sido exploradas como uma alternativa para aumentar a faixa operacional dos coletores de energia piezoelétrica. Além disso, ligas com memória de forma, do inglês *shape memory alloys* (SMAs) apresentam acoplamento termomecânico e a característica de modificar suas propriedades mecânicas devido a transformação de fase sólida que pode ser induzida por temperatura e carregamento mecânico. Este trabalho investiga o uso sinérgico de materiais piezoelétricos e o comportamento constitutivo não linear de ligas com memória de forma com o objetivo de fornecer características de adaptabilidade e aumentar a faixa de operação do coletor. Um modelo constitutivo com cinética de transformação de fase assumida é desenvolvido para descrever o comportamento constitutivo da SMA em condições dinâmicas. Um aparato experimental é construído para caracterizar o comportamento dinâmico de um coletor de energia SMA-piezoelétrico e avaliar o coletor em condições operacionais. As análises consideram a influência da transformação de fase SMA induzida por temperatura e carregamento mecânico separadamente e avaliam a resposta no domínio da frequência do coletor SMA-piezoelétrico em diferentes condições de uso. Posteriormente, encontra-se uma boa correlação teórico-experimental. Os resultados revelam que a adição de um elemento de SMA em um coletor de energia piezoelétrico é capaz de alterar sua resposta no domínio da frequência e aumentar a faixa operacional via estímulo térmico e mecânico.

Palavras-chave: Colheita de Energia, Materiais Piezoelétricos, Ligas com Memória de Forma, Análise Experimental, Simulação Numérica.

Summary

List of Figures **VII**

List of Tables **XVI**

List of Symbols **XXI**

1 Introduction **1**

2 Energy Harvesting **5**

2.1 Aspects of Energy Harvesting 5

2.2 Vibration Energy Harvesting 9

2.2.1 Electrostatic Energy Harvesting 15

2.2.2 Electromagnetic Energy Harvesting 16

2.2.3 Magnetostrictive Energy Harvesting 17

2.2.4 Piezoelectric Energy Harvesting 17

2.3 Strategies to Broaden the Bandwidth 28

2.3.1 Multi-stable Systems 29

2.3.2 Non Smoothness Impact (End-stop) 31

2.3.3 Geometries and Configurations 33

2.3.4 Synergistic use of Smart Materials 34

3 Shape Memory Alloys **36**

3.1 Shape Memory Effect 39

3.2 Pseudoelastic Effect 42

3.3 Shape Memory Alloys in Dynamical Systems 44

3.4 Shape Memory Alloy Constitutive Models 48

4 Methodology **55**

4.1 Experimental Methodology . . . 57

4.1.1 Thermomechanical Characterization . . . 57

4.1.1.1 SMA Wire Characterization . . . 58

4.1.1.2 Martensite SMA Helical Spring Characterization . . . 62

4.1.1.3 Austenite SMA Helical Spring Characterization . . . 66

4.1.2 Experimental Synergisctic Piezoelectric Energy Harvester with SMA . . . 68

4.2 Mathematical Modeling . . . 70

4.2.1 SMA Polynomial Model with Assumed Kinetic Phase Transformation . . . 70

4.2.1.1 Mechanical Oscillator with SMA element . . . 75

4.2.2 Piezoelectric Energy Harvester with SMA Martensite Helical Spring . . . 79

4.2.3 Piezoelectric Energy Harvester with SMA Austenite Helical Spring . . . 82

5 Results and Discussion **89**

5.1 SMA Polynomial Model with Assumed Kinetics Phase Transformation . . . 89

5.1.1 Mechanical Oscillator with SMA element . . . 96

5.1.1.1 Free Vibration . . . 97

5.1.1.2 Sweep Response . . . 100

5.1.1.3 Stationary Forcing Frequency Response . . . 104

5.2 Piezoelectric Energy Harvester with SMA Martensite Helical Spring . . . 108

5.2.1 Sweep Response . . . 108

5.2.2 Stationary Forcing Frequency Response . . . 115

5.3 Piezoelectric Energy Harvester with SMA Austenite Helical Spring . . . 120

5.3.1 Quasi Static Analysis . . . 120

5.3.2 Dynamical Analysis . . . 124

6 Conclusions and Future Perspective **133**

References 137

List of Figures

2.1 Methods for energy harvesting and electrical power conversion capacity. (a) Hydroelectric at China - 22500 MW [36]. (b) Solar power plant complex at the USA - 354 MW [37]. (c) Offshore oil extraction at Brazil [38] - 100 MW [39]. (d) Ocean wind farm at Scotland - 588 MW [40]. (e) Nuclear power plant at France - 4250 MW [41]. (f) Geothermal energy harvesting in Iran - 230 KW [42]. (g) Ocean energy harvesting at Brazil - 100 KW [43]. 6

2.2 Total world energy supply by resource from 1990 to 2018. [45] 7

2.3 Electrical energy evaluation from 1990 to 2018.(a) Total world energy consumption. (b) Renewable electricity harvesting. [45] 9

2.4 Number of publications about vibration energy harvesting from 1990 to 2020 [68]. 11

2.5 Number of publications about vibration energy harvesting from 1990 to 2020 [69]. 12

2.6 Major publishers associated to the topic of vibration energy harvesting [69]. . . . 12

2.7 Top journals about vibration energy harvesting research [69]. 13

2.8 Most relevant fields of study on vibration energy harvesting [69]. 13

2.9 Countries with more impact in vibration energy harvesting research by percentage [69]. 14

2.10 Piezoelectric quartz crystalline cell and direct effect representation. 18

2.11 Self powered piezoelectric devices. (a) Temperature and humidity sensor [5]. (b) Cardiac pacemaker [14]. (c) Load cell sensor [97]. (d) Arterial pulse monitor [12]. (e) Smart watch [98]. 19

2.12 Traditional cantilever beam configuration in piezoelectric energy harvesting experiments. (a) [16]. (b) [17]. (c) [102]. (d) [102]. 20

2.13 Basic structure of piezoelectric energy harvesters: (a) Bimorph structure, (b) Unimorph structure. Modes of piezoelectric conversion of input mechanical strain depending on the relative direction of the stress and the electric field. (c) d_{31} mode. (d) d_{33} mode. Adapted from [101]. 21

2.14 Traditional piezoelectric energy harvester model represented by a single degree of freedom and discrete parameters. Adapted from [18] 24

2.15 Piezoelectric energy harvesting for exoskeleton.(a) Experimental study of human walk energy harvesting [13]. (b) Human exoskeleton [115]. 26

2.16 Alternatives to piezoelectric energy harvesters for smart cities. (a) Tyre compression for tire pressure measure [124]. (b) Walk movement for train station energy supply [128]. (c) Smart shoe powered by piezoelectric elements [129]. 27

2.17 Piezoelectric energy harvesting for wild life monitoring (a) Prototype mounted on a beetle [130]. (b) Data logger mounted to western sandpiper [131]. 28

2.18 Bi-stable piezoelectric energy harvester system. (a) Schematic representation of the cantilever beam configuration with magnetic masses. (b) Restoring force represented by Duffing equation. (c) System potential energy. (d) Output power frequency response. Adapted from Maaer et al. [135] 29

2.19 (a) Poly-stable piezoelectric harvester with magneto tip masses. (b) energy-harvester in a wall ship. (c) Harvester installed in an ocean buoy. (d) installed under a bridge. Adapted from [137] 31

2.20 Piezoelectric harvester system with stop ends impact constrain. (a) Experiment apparatus and schematic. (b) Two degree of freedom representation. (c) Nonlinear response for upward and downward frequency sweep. Adapted from [145] . . 33

2.21 Piezoelectric energy harvester inspired in a cochlea configuration. (a) Cochlea illustration design. (b) Harvester prototype design. (c) Experimental setup. (d) Relative displacement frequency response. [154] 34

3.1 NiTi Shape memory alloy crystalline cell. (a) Austenite phase. (b) Martensite phase. Adapted from Rao et al. [30]. 37

3.2 Differential scanning calorimetry process. Characteristic curves for phase transformation critical temperatures determination. Adapted from Rao et al. [30]. . . 38

3.3 Shape memory effect representation. Stress × Strain × Temperature diagram. . 39

3.4 Flexible wearable shape memory alloy actuator [172] 41

3.5 Bio inspired wing morphing structures by *SMA* composite actuation. (a) Illustrative design. (b) Experimental prototype view actuation. [178] 42

3.6 Pseudoelastic effect representation. Stress × strain diagram. 43

3.7 Schematic of prototypes to evaluate pseudoelastic effect for vibration control. (a) Nae et al. [182] uses *SMAs* wires. (b) He et al. [184] uses *SMA* helical spring. . . 44

3.8 Experimental measurement of *SMA* temperature for vibration control. (a) Archetype for a single degree of freedom with base excitation and temperature graphical measurement. (b) Experimental results showing amplitude reduce and resonance shift. Adapted from [180]. 45

3.9 *SMA* absorber system developed by Ghasemi et al. [197]. (a) Detail drawing of the *SMA* damper. (b) Sketch of jacket platforms evaluated. (c) Percentage of maximum displacement reduced for different values of absorber mass coefficient (α). Adapted from [197] 46

3.10 *SMA* for vibration mitigation in mono pile offshore wind turbine model. (a) Schematic lateral and frontal view showing side-to-side motion. (b) Mono-pile assembly. (c) *SMA* stiffener tendon from root to tip of the blade. Adapted from [198] 47

3.11 Phase transformation stress surfaces as a function of temperature. (a) Tanaka et al. [215], Liang and Rogers [216]. (b) Brinson [34]. 50

4.1 Traditional piezoelectric energy harvester submitted to base vibration. (a) Cantilever beam configuration. (b) Single degree of freedom archetype. 55

4.2 *SMA* base vibration systems archetypes. (a) Mechanical oscillator with a *SMA* element. (b) Piezoelectric energy harvester with *SMA* martensite helical spring and phase transformation induced by temperature. (c) Piezoelectric energy harvester with *SMA* austenite helical spring with phase transformation induced by mechanical load. 56

4.3 *SMA* elements used in the analysis: wire, martensite helical spring and austenite helical spring. 58

4.4 Differential scanning calorimetry of peseudoelastic wire sample $d_W = 0.9\ mm$. (a) Experimental setup. (b) Phase transformation temperature. 59

4.5 Experimental tensile test for *SMA* wire sample $d_W = 0.9\ mm$. (a) Experimental setup. (b) Stress-strain curves for different temperature conditions. 60

4.6 Experimental determination of *SMA* Young's modulus and critical stresses phase transformation. (a) $T = 243$ K. (b) $T = 303$ K. (c) $T = 323$ K. (d) $T = 343$ K. . 61

4.7 Experimental critical phase transformation stress surface as a function of temperature. 62

4.8 Differential Scanning Calorimetry analysis showing phase transformation temperatures of a martensite helical spring sample. 63

4.9 Experimental analysis of the temperature electrical current. (a) Experimental apparatus of the martensite helical spring for the measurement through infrared and thermocouple sensors. (b) Temperature-electrical current diagram. 64

4.10 Experimental quasi static load tests of the *SMA* mastensite helical spring. (a) Experimental apparatus. (b) Force × displacement curves considering different electrical currents. Ambient (low) temperature - without electrical current (0 A); and high temperature - with 1.5 A. 65

4.11 Differential scanning calorimetry test of austenite helical spring. 66

4.12 Austenite helical spring quasi static tests. (a) Force × displacement diagram. Stress × strain diagrams: (b) $d_{SMA}^{max} = 10$ mm. (c) $d_{SMA}^{max} = 20$ mm. (d) $d_{SMA}^{max} = 30$ mm 67

4.13 Experimental apparatus of the energy harvester with synergistic use of piezoelectric and shape memory alloy elements. The system is composed of a cantilever beam with a piezoelectric element connected to a shape memory alloy spring, being excited in the vertical direction by an electrodynamics shaker 69

4.14 Experimental setup for synergistic use of piezoelectric materials for energy harvesting. (a) Termocouple T type. (b) Electrical current font. (c) Electrical resistance board. (d) Work station. (e) Infrared temperature sensor. (f) Arduino board. (g) Data acquiring system. 70

4.15 Iterative algorithm for convergence: *Prescribed* ϵ 74

4.16 Algorithm for analytical solution: *Prescribed* ϵ 75

4.17 A schematic illustration of a vibration based dynamical system with the addition of a *SMA* element. (a) Cantilever beam configuration and continuum elements. (b) Single degree of freedom and discrete parameters. 76

4.18 Dynamical model of the energy harvester with synergistic use of piezoelectric and *SMA* martensite helical spring. (a) Cantilever beam. (b) Its representation as a single degree of freedom oscillator. 79

4.19 Synergistic use of piezoelectric energy harvester coupled to *SMA* austenite helical spring. (a) Cantilever beam representative illustration. (b) Detail for electronic mechanical actuator to promote an initial preload variation. 85

4.20 Dynamical model of the energy harvester with synergistic use of piezoelectric and austenite *SMA* helical spring as a single degree of freedom and its preload stages. 86

4.21 Representative time evolution in the SMA-piezoelectric energy harvester. (a) Relative displacement. (c) Velocity 86

5.1 Proposed assumed kinetic phase transformation model compared with experimental data for different temperature conditions: (a) T = 243 K. (b) T = 303 K. (c) T = 323 K. (d) T = 343 K. 90

5.2 Comparison of traditional models with assumed kinetics transformation and the formulation proposed. Tanaka: (a) Pseudoelastic effect, (b) Shape memory effect. Liang & Rogers: (c) Pseudoelastic effect, (d) Shape memory effect. Brinson: (f) Pseudoelastic effect, (f) Shape memory effect. 92

5.3 Comparison of Brinson and proposed polynomial model for prescribed strain load. (a) Pseudoelastic effect. (b) Shape memory effect. (c) Martensite reorientation. . 93

5.4 Iterative number of steps for Brinson [34] model in prescribed strain load and phase transformation induced by mechanical load. 94

5.5 Control parameters B_M and B_A analysis for polynomial model with assumed kinetic transformation. (a) Stress × strain diagram: Phase transformation induced by temperature. (b) Strain × temperature diagram: Phase transformation induced by mechanical load. 95

5.6 Subloop analysis for the polynomial model with assumed kinetic phase transformation for $T > A_f$. (a) Stress × Strain diagram. (b) Prescribed strain. (c) Young's modulus. (d) Martensite volume fraction variation. 96

5.7 Subloop analysis of polynomial model for $\sigma = 0$. (a) Strain × temperature diagram. (b) Prescribed temperature. (c) Strain and (d) martensite volume fraction time evolution. 96

5.8 High temperature free vibration for different initial conditions in free vibration analysis: (a), (e) and (i) present displacement time history. (b), (f) and (g) show stress-strain curves. (c), (g) and (k) show the martensite volume fraction. (d), (h) and (l) present the phase spaces. 98

5.9 Low temperature free vibration for different initial conditions in free vibration analysis: (a), (e) and (i) present displacement time history. (b), (f) and (g) show stress-strain curves. (c), (g) and (k) show the martensite volume fraction. (d), (h) and (l) present the phase spaces. 99

5.10 External undamped ($c = 0$) damped system ($c = 0.05Ns/m$) free vibration analysis. (a) Displacement time evolution. (b) Phase space. (c) Stress $\times$ strain diagram. (d) Martensite time evolution. 100

5.11 Temperature influence analysis $A_b = 0.1$ m/s^2. (a) Frequency response. (b) Stress $\times$ strain diagrams. 101

5.12 Frequency response for different values of base amplitude for *SMA* linear elastic behavior. (a) Maximum displacement. (b) Maximum stress. 101

5.13 Nonlinear frequency response for conditions with small values of *SMA* phase transformation. (a) Maximum displacement. (b) Maximum stress. (c) Maximum martensite volume fraction formed. 102

5.14 Nonlinear frequency response for incomplete phase transformation. (a) Maximum displacement. (b) Displacement Poincaré section. (c) Maximum strain. (d) Maximum martensite volume fraction formed. 103

5.15 Nonlinear frequency response with complete phase transformation. (a) Maximum displacement. (b) Displacement Poincaré section. (c) Maximum strain. (d) Maximum martensite volume fraction formed. 104

5.16 System time domain responses in stationary forcing frequency for different levels of base amplitude. $A_b = 1$ m/s^2 from (a) to (c). $A_b = 5$ m/s^2 from (d) to (f) and $A_b = 25$ m/s^2 from (g) to (i). 105

5.17 *SMA* element time domain responses in stationary forcing frequency for different levels of base acceleration. $A_b = 1$ m/s^2 from (a) to (c). $A_b = 5$ m/s^2 from (d) to (f) and $A_b = 25$ m/s^2 from (g) to (i). 106

5.18 Stationary forcing frequency analysis for $A_b = 25$ m/s^2. (a) Frequency response. From (b) to (c) phase spaces. From (e) to (g) martensite time evolution. From (h) to (j) stress × Strain diagrams. 107

5.19 Stationary forcing frequency analysis $b_b = 26$ m/s^2. (a) Frequency response diagram. From (b) to (d): Stress × Strain diagrams. (e) Martensite time evolution. (f) Phase space. 108

5.20 Analysis of the energy harvester maximum output power as a function of external resistance load for low and high *SMA* temperature conditions. 109

5.21 Experimental, analytical and numerical results of the energy harvester frequency response. System adaptability is represented by the temperature dependent resonant conditions. (a) Maximum Displacement. (b) Maximum Output Power. (c) Maximum Input Power. (d) Maximum Efficiency. 110

5.22 Energy harvester bandwidth analysis highlighting the adaptive capacity provided by shape memory alloys, increasing of the output power. (a) Numerical simulations. (b) Experimental data. 111

5.23 *SMA* martensite helical spring temperature measurement by infra red sensor and thermocouple during frequency sweep. 112

5.24 Numerical output power frequency response for *SMA* piezoelectric energy harvester and phase transformation induced by temperature. (a) 2D diagram view. (b) 3D diagram view. 113

5.25 Numerical-experimental correlation output power frequency response for *SMA* piezoelectric energy harvester and phase transformation induced by temperature. 114

5.26 Numerical simulation varying ω and T. (a) Applied temperature variation. (b) Harvester natural frequency and *SMA* martensite volume fraction temperature dependency. 115

5.27 Energy harvester steady state response comparing low and high temperature resonant stationary conditions. (a) Force-displacement curve. (b) Phase space. . . . 115

5.28 Energy harvester force-displacement curves comparing low and high temperature resonant stationary conditions. (a) Numerical simulations. (b) Experimental data. 116

5.29 Force-displacement analysis for low and high temperature resonant stationary conditions. (a) Mean stiffness. (b) Dissipated energy. 117

5.30 Energy harvester output power time history for a fixed forcing frequency, comparing low and high temperature responses. (a) Numerical output power (ω = 32.96 Hz for low temperature and ω = 35.61 Hz for high temperature). (b) Experimental output power (ω = 32.86 Hz for low temperature and ω = 35.35 Hz for high temperature). 117

5.31 Time evolution of the energy harvester response considering the temperature increase and a forcing frequency of 35.61 Hz. (a) Displacement. (b) Output Power. 118

5.32 Details about the energy harvester steady state responses for ω = 35.61 Hz and different temperatures. (a) Low temperature displacement: $T < T_M$. (b) High temperature displacement: $T > T_A$. (c) Low temperature output power: $T < T_M$. (d) High temperature output power: $T > T_A$. 119

5.33 SMA-piezoelectric energy harvester response considering the temperature increase and a forcing frequency of 35 Hz. (a) Low temperature (0.0 A). (b) High temperature (2.5 A). 120

5.34 Austenite *SMA* helical spring polynomial model and experimental quasi static comparison. (a) Force × Displacement diagram for different maximum load amplitude. Associated equivalent Stress × Strain diagram for: (a) ϵ_{max} =0.01. (b) ϵ_{max} =0.02 121

5.35 Expended work estimation via Force × Displacement diagram for PL = 1.5 N. (a) Forward phase transformation (b) Reverse phase transformation. 122

5.36 Expended work estimation attributed to preload values in concern. 122

5.37 *SMA* different temperature conditions. (a) Force × Displacement. (b) Equivalent shear stress. (c) Equivalent martensite volume fraction time evolution. 123

5.38 Incomplete *SMA* phase transformation and subloops. (a) *SMA* helical spring axial Force × Displacement. (b) Prescribed shear strain. Equivalent shear stress. (d) Equivalent martensite volume fraction time evolution. 123

5.39 Maximum values in frequency response analysis for $A_b = 10m/s^2$. (a) Relative displacement. (b) Output power. (c) Input mechanical power. (d) Efficiency. (e) Equivalent *SMA* shear stress. (f) Equivalent *SMA* martensite volume fraction. . 125

5.40 (a) Maximum output power frequency response analysis for $A_b = 10m/s^2$. (b) Output power comparison in steady state response for stationary forcing frequency. 126

5.41 Maximum values in frequency response analysis for $A_b = 30$ m/s^2. (a) Relative displacement. (b) Output power. (c) Input mechanical power. (d) Efficiency. (e) Equivalent *SMA* shear stress. (f) Equivalent *SMA* martensite volume fraction. . 127

5.42 Output power analysis. (a) Maximum output power frequency response for $A_b = 30$ m/s^2. (b) Output power comparison in steady state response for stationary forcing frequency $\omega = 26.67$ Hz. 128

5.43 Stationary forcing frequency analysis. (a) *SMA* spring axial Force $\times$ displacement. (b) Equivalent shear Stress $\times$ Strain time evolution. (c) Equivalent martensite volume fraction time evolution. 128

5.44 Stationary forcing frequency analysis. (a) Phase space diagram. (b) Relative displacement time evolution. (c) Relative displacement steady state response. . . 129

5.45 Analysis of $PL = 0.5$ N. (a) Output power frequency response for $A_b = 30$ m/s^2. For stationary forcing frequency and $\omega = 29.6$ Hz: (b) Force $\times$ Displacement, (c) phase space and (d) output power. For $\omega = 29.4$ Hz, (e) Force $\times$ Displacement, (f) phase space and (g) output power. 130

5.46 Maximum output power diagram for preloads and base vibration amplitudes. . . 131

5.47 Required time to compensate static load condition in *SMA* austenite helical spring. 131

List of Tables

1 Vibration sources associated to maximum acceleration level and frequency peaks. Adapted from [54]. 10

2 Summary power consumption of typical electronic sensors and devices. 15

3 *SMA* elements geometrical properties. 58

4 *SMA* wire experimental constitutive parameters. 62

5 *SMA* martensite helical spring experimental parameters. 66

6 *SMA* austenite helical spring experimental constitutive parameters. 68

7 Single degree of freedom mechanical oscillator with *SMA* element parameters. . . 78

8 Single degree of freedom piezoelectric energy harvester with *SMA* martensite helical spring parameters. 82

9 Single degree of freedom piezoelectric energy harvester with *SMA* austenite helical spring parameters. 87

10 Time simulation for strain prescribed load in Brinson [34] model and the proposed polynomial model wish assumed kinetic phase transformation 95

List of Symbols

α	Axial phase transformation coefficient
α_s	Shear phase transformation coefficient
$\bar{E}_i$	Piezoelectric electric field
β	Martensite volume fraction
β_S	Martensite volume fraction induced by stress
β_T	Martensite volume fraction induced by temperature
χ	Duffing cubic therm
δ	Kronecker delta
ϵ	Strain tensor
ϵ_{ij}	Strain tensor
η	Harvester efficiency
Γ	Time period
γ	Shear strain
γ_p	Helical spring shear strain developed on the wire surface
γ_R	Helical spring residual shear strain
$\hat{\sigma_{ij}}$	Cauchy stress tensor
κ	Piezoelectric coupling therm
Λ	Beam volume
μ_{ij}	Permittivity constant
ν	Dimensionless frequency
Ω	Time frequency
Ω_N	Natural frequency
Φ	Helmholtz free energy

ρ	Mass density
σ_f	SMA variant reorientation finish stress
σ_s	SMA variant reorientation start stress
σ_{ff}	SMA forward transformation finish stress
σ_{fs}	SMA forward transformation start stress
σ_{ij}	Second Piola-Kirchhoff stress tensor
σ_{ij}	Stress tensor
σ_{rf}	SMA reverse transformation finish stress
σ_{rs}	SMA reverse transformation start stress
τ	Shear stress tensor
τ_f	SMA variant reorientation finish shear stress
τ_s	SMA variant reorientation start shear stress
Θ	Thermal transformation coefficient
θ	Piezoelectric electromechanical coupling
$\tilde{\sigma}$	Normalized stress
$\tilde{T}$	Normalized temperature
Υ	Duffing linear therm
ζ	Viscous damping factor
a	Helical spring wire radial coordinate
a_A	Tanaka first reverse constant
A_b	Base vibration maximum amplitude
A_f	Austenite phase transformation finish temperature
a_M	Tanaka first forward constant
A_p	Piezoelectric element superficial area
A_s	Austenite phase transformation start temperature
b	Beam width

B_A Reverse phase transformation control parameter

b_A Tanaka second reverse constant

B_M Forward phase transformation control parameter

b_M Tanaka second forward constant

c Viscous damping coeffiecient

C_A Austenite stress-temperature coefficient

C_M Martensite stress-temperature coefficient

C_p Electric circuit capacitance

c_s Support damping

C_{ijkl} Piezoelectric elastic constant

D_i Piezoelectric electric displacement tensor

d_W SMA wire diameter

D_{AS} Austenite helical spring major diameter

d_{AS} Austenite helical spring minor diameter

d_{ij} Piezoelectric operation mode

D_{MS} Martensite helical spring major diameter

d_{MS} Martensite helical spring minor diameter

dt Increment of time

E Young's modulus

E_A Austenite Young's modulus

E_M Martensite Young's modulus

e_{ijk} Piezoelectric constant

f_A Reverse phase transformation hardening function

f_M Forward phase transformation hardening function

F_{SMA} Axial force in SMA element

g Gap

G_A Austenite shear modulus

G_M Martensite shear modulus

H Electric enthalpy density

I Beam bending inertia moment

i Electrical current

K Kinetic energy

k Linear stiffness

k_s Support stiffness

k_{beam} Beam linear bending stiffness

k_{eq} Equivalent stiffness

k_{SMA} SMA element axial stiffness

L Beam length

L_W SMA wire length

L_{AS} Austenite helical spring length

L_{MS} Martensite helical spring length

M Beam bending moment

m Body mass

M_f Martensite phase transformation finish temperature

M_s Martensite phase transformation start temperature

M_t Tip mass

m_{eq} Equivalent mass

N_{AS} Austenite helical spring number of spires

N_{MS} Martensite helical spring number of spires

p Tolerance

P_{in} Harvester input power

P_{out} Harvester output power

PL	Preload
R	Electric circuit resistance
r	Dimensionless electromechanical factor
S	Entropy density
s	Beam reference coordinate
T	Temperature
t	Time
t_p	Piezoelectric element thickness
U	Stored energy
u	Internal energy
V	Piezoelectric voltage
W	Work
w	Beam deflection
X	Material coordinate
x	Body mass absolute displacement
y	Base vibration displacement
z	Body mass relative displacement

1 Introduction

Technological and scientific development is increasingly dependent on electrical energy sources every decade. Historically determined, human beings figured out diverse methods to turn one kind of energy into another for a specific purpose. However, over the last century, fossil fuels have been exhaustively used and established as one of the prior energy sources. The twenty-first century begins with a consistent concept of environmental care and changes in the way people and organizations manipulate energy [1, 2].

Energy does not present a closed definition in science, meaning different ideas in each specific area. An embracing definition of energy in engineering can be attributed to the capability to accomplish work [3]. Based on that, energy has been harvested with the objective to power machines and devices to increase human life options. Among various forms of energy, electrical energy is considered an attractive energy resource and has become popular due to safe storage, transport, and practical use [2, 4].

Environmental issues are not the unique reason for energy harvest sources diversity. New concepts of engineering projects require that energy must be harvested at the work spot. There exist situations where the access becomes so expensive or inappropriate that the use of power cables becomes impracticable and is also not desirable to have a battery replacements routine. That is the case of devices operating in remote areas as aerospace [5, 6, 7, 8], oil wells [9, 10, 11], outside [12, 13] and inside [14, 15] of living beings body.

Piezoelectric materials come up as a great alternative to power supply electronic devices in a way to avoid or reduce the use of power cables and battery components [16, 17, 18, 19]. Piezoelectric materials are classified as smart materials due to electromechanical coupling meaning connection between electrical and mechanical physical domains. When a mechanical load is applied to a piezoelectric material, it promotes geometrical changes in original shape (strain), and an electrical potential between the material extremities is observed. This is named the direct piezoelectric effect and represents the principle of piezoelectric energy harvesting [5, 20, 21]. The mechanical loading process can be repeated in an oscillatory motion promoting an alternated electrical current used to power devices or recharge batteries via an electrical circuit [18, 22, 23].

Thus, mechanical vibrations can be considered as a potential energy source with a lot of opportunities to apply piezoelectric harvesters and convert kinetic energy into electrical power for low power consumption devices. It includes wireless sensor nodes and microscale electromechanical systems (*MEMS*).

A piezoelectric energy harvester can be represented by a mechanical oscillator connected to an electrical system by a piezoelectric element [18, 24]. In general, electromechanical systems involve dynamic characteristics and present maximum energy conversion when the external frequency matches the harvester's natural frequency, and therefore, the harvesting system works in resonant conditions. In fact, considering that ambient vibrations are unpredictable and can usually vary in over a range of frequencies, traditional piezoelectric energy harvesters that operates in the linear-elastic range, present narrow bandwidth and operational range [25, 26, 27].

Literature disposes of several investigations about methods to increase harvesting capacity and nonlinearities have shown as a promising approach [28]. Nonlinearities allow to increase energy harvesting operational range and bring the concept of adaptability and environment interaction. The synergistic use of smart materials for energy harvesting is an innovative field [29].

This thesis purposes to investigate the synergistic use of piezoelectric materials and shape memory alloys (*SMAs*) with the objective to enhance the energy harvesting capacity over a range of frequencies. Shape memory alloys present as essential thermomechanical characteristics the solid phase transformations induced either by stress or by temperature fields [30, 31, 32]. Typically, *SMAs* have two phases, austenite and martensite. The shape memory effect, where phase transformation occurs due to temperature variation, involves geometrical shape recovery. In addition, the pseudoelastic effect presents phase transformation induced by mechanical load. The phenomena involved in shape memory alloys include changes in mechanical properties such as Young's modulus and hysteresis which is associated with the energy dissipated during the thermomechanical load process [33].

In this way, it is possible to explore the *SMAs* remarkable effects to change the harvester's dynamic characteristics as stiffness and damping in order to increase the energy conversion for a range of external excitation frequencies. The main contribution of this thesis is the synergistic use of both smart materials for energy harvesting. Moreover, a constitutive model with assumed kinetics phase transformation to describe *SMAs* constitutive behavior is developed. The model provides explicit equations for prescribed strain load which is also a fundamental contribution of this work.

Chapter 2 presents a literature review about energy harvesting methods. Aspects of global energy harvesting are shown to enforce the necessity of diversification in energy harvesting sources. Mechanical vibrations emerge as an alternative source with different methods to convert kinetic energy into electrical power. The chapter focuses on piezoelectric materials principles and strategies to broaden piezoelectric harvester frequency responses.

Chapter 3 deals with shape memory alloys and their remarkable effects: shape memory effect and pseudoelastic effect. A literature review presents the state of the art of *SMAs* development and its specific application to dynamic systems like passive and active vibration control. In addition, a subsection presents a review of traditional *SMAs* constitutive models with assumed phase transformation kinetics and the mathematical modeling involved to represent *SMA* constitutive behavior.

Chapter 4 describes the methodology proposed in this thesis to investigate the synergistic use of piezoelectric materials and shape memory alloys for energy harvesting. The methodology addresses the influence of *SMA* phase transformation induced by temperature and mechanical load, separately, with the objective to alter output power frequency response curves and so, extend the harvester operational range. Therefore, the methodology is based on experimental procedures and mathematical modeling of the SMA-piezoelectric harvester including analytical solutions and numerical simulations.

The experimental procedure starts with the thermomechanical characterization of *SMAs* commercial samples. A *SMA* wire sample is first characterized with the objective to evaluate constitutive parameters for the proposed *SMA* model with assumed kinetic phase transformation. In sequence, two *SMA* helical springs are characterized for further SMA-piezoelectric energy harvesting analyses. One helical spring presents a martensite phase stable at room temperature and is applied to investigate the influence of phase transformation induced by temperature, while another *SMA* helical spring presents an austenite phase stable at room temperature and is employed to investigate the influence of phase transformation induced by mechanical load. The *SMA* helical springs are named martensite and austenite helical springs, respectively, attributed to the stable phase at room temperature. The characterization includes differential scanning calorimeter (*DSC*) and quasi static tensile tests of the respective *SMAs* elements.

After that, an experimental apparatus is built considering the piezoelectric harvester in a cantilever beam configuration and connected to one of the *SMAs* helical springs at the free end. The system is exited in the transverse direction and output power is measured in an external electrical resistance element. Experiments are carried out in order to obtain fundamental parameters for the mathematical modeling and characterize the harvester when submitted to a dynamical load.

The mathematical modeling starts with the proposed *SMA* constitutive model with assumed kinetic phase transformation development. The model is based on Brinson [34] model and uses two consecutive second-order polynomials functions to represent each SMA phase transformation

in prescribed strain problems. In addition, two new parameters are introduced which allow controlling of phase transformation response. In a first investigation, the proposed *SMA* model is evaluated for quasi-static conditions and dynamical load in a single degree of freedom mechanical oscillator. This model allows expressing the *SMA* constitutive relation in dynamical problems without the use of iterative algorithms.

The energy harvester is so represented by a single degree of freedom oscillator with discrete parameters submitted to base vibration and connected to an electrical circuit by a piezoelectric element. A second investigation evaluates the *SMA* martensite helical spring connected to the piezoelectric harvester. Phase transformation induced by temperature via Joules's effect is represented based on experimental characterization. Its influence on harvester output power frequency response is investigated through classical analytical equations, numerical simulations, and experimental tests.

The third investigation treats the piezoelectric harvester as a single degree of freedom model connected to the *SMA* austenite helical spring. Afterward, the system remains at constant temperature and *SMA* phase transformation is induced by initial pre-loads, and later, mechanical vibrations.

Chapter 5 deals with results and discussion. The objective of this section is to compare experimental results with simulations employing the mathematical modeling described in Chapter 4 (Methodology). Results explore the proposed model capacity to represent SMA-piezoelectric energy harvester behavior and also highlights the system frequency response dependence on temperature and mechanical load. In sequence, the synergistic use of piezoelectric materials and shape memory alloys for energy harvesting is investigated for different configurations. The harvester performance is investigated considering the output power in frequency response diagrams and also for stationary forcing frequency. Numerical, analytical, and experimental analyses are developed and a good theoretical-experimental correlation is obtained.

Chapter 6 presents conclusions and perspective for future works. The contributions to the development of adaptable harvesters devices that uses smart materials are of concern. In addition, the evaluation of *SMA* phase transformation induced by temperature and mechanical load is compared by considering the energy used to promote the phase transformation.

2 Energy Harvesting

Over the last twenty years, energy harvesting received great attention in science becoming interdisciplinary and multi-field in engineering. It is important to state that energy should not be referred to as created or even lost in common engineering applications. One kind of energy can only be converted into another being a consequence of human action or natural process [1, 3]. Scientific development shows up as dependent on electrical energy motivating human beings to figure out different methods to convert different kinds of energy into electrical power. This chapter deals with aspects and literature reviews about energy harvesting with a focus on mechanical vibration and piezoelectric materials.

2.1 Aspects of Energy Harvesting

The seeks for energy harvesting starts with the necessity to power supply devices and machines. Different devices and machines present intrinsic necessities and project restrictions. The identification of energy sources available in nature is a determinant step in energy harvesting. Usually, this kind of energy must be converted to a convenient form via a harvester device or system. [35].

The concept of energy storage means that energy can be converted to a convenient kind and contained in an element (batteries or fuel cells) to provide some amount of this energy in order to do work. Energy transport can be understood when energy is converted in one local spot and moved to another for a determined workable reason. An example of this is cities where energy supply comes from power stations located kilometers far away.

Large scales of energy harvesting methods pretend to supply large demands in cities for transport, ambient conditioning, and industrial complexes. Fig. 2.1 shows examples of sources and methods for energy harvesting in power stations around the globe. The total electrical power capacity is mentioned and can be attributed to the state of scientific development of each method.

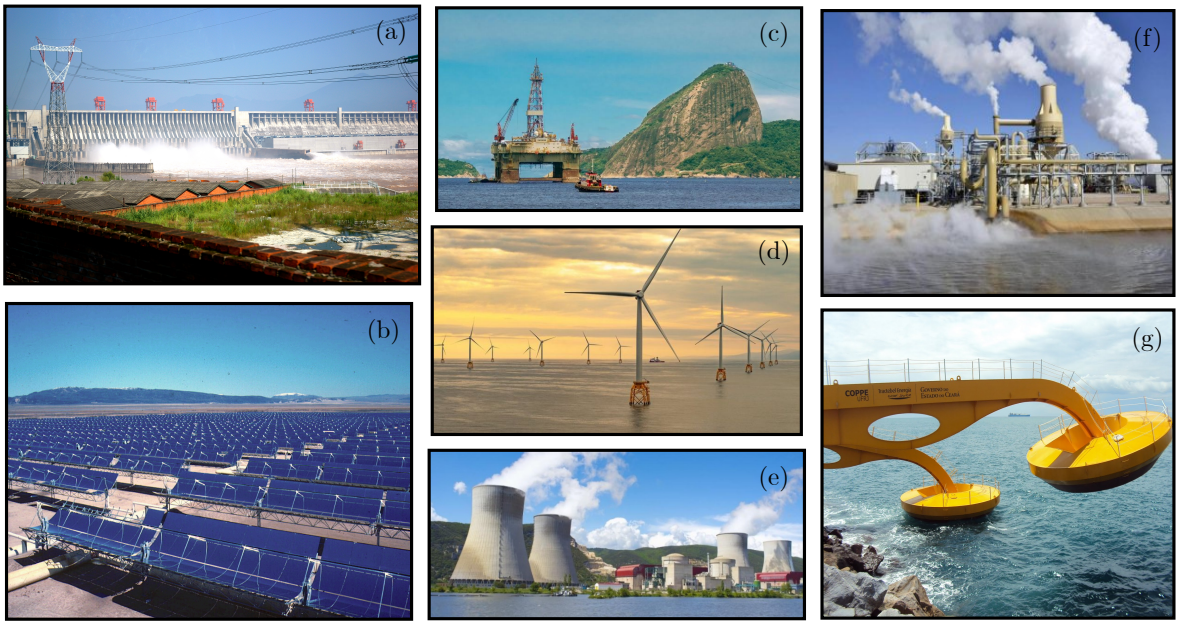


Fig. 2.1: Methods for energy harvesting and electrical power conversion capacity. (a) Hydroelectric at China - 22500 MW [36]. (b) Solar power plant complex at the USA - 354 MW [37]. (c) Offshore oil extraction at Brazil [38] - 100 MW [39]. (d) Ocean wind farm at Scotland - 588 MW [40]. (e) Nuclear power plant at France - 4250 MW [41]. (f) Geothermal energy harvesting in Iran - 230 KW [42]. (g) Ocean energy harvesting at Brazil - 100 KW [43].

An ancient method for energy conversion is the process of burning wood, coal, oil, and natural gases. It can be considered the principle of the first mechanical engines where heat is converted into kinetic energy. Fossil fuels become the primary energy source taking a huge majority in overall energy consumption [35, 44]. As a consequence, alternative sources and methods arise in a group named alternative energies. It includes all kinds of energy not based on fossil fuels [45]. Fig. 2.2 show the domain of oil, coal, and natural gas compared to other resources in the world's total energy supply from 1990 to 2018.

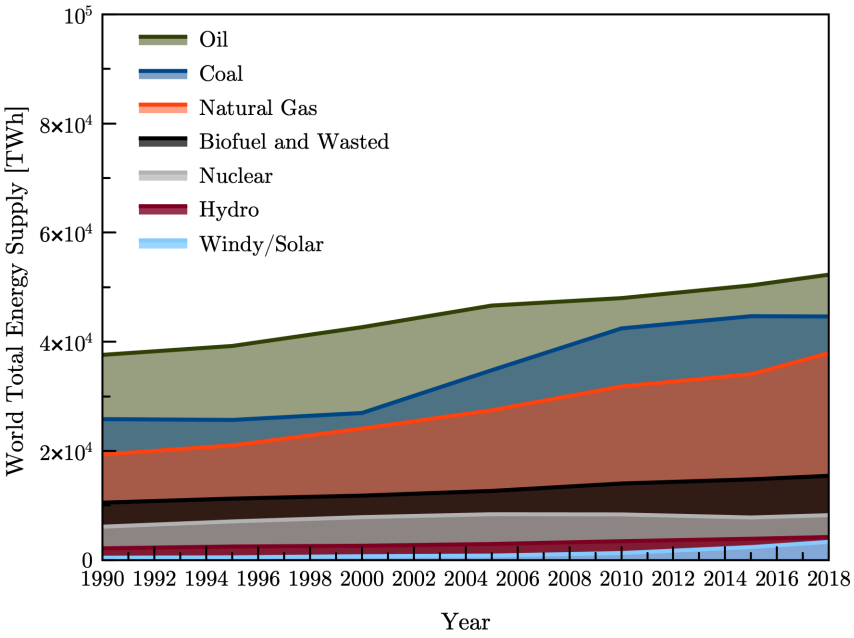


Fig. 2.2: Total world energy supply by resource from 1990 to 2018. [45]

A polemic alternative resource in discussion is nuclear energy. The massive energy contained inside radioactive atoms is well known. However, all the dangers involved in nuclear power plants and accidents that happened in history put this source of energy on a hard way path for development [44, 35]. Despite all difficulties, enforces in materials science keep developing nuclear energy harvesting methods with improvements in reliability, safety, and economics [46].

Fossil fuels and radioactive materials are based on finite resources and they also produce as a result of the harvesting process, an undesirable residue. For these reasons, they can be considered nonrenewable and nonclean energy resources.

On the other hand, the sun is considered a renewable and clean energy source due to its long period of existence and free of pollutant emissions in the conversion process. Also, is considered the major power source available on the earth. Nevertheless, it represents just a small part of the total amount of energy converted on a global scale [35] (see Fig. 2.2). A photovoltaic cell is able to convert sunlight into electricity by the physical process named photoelectric effect. Light is absorbed and transferred to electrons in the atoms of photovoltaic cells. With the increasing energy, electrons escape from their normal positions promoting an electrical flow in an electrical circuit associated [47].

Wind, as the airflow between low and high-pressure regions, is considered a clean and sustainable energy source since it is renewable, widely distributed, and plentiful. Windmills used for

electricity harvesting are called wind turbines. The blades are connected to a shaft and the shaft to an electric generator. Their cycle consists of the capture of the wind kinetic energy and its conversion into electrical power [47]. Wind energy harvesting arises as a great alternative for diverse areas with a high incidence of strong wind.

Gravitational energy harvesting can integrate hydroelectricity, tidal, and ocean waves. Hydroelectricity presents massive potential for energy harvesting. Huge power stations are able to convert sufficient energy for entire cities and towns. Water is stored in reservoirs and drooped from certain altitudes activating turbines for energy harvesting. The main advantage of this method is the natural capability of the hydro plant to respond to an increase or decrease in demand [44]. The great challenge of this method is that hydro stations can drastically modify the landscaping and biodiversity and interferes with the local ecosystem with a high potential for irreversible damage. A carefully and detailed study of mentioned limitations is crucial for hydroelectricity development.

Tidal and ocean waves energy harvesting is considered one of the most feasible future technologies. Energy from ocean waves is converted from the potential and kinetic energy of the natural oscillation of ocean waves into electricity. However, the construction cost of wave power plants is not mature enough for large-scale installations due to the complexities, sea conditions, and difficulty of interconnection and transmission of electricity through turbulent water bodies [47, 44].

Fig. 2.3(a) shows a total world electricity consumption while Fig. 2.3(b) deals with the contribution by mentioned methods in a period from 1990 to 2018. Both of them show continued growth with significant rise curves. However, the total amount of energy harvested via alternative sources is still far from the total world requirement. It becomes evident the relation between how much energy is consumed and how much alternative sources are able to develop in order to attend to this demand.

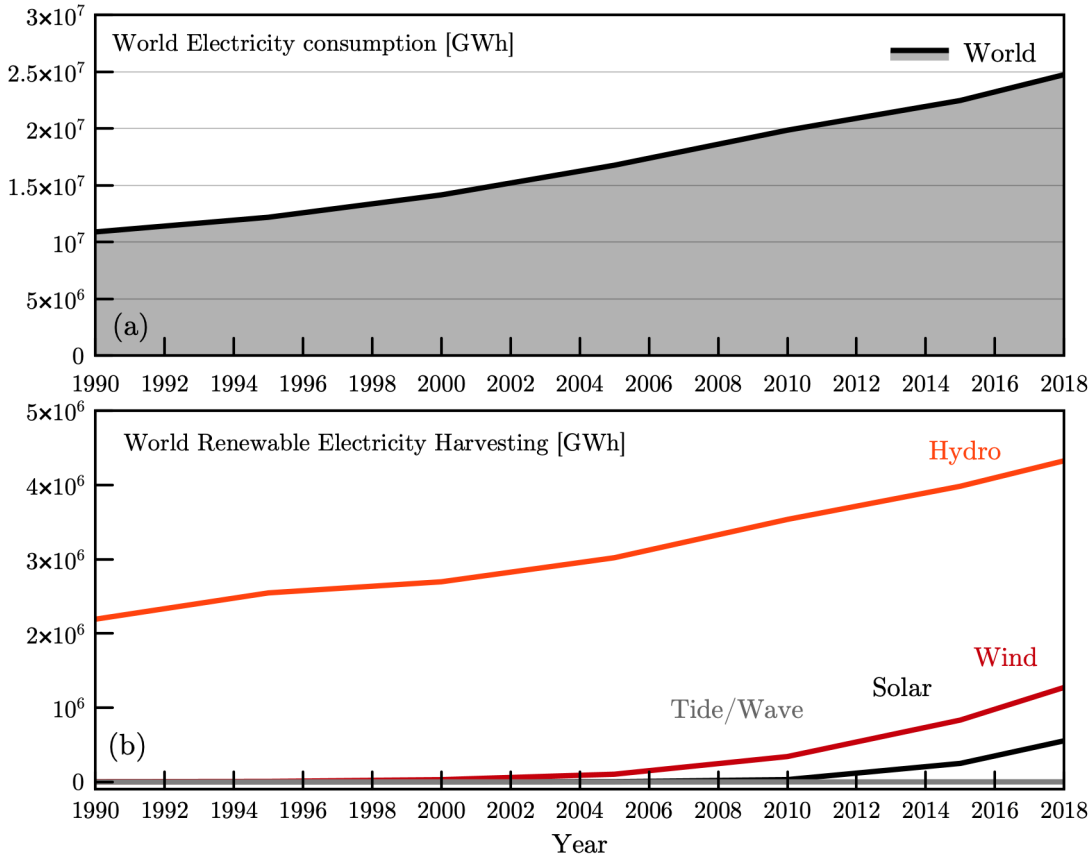


Fig. 2.3: Electrical energy evaluation from 1990 to 2018.(a) Total world energy consumption. (b) Renewable electricity harvesting. [45]

Those methods for energy harvesting can be configured for even large or small scale sizes. In addition, the advance in microelectronic mechanical systems *(MEMS)* brings the concept of the internet of things *(IoT)* and wireless sensor network *(WSNW)* and suggests different methods to power supply low power consumption devices [48, 49, 50]. So, kinetic energy available in the environment appears as a great energy resource to power supply *MEMS* and has motivated studies and research in mechanical vibration energy harvesting all over the globe. [18, 48, 51].

2.2 Vibration Energy Harvesting

Literature presents several authors who proposed definitions for vibration energy harvesting considering a source of mechanical vibrations available in the environment, a device able to convert kinetic energy into electrical power, and an electric circuit to rectify the signal. [5, 20, 21, 52, 53].

Table 1 indicates vibration sources and their respective maximum acceleration levels and the frequency peaks where it occurs. The basis of Table 1 is Khan and Qadir [54] which contains most

of the items in it. The authors also classify the vibration sources according to their intensity into low, medium, and high categories. This is relevant information that helps in vibration harvester's designs and projects.

Table 1: Vibration sources associated to maximum acceleration level and frequency peaks. Adapted from [54].

Category	Vibration energy source	Max. Accel. (m/s^2)	Freq. peak (Hz)	Ref.
Low	Refrigerator	0.09	110	[55]
($\leq$ 0.9 m/s^2)	Surroundings (busy office)	0.19	100	[56]
	Boat	0.2	-	[57]
	Metallic Stairs	0.29	28	[58]
	Trees	0.01-0.49	0.1-0.8	[18, 59]
	Wash machine	0.49	109	[60]
	A building wall	0.49	10	[61]
	Window near a busy road	0.68	100	[56]
	Van, bus, Train, tractor	0.5-0.7	-	[57]
	Drill machine (100 rpm)	0.78	150	[55]
	Drill machine (200 rpm)	0.88	178	[55]
Medium	Bicycle	1	-	[57]
(0.9-9.81 m/s^2)	Airplane cabin	1.07	12.7	[54]
	Agricultural vehicle	1.5	-	[57]
	Air conditioner (compressor)	2.06	59	[56, 18]
	Doors frame vibration	3.04	125	[56]
	Automobile panel	3.04	13	[56]
	Automobile compartment	5.98	33	[62]
High	Automobile engine	12	200	[62]
($>$ 9.81 m/s^2)	Centrifugal fan	14.7	307	[63]
	Drone	39.2	70-230	[64]
	Electric motor	0.01-49	0.50-80	[59]
	Container shipping	91.9	1-15	[65]
	Human motion	0.5-98.1	0.1-10	[59]

Toprak and Tigli [66] and Palosaari [67] present diagrams to show the increased number of publications about electrostatic, electromagnetic, and piezoelectric energy harvesting in the period

between 2003 and 2016. Beeby and White [48] also show an increase in vibration energy harvesting research and attribute this effect to the exponential increase in the number of publications about wireless sensor networks during this period. In order to develop this approach, Fig. 2.4 refers to current research in January 2021 from Google.Scholar [68] database and compares the most studied methods for vibration energy harvesting. Electromagnetic energy harvesting presents the major number of publications reaching more than the sum of the other three methods. It is also possible to note that piezoelectric energy harvesting has already passed the mark of 15 thousand publications.

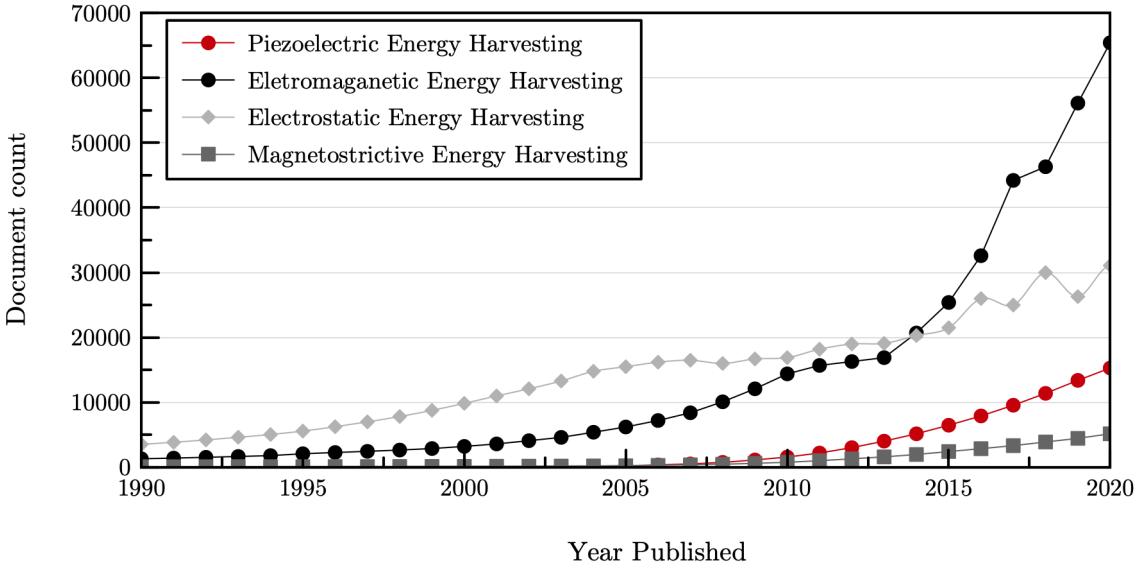


Fig. 2.4: Number of publications about vibration energy harvesting from 1990 to 2020 [68].

Another database called Lens.org [69] gives similar analyses and explores academic research in detail. Fig. 2.5 correlates the number of academic publications with the year of publication and highlights the types of publications from 1990 until 2020, collected in May of 2021. This analysis enhances the idea that since the 2000 year the number of publications in *"vibration energy harvesting"* experiences an exponential increase presenting a maximum number in 2018. Note in Fig. 2.5 the relevance of journal articles in overall academic production. It represents the majority of scientific production in this theme.

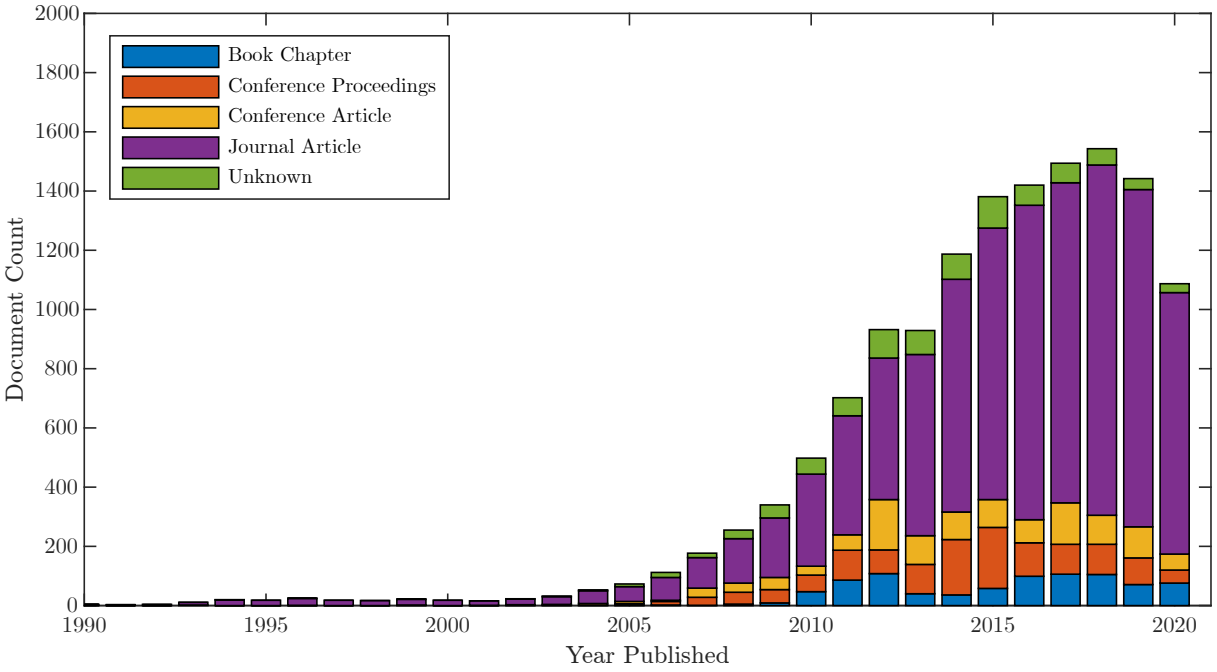


Fig. 2.5: Number of publications about vibration energy harvesting from 1990 to 2020 [69].

Fig. 2.6 lists the publishers who have the most published articles on *"vibration energy harvesting"*. The great majority stays concentrated in the top 3: Elsevier, IEEE, and IOP Publishing according to Lens.org [69]. Fig. 2.6 also shows that there is a wide spread of publications ("*Others*") in publishers than the main publishers.

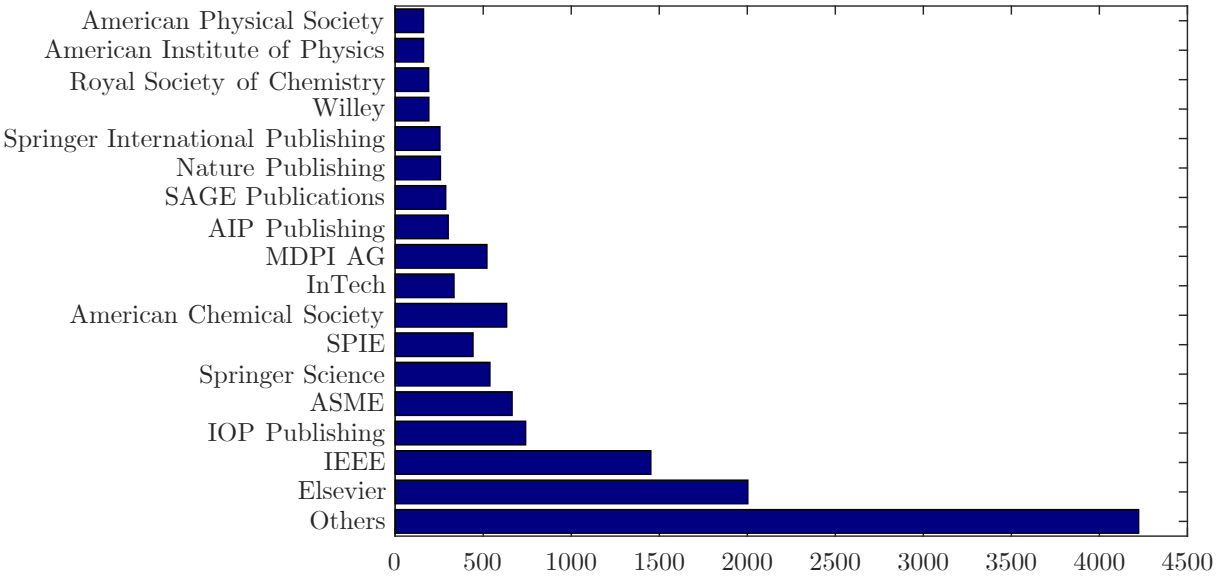


Fig. 2.6: Major publishers associated to the topic of vibration energy harvesting [69].

Fig. 2.7 present the scientific journals that published the larger number of scientific papers. With the exception of Smart Materials and Structures, which has the largest number of publications,

the other journals in the Top 10 for "*vibration energy harvesting*" have similar numbers.

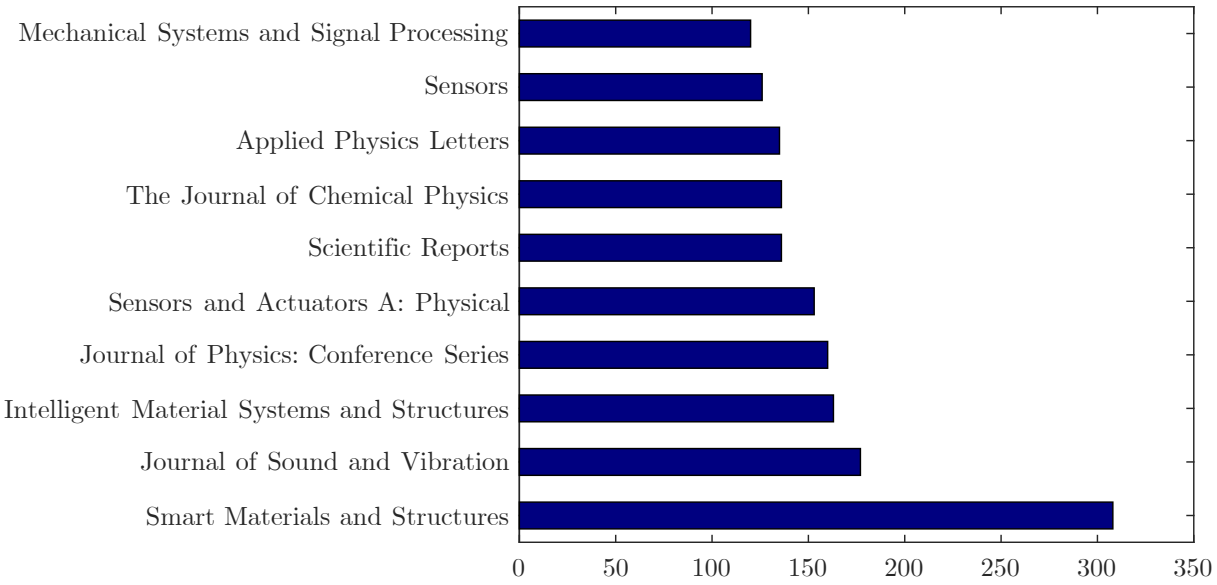


Fig. 2.7: Top journals about vibration energy harvesting research [69].

Fig. 2.8 deals with the most relevant fields of study in vibration energy harvesting. Piezoelectricity occupies the 5^{th} place in Lens.org ranking, indicating the importance of this area.

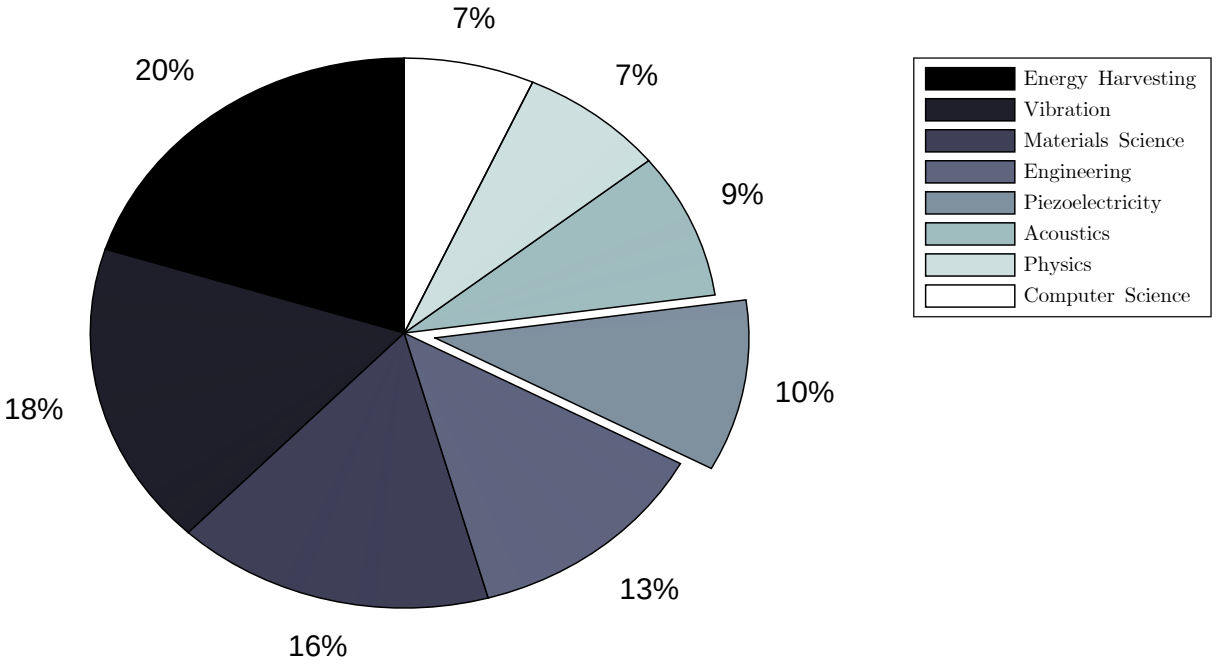


Fig. 2.8: Most relevant fields of study on vibration energy harvesting [69].

Fig. 2.9 indicates that most scientific research is developed by the United States and China. Both represent half of the total publications. The United Kingdom follows in third place in "*vibration energy harvesting*" research while other expressive countries fill the rest of the chart.

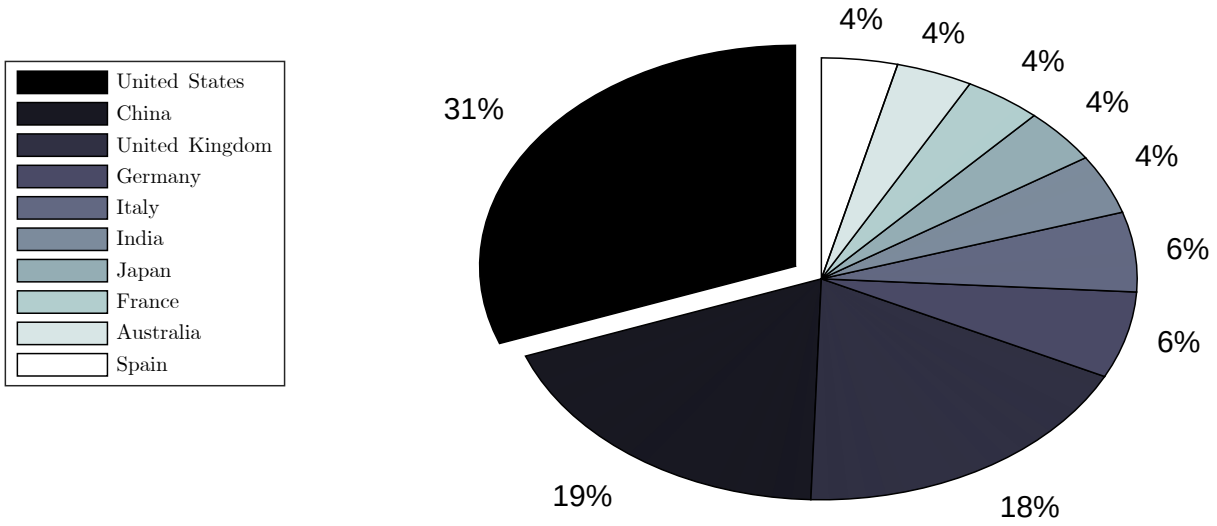


Fig. 2.9: Countries with more impact in vibration energy harvesting research by percentage [69].

Recent advances in *MEMS*, *IOT* and smart power management concept brought down the power requirements for sensors and electronic devices. Table 2 provide a summary of typical electronic devices with their respective power requirement. It should be pointed out that the conditions of use are determinant to establishing the total power needed to keep the device operating at high performance. So, Table 2 considers the average power requirement for specific models of low power devices. In this sense, vibration energy harvesting can be considered as an alternative to power supply or charge a battery for intermittent operation in those kinds of sensors.

Table 2: Summary power consumption of typical electronic sensors and devices.

Sensor / Device	Required power (mW)	Reference
Bluetooth transceiver	100	[70]
GPS receiver chip	15	[71, 72]
Motion sensor	14.4	[72, 73]
Strain gauge	9	[74]
Cell phone (stand by)	8	[71, 72]
Temperature sensor	0.02 / 0.5-5	[71, 72] / [75]
CO_2 sensor	3.5	[76]
Acceleration sensor	0.3-3	[71, 72, 75, 77]
Humidity sensor	1	[71, 72, 78]
Pressure sensor	0.5	[71, 72, 79]
Cardiac peacemaker	0.1	[80]
Hearing aid	0.07-0.1	[70, 80]
Electronic watch	0.001	[70, 80]
A-D conversion	0.001	[71, 72, 81]

Next subsections describe the principal methods for vibration energy harvesting. Among different methods to convert mechanical vibration kinetic energy into electrical power, Cook-Chennault et al. [82] compares in a power density × voltage diagram different methods for energy harvesting where piezoelectric materials fill the major area in the diagram. The combination of piezoelectric materials with mechanical vibrations and the significant increase in *MEMS* establishes an important field, which is the focus of this work, called piezoelectric energy harvesting.

2.2.1 Electrostatic Energy Harvesting

Electrostatic energy harvesting is a representative method usually applied to power supply MEMS [54]. The principle of electrostatic conversion involves the variable capacitor concept which consists of two conductors separated by a dielectric material. Conductors are placed in an electric field and the conductors move in relation to each other and an electrical current can be detected [83, 84].

In this way, Beeby and O'donnell [83] presents an emblematic study with emphasis on electrostatic elements for vibration energy harvesting. The output voltages produced by an electrostatic

harvester are relatively high ($> 10\ V$) [48, 85]. A great advantage of the electrostatic device is that harvester energy density can significantly increase by decreasing the capacitor volume, thereby facilitating miniaturization. The major disadvantage of this method is that an external voltage source is required to create an electric field [84].

Recent research show improvements in electrostatic energy harvesting techniques. Zhang et al. [86] studies a design with a dual resonant structure, which consists of two cantilever-mass subsystems each with a mass attached at the free edge of a cantilever. Tao et al. [87] presents a sandwich-structured MEMS with two opposite charges integrated into a single electrostatic device. Compared to a conventional two-plate configuration where the maximum charge can only be induced when the movable mass reaches its lowest position, the proposed harvester is capable of creating maximum charge induction at both the highest and the lowest extremes, leading to an enhanced output performance. Miljkovic et al. [88] demonstrates a surface engineered platform with the expectation to be low cost and scalable for different levels of energy harvesting and electric power storage.

2.2.2 Electromagnetic Energy Harvesting

In a similar way, electromagnetic harvesters have been used for many years. Basically, a coil within a magnetic field moves and electrical current flows according to Faraday's law. This mechanism is utilized to convert motion (vibration) into electrical energy and no separate voltage source is required [84]. There exist a series of spring/mass configurations, which can be assembled with various types of magnetic materials. The output power response can consist of a high electrical current with low voltage or high voltages with low electrical current. Comparatively, with other methods, electromagnetic energy harvesting is characterized by work with high output electrical current values and low voltages ($< 1\ V$) [48, 85].

Mitcheson et al. [89] worked on design guides for optimizing several forms of vibration-driven MEMS devices with electromagnetic elements in the early 2000 years. Wang and H. [90] shows an electromagnetic energy harvester to convert fluid flow-induced vibration into electrical power by electromagnetic induction. The authors show an instantaneous power of 0.4 μW under an excitation frequency of 30 Hz and a pressure amplitude of 254 Pa in the pressure chamber. Carneiro et al. [91] presents a review analysis focused on electromagnetic energy harvesting using magnetic levitation architectures. Electric power densities around 8 mW/cm^3 have been achieved and maximum output power of 6.5 W for a volume up to 235 cm^3. Authors also treat the potential of electromagnetic harvesters for large-scale and small-scale applications.

2.2.3 Magnetostrictive Energy Harvesting

Smart materials take an important position in vibration energy harvesting. Examples of smart materials are Magnetoreologic fluids (present a Newtonian behavior without the presence of a magnetic field and nonlinear behavior when an electromagnetic field is applied [92, 93]. Magnetostrictive materials (present magneto-mechanical coupling) [94] and shape memory alloys (thermomechanical coupling) [31, 33].

Narita and Fox [95] gives an overview of energy harvesting in smart materials and systems. A magnetostrictive material submitted to a variable strain field can be surrounded by a pickup coil on which electrical current is induced due to the magnetic field according to Faraday's law.

Wang and Yuan [94] present results of experiments with magnetostrictive materials for energy harvesting. The maximum output power and power density can reach 200 μW and 900 $\mu W/cm^3$, respectively, at a frequency of 58 Hz and Clemente et al. [96] uses magnetostrictive energy harvesters for a bridge structural health monitoring. Mechanical oscillations induced by traffic passing are converted into electrical power. Magnetostrictive energy harvesting still has a lot to be explored in the next decades with the high development of materials sciences and smart materials properties.

2.2.4 Piezoelectric Energy Harvesting

Piezoelectric materials are classified as smart materials due to electromechanical coupling. When submitted to a mechanical loading, an electrical polarization is induced and it is a function of the applied mechanical stress (direct effect). Piezoelectric materials also exhibit the converse piezoelectric effect (develops shape deformation when an electric field is applied) [5, 18, 20, 25].

First experimental register of piezoelectric effect dates of 1880 by Jacques and Pierre Currie, a phenomenon observed in crystals such as tourmaline, quartz, or Rochelle salt. The direct piezoelectric effect occurs in ferroelectric materials presenting electrical charge polarization able to is induced by mechanical load. At a free stress state, the internal electrical dipoles are in equilibrium. The mechanical load promotes distortion in electrical dipoles resulting in electrical charge movement. Fig. 2.10 illustrates a generic piezoelectric quartz crystalline cell formed by oxygen (negative charge) and silicon atoms (positive charges). Tensile and compression loads are responsible for dipole distortion in the opposite direction which is the principle of piezoelectric energy harvesting.

The total amount of electrical power obtained from natural piezoelectric materials did not meet the machines' energy demand at its discovery time. Also, these crystals present high stiffness

properties and fragile behavior susceptible to crack failure. The first engineer application of piezoelectric materials is in 1917 by Paul Langevin in an ultrasonic device (sonar) to detect submarines in the first world war. The device consisted of a composite plate made of steel and piezoelectric quartz, and a hydrophone to detect the returned echo.

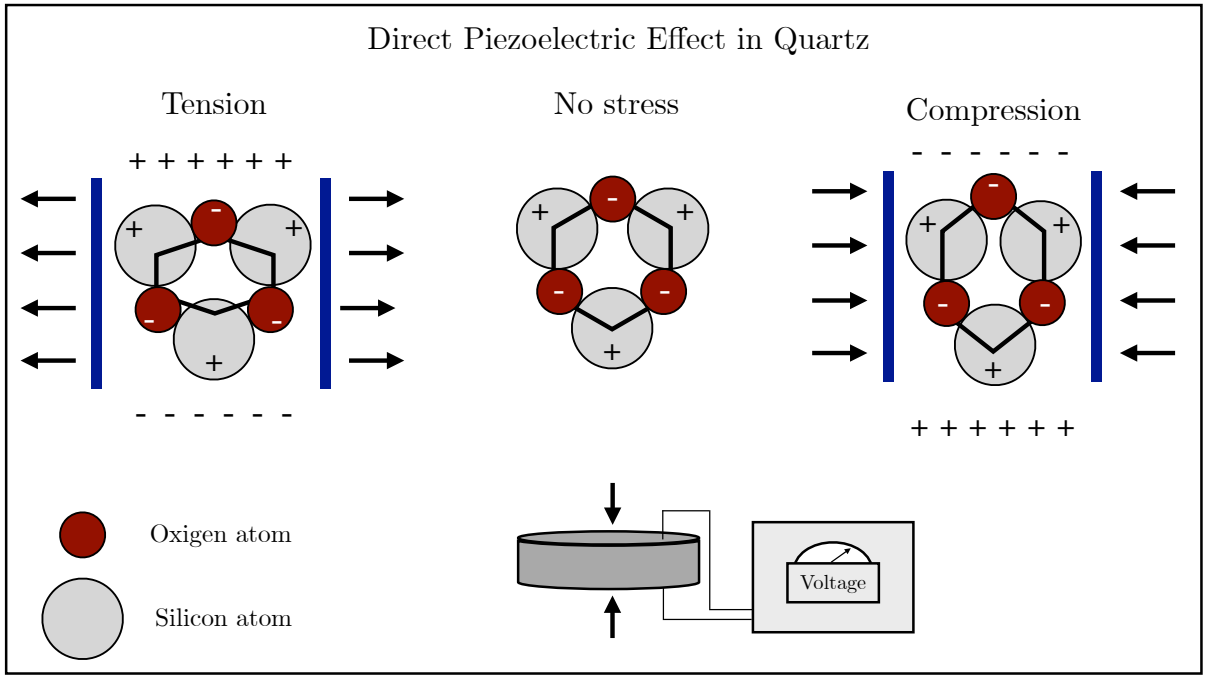


Fig. 2.10: Piezoelectric quartz crystalline cell and direct effect representation.

Significant improvements in materials sciences allow now to manufacture synthetic piezoelectric materials in a controlled environment resulting in high electromechanical coupling and mechanical strength, for example, PZTs (lead zirconate titanate). In addition, PVDF (vinylidene polyfluorene) represents another synthetic piezoelectric material with low electromechanical coupling but significant flexibility being able to reach high levels of deformation. The use of piezoelectric materials to power machines and devices considerably increased since 1990. Fig. 2.11 shows examples of self-powered devices that use piezoelectric materials.

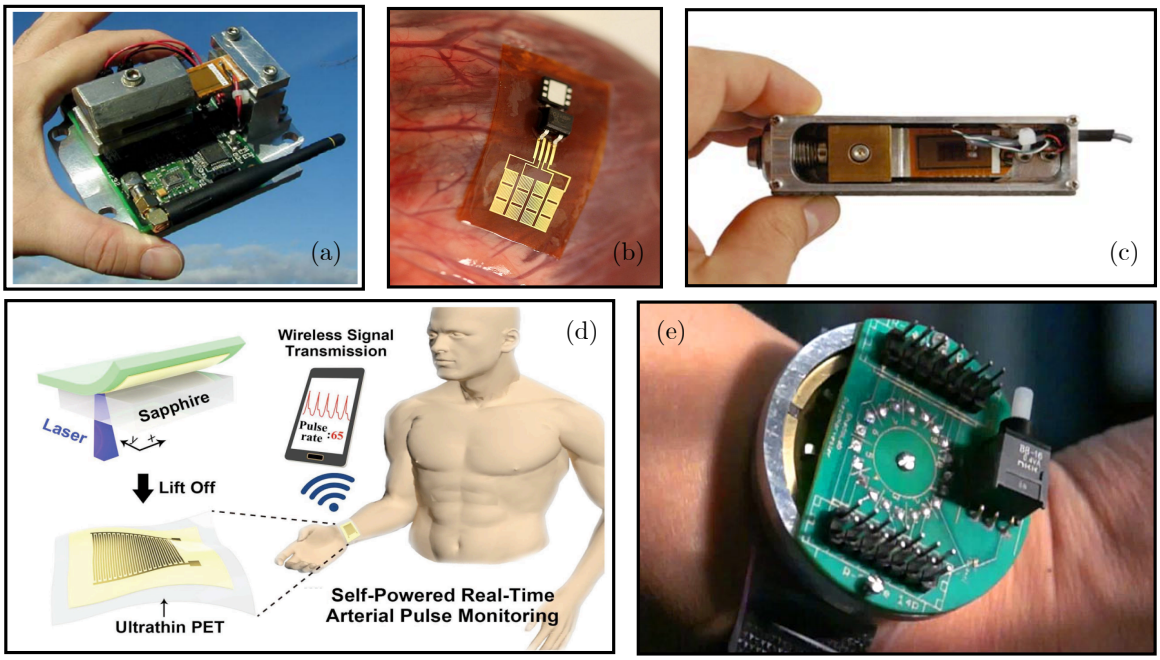


Fig. 2.11: Self powered piezoelectric devices. (a) Temperature and humidity sensor [5]. (b) Cardiac pacemaker [14]. (c) Load cell sensor [97]. (d) Arterial pulse monitor [12]. (e) Smart watch [98].

Contributions for piezoelectric energy harvesting can be found in several reviews for the theme including history, fabrications process, and applications [15, 53, 99, 100, 101]. The main configuration of a piezoelectric energy harvester consists of a cantilever beam submitted to base vibration motion in the transverse direction.

Fig. 2.12 shows examples of experimental research in early piezoelectric harvesting studies. The cantilever beam configuration is exploited with a focus on the relative displacement between the clamped base and the free end which is responsible for beam deformation. The relative displacement amplitude can be observed as a function of the base vibration amplitude.

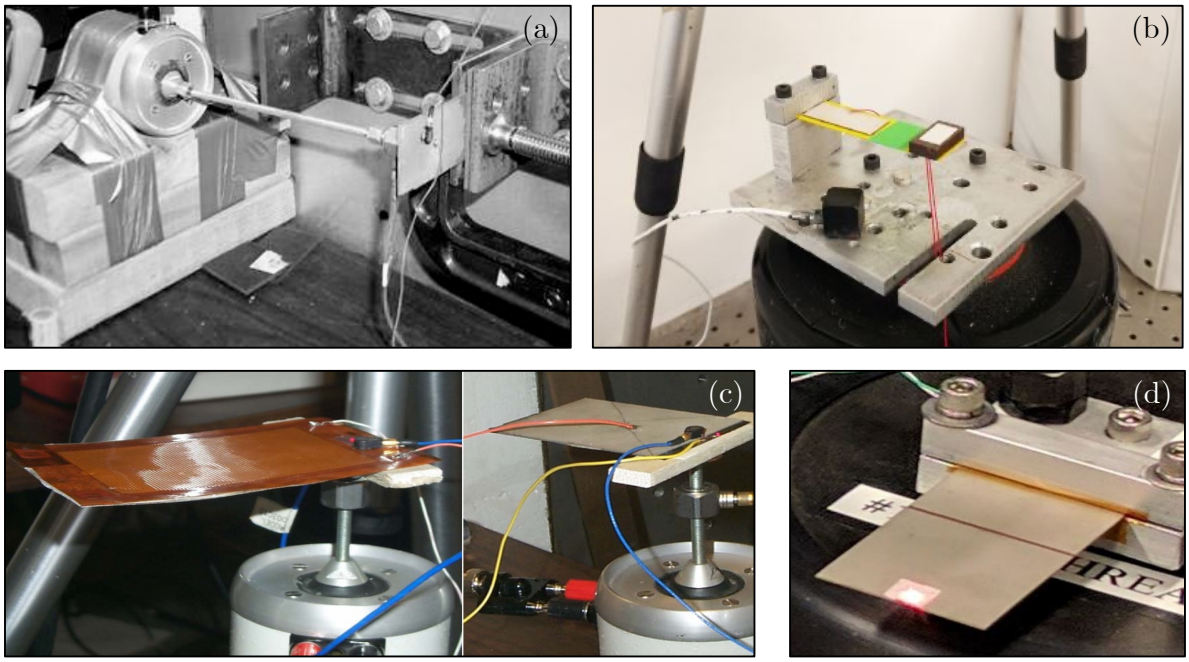


Fig. 2.12: Traditional cantilever beam configuration in piezoelectric energy harvesting experiments. (a) [16]. (b) [17]. (c) [102]. (d) [102].

With the objective to improve the mechanical strength and keep the electromechanical properties, piezoelectric harvesters are designed in layers containing a structural substrate and thin sheets of piezoelectric material. So, a piezoelectric cantilever beam can be characterized as a composite beam by its number of piezoelectric layers [18, 19, 101]. The most common configurations are unimorph and bimorph which present one and two layers with piezoelectric properties and are shown in Fig. 2.13(a) and (b), respectively.

Also, piezoelectric cantilever beams can present operation mode according to load and polarization direction. The most common is d_{31} and d_{33} which means that load and polarization occur in transverse and axial planes as shown in Fig. 2.13(c) and (d), respectively. The literature points out that the d_{31} mode configuration is more usual in piezoelectric harvesters.

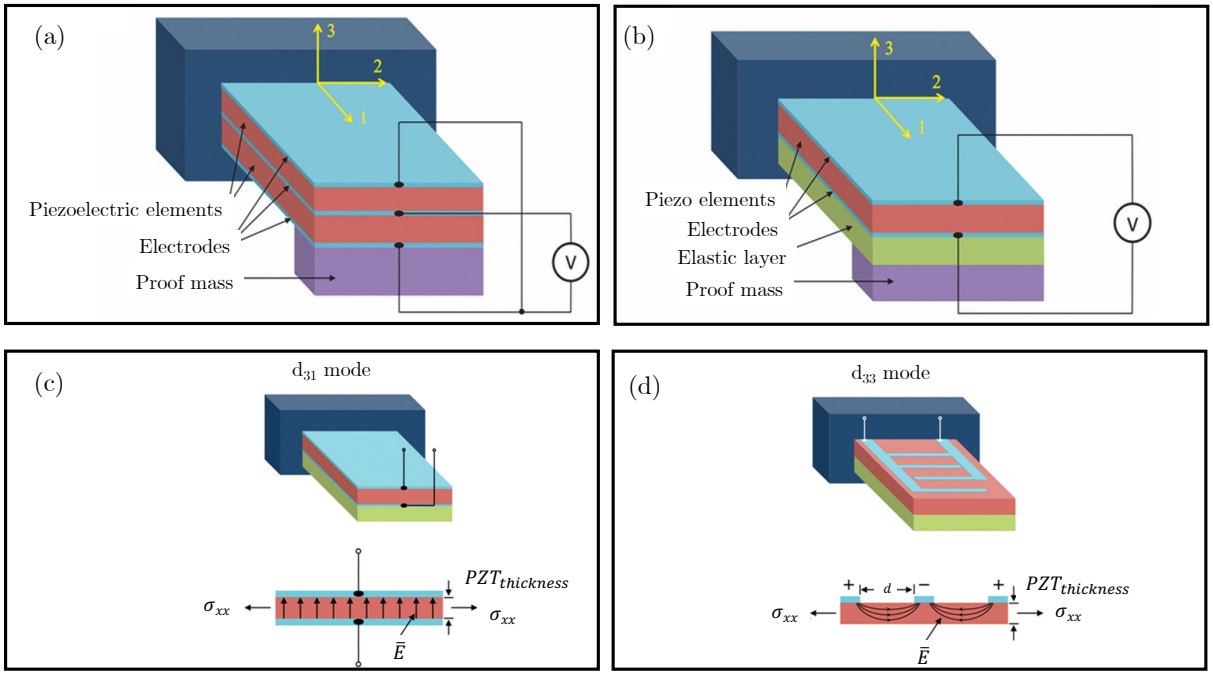


Fig. 2.13: Basic structure of piezoelectric energy harvesters: (a) Bimorph structure, (b) Unimorph structure. Modes of piezoelectric conversion of input mechanical strain depending on the relative direction of the stress and the electric field. (c) d_{31} mode. (d) d_{33} mode. Adapted from [101].

In a dynamical load environment, the beam relative displacement of clamped and free end is responsible for beam deflection promoting the direct piezoelectric effect, and consequently, an alternated electrical current. The first law of thermodynamics deals with the principle of conservation of energy and can be applied for a linear continuum piezoelectric element as follows [5, 27]:

$$\dot{U} = \sigma_{ij}\dot{\epsilon}_{ij} + \bar{E}_i\dot{D}_i \tag{1}$$

where U means the stored energy density of the piezoelectric continuum during load and unload, σ_{ij} is the stress tensor, ϵ_{ij} is the strain tensor, $\bar{E}_i$ is the electric field vector, D_i is the electric displacement tensor and the over dot represents differentiation with respect to time ($\dot{\bullet} = \frac{d\bullet}{dt}$). Therefore, the electric enthalpy density H is given by:

$$H = U + \bar{E}_i D_i \tag{2}$$

substituting Eq. (1) into derivative of Eq. (2) gives:

$$\dot{H} = \sigma_{ij}\dot{\epsilon}_{ij} + D_i\dot{\bar{E}}_i \tag{3}$$

implies $H = H(\epsilon_{ij}, \bar{E}_i)$ and stress and electrical displacement tensors can be derived from Eq. (2) as Erturk and Inman [5]:

$$\sigma_{ij} = \frac{\partial H}{\partial \epsilon_{ij}}, \qquad D_i = -\frac{\partial H}{\partial \bar{E}_i} \tag{4}$$

Equation of the electric enthalpy density in the linearized theory of piezoelectricity can be expressed as:

$$H = \frac{1}{2} C^{\bar{E}}_{ijkl} \epsilon_{ij} \epsilon_{kl} - e_{kij} \bar{E}_k \epsilon_{ij} - \frac{1}{2} \mu^{\epsilon}_{ij} \bar{E}_i \bar{E}_j \tag{5}$$

where $C^{\bar{E}}_{ijkl}$, e_{kij} and μ^{ϵ}_{ij} represent the elastic, piezoelectric, and permittivity constants, respectively. Superscripts $\bar{E}$ and ϵ denote that respective constants are evaluated at the constant electric field and constant strain, respectively.

Considering $\partial \epsilon_{ij} / \partial \epsilon_{ji} = \delta_{ij}$ where δ_{ij} is *Kronecker Delta* and assuming δ_{ij} is equal to one when $_i$ equal to $_j$ and zero when $_i$ different to $_j$, leads to:

$$\sigma_{ij} = C^{\bar{E}}_{ijkl} \epsilon_{kl} - e_{kij} \bar{E}_k \tag{6}$$

$$D_i = e_{ikl} \epsilon_{kl} + \mu^{\epsilon}_{ik} \bar{E}_k \tag{7}$$

which represents the linear constitutive equations for an arbitrary piezoelectric element.

Piezoelectric energy harvesting studies start with Williams and Yates [22]. Authors assume the harvester physical model as a single degree of freedom (SDOF) with lumped parameters submitted to base vibration. Piezoelectric coupling is represented by an extra dissipative element. Later, Du Toit et al. [18] considers the harvester as a mechanical oscillator coupled to an external electrical circuit by a piezoelectric element. So, Eq. (6) and Eq. (7) can be expressed in *Voigt* notation for a cantilever piezoelectric beam in d_{31} mode as:

$$\sigma_1 = C^{\bar{E}}_{11} \epsilon_1 - e_{31} E_3 \tag{8}$$

$$D_3 = e_{31} \epsilon_1 + \mu^{\epsilon}_{33} E_3 \tag{9}$$

The piezoelectric cantilever beam configuration can be so represented by a single degree of freedom system and movement equations expressed as two coupled differential equations as follow:

$$m\ddot{z} + c\dot{z} + kz - \theta V = -m\ddot{y} \tag{10}$$

$$\theta\dot{z} + C_p\dot{V} + \frac{V}{R} = 0 \tag{11}$$

where $y(t)$ is the base displacement, $z(t)$ is the relative displacement between base and body, and $V(t)$ is the electrical voltage in the piezoelectric element. The harmonic base excitation is expressed by $\ddot{y} = A_b \sin(\Omega t)$ where A_b represents the maximum base vibration amplitude and Ω is the driven frequency. m represents the body mass, c is the total damping coefficient, and k is a linear stiffness providing restore forces. θ, C_p, and R represent the electromechanical coupling, piezoelectric capacitance, and total load resistance for a closed-circuit condition.

Du Toit et al. [18] uses Laplace transforms to solve governing equations (Eq. (10) and Eq. (11)) and determine an analytical expression for the magnitudes of the displacement, voltage, and the harvested power as follow:

$$\left|\frac{z}{m\ddot{y}}\right| = \frac{1}{k}\frac{\sqrt{1+(r\nu)^2}}{\sqrt{(1-(1+2r\zeta)\nu^2)^2 + ((1+\kappa^2)r\nu + 2\zeta\nu - r\nu^3)^2}} \tag{12}$$

$$\left|\frac{V}{m\ddot{y}}\right| = \frac{1}{\theta}\frac{r\kappa^2\nu}{\sqrt{(1-(1+2r\zeta)\nu^2)^2 + ((1+\kappa^2)r\nu + 2\zeta\nu - r\nu^3)^2}} \tag{13}$$

$$\left|\frac{P_{out}}{m\ddot{y}^2}\right| = \frac{\Omega_N}{k}\frac{r\kappa^2\nu^2}{(1-(1+2r\zeta)\nu^2)^2 + ((1+\kappa^2)r\nu + 2\zeta\nu - r\nu^3)^2} \tag{14}$$

where $\Omega_N = \sqrt{k/m}$, $\zeta = c/(2\sqrt{mk})$, $r = \Omega_N R C_p$ and $\kappa^2 = \theta/(kC_p)$. $\nu = \Omega/\Omega_N$ represent the ratio between base vibration frequency and system natural frequency.

Fig. 2.14 shows a traditional single degree of freedom model with discrete parameters used to represent a piezoelectric energy harvester. Besides that, the associated frequency response using Du Toit et al. [18] parameters shows the narrow bandwidth. Authors adopt a criterion for bandwidth measurement that considers the frequency range associated with the maximum output power value multiplied by a factor of $\sqrt{2}/2$ (root mean square).

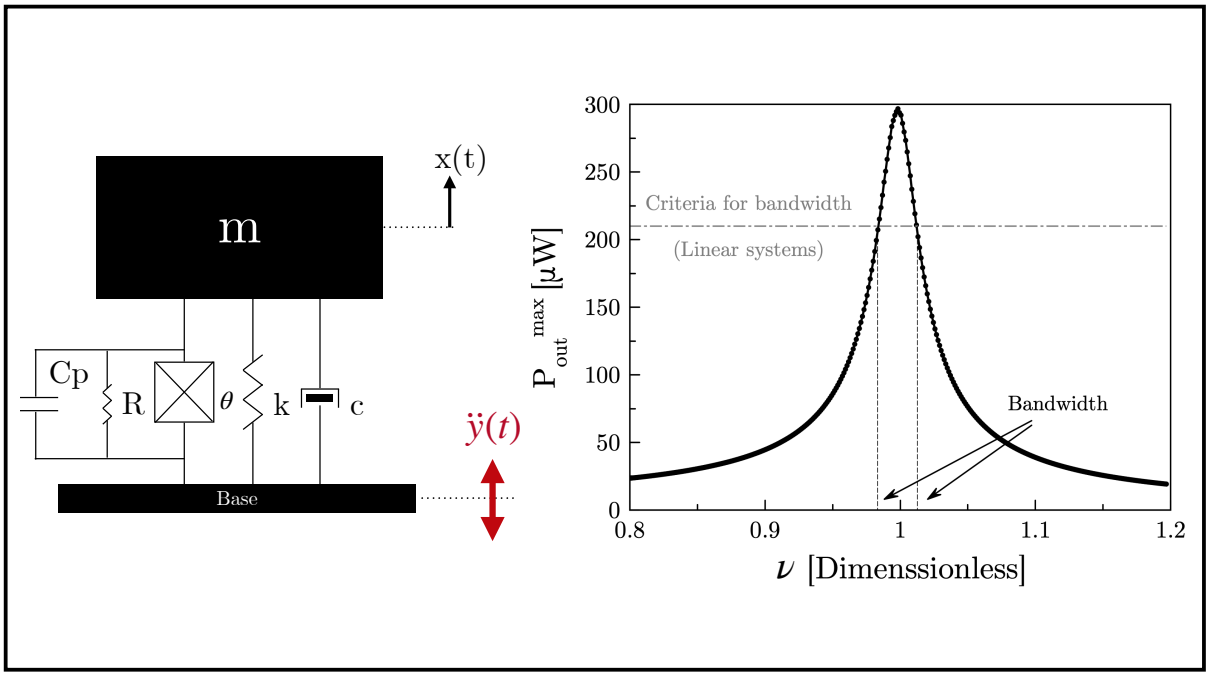


Fig. 2.14: Traditional piezoelectric energy harvester model represented by a single degree of freedom and discrete parameters. Adapted from [18]

Erturk and Inman [103] exposes a correction factor for lumped parameters modeling in piezoelectric cantilever beam energy harvesting analyses. Bhaskaran et al. [52] make progress in continuous cantilever beam modeling as a single degree of freedom. Yang et al. [102] derive an expression for linear vibration of cantilever beam and present discussion about efficiency in energy conversion rate.

Another interesting approach is the use of the finite element method (FEM) to solve differential equations with boundary conditions. de Marqui et al. [104] develops a finite element analysis for a piezoelectric cantilever beam with a resistance element and base vibration for energy harvesting in aircraft. Kumar et al. [105] use the first-order shear deformation theory and linear piezoelectric theory with FEM analysis to evaluate the performance of various piezoelectric materials for the unimorph cantilever configuration piezoelectric energy harvester. Ravi and Zilian [106] investigates the multiphysics interaction between fluid flow, electromechanical coupling of the piezoelectric materials, and the controlling electrical circuit. A fully three-dimensional coupled model is purposed and the weighted residuals method is applied to establish a mixed integral equation. Afterward, the Galerkin method is applied to integrate the monolithic model in the time domain. Wang and Ko [107] presents a numerical-experimental correlation for a vortex-induced vibration piezoelectric energy harvester. A finite element analysis is developed with the aim to estimate the converted voltage of a piezoelectric laminate sample subjected to a

distributed load. This method allows for the evaluation of the effects of piezoelectric sample dimensions, applied fluid pressure, and types of piezoelectric layers for energy harvester.

Experimental research in piezoelectric energy harvesting was earlier developed by Sodano et al. [16] and Sodano et al. [17] where authors evaluate the capability of commercial piezo patches to recharge nickel-metal batteries. Gambier et al. [108] compares piezoelectric, solar, and thermal energy harvesting for hybrid low-power devices supported with thin-film batteries. It is shown through measurements that 1 mAh of a thin-film battery can be charged in 20 min using solar energy (for a solar irradiance level of 223 W/m^2), in 40 min using thermal energy (for a temperature difference of 31 K) and in 8 h using vibration energy (for a harmonic base acceleration input of 0.5g at 56.4 Hz). Bouzelata et al. [109] purposes a rectifier bridge to promote a stable output voltage at 40 V and significantly decrease the time needed to fully recharge a storage unit such as a lead-acid type electrochemical battery.

The capability to remote measure and control sensitive devices inside of leaving beings is an attractive area for piezoelectric energy harvesting. Ali et al. [15] report a class of devices supplied by piezoelectricity for biomedicine applications such as artificial retina systems, hearing aids, and gastric monitor sensors. Dagdeviren et al. [14] deals with energy harvesting from an animal's heart, lungs, and diaphragm. This technique explores organs with large shape deformation and can represent a fundamental source of power for pacemakers and intra-body implants. In addition, Kumar et al. [110] shows a device for blood pressure variation measurements and Zhao et al. [111] a wearable electronic skin for tasty able to identify beverages or fruits taste supplied by piezoelectric elements and with no need for external electric power.

Human body movement can also be considered a potential source of kinetic energy [13]. Expeditions for civil or military missions present an increased demand for electrical power since a significant quantity of devices is carried. In this way, Granstorm et al. [112] finds sufficient energy in backpack straps for battery recharges. Bai et al. [113] and Yeo et al. [98] work for a self-powered smartwatch and caps. Kim et al. [114] evaluate nano portable and wearable electronics to be used in daily lives as sensors added to clothes with self-charging.

Fig. 2.15(a) shows Gao et al. [13] experimental study of piezoelectric energy harvesting from a knee. Results show that a harvester with only 307 g can generate 1.60 mW without increasing the human effort required for walking. Fig. 2.15(b) shows a high technological human exoskeleton used for rehabilitation where the seeking for reducing total weight is a crucial task. The exoskeleton prototype requires a series of sensors and actuators that could be autonomous avoiding or reducing the use of battery components by using piezoelectric elements to convert the

movement energy into electrical power.

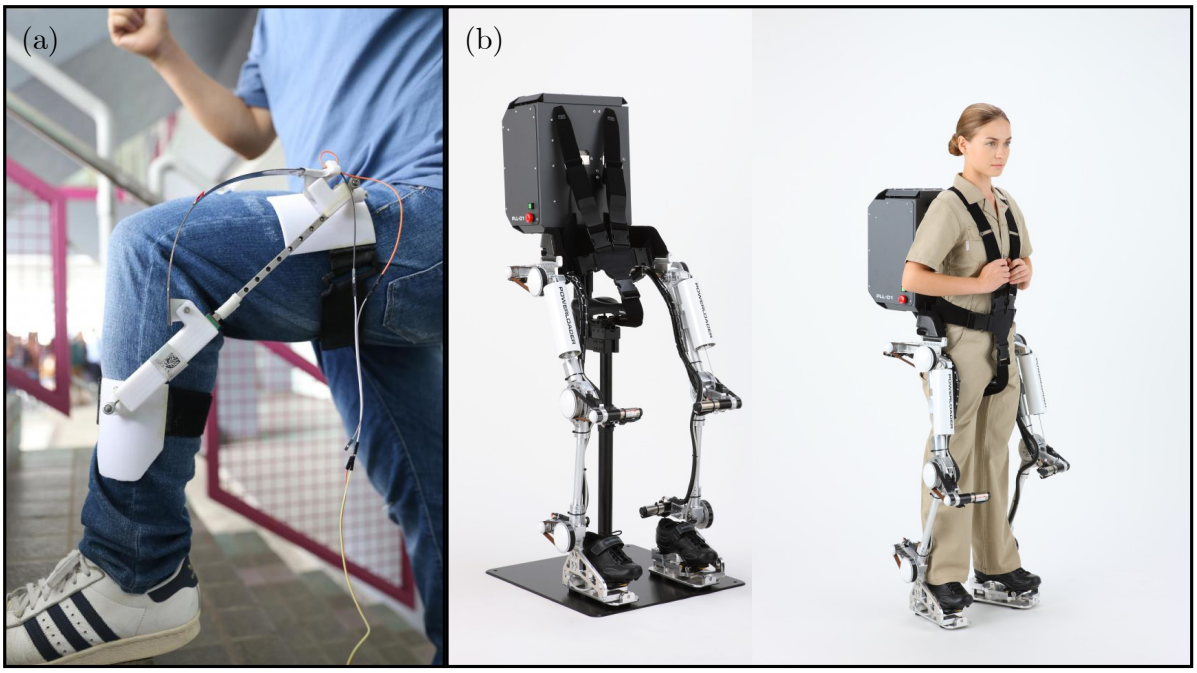


Fig. 2.15: Piezoelectric energy harvesting for exoskeleton.(a) Experimental study of human walk energy harvesting [13]. (b) Human exoskeleton [115].

New concepts of smart cities bring the idea to monitor and integrate sensors in urban centers to provide information on weather, traffic, and public security. Rain and windy forces have been widely used to excite piezoelectric patches and power supplies sensors and batteries [116, 117, 118, 119, 120]. Arms et al. [121] and Erturk and Inman [25] develop self powered temperature and humidity sensor for space stations. Nowadays urban center buildings are full of monitor sensors.

Zhao et al. [122] establish a theoretical model for piezoelectric energy harvesting from a pavement subjected to a moving vehicle. The study is conducted to investigate the effects of several important factors such as the vehicle types, speed, external resistive load, the arrangement of harvesters, and the road surface on energy output. Makki and Iliev [123, 124, 125] implemented piezoelectric patches to harvest energy from automotive tires and currently measure the tires pressure. Different authors purposes that impact energy between floor and vehicle can be converted through piezoelectric materials allowing a reduction in energy station consumption [126, 127]. Fig. 2.16(a) illustrates Makki and Iliev [125] prototype while Fig. 2.16(b) show examples of Tokyo railway stations that use special flooring tiles installed in front of ticket turnstiles and sidewalk to harvest energy [128]. Fig. 2.16(c) shows a similar principle which makes use of the bending of shoe sole and the pressure exerted on the heels can be harvested to power supply

a small sensor for a smart shoe [129].

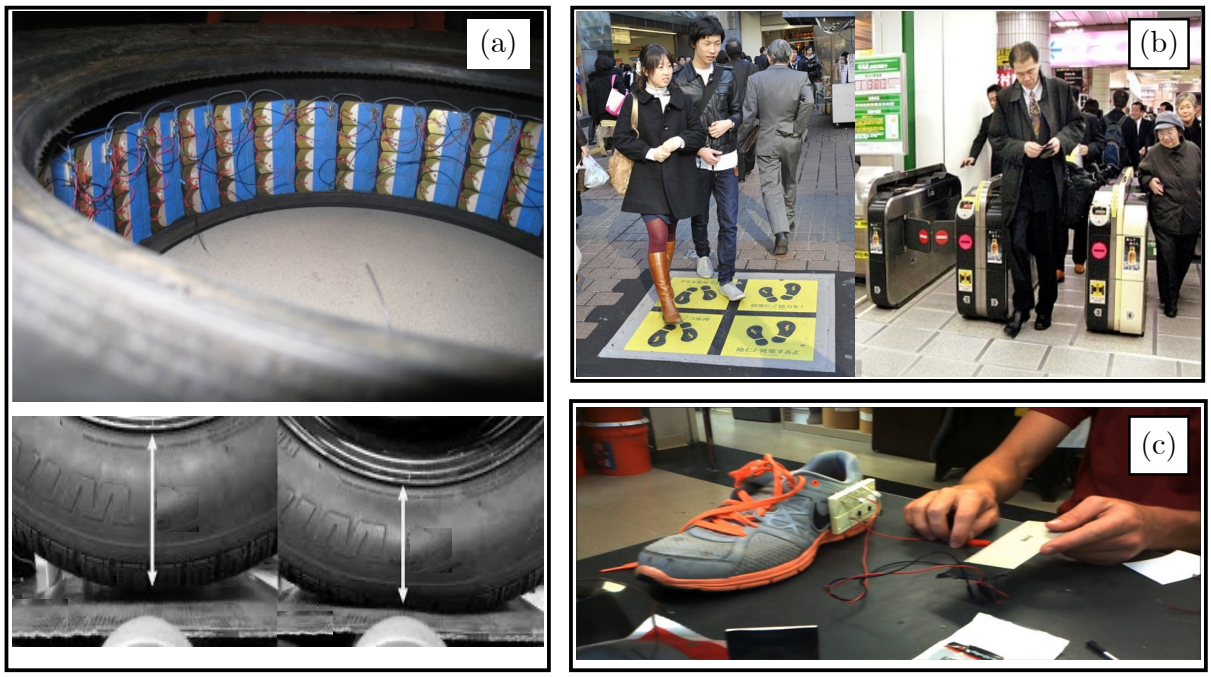


Fig. 2.16: Alternatives to piezoelectric energy harvesters for smart cities. (a) Tyre compression for tire pressure measure [124]. (b) Walk movement for train station energy supply [128]. (c) Smart shoe powered by piezoelectric elements [129].

In a similar way Ethem et al. [130] study the design, fabrication, and testing of a piezoelectric energy scavenger able to harvest power from the wing motion of a Green June Beetle (Cotinis Nitida) during its tethered flight. Authors report that the use of two generators (one on each wing) can result in more than 45 μW of power per insect. The project aims to power a wildlife tag over the course of multiple migratory seasons and is shown in Fig. 2.17 (a). Fig. 2.17 (b) refers to Shafer et al. [131] where authors investigate energy harvesting on birds. The prototype is carefully designed to match the flight acceleration frequency and present a low mass to be carried by the birds. Results demonstrate that there exists a significant amount of power available for harvest during flight.

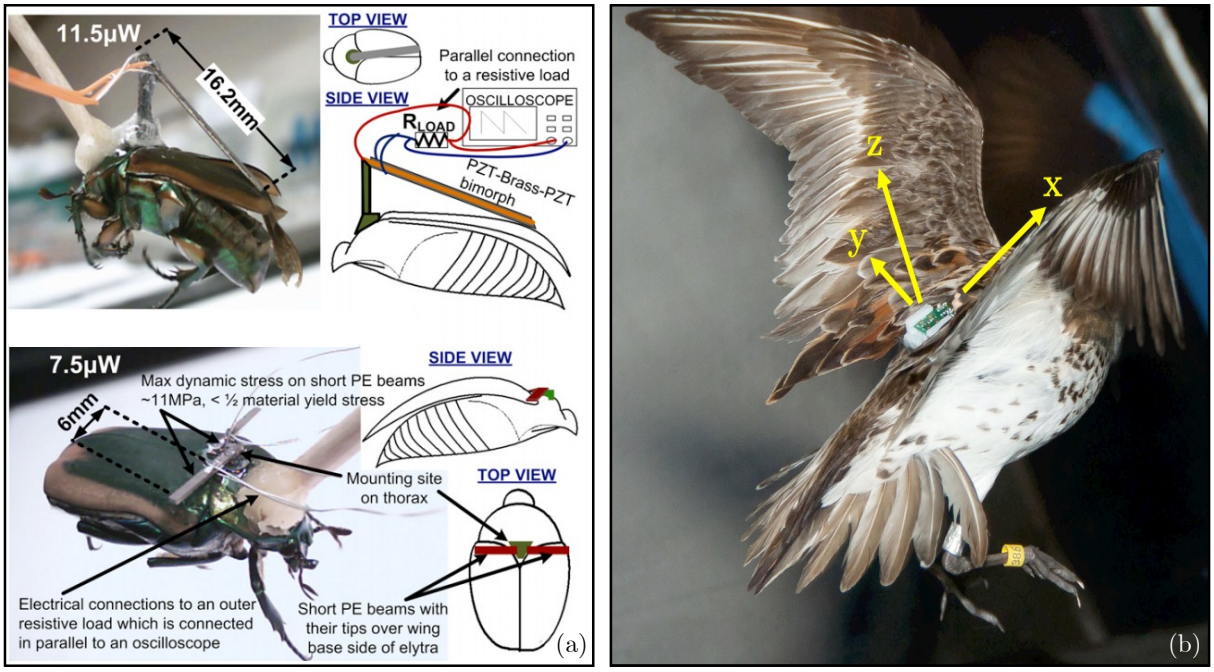


Fig. 2.17: Piezoelectric energy harvesting for wild life monitoring (a) Prototype mounted on a beetle [130]. (b) Data logger mounted to western sandpiper [131].

By investigating the piezoelectric energy harvesting process, one can note the dynamic characteristics involved in this phenomenon and the importance of using equations of motion to mathematically represent and predict the harvester response. Dynamical systems present a specific condition of movement amplification when the excitation source frequency is near to the system's natural frequency (resonance). However, environmental sources can be unpredictable changing external forcing frequency and amplitude during operation. So, piezoelectric energy harvester's designs focus on this relation between the external source and the system's natural frequency. Innovative projects consider the incorporation of strategies to broaden the bandwidth and increase the harvester's operational range.

2.3 Strategies to Broaden the Bandwidth

Piezoelectric energy harvesters working in environmental conditions are susceptible to a wide range of forcing frequencies and amplitudes. The seek for a harvester device able to adapt according to external conditions is a key challenge in piezoelectric energy harvesting.

A common approach is a high-damped inertial generator. This method promotes a lower peak output power but a broader frequency response [19, 48]. Nonlinearities are also a promising approach for broadening bandwidth in dynamic systems. Nonlinear harvesters present variable resonant frequency as a function of amplitude and output power peaks shift [28, 48, 132].

Nonlinearities are present in most reals mechanical systems. In order to simplify device modeling, linear behavior is assumed and nonlinear terms are neglected beside linear ones [133]. Moreover, for specific cases, nonlinearities can not be neglected becoming of total relevance for dynamical system characterization. Nonlinearities in mechanical systems have their origin in constitutive relations or large geometrical changes.

This subsection is dedicated to presenting a literature review of strategies to broaden piezoelectric device's bandwidth for energy harvesting and increase operational range. Also, it introduced the combination of smart materials and nonlinear effects for energy harvesting.

2.3.1 Multi-stable Systems

The main idea is to tune a monostable response into a bistable or multi-stable one. It means a system that oscillates around one equilibrium point starts to oscillate around two or more equilibrium points. The use of magnetic tip masses is one of the most common methods to evaluate a bi-stable piezoelectric energy harvester and it is shown in de Paula et al. [134]. Depending on magnetic masses orientation, curves in Fig. 2.18 can present hardening or softening effects warping the traditional curve (gray) associated with a linear behavior.

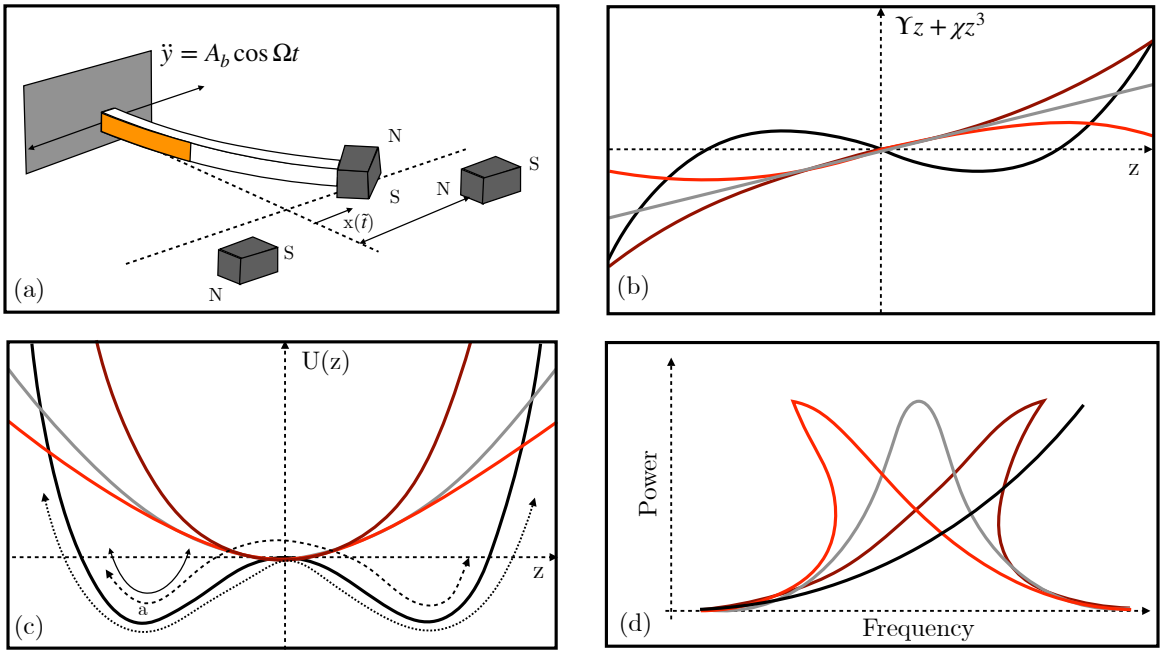


Fig. 2.18: Bi-stable piezoelectric energy harvester system. (a) Schematic representation of the cantilever beam configuration with magnetic masses. (b) Restoring force represented by Duffing equation. (c) System potential energy. (d) Output power frequency response. Adapted from Maaer et al. [135]

The cantilever beam with magnetic tip masses in the free end submitted to harmonic base

vibration in Fig. 2.18(a) can be modeled as a single degree of freedom mechanical oscillator connected to an external electrical circuit by a piezoelectric element. The beam stiffness can be represented by a *Duffing* equation that introduces a nonlinear term as follows:

$$m\ddot{z} + c\dot{z} + (\Upsilon z + \chi z^3) - \theta V = -mA_b \cos(\Omega t) \tag{15}$$

$$\theta\dot{z} + C_p\dot{V} + \frac{V}{R} = 0 \tag{16}$$

Eq. (15) and Eq. (16) can be used to model the dynamical system in Fig. 2.18 leading to a bi-stable response and dynamical jumps or even chaotic responses. Note that for small values of relative displacement ($z(t) = x(t) - y(t)$), the cubic therm that follows χ in Eq. (15) can be neglected in comparison with the linear term $\Upsilon z(t)$. For high values of $z(t)$, the cubic therm becomes more significant than the linear, promoting nonlinear trajectories.

This method receives great attention due to easy assembly and vast options of configurations able to promote different responses of linear devices. Younesian and Alam [136] studies multi-stable piezoelectric harvesters, composed of a nonlinear restoring mechanism to significantly enhance operational range in ocean waves environment. Further, Deng et al. [137] presents a cubic design (see Fig. 2.19) of a piezoelectric energy harvester for ocean structures capable to achieve exponential growth in several stable equilibrium states. In contrast with linear piezoelectric harvesters, experiments with the cubic design show a large work bandwidth and an increase of 760% in power density.

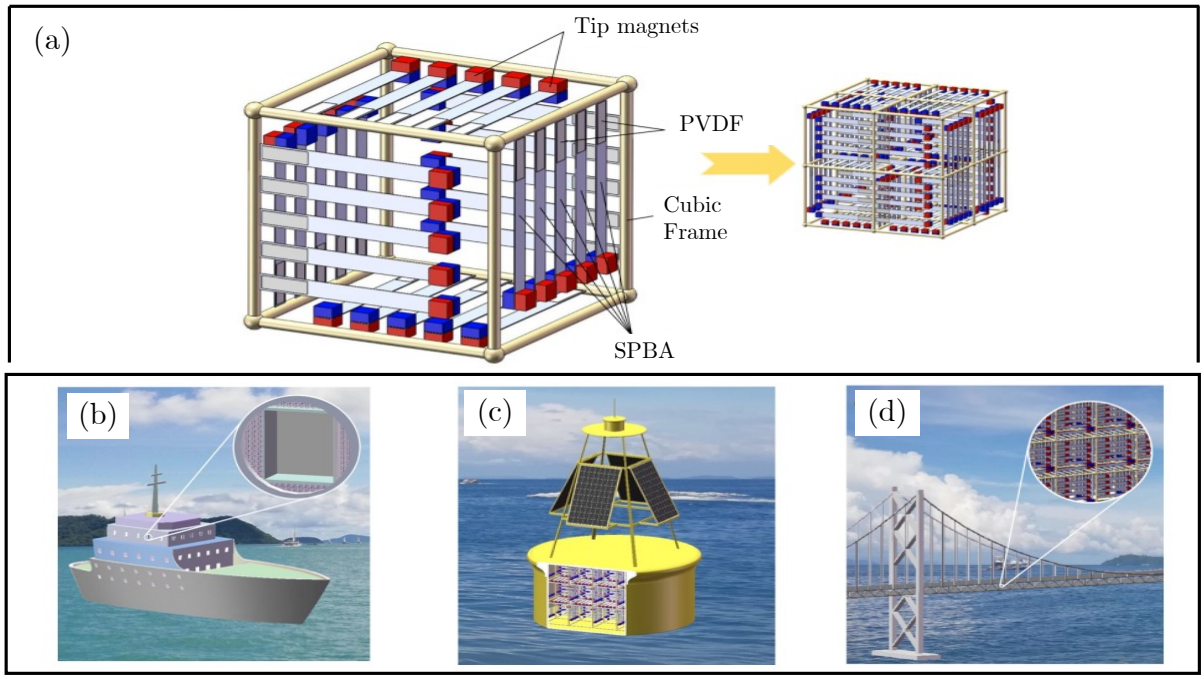


Fig. 2.19: (a) Poly-stable piezoelectric harvester with magneto tip masses. (b) energy-harvester in a wall ship. (c) Harvester installed in an ocean buoy. (d) installed under a bridge. Adapted from [137]

An interesting method to increase piezoelectric energy harvesters with magnetic tip masses is shown by Wang et al. [138] where the author's purpose is to control the external magnetic field by a helical coil with induced electrical current. It gives the harvester ability to adapt and interact with vibration source oscillations. In addition, Dhote et al. [139] evaluates a remarkable characteristic of the nonlinear dynamical behavior of different results for frequency sweep in forward and backward directions. Experimental results and numerical simulations show benefits as a slight increase in harvester bandwidth and 10% in maximum output voltage magnitude according to initial conditions.

2.3.2 Non Smoothness Impact (End-stop)

Another method to increase piezoelectric energy harvester's bandwidth is the use of end stoppers. The mathematical representation of these systems involves discontinuity in movement equations which can lead the harvester to a nonlinear behavior with better performance in a larger range than linear harvesters [140]. Ai et al. [141] reports a piezoelectric harvester separated by an initial distance of a rigid support-impact system. This distance is defined as a gap (g) and the ratio between support and oscillator stiffness is evaluated. For different relations, it is possible to achieve maximum output power peaks at different frequencies. Ai et al. [141] represents the end-stop piezoelectric system as a single degree of freedom that is generally attributed to

non-smoothness piezoelectric energy harvesters:

$$m\ddot{z} + c\dot{z} + kz - \theta V = -m\ddot{y} \quad \text{if x} < \text{g (without impact)} \tag{17}$$

$$m\ddot{z} + (c - c_s)\dot{z} + kz + k_s(z - g) - \theta V = -m\ddot{y} \quad \text{if x} \geq \text{g (with impact)} \tag{18}$$

$$\theta\dot{z} + C_p\dot{V} + \frac{V}{R} = 0 \tag{19}$$

Where Eqs. (17) to (19) can be associated with the governing equations of motion for a piezoelectric harvester device with and without impact in rigid support.

Beyond that, Liu et al. [142], Liu et al. [143] and Liu et al. [144] present a series of configurations for one and two degree of freedom using stop ends. The authors suggest using a second piezoelectric cantilever beam as the stop. This approach is able to significantly increase the harvester operational range and also the total amount of energy converted. In a particular way, Su [145] explores an innovative configuration of a piezoelectric energy harvester system composed of two coupled cantilevers beams and a piezoelectric element. The experimental apparatus is shown in Fig. 2.20(a) while (b) illustrates the representation of a two degree of freedom oscillator used in the numerical simulations developed.

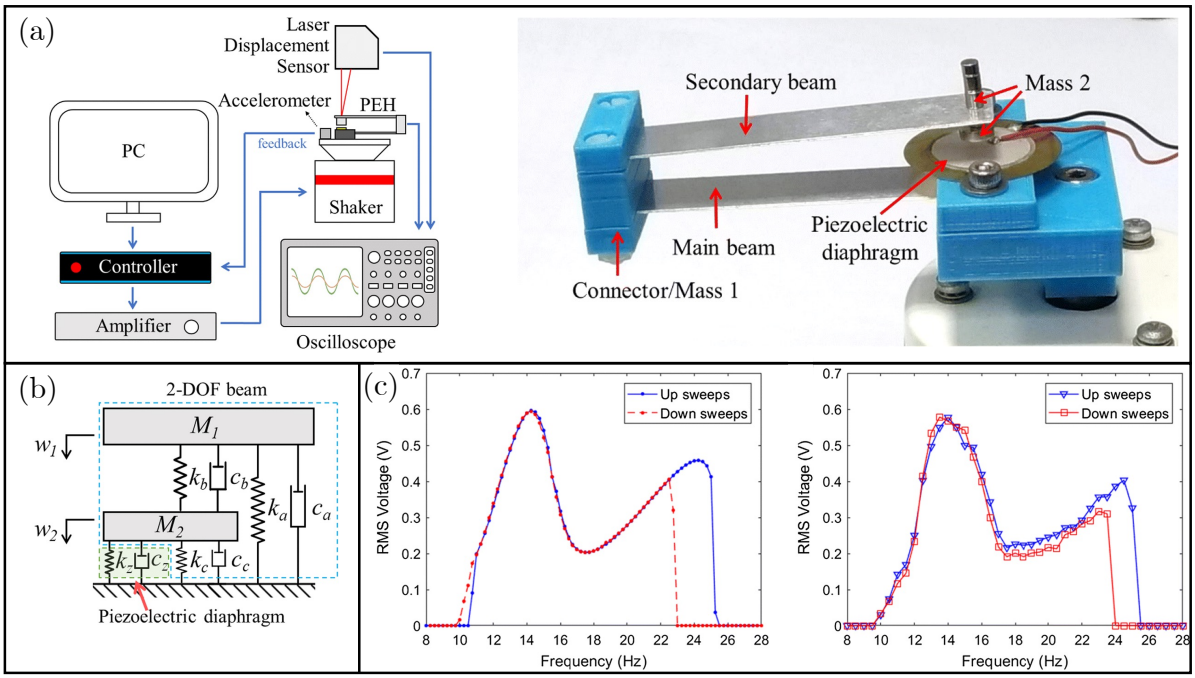


Fig. 2.20: Piezoelectric harvester system with stop ends impact constrain. (a) Experiment apparatus and schematic. (b) Two degree of freedom representation. (c) Nonlinear response for upward and downward frequency sweep. Adapted from [145]

The impact energy is converted into electrical power and the output voltage is shown and Fig. 2.20(c) for numerical and experimental cases. The results enhance the nonlinear characteristic of different responses in forward and backward sweep and also allows to note the increase in harvester operational range.

2.3.3 Geometries and Configurations

The total strain which a piezoelectric sample suffers when a mechanical load is applied is significantly attributed to its geometry and shape and so, the converted energy [146, 147, 148, 149]. Emam et al. [150] show results for a piezoelectric plate instead of a cantilever beam configuration. Moura and Erturk [151] studies a cantilever beam with gradient cross-section while Wang et al. [152] reports an increase in harvesters bandwidth by experiments with a zig zag shape piezoelectric cantilever beam. Sun et al. [153] show a net configuration to obtain larger strain levels and consequently increase output power.

Karadag and Topaloglu [26] purposes a piezoelectric cantilever beam with a linear actuator clamped on the free end. In this way, it is possible to control the harvester's size and mass distribution. Results show a shift around 8% of resonance frequency compared with the initial configuration.

In the same way, Güleç et al. [154] builds a bio-inspired design of a cochlea piezoelectric energy harvester with multiple cantilever beams. Each piezoelectric cantilever beam presents different lengths and gradient cross-sections resulting in different natural frequencies. This configuration is represented in Fig. 2.21(a) and (b) and is able to achieve multiple resonance peaks as shown in Fig. 2.21(c).

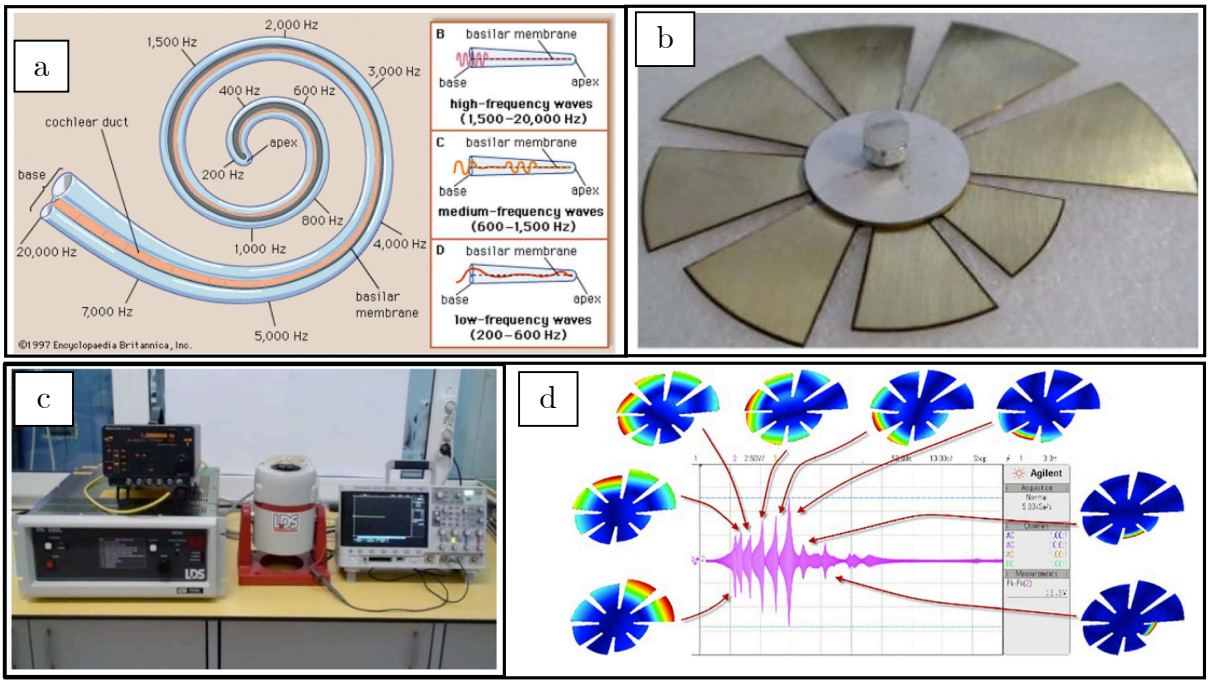


Fig. 2.21: Piezoelectric energy harvester inspired in a cochlea configuration. (a) Cochlea illustration design. (b) Harvester prototype design. (c) Experimental setup. (d) Relative displacement frequency response. [154]

2.3.4 Synergistic use of Smart Materials

The synergistic use of smart materials is an innovative field that suggests attention and an accurate approach [29]. Avirovik et al. [155] develops a hybrid device with piezoelectric material and *SMA* elements for dual functionality, both as actuator and energy harvester. de Souza and de Marqui [6] studies the dynamical influence of pseudoelastic helical springs coupled to a two degree of freedom airfoil device subjected to different levels of pre-load. Numerical and experimental results explore the martensite phase transformation for both structural damping and energy harvesting.

Silva et al. [156] presents a numerical analysis of a SMA-piezoelectric energy harvesting system where both temperature-induced and stress-induced phase transformations are in concern. Results indicate that the inclusion of a *SMA* element is able to extend the operational range by a shift in output power frequency response. Silva et al. [156] and Adeodato et al. [157, 158, 159] developed numerical models and experimental procedures to investigate the temperature influ-

ence of *SMA* phase transformation coupled to a piezoelectric energy harvester, using thermal and kinetic energy to obtain electrical power in a wide range of frequencies through piezoelectric materials and shape memory alloys.

Hybridization of harvester devices is a new tendency which brings the concept to use different resources to power supply *MEMS* or batteries. The development of synergistic use of smart materials depends on the understanding of physical domains coupled and involved in the dynamical process. The next section deals with the principles of shape memory alloys for the purposes of this thesis.

3 Shape Memory Alloys

The combination of two or more chemical elements being one of than a metal gives the name metal alloy. Plenty of metal alloys have been studied and employed in industry and daily life. An example of this is steel which is the combination of iron and carbon in a certain proportion [160, 161]. For many years, researchers focused on metal alloys mechanical properties and their thermomechanical coupling. It means, the connection between mechanical and thermal physical fields. Relevant works treat thermomechanical coupling in traditional metal alloys. [162, 163].

Shape memory alloys *SMAs* is a group of metal alloys that present a high level of thermomechanical coupling when compared with traditional materials in the industry. Examples of *SMAs* are copper shape memory alloys (Cu-Al-Ni and Cu-Zn-Al), iron shape memory alloys (Fe-Mn-Si and Fe-Pt), and nickel shape memory alloys (Ni-Ti, Ni-Ti-Pd, Ni-Mn-Ga) [31, 164]. This thesis focuses on shape memory alloys composed of NiTi (Nitinol) one of the most used in industry and research.

The attractive *SMA* thermomechanical coupling is able to promote geometrical shape and size recovery due to solid micromechanical phase transformation. *SMAs* are also able to dissipate considerable energy when submitted to cyclical loads under specific conditions. Those intrinsic characteristics are attributed to the shape memory effect and pseudoelasticity phenomena.

Nitinol *SMAs*, usually, present two phases being them austenite as body-centered cubic crystal cell (CCC) and martensite as tetragonal, orthorhombic, or monoclinic as it is shown in Fig. 3.1. Phase transformation can be induced by mechanical load or temperature variation. During phase transformation, distortion propagation and shear stress between grain planes contribute to solid body change. The austenite phase is characterized by symmetry in crystal cells while martensite presents asymmetric grain orientation. In addition, the austenite phase is stable at high temperatures and in a free stress state while martensite is stable at low temperatures or at high temperatures and high levels of stress.

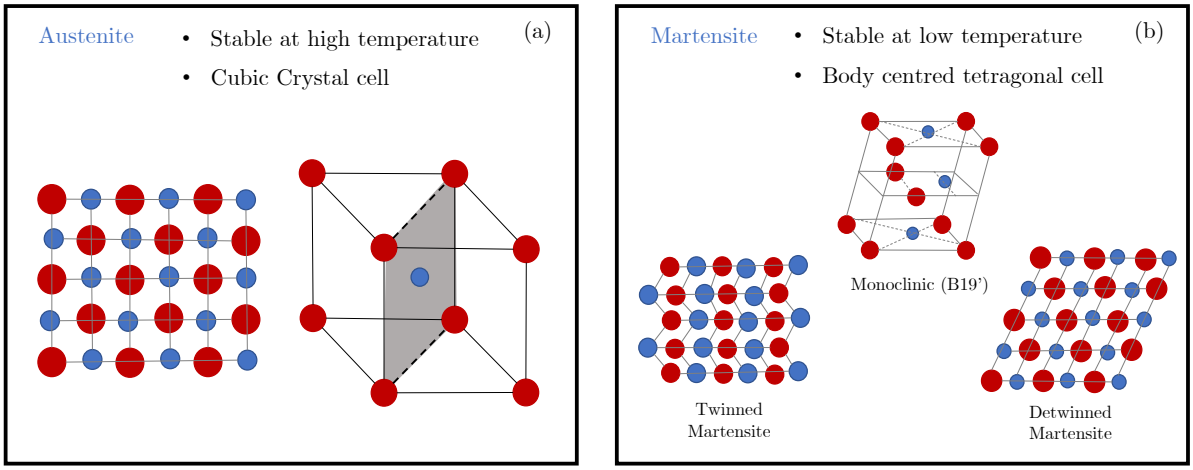


Fig. 3.1: NiTi Shape memory alloy crystalline cell. (a) Austenite phase. (b) Martensite phase. Adapted from Rao et al. [30].

This work considers low temperature a temperature where the martensite phase is stable and free of stress ($T < M_f$). On the other hand, high temperature is attributed to a temperature where the austenite phase is stable and free of stress ($T > A_f$). Also, temperatures where phase transformation starts are designated as M_s and A_s for martensite and austenite, respectively. They represent important *SMA* constitutive parameters called critical phase transformation temperatures or just critical temperatures.

Several methods exist for *SMA* critical temperatures estimation. One example consists of a "bend and free recovery" test where a *SMA* specimen (wire, tube, or bar) is submitted to a mechanical load and unloads at low temperature ($T < A_s$), promoting martensite reorientation and consequently a permanent strain. The specimen is then heated, and its shape configuration and temperature are monitored. In this way, when the sample starts to recover its initial shape, can be approximately determined A_s, and the temperature at which recovery is completed is declared to be approximately equal to A_f. The "bend and free recovery" method should be considered as a qualitative method of measuring two of the four transformation temperatures [31].

The standard method used to determine critical temperatures is the differential scanning calorimeter (*DSC*). *DSC* method considers small material samples under zero stress and the energy necessary to perform a prescribed temperature path able to promote phase transformation [31]. *DSC* method is able to determine critical forward phase transformation temperatures, A_s and A_f, and also the reverse critical phase transformation temperatures, M_s and M_f, which consist

of the start and finish temperatures to form the martensite phase in *SMA* cooling process.

A schematic of the *SMA DSC* test result is shown in Fig. 3.2 where tangent lines are used to determine critical temperatures. The principle of this method is that the *SMA* sample undergoes a phase transformation and consequently more or less heat flow is required to keep *SMA* sample temperature the same as the reference temperature [31, 30, 32].

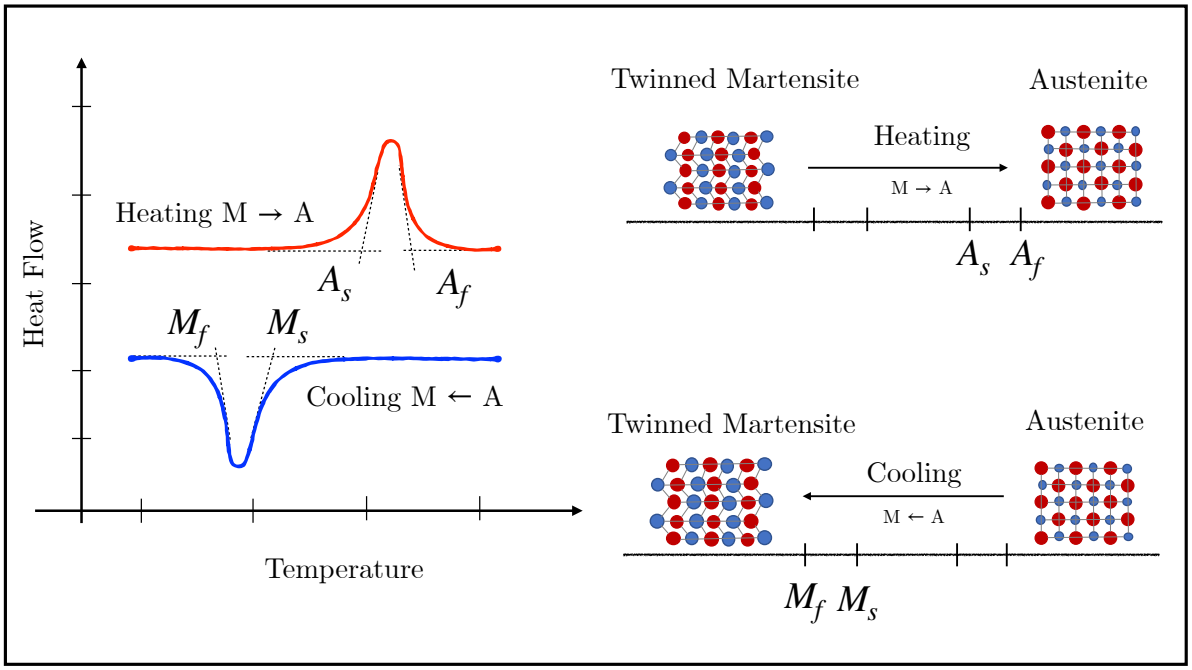


Fig. 3.2: Differential scanning calorimetry process. Characteristic curves for phase transformation critical temperatures determination. Adapted from Rao et al. [30].

Several factors such as fabrication process, strain rate, heat treatment, and load history can influence critical temperatures and stresses. *SMA* behavior presents phenomenons as non-isotropic behavior, structural and functional fatigue, presence of a R phase, and transformation induced plasticity (*TRIP*) [31, 165]. Therefore the analyses and the modeling of the shape memory alloys behavior need a very careful and detailed thermomechanical characterization.

Considering a *SMA* wire sample in a condition "*as received*" where load history is null, fabrication process and chemical composition are determinants in critical parameters. The relation between work temperature and critical transformation temperatures, and the state of stress/strain, is determinant to govern material's behavior. The next subsections describe *SMA* remarkable effects and their use in dynamic systems. Also, traditional constitutive mathematical modeling is shown for assumed phase transformation kinetics models.

3.1 Shape Memory Effect

In order to describe a full cycle of a *SMA* sample presenting shape memory effect (*SME*), the mechanical load is applied in a condition of constant temperature and below the sample's M_f. If the sample is obtained from a cooling process and free of stresses, the twinned martensite phase is stable as shown in axes origin in Fig. 3.3. When a mechanical load is applied, the material presents a linear elastic behavior until loading values reach the first critical stress for martensite reorientation (σ_s). From this point, shear stresses in the crystalline cell promote distortion movement in a way to transform twinned martensite into detwinned martensite. The material presents a nonlinear relation in stress (σ) and strain (ϵ) until the second critical stress reorientation. When load levels reach the second critical reorientation stress (σ_f), the material starts to present a linear elastic behavior again if the load continues to increase. Afterward, if the *SMA* sample is unloaded, a residual strain can be observed and the material preserves the form and shape obtained from the load process [30, 31, 32, 33].

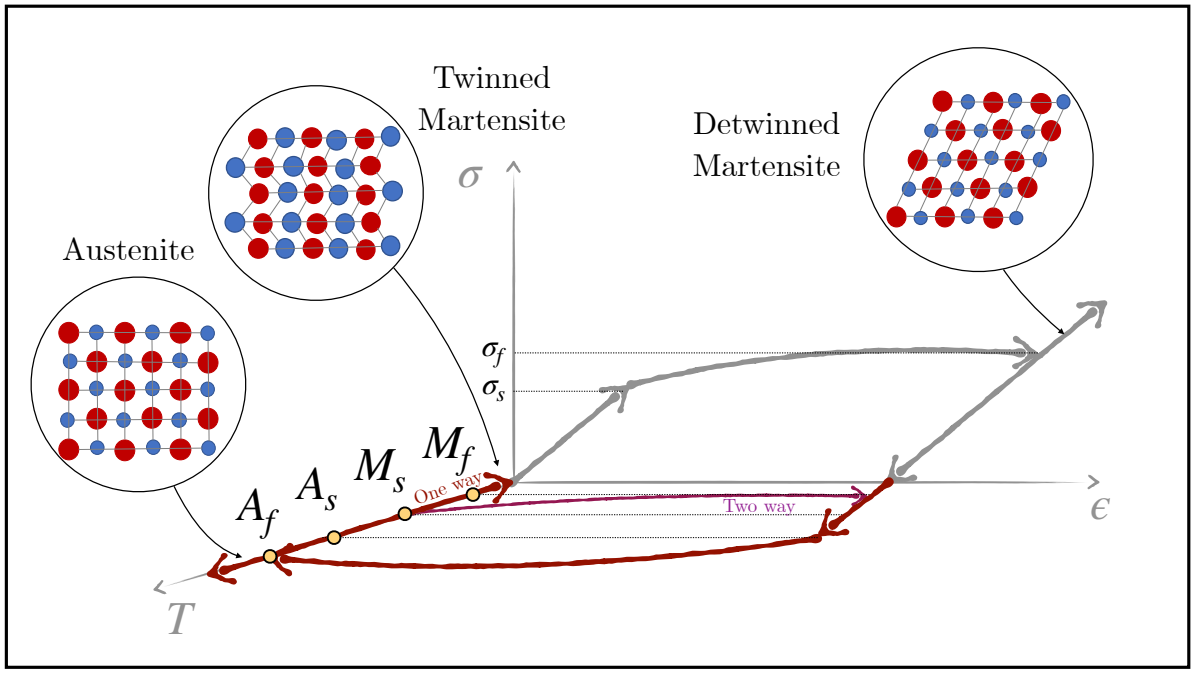


Fig. 3.3: Shape memory effect representation. Stress × Strain × Temperature diagram.

In sequence, at a free of stress state, the *SMA* sample is submitted to a specific heating process and when the temperature reaches austenite critical start temperature (A_s), shape recovery begins eliminating residual strain. The detwinned martensite transforms into full austenite at A_f and this phenomenon is called the shape memory effect, where phase transformation is induced by temperature variation [30, 31, 32, 33]. The cycle finishes with *SMA* cooling and phase transformation from austenite to twinned martensite between M_s and M_f temperatures.

However, *SMA* shape memory effect presents some operational limitations and restrictions attributed to the time required for *SMA* temperature variation. Usually, the heating and cooling process involves convection phenomena. If there is not a significant heat exchange, the actuation can be considered too slow for some specif applications. Another characteristic is that a common *SMA* sample does not return to a deformed macroscopic shape when low temperature is established again ($T < M_f$). It suggests the load would be applied each time $A \rightarrow M$ phase transformation occurs. For this reason, this is named *one way* shape memory effect.

A potential solution can be achieved by submitting the *SMA* sample to a training process with assisted stress. The training process consists of a series of thermal cycles of heating and cooling with constant stress. During the cooling process, *SMA* goes from austenite to detwinned martensite due to load action. This technique allows the material to associate a macroscopic form for each (low and high) temperature condition, respectively. This is named *two way* shape memory effect and after the sample has been trained, it is able to occur in a free stress condition.

Phase transformation during *SME* can promote huge restoring forces if restrictions in the movement are imposed. For this reason, shape memory alloys can be employed for mechanical actuation [166]. Jani et al. [167] presented a review about recent progress and developments in shape memory alloy actuators with different designs, methods, techniques, and approaches. Monteiro et al. [168] and Monteiro et al. [166] evaluated the restore capacity of different *SMA* actuator configurations. de Oliveira et al. [169] discussed some aspects of the thermomechanical characterization of *SMA* actuators.

Vaidyanathan and Chiel [170] uses shape memory alloy elements to actuate bioinspired devices. Lee et al. [171] takes origami-inspired structures to develop an adaptive device able to change its form and shape according to environmental conditions. Later, Copaci et al. [172] developed a new flexible *SMA* actuator that provides movement freedom and a better integration in wearable robots shown in Fig. 3.4. The design of exoskeleton prototypes demonstrates the utility and advantages offered by mechanical actuators to improve comfort and adaptability.

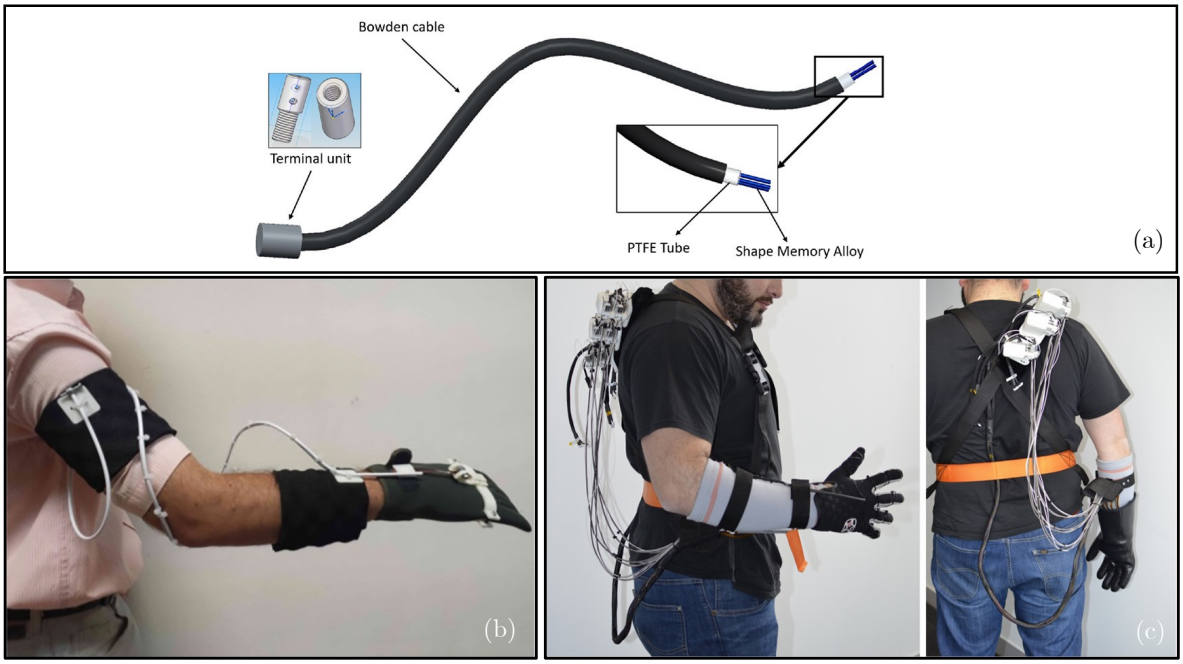


Fig. 3.4: Flexible wearable shape memory alloy actuator [172]

The shape memory effect can contribute to the concept of morphing structures and is used in aircraft projects. Aircraft morphing can be considered as the capacity of an aircraft to change its geometry and shape during the flight. Flaps, spoilers, and control are specific localized devices that allow changing the aerodynamics characteristics of the wings during flight, but in general, morphing in aerospace is associated with geometrical changes, using smart materials such as shape memory alloys [173, 174]. Hartl et al. [175] presents an experimental characterization of NiTi to build a *SMA* beam actuators and incorporate it into a morphing aerospace structure. Based on this article, Hartl et al. [176] focuses on experimental validation by using a three-dimensional thermomechanical constitutive model.

Pankonien et al. [177] purposes the synergistic use of piezoelectric materials and shape memory alloys to active wing flaps in an airfoil. The smart materials properties are used in combination to provide high work density and accurate bandwidth for bending. The innovative design allows for an increase in the static wing tip deflection when compared to conventional actuators. Han et al. [178] investigates the aerodynamic performance of a morphing wing for an unmanned aerial vehicle that mimics the wing-tip of birds as shown in Fig. 3.5. Authors apply a smart composite, composed of *SMA* wires and glass fibers embedded in a soft polymeric matrix. Experiments are conducted considering different diameters and numbers of embedded *SMA* wires.

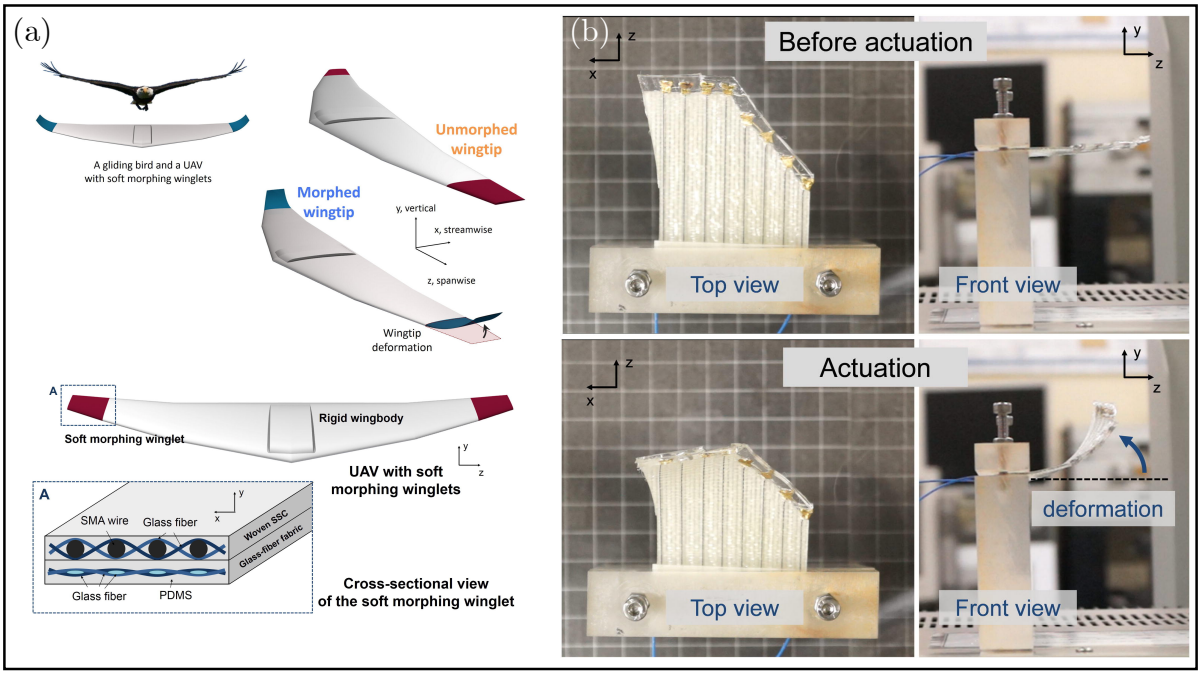


Fig. 3.5: Bio inspired wing morphing structures by *SMA* composite actuation. (a) Illustrative design. (b) Experimental prototype view actuation. [178]

Shape memory effect is also employed in active control for vibration mitigation. A *SMA* structure or device presents the potential to significantly change its Young's modulus due to temperature control promoting a shift in system natural frequency [31, 33, 179, 180]. Evidently, on the other hand, active control can also be used to increase system response for energy harvesting.

3.2 Pseudoelastic Effect

Pseudoelastic effect is able to occur when work temperature for *SMA* element remains above A_f. The Austenite phase is stable in a condition free of stress. When a mechanical load is applied, linear behavior is observed until stresses reach forward transformation critical stress value (σ_{fs}). Furthermore, phase transformation is induced by mechanical load involving Young's modulus variation. A nonlinear relation between σ and ϵ is established until $\sigma = \sigma_{ff}$, as shown in Fig. 3.6.

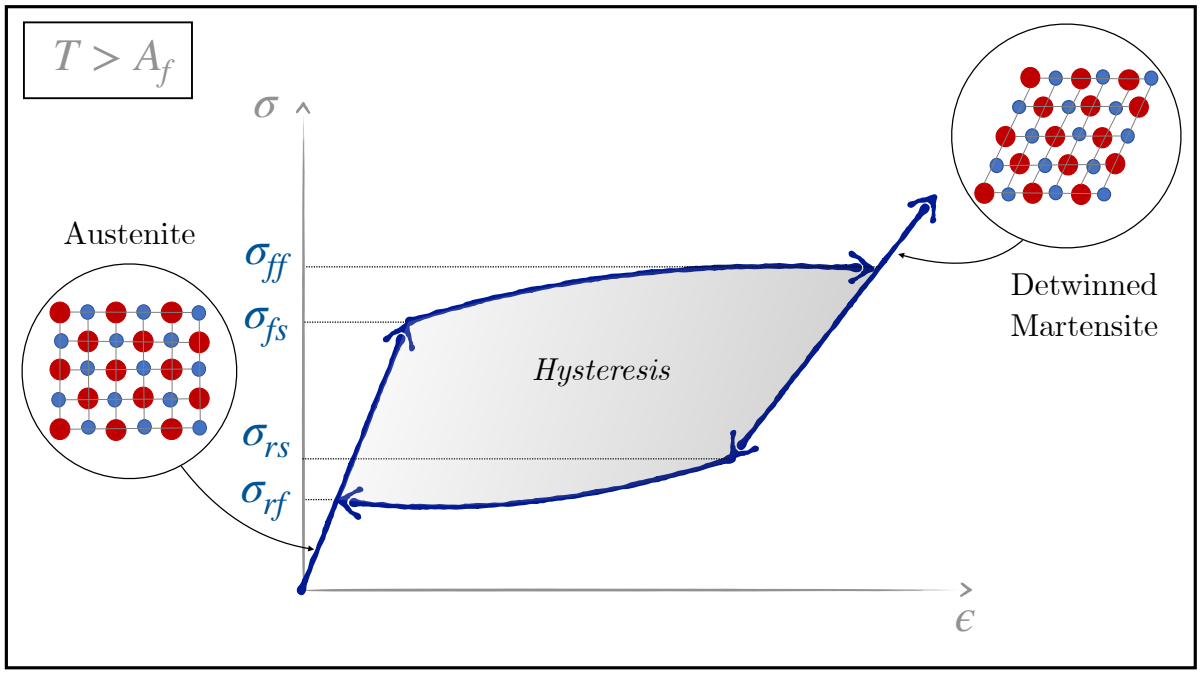


Fig. 3.6: Pseudoelastic effect representation. Stress × strain diagram.

Once full transformation happens, the material presents again a linear elastic constitutive behavior with martensite mechanical properties. The unloading process promotes reverse transformation in a different pathway than forward leading to an area between curves associated with a hysteresis loop. This behavior occurs due to energy dissipation during the loading and unloading process [30, 31, 32, 33].

Therefore, *SMA* elements presenting pseudoelastic effect are often employed in dissipative structures and devices. Kwon et al. [181] proposes a novel pseudoelastic *SMA* gear with a mesh washer for gear wheels. The results of the system transmissibility curve from the *SMA* gear analysis indicate that this configuration allows for reducing the torsional stiffness compared to the conventional gears.

Nae et al. [182] proposes a method for active tuning pseudoelastic wires by use of Joule's effect and airflow to control a cantilever beam vibration amplitude. The *SMA* stress-strain curve is modified by the thermomechanical state with the aim to adjust system stiffness and damping characteristics to avoid resonance phenomena. He et al. [183, 184] presents theoretical and experimental approaches to making a rotor-bearing system pass through the critical speed safely by SMA thermomechanical control. *SMA* helical springs are employed to build a pedestal bearing for the rotor-bearing system. The authors use the principle of the dynamic absorber to estimate system stiffness in order to keep the rotor shaft usually situated near anti-resonance. Fig. 3.7 present emblematic sketches for Nae et al. [182](a) and He et al. [184](b).

The applicability of shape memory alloys in dynamical systems is vast and requires a detailed analysis. The next subsection deals with *SMAs* submitted to dynamical load for passive and active vibration control.

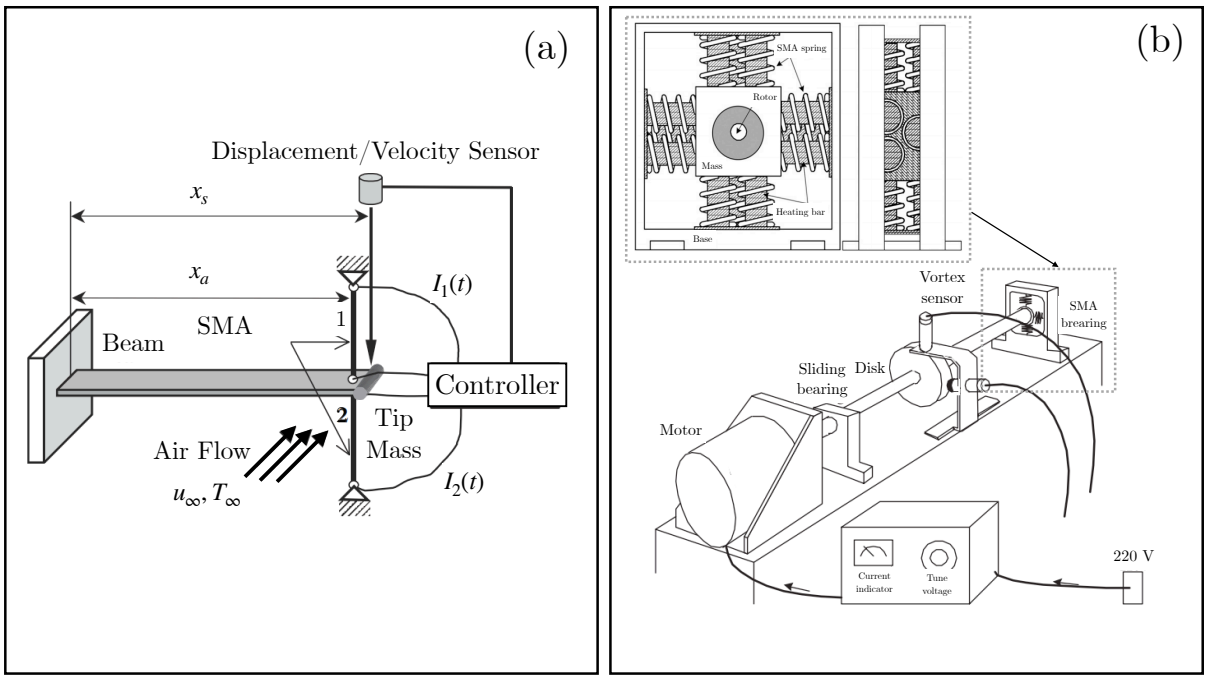


Fig. 3.7: Schematic of prototypes to evaluate pseudoelastic effect for vibration control. (a) Nae et al. [182] uses *SMAs* wires. (b) He et al. [184] uses *SMA* helical spring.

3.3 Shape Memory Alloys in Dynamical Systems

Shape memory alloys (*SMAs*) have been used in dynamical projects over the last 2 decades due to their expressive thermomechanical coupling [31, 32, 33]. As mentioned before, strain rate presents an essential parameter in *SMA* behavior [185]. The frequency of load in which a *SMA* sample is submitted can determine if the material is under dynamical forces and so, a dynamical approach is required. This section treats *SMA* elements in engineering for dynamic systems like passive and active vibration control.

The design of *SMA* elements for dynamical systems need to include a proper investigation of fatigue life. Smart materials present both structural and functional fatigue. Shape memory alloy fatigue has been studied by several references [185, 186, 187, 188] showing that one of the major relevant aspects to shortening fatigue life is the maximum stress of the loading process.

Furthermore, thermomechanical coupling induces a temperature increase in a *SMA* sample if the heat exchange is not capable to dissipate this energy until the end of the load cycle. Temperature measurement is a difficult task in SMA elements even more in dynamical systems. As an

appropriate methodology, Cismasiu and Santos [189] estimates a significant increase in *SMA* wire temperature through a thermocouple sensors. In a different way, de Aguiar et al. [180] shows an experimental work about one and two degrees of freedom system where a *SMA* helical spring is heated via Joule's effect. Results explore the ability to shift system response from a critical condition to a stable one. The authors use an infrared thermographic camera (*FLIR-320*) to evaluate colored images of a *SMA* helical spring and compare them with a scale. Figure Fig. 3.8 shows the archetype and results in concern. Besides that, Li and Feng [179] previously analyze the influence of temperature and mechanical load in a frequency response curve and the phenomenon of resonance peak shift.

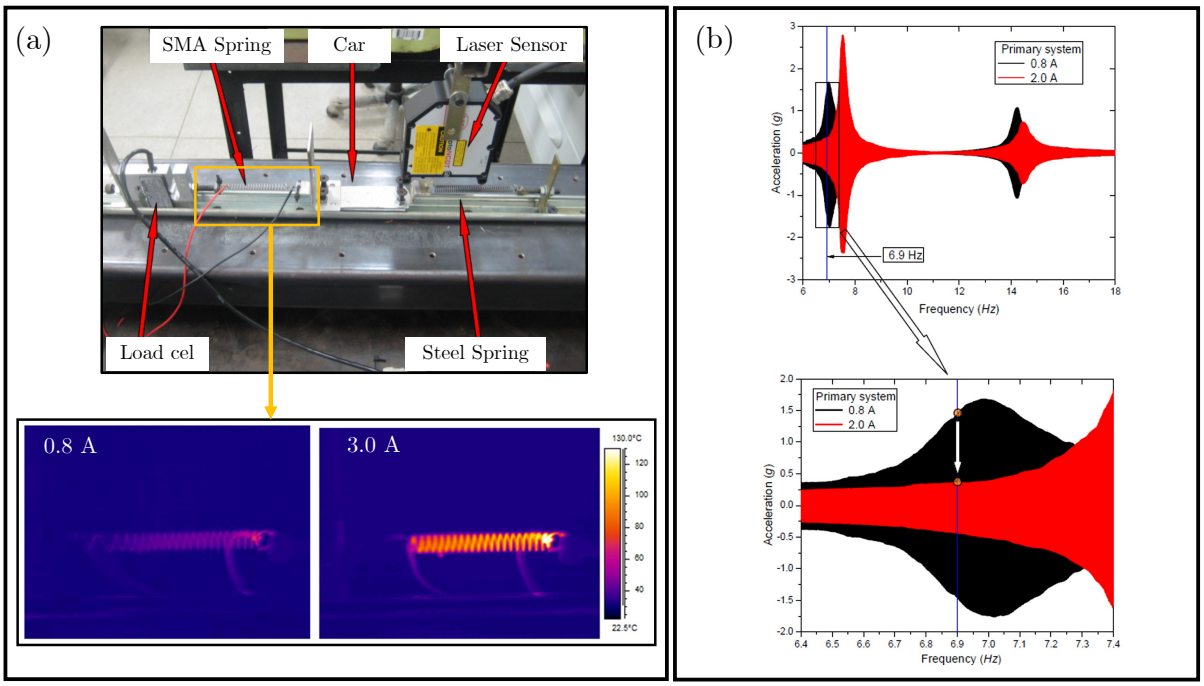


Fig. 3.8: Experimental measurement of *SMA* temperature for vibration control. (a) Archetype for a single degree of freedom with base excitation and temperature graphical measurement. (b) Experimental results showing amplitude reduce and resonance shift. Adapted from [180].

In a different approach, Saadat et al. [190] and Han et al. [191] present overviews for seismic applications of NiTi shape memory alloys. Wang et al. [192] and Varela and Saiddi [193] perform experimental analyses of vibration attenuation devices with pseudoelastic elements. Vignoli et al. [194] deals with numerical simulations about a pseudoelastic element embedded in a composite bar for vibration attenuation in earthquake structures. Casagrande et al. [195] investigates the use of *SMA* pseudoelastic wires to floor isolation in strategic building floors like power plants, military headquarters, and hospitals.

The use of pseudoelastic elements in structural damping goes further in Enferadi et al. [196]

and Ghasemi et al. [197] where the authors purposed to apply a *SMA* vibration absorber as an additional degree of freedom for wave-induced vibration control of offshore jacket platforms. Fig. 3.9(a) shows the absorber device composed of *SMA* unidimensional elements. Fig. 3.9(b) present the offshore jacket platforms evaluated while in Fig. 3.9(c) it is possible to see the maximum displacement reduction for both jackets.

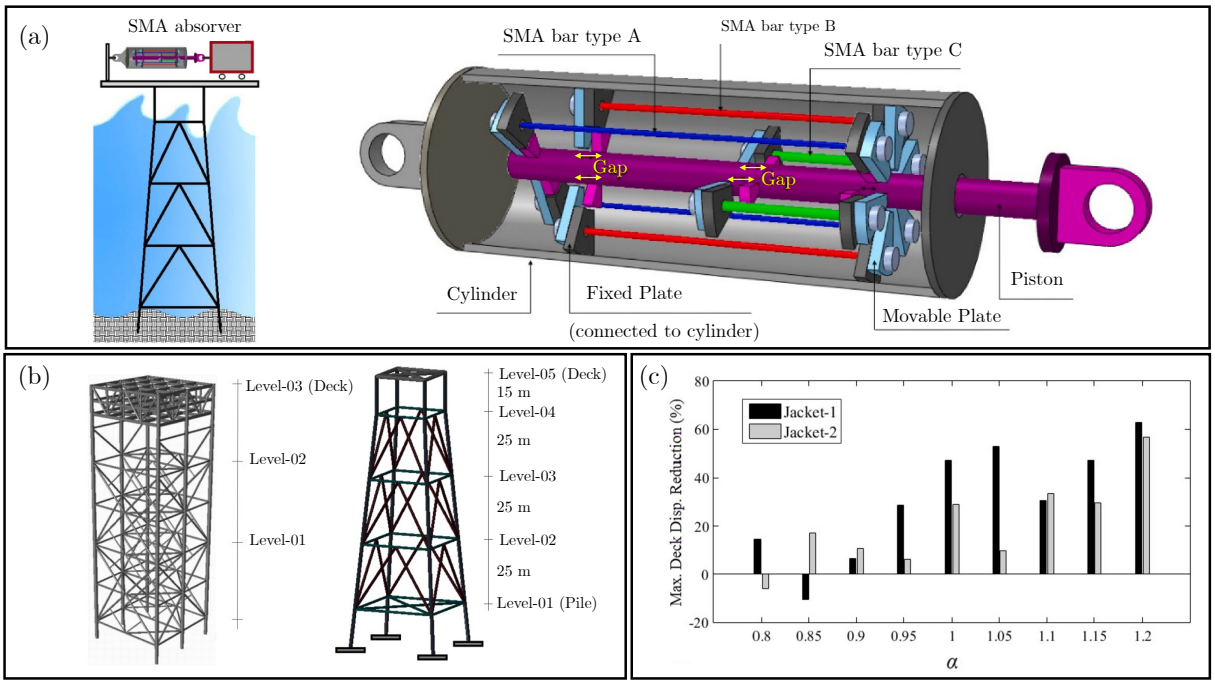


Fig. 3.9: *SMA* absorber system developed by Ghasemi et al. [197]. (a) Detail drawing of the *SMA* damper. (b) Sketch of jacket platforms evaluated. (c) Percentage of maximum displacement reduced for different values of absorber mass coefficient (α). Adapted from [197]

Furthermore, Das et al. [198] considers the attenuation of multi-megawatt wind turbines with large flexible blades that often exhibit significant vibration when exposed to turbulent wind. The authors propose to change the longitudinal stiffness of the blades by using the tendon concept with shape memory alloy wire. Numerical results enhance the efficiency and advantage of *SMA* stiffener phenomena attributed to thermodynamical coupling. Fig. 3.10(a) shows an illustrative offshore wind turbine device, Fig. 3.10(b) the sketch view of the system engine and Fig. 3.10(c) the wind turbine blade with a SMA wire submitted to thermomechanical load.

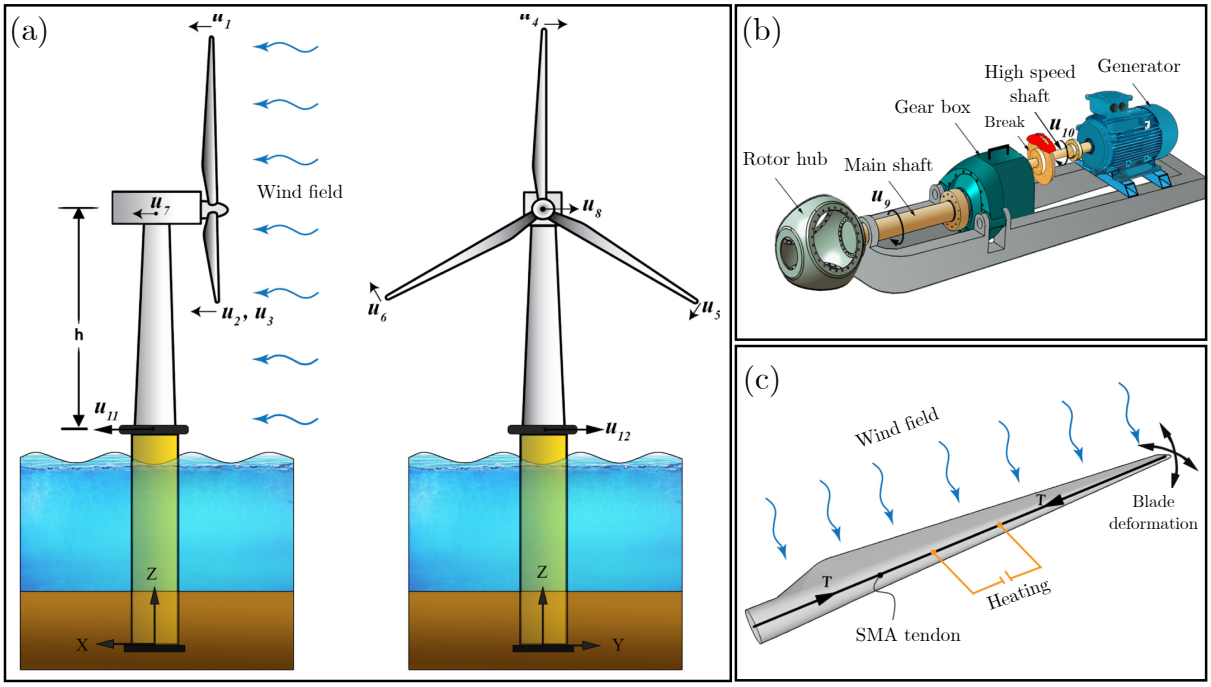


Fig. 3.10: *SMA* for vibration mitigation in mono pile offshore wind turbine model. (a) Schematic lateral and frontal view showing side-to-side motion. (b) Mono-pile assembly. (c) *SMA* stiffener tendon from root to tip of the blade. Adapted from [198]

Relevant aspects of pseudoelastic oscillators behavior are studied by Bernardini and Vestroni [199] in frequency response diagrams dealing with martensite phase transformation and regions where periodicity can change. In addition, Bernardini and Rega [200] and Bernardini and Rega [201] explores chaotic behavior.

Doaré et al. [202] experimentally observes dynamical jumps for angular displacement measured in frequency response diagrams for a pseudoelastic wire at torsional load. de Souza and de Marqui [203] studies a typical airfoil with superelastic helical springs while Borges et al. [204] investigates damping capacity in pseudoelastic helical springs for active and passive control of a rotor-bearing system.

Based on this subsection, it is possible to note *SMA* the applicability in dynamic systems and the importance of carefully modeling *SMA* behavior. Next subsection deals with proper mathematical modeling of the constitutive behavior of *SMAs* with a focus on dynamical problems. Note that models with assumed kinetic phase transformation are built in a way to evaluate martensite volume fraction as a function of applied stress. It leads to a stress-prescribed problem.

3.4 Shape Memory Alloy Constitutive Models

The task to mathematically describe the constitutive behavior and the phenomena involved in *SMA* phase transformation is a key challenge that has inspired several authors to find consistent models and formulations. The objective of this section is to provide a mathematical basis for shape memory alloy effects modeling.

A large number of review papers about shape memory alloys constitutive models can be found in literature enhancing different approaches and methods [165, 205, 206, 207]. Paiva and Savi [165] explore the main constitutive models for five phenomenological theories. In general, these models deal with the macroscopic *SMA* thermomechanical behavior for a uniaxial load. In addition, Cisse et al. [207] presents a review including microscopic, micro-macro, and macroscopic models for uniaxial and triaxial loads. The paper categorizes the macroscopic models: based on plasticity theory and derived from thermodynamic potentials.

According to the standard generalized materials formalism, the thermodynamic state of a material sample at any given moment can be expressed by the knowledge of a set of variables known as state variables [162]. State variables can be dived into internal and observed variables. Typically, strain and temperature are adopted as observed variables for elasticity and plasticity phenomena. For shape memory alloys, there is a need to consider internal variables to represent the changes in thermodynamics state [165].

The literature presents several authors who proposed models to represent the *SMA* thermomechanical constitutive behavior. Falk [208] uses a polynomial equation to represent shape memory alloys phenomenology. Although very useful for dynamical problems, Falk [208]'s model does not consider internal variables and does not capture essential phenomena in *SMA* as hysteresis and dissipation. Later, Fremond [209, 210] proposed a model with assumed phase transformation kinetics for the thermomechanical response of *SMA* where phase transformations are described by two internal variables associated with volume fractions of two martensite variants.

Afterward, alternatives were developed considering different possibilities of the phase transformation function [207]. Boyd and Lagoudas [211] and Souza et al. [212] proposed models such as phase transformation and martensite reorientation are mathematically represented by loading functions and follow the classical plasticity theory. Soon, Bhattacharyya and Lagoudas [213] employed statistical physics to simulate strain recovery in phase transformation induced by temperature. The authors proposed an additional parameter that considers the material degradation over thermomechanical load cycles. Later, Fischlschweiger and Oberaigner [214] developed a rate formalism for martensite phase transformations based on statistical physics.

Based on that, *SMA* constitutive models with assumed phase transformation kinetics is a class of model that has broad use, adopting a mathematical expression to describe the phase transformation kinetics. Originally proposed by Tanaka et al. [215] using an exponential law, other approaches were proposed later on.

Considering a one-dimensional model of a *SMA* sample submitted to a uniaxial load, the thermodynamics principles, the energy balance, and Clausius-Duhem inequality, the thermodynamics of a *SMA* sample is attributed to the state variables (ϵ,T,β). Where ϵ represents the strain and β the martensite volume fraction governed by σ and T states. By introducing the Helmholtz free energy: $\Phi = U - TS$, where U is the internal energy and S the entropy, the Clausius-Duhem inequality can be written as:

$$\sigma = \rho_0 \frac{\partial \Phi(\epsilon, \beta, T)}{\partial \epsilon} = \sigma(\epsilon, \beta, T) \tag{20}$$

Eq. (20) can be considered the general mechanical constitutive expression for shape memory alloys and can be rewritten in the differential form as follow:

$$d\sigma = \frac{\partial \sigma}{\partial \epsilon} d\epsilon + \frac{\partial \sigma}{\partial \beta} d\beta + \frac{\partial \sigma}{\partial T} dT \tag{21}$$

The differential form of the constitutive equation considers the state variables, σ, ϵ, T, and the internal variable β to represent martensite volume fraction. Therefore, the following constitutive equation is proposed in the rate form:

$$\dot{\sigma} = E\dot{\epsilon} + \alpha\dot{\beta} + \Theta\dot{T} \tag{22}$$

where E represents Young's modulus, Θ the thermal dilatation coefficient, and $\alpha = -E\epsilon_R$ with ϵ_R as the maximum recoverable strain and the *SMA* functions assume the following form:

$$E(\epsilon, \beta, T) = \rho_0 \frac{\partial^2 \Phi}{\partial \epsilon^2}, \quad \alpha(\epsilon, \beta, T) = \rho_o \frac{\partial^2 \Phi}{\partial \epsilon \partial \beta}, \quad \Theta(\epsilon, \xi, T) = \rho_0 \frac{\partial^2 \Phi}{\partial \epsilon \partial T} \tag{23}$$

Phase transformation kinetics is assumed by considering a mathematical expression essentially described considering two possibilities: forward austenite-martensite transformation $A \rightarrow M$; and reverse, martensite-austenite transformation $M \rightarrow A$. Each one of them is defined by critical stress levels that are functions of temperature. Basically, critical stress defines a hypersurface in stress-temperature space, similar to the plastic yield surface, defining the phase transformation

region. In general, it is important to identify the start and finish of austenite-martensite phase transformation - σ_{rs} and σ_{rf}; and the start and finish of martensite-austenite phase transformation - σ_{fs} and σ_{ff}. Experimental observations attest that a linear temperature dependence for high temperatures can be adopted [216]. Nevertheless, low-temperature behavior shows a different pattern [34]. Fig. 3.11(a) presents the critical phase transformation stress surfaces and their temperature dependence for Tanaka et al. [215], Liang and Rogers [216] while Fig. 3.11(b) deals with Brinson [34] and the model developed in this thesis.

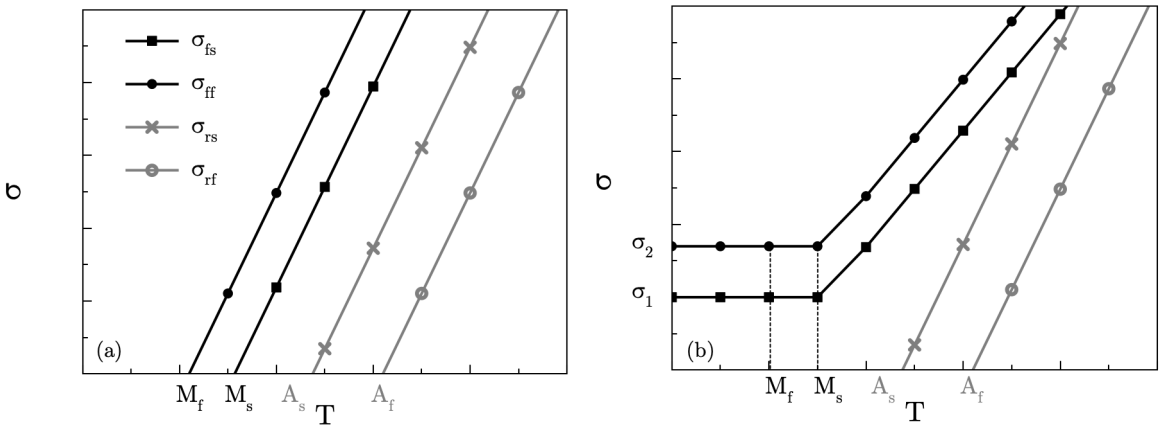


Fig. 3.11: Phase transformation stress surfaces as a function of temperature. (a) Tanaka et al. [215], Liang and Rogers [216]. (b) Brinson [34].

Critical stresses phase transformation are attributed to critical temperatures in Fig. 3.11(a) and defined as:

$$\begin{aligned} \sigma_{fs} &= C_M(T - M_s) \quad \sigma_{rs} = C_A(T - A_s) \\ \sigma_{ff} &= C_M(T - M_f) \quad \sigma_{rf} = C_A(T - A_f) \end{aligned} \tag{24}$$

Based on that, it is possible to define the phase transformation region, describing its kinetics using the following equations.

$$\beta = \beta_0 + (1 - \beta_0) f_M(\tilde{\sigma}, \tilde{T}) \qquad A \rightarrow M \tag{25}$$

$$\beta = \beta_0 f_A(\tilde{\sigma}, \tilde{T}) \qquad M \rightarrow A \tag{26}$$

where $0 \leq \tilde{\sigma} \leq 1$ and $0 \leq \tilde{T} \leq 1$ are normalized stress and temperature, defined as a function of critical stress and temperature transformation values for the forward and reverse transformation,

respectively and they are define according to the expressions:

$$\begin{aligned}
&\bullet \text{ If } \dot{T} = 0,\ \dot{\sigma} > 0\ \&\ \sigma_{fs} \leq \sigma \leq \sigma_{ff} \\
&\qquad\qquad \tilde{\sigma} = \frac{\sigma - \sigma_{fs}}{\sigma_{ff} - \sigma_{fs}} \\
&\qquad\qquad\qquad\qquad A \rightarrow M \\
&\bullet \text{ If } \dot{\sigma} = 0,\ \dot{T} < 0\ \&\ M_f \leq T \leq M_s \\
&\qquad\qquad \tilde{T} = \frac{T - M_s}{M_f - M_s}
\end{aligned} \tag{27}$$

$$\begin{aligned}
&\bullet \text{ If } \dot{T} = 0,\ \dot{\sigma} < 0\ \&\ \sigma_{rf} \leq \sigma \leq \sigma_{rs} \\
&\qquad\qquad \tilde{\sigma} = \frac{\sigma - \sigma_{rf}}{\sigma_{rs} - \sigma_{rf}} \\
&\qquad\qquad\qquad\qquad M \rightarrow A \\
&\bullet \text{ If } \dot{\sigma} = 0,\ \dot{T} > 0\ \&\ A_s \leq T \leq A_f \\
&\qquad\qquad \tilde{T} = \frac{T - A_f}{A_s - A_f}
\end{aligned} \tag{28}$$

It is important to state that $\tilde{\sigma}$ and $\tilde{T}$ are within the interval between zero and 1. If $\dot{\sigma} = 0$, than $\tilde{\sigma} = 0$. And if $\dot{T} = 0$, than $\tilde{T} = 0$.

The essential point related to this kind of model is the expression employed to describe the phase transformation kinetics, defined from the hardening functions $f_M(\tilde{\sigma}_M, \tilde{T})$ and $f_A(\tilde{\sigma}_A, \tilde{T})$.

Tanaka et al. [215] proposed a model representing volume fraction β as exponential functions.

$$\beta = 1 - \exp\left[a_M(M_s - T) + b_M\sigma\right] \qquad A \rightarrow M \tag{29}$$

$$\beta = \exp\left[a_A(A_s - T) + b_A\sigma\right] \qquad M \rightarrow A \tag{30}$$

where $a_M = -2\ln(10)/(M_s - M_f)$, $b_M = a_M/C_M$, $a_A = 2\ln(10)/(A_f - A_s)$ and $b_A = a_A/C_A$. Since exponential functions are of concern, it is important to define the end of phase transformation assuming that the end of transformation occurs with $\beta \geq 0.99$, for example.

Note that Tanaka's original model does not consider initial values of β (β_0) which is a determinant variable for sub loops. Beyond that, the authors consider different functions for forward and reverse transformations. This entails no change of concavity in phase transformation curves.

On this thesis *SMA* proposed model, volume fraction β can be expressed in terms of $\tilde{\sigma}_M$ and $\tilde{\sigma}_A$:

$$\beta = \beta_0 + (1 - \beta_0)[1 - \exp\left(-2\pi(\tilde{\sigma} + \tilde{T})\right)] \qquad A \rightarrow M \tag{31}$$

$$\beta = \beta_0[1 - \exp\left(-2\pi(\tilde{\sigma} + \tilde{T})\right)] \qquad M \rightarrow A \tag{32}$$

Eq. (31) and Eq. (32) represent exponential equations considering the initial value of martensite volume fraction and also the same function for forward and reverse transformations ($f_M = f_A$). The results to compare both pairs of equations are in section 5.1 and leads to a similar result. The change in concavity is preserved as in the following models.

Liang and Rogers [216] proposed trigonometric functions for phase transformation kinetics adopting the same critical transformation stress values, expressed as a linear function of temperature as follows:

$$\beta = \beta_0 + (1 - \beta_0)\left[\frac{1}{2} - \frac{1}{2}\cos\left(\pi(\tilde{\sigma} + \tilde{T})\right)\right] \qquad A \rightarrow M \tag{33}$$

$$\beta = \beta_0\left[\frac{1}{2} - \frac{1}{2}\cos\left(\pi(\tilde{\sigma} + \tilde{T})\right)\right] \qquad M \rightarrow A \tag{34}$$

Brinson [34] improved the models with assumed transformation kinetics dividing volume fraction into two distinct martensite fractions, one induced by temperature (β_T) and the other induced by stress (β_S): $\beta = \beta_T + \beta_S$. In addition, different Young's modulus for austenite and martensite is assumed and a more realistic description is employed to describe the critical phase transformation stress values. The model also makes a distinction between twinned martensite (M) and detwinned martensite (M^+).

In order to present the model, consider the form of the transformation kinetics, described by the following trigonometric equations:

$$\beta_S = \beta_{S0} + (1 - \beta_{S0})\left[\frac{1}{2} - \frac{1}{2}\cos\left(\pi\tilde{\sigma}\right)\right] \qquad A \rightarrow M^+ \;\;\&\;\; M \rightarrow M^+ \tag{35}$$

$$\beta_T = \beta_{T0} - \frac{\beta_{T0}}{1 - \beta_{S0}}\left(\beta_S - \beta_{S0}\right) \qquad M \rightarrow M^+ \tag{36}$$

$$\beta_T = \beta_{T0} + (1 - \beta_{T0}) \left[\frac{1}{2} - \frac{1}{2} \cos(\pi \tilde{T}) \right] \qquad A \rightarrow M \tag{37}$$

$$\beta_S = \beta_{S0} \left[\frac{1}{2} - \frac{1}{2} \cos(\pi \tilde{\sigma}) \right] \qquad M^+ \rightarrow A \tag{38}$$

$$\beta_S = \beta_{S0} \left[\frac{1}{2} - \frac{1}{2} \cos(\pi \tilde{T}) \right] \qquad M^+ \rightarrow A \tag{39}$$

$$\beta_T = \beta_{S0} \left[\frac{1}{2} - \frac{1}{2} \cos(\pi \tilde{T}) \right] \qquad M \rightarrow A \tag{40}$$

The $A \rightarrow M$ phase transformation stress values are described by the following equations:

$$\begin{aligned} \sigma_{fs} &= \sigma_s + C_M(T - M_s) \\ \sigma_{ff} &= \sigma_f + C_M(T - M_s) \end{aligned} \tag{41}$$

and for reverse phase transformation, $M \rightarrow A$, critical stresses values are defined by:

$$\begin{aligned} \sigma_{rs} &= C_A(T - A_s) \\ \sigma_{rf} &= C_A(T - A_f) \end{aligned} \tag{42}$$

For a low temperature condition ($T < M_f$), the process of variant reorientation ($M \rightarrow M^+$) is defined by critical variant reorientation stresses are σ_s and σ_f, respectively, and martensite variant reorientation is described by Eq. (35) and Eq. (36).

In addition, Young's modulus is described by considering a kind of rule of mixtures of the austenite and martensite values, being expressed by:

$$E = E_A + \beta(E_M - E_A) \tag{43}$$

Note that for Liang and Rogers [216] and Brinson [34] models this representations gives the same result as original equations. Therefore, the representation exposed in this section is able to unify the models presented by the use of $\beta = \beta_0 + (1 - \beta_0) f_M$ and $\beta = \beta_0 f_A$ and $f_M = f_A$ for each model.

Enemark et al. [217] and Enemark et al. [218] proposed a change into hardening functions introducing *Bézier* second and third-order polynomial functions, respectively. The second-order *Bézier* function implies the use of two successive polynomial equations to describe martensite phase transformation. The smoothness is controlled by the non-negative coefficients and the solution can be found by applying traditional formulas. Different hardening functions are compared showing that internal subloops have a good agreement with experimental data.

Based on the assumed kinetic transformations models for *SMA* shown in references, it is possible to evaluate the martensite volume fraction of an *SMA* element by the applied stress state and temperature condition. However, the use of exponential [215] and trigonometric [216, 34] functions implies no analytical solution for a prescribed strain problem and requires iterative numerical procedures to solve the equation.

The synergistic use of *SMA* and piezoelectric materials adopt the idea to use kinetic and thermal energy (mechanical vibration and heat) in order to increase the operational range where a piezoelectric harvester can assume optimal conditions of energy conversion even for uncertain vibration sources. So, the next section describes a methodology to evaluate the purposed system containing an experimental approach and constitutive modeling for strain prescribed problems with an analytical solution.

4 Methodology

This chapter describes the methodology to evaluate the synergistic use of piezoelectric materials and shape memory alloys for energy harvesting with the objective to increase the harvester's operational range. The most used configuration of a traditional piezoelectric energy harvester is a cantilever beam submitted to base-vibration excitation. The dynamical response of a continuum cantilever beam can be modeled as a single degree of freedom mechanical oscillator considering the first mode shape of vibration for the free end and discrete parameter.

Fig. 4.1(a) shows a schematic illustration of a piezoelectric element coupled to a cantilever beam where $\ddot{y}(t)$ is the base acceleration and $x(t)$ is the absolute displacement of the tip end, referred to an inertial referential. Fig. 4.1(b) shows its archetype representation in a single degree of freedom mechanical oscillator connected to an external electric circuit (capacitance, C_p, and electrical resistance, R) by a piezoelectric element, represented by its electromechanical coupling, θ. The beam mass is represented by m while the stiffness is represented as a linear restoring force parameter k, while the general damping is c.

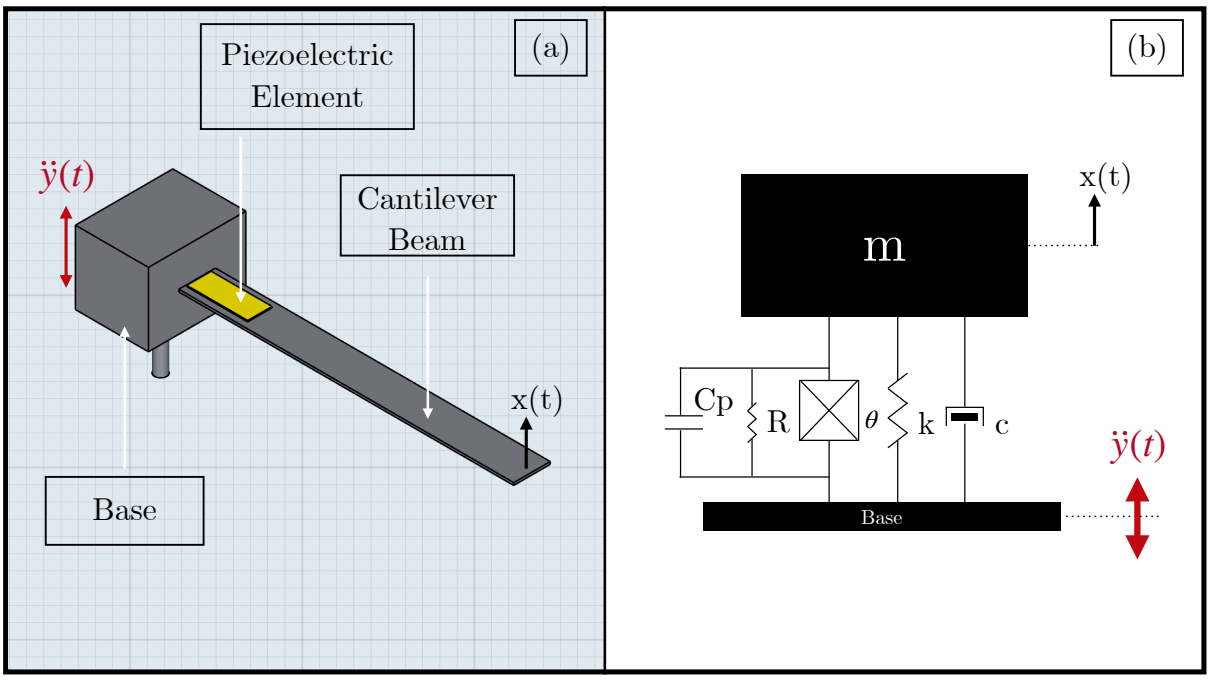


Fig. 4.1: Traditional piezoelectric energy harvester submitted to base vibration. (a) Cantilever beam configuration. (b) Single degree of freedom archetype.

This work considers the introduction of a *SMA* element able to alter its shape and mechanical properties due to martensite phase transformation. In a physical model, one end of the *SMA* element is attached to the harvester system by the free end of the beam while the other end is

fixed to a rigid support. The support is able to move to promote an initial load (preload) to the system. Besides that, the methodology in concern involves an experimental approach and mathematical modeling including analytical solutions and numerical simulations.

A constitutive model with kinetic phase transformation is developed to represent the constitutive behavior of the *SMA* element. For this reason, the first approach consists to evaluate the constitutive model for a *SMA* element in a mechanical oscillator with base vibration according to Fig. 4.2(a).

In addition, *SMA* phase transformation can be induced by temperature change (shape memory effect) or mechanical load (pseudoelastic effect). For this reason, this thesis explores a SMA-piezoelectric energy harvesters system in two configurations: one contains a *SMA* helical spring presenting a martensite phase stable at room temperature (Fig. 4.2(b)), and another considers a *SMA* helical spring presenting austenite phase stable at room temperature (Fig. 4.2(c)). In this way, it is possible to investigate the influence of martensite phase transformation induced by temperature and mechanical load, separately, in the synergistic use of both smart materials for energy harvesting.

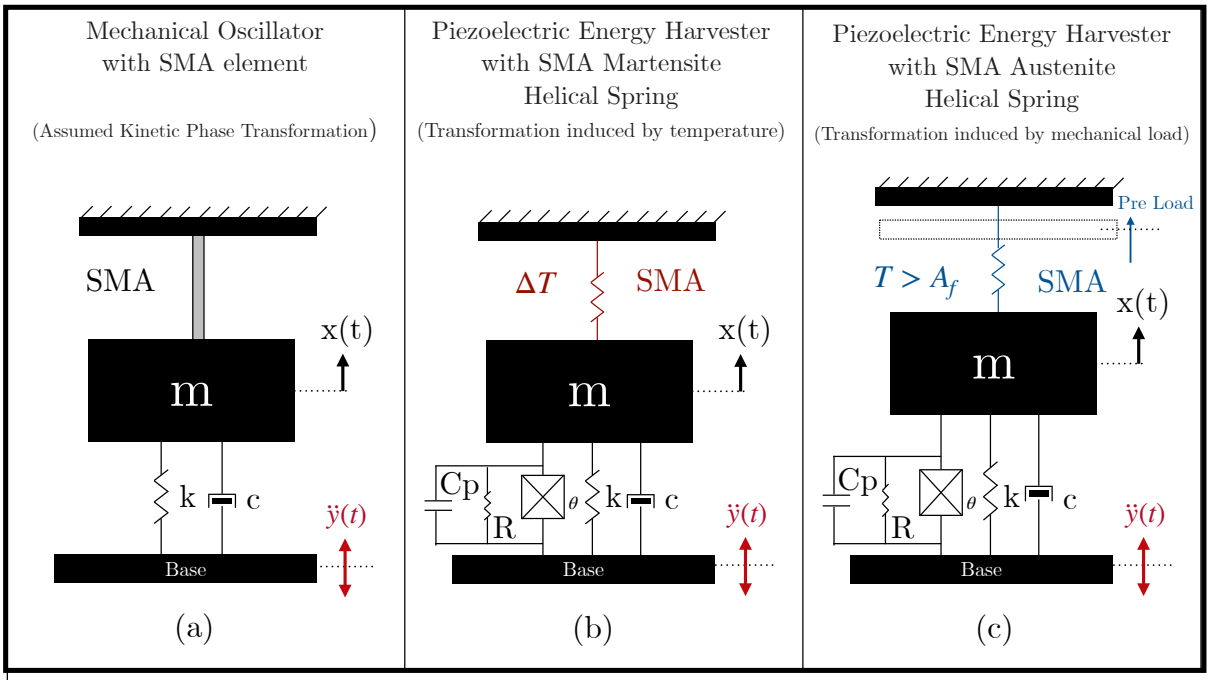


Fig. 4.2: *SMA* base vibration systems archetypes. (a) Mechanical oscillator with a *SMA* element. (b) Piezoelectric energy harvester with *SMA* martensite helical spring and phase transformation induced by temperature. (c) Piezoelectric energy harvester with *SMA* austenite helical spring with phase transformation induced by mechanical load.

Fig. 4.2(b) deals with shape memory effect. Experimental and numerical analyses are performed

showing the enhanced capabilities of the system due to the adaptability provided by shape memory alloys. A piezoelectric beam excited by an electrodynamic shaker is connected with *SMA* martensite helical spring that allows the exploitation of its remarkable characteristics in order to change system properties with temperature variations through Joule's effect. Afterward, the nonlinear dynamics of the energy harvesting system are investigated by exploiting the *SMA* adaptive behavior.

Fig. 4.2(c) evaluates a piezoelectric energy harvesting system coupled to a *SMA* helical spring presenting austenite phase stable at room temperature ($T > A_f$). Phase transformation occurs due to mechanical load considering constant temperature conditions. Numerical simulations allow for investigating the influence of quasi-static preload and dynamical load in *SMA* phase transformation and its capacity to make the harvester interact with external conditions changes in the excitation source. Moreover, nonlinear dynamics of the harvester system are investigated to increase energy conversion.

4.1 Experimental Methodology

This subsection is dedicated to presenting and describing the experimental methodology developed in this work to evaluate the synergistic use of piezoelectric materials and shape memory alloys for energy harvesting.

The experimental methodology starts with a thermomechanical characterization of *SMA* elements. The objective of experimental characterization is to explore *SMA* effects and phenomena involved in the martensite solid phase transformation process. Also, it allows to determine the parameters of the model used to develop the numerical simulations. In sequence, an experimental apparatus presents the application of a *SMA* helical spring connected to a piezoelectric electromechanically coupled cantilever beam for an energy harvester submitted to base vibration.

4.1.1 Thermomechanical Characterization

This subsection evaluates the three *SMA* elements in concern. Fig. 4.3 shows a representation of *SMA* samples being an austenite wire, a martensite helical spring, and an austenite helical spring. The therm austenite/martensite helical spring means that the element presents an austenite/martensite phase stable at room temperature. Basically, the tests consist of *DSC* and load-unloading tensile tests for different temperature and maximum load conditions.

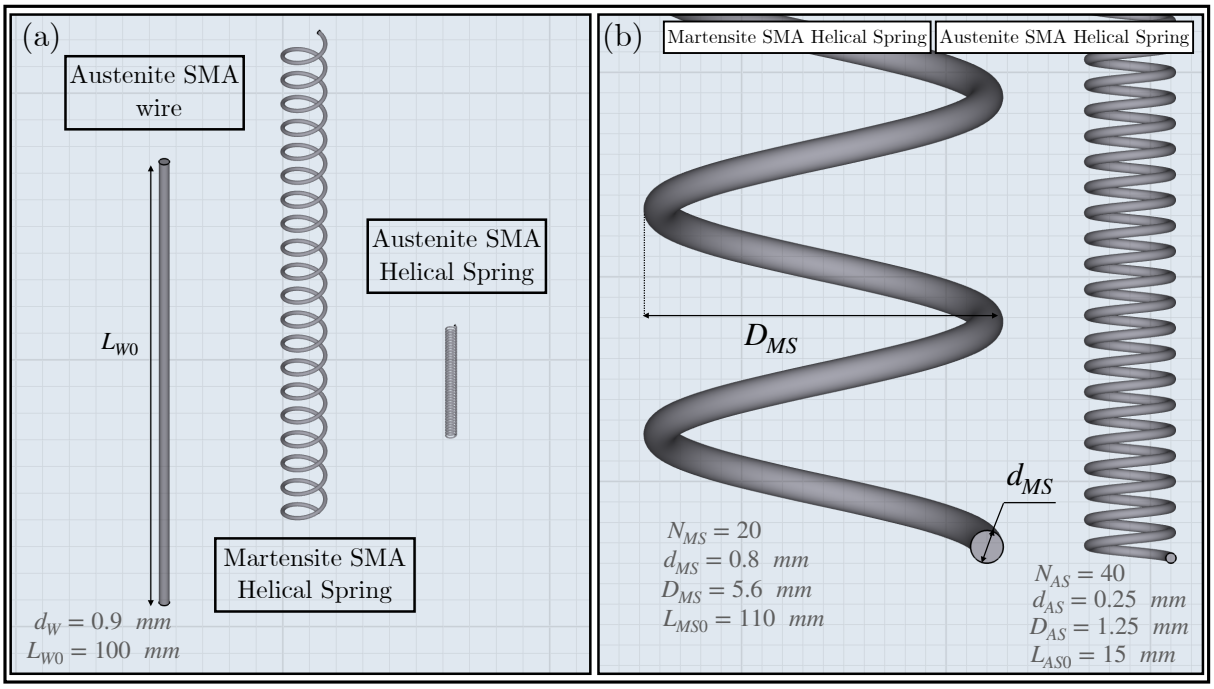


Fig. 4.3: *SMA* elements used in the analysis: wire, martensite helical spring and austenite helical spring.

At Fig. 4.3, letters d, D, L and N refers to minor diameter, major diameter, length and number of spires, respectively. The subscript $_W$ means wire while $_{MS}$ and $_{AS}$ are attributed to the martensite and austenite helical springs. Finally, the $_0$ indicates initial state. Table 3 indicates principal geometrical parameter for the *SMA* elements in concern.

Table 3: *SMA* elements geometrical properties.

SMA wire	d_W (mm)	L_0 mm)		
	0.09	100		
Martensite helical spring	d_{MS} (mm)	L_{MS0} (mm)	D_{MS} (mm)	N_{MS}
	0.8	110	5.6	20
Austenite helical spring	d_{AS} (mm)	L_{AS0} (mm)	D_{AS} (mm)	N_{AS}
	0.25	15	1.25	40

4.1.1.1 SMA Wire Characterization

The thermomechanical characterization of the *SMA* wire starts considering Differential Scanning Calorimeter - *DSC* (Netzsch DSC 200 F3) tests in order to identify the phase transformation temperatures. An *NiTi SMA* wire provided by *Sandinox* with $d_W = 0.9$mm diameter and

L_{W0} = 220mm length is of concern. It starts with a *DSC* tests with the aim to identify phase transformation temperatures. Fig. 4.4(a) shows the experimental setup for *DSC* tests at Mecanon-UFRJ laboratory. A small sample of *SMA* wire (5 - 15 μg) from *Sandinox* is tested considering a prescribed temperature and monitoring the necessary energy. Results are presented in Fig. 4.4(b) highlighting the critical phase transformation temperatures.

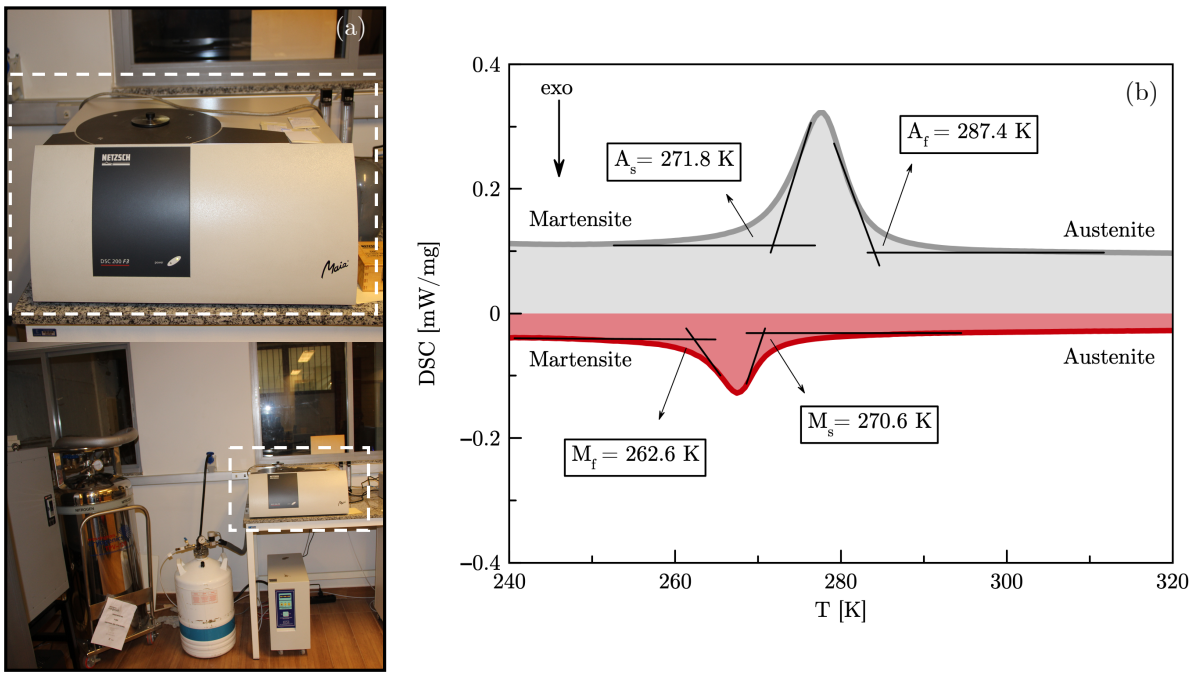


Fig. 4.4: Differential scanning calorimetry of peseudoelastic wire sample $d_W = 0.9\ mm$. (a) Experimental setup. (b) Phase transformation temperature.

Mechanical characterization is carried out considering quasi-static mechanical load and unload at different temperatures. A wire with L_{W0} = 220mm length is of concern using 60 mm to clamp the wire in a tensile machine at each end. Fig. 4.5(a) shows the experimental station for tensile tests. An Intron 5982 universal testing machine is employed considering a controlled displacement rate of 4.5 mm/min for a total of 5 cycles. A training process is employed before the tests impose a series of 20 cycles. Stress-strain diagrams are presented in Fig. 4.5(b) showing typical pseudoelasticity and martensite reorientation.

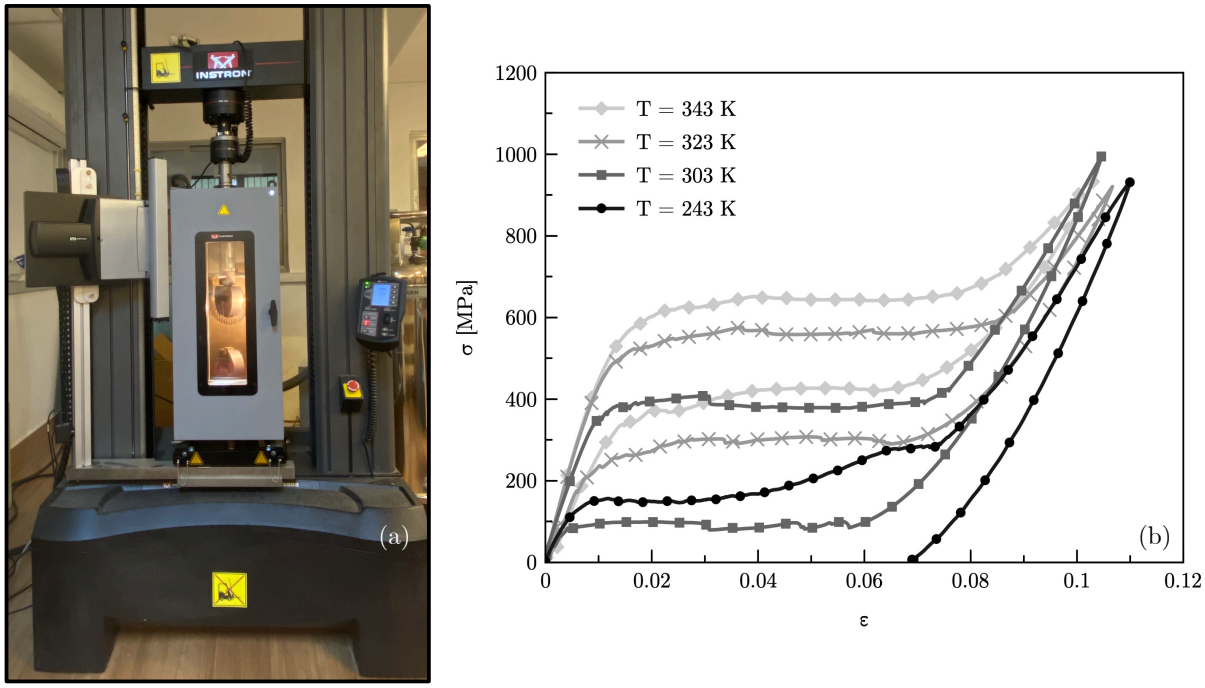


Fig. 4.5: Experimental tensile test for *SMA* wire sample $d_W = 0.9\ mm$. (a) Experimental setup. (b) Stress-strain curves for different temperature conditions.

Young's modulus can be estimated by considering the angular coefficient of the linear range of the curve, based on procedures presented in Savi et al. [219]. Different modulus is estimated for martensite and austenite phases. Austenite phase Young's modulus is measured at high temperature ($T > A_f$) through a linear interpolation of points in the range from 20% to 30% of maximum load for the austenite phase. Similarly, points from 80% to 90% of maximum load are considered for linear interpolation for the martensite Young's modulus. This methodology reduces the influence of instability effects related to experimental measurements at the beginning of the test and the load reversal regions. For low temperatures ($T = 243$ K), points from 5% to 10% are considered for linear interpolation. Critical stress phase transformations are estimated by considering the same procedure. Linear interpolations are carried out in order to estimate the start and finish of phase transformation points. Fig. 4.6 presents auxiliary pictures, used for the estimation of phase transformation critical stress values and Young's modulus, for different temperatures.

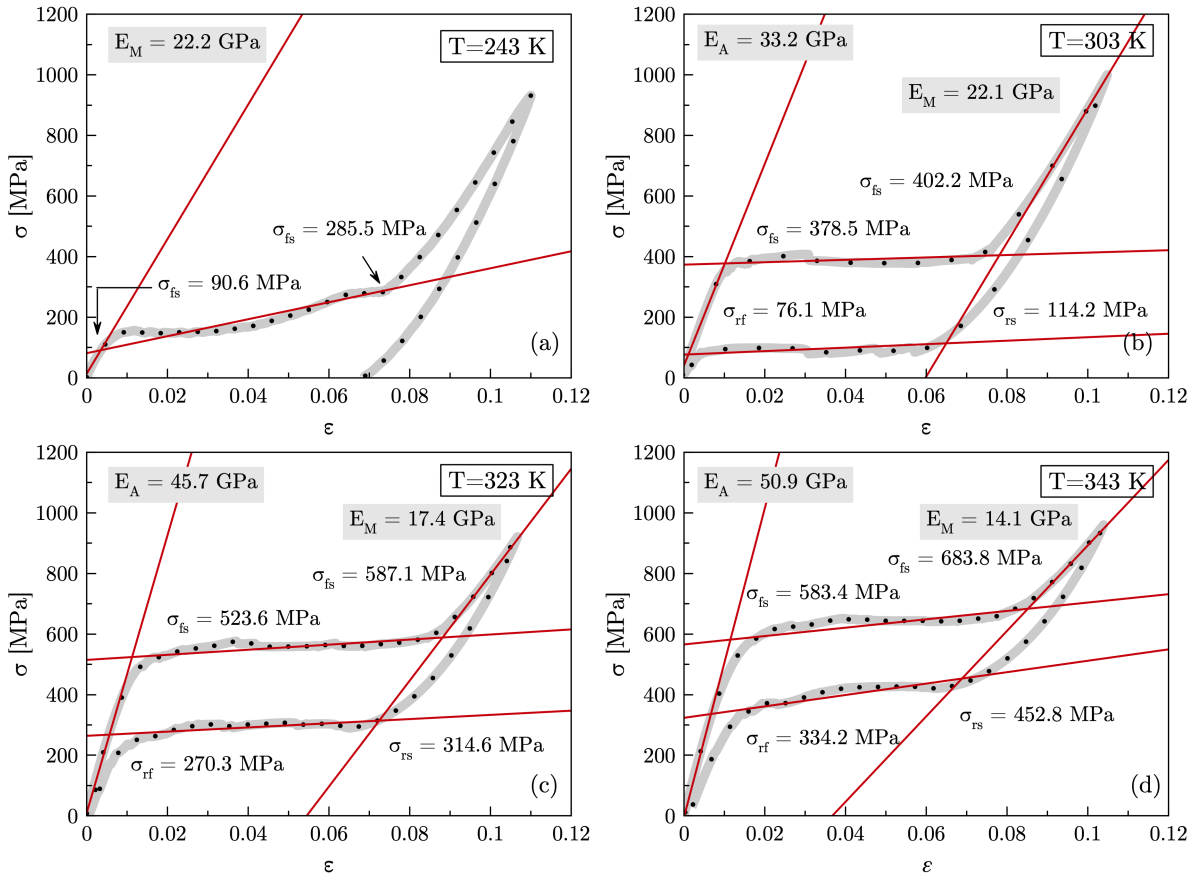


Fig. 4.6: Experimental determination of *SMA* Young's modulus and critical stresses phase transformation. (a) $T = 243$ K. (b) $T = 303$ K. (c) $T = 323$ K. (d) $T = 343$ K.

Based on the critical phase transformation stress values evaluated at different temperatures, it is possible to build the critical phase transformation stress surfaces, presented in Fig. 4.7. Once the model considers constant the critical stresses for temperatures below M_s, red points in Fig. 4.7 indicates a theoretical value assumed for $T = 243$ K. Note also that red lines are built by the linear interpolation of experimental results. For this reason, they do not coincide with the theoretical points as shown in Fig. 3.11.

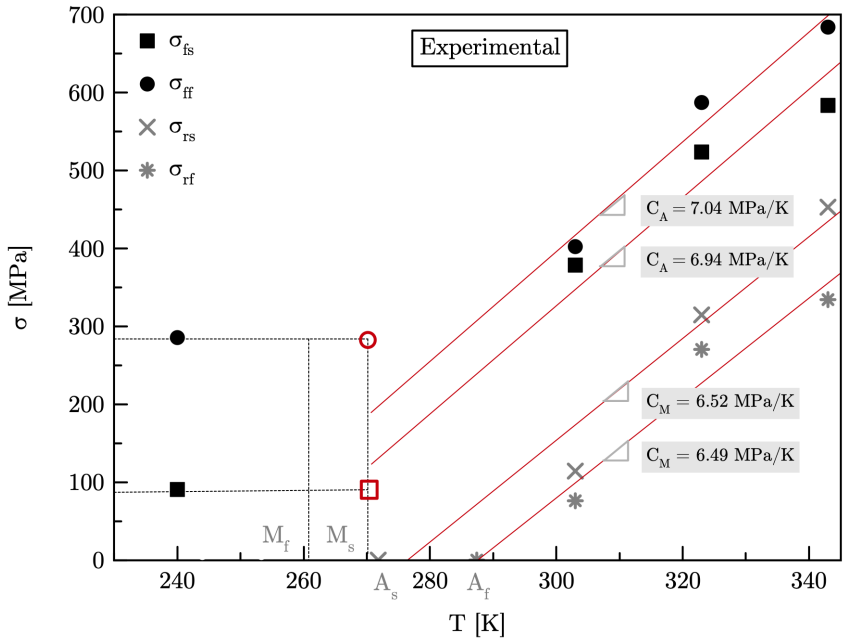


Fig. 4.7: Experimental critical phase transformation stress surface as a function of temperature.

Table 4 summarizes the constitutive parameters characterized by the thermomechanical tests. Austenite and martensite Young's modulus are determined by the arithmetic mean of measured values in Fig. 4.6. In addition, C_A and C_M are estimated by the mean of respective slopes presented in Fig. 4.7.

Table 4: *SMA* wire experimental constitutive parameters.

M_s (K)	M_f (K)	A_s (K)	A_f (K)	σ_s (MPa)	σ_f (MPa)
270.6	262.6	271.8	287.4	90.6	285.5
E_A (GPa)	E_M (GPa)	C_A (MPa/K)	C_M (MPa/K)	ϵ_R	
43.2	18.9	7	6.5	0.06	

4.1.1.2 Martensite SMA Helical Spring Characterization

This subsection deals with the characterization of the martensite *SMA* helical spring provided by *Dynalloy*. Fig. 4.8 present results for differential scanning calorimetry tests attributed to *SMA* helical spring in concern following the same procedures developed for the *SMA* wire sample.

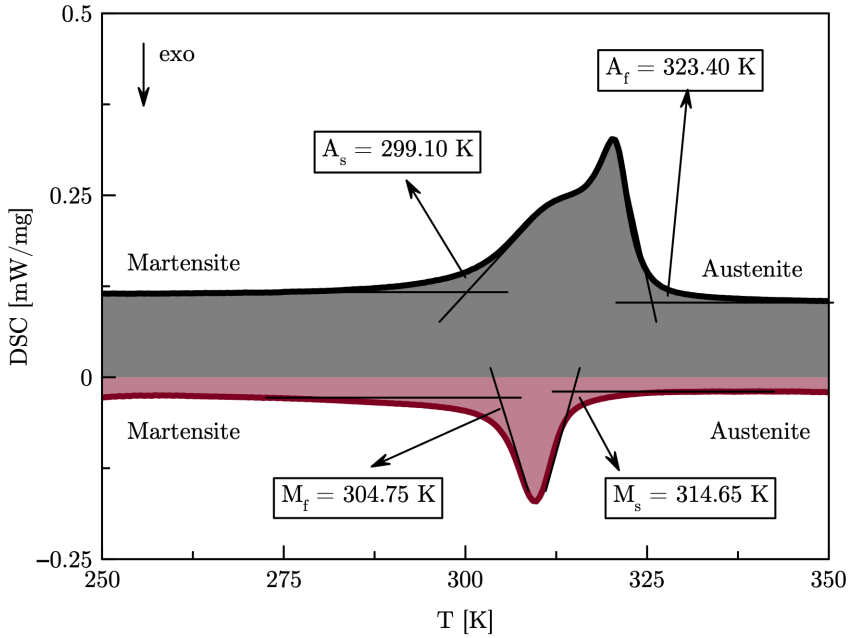


Fig. 4.8: Differential Scanning Calorimetry analysis showing phase transformation temperatures of a martensite helical spring sample.

Fig. 4.8 also shows the values of phase transformation temperatures. It should be pointed out that ambient temperature is associated with the martensite phase.

Since temperature is induced by the Joule effect, the relation between electric current and temperature can be estimated by considering a contactless infrared sensor (MLX90614 GY-906) that uses an Arduino Uno board for data acquisition. In order to compare temperature measurement, a thermocouple T type is also employed. *SMA* spring is connected with two fixed terminals to which a current from 0.0 A to 2.5 A is applied with an increment of 0.1 A and an interval of 60 s between each increment. This allows one to build a temperature-electrical current curve, presented in Fig. 4.9, where the phase transformation temperatures obtained from *DSC* analysis are represented. Note that the infrared and thermocouple sensors present similar results in the range of *DSC* phase transformation temperatures were obtained. A short deviation is detected only for temperatures related to 2.0 A and higher.

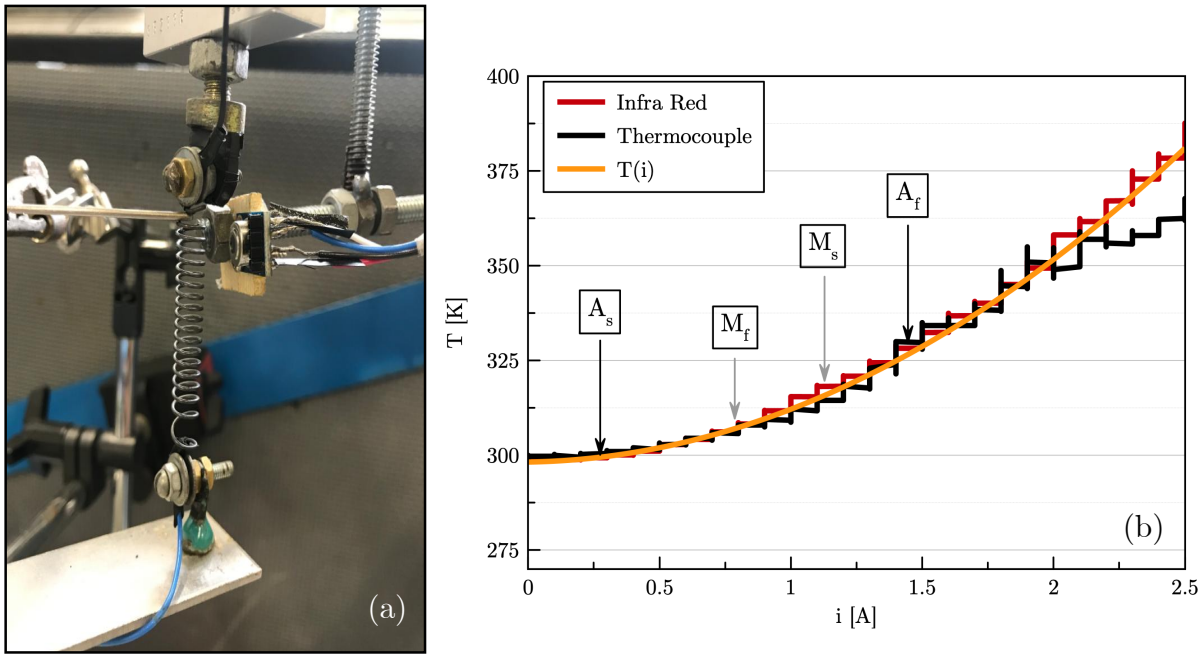


Fig. 4.9: Experimental analysis of the temperature electrical current. (a) Experimental apparatus of the martensite helical spring for the measurement through infrared and thermocouple sensors. (b) Temperature-electrical current diagram.

Concerning the Joule effect, experimental tests presented in Fig. 4.9 are employed in order to define a temperature-electric current relation as follows,

$$T(i) = 12.78i^2 + 1.14i + 25 \tag{44}$$

where i is the electrical current. Besides, phase transformation temperatures are assumed to be defined based on the *DSC* temperatures. The orange line in Fig. 4.9(b) refers to Eq. (44) obtained by quadratic interpolation between the points contained in the interval of 0 A to 2.5 A. The infrared sensor is selected for the reason to present a non-contact method to measure the temperature which can be considered more appropriate for dynamical experimental tests, further developed in this thesis.

The *SMA* spring is now characterized by a quasi-static mechanical tensile test. Force-displacement curves are built by using an Instron testing system (5966 model) with a controlled displacement rate of 10 mm/min. Tests are carried out for different constant electric currents (0 A and 1.5 A). It is important to mention that both spring terminals were electrically isolated to avoid parasite currents and damage accidents. Fig. 4.10 presents force-displacement curves for the quasi-static tests, showing shape memory effect behavior for low temperature (0 A) and pseudoelastic effect

for high-temperature behavior (1.5 A).

Stiffness can be estimated by considering the slope of the linear part of the curve, following the procedure presented by Savi et al. [219]. The slope is calculated considering points selected in the region from 30% to 70% of the maximum load for martensite (0.0 A). Analogously, considering points from 10% to 40% of the maximum load for austenite (1.5 A). This methodology reduces the influence of instability effects related to experimental measurements at the beginning of the test and at the load reversal regions. This analysis indicates a spring stiffness equivalent to $k_A = 216$ N/m for detwinned martensite and $k_M = 288$ N/m for the austenite phase. Note that, the application of electric current causes the increase of the critical stress level where phase transformation begins to occur.

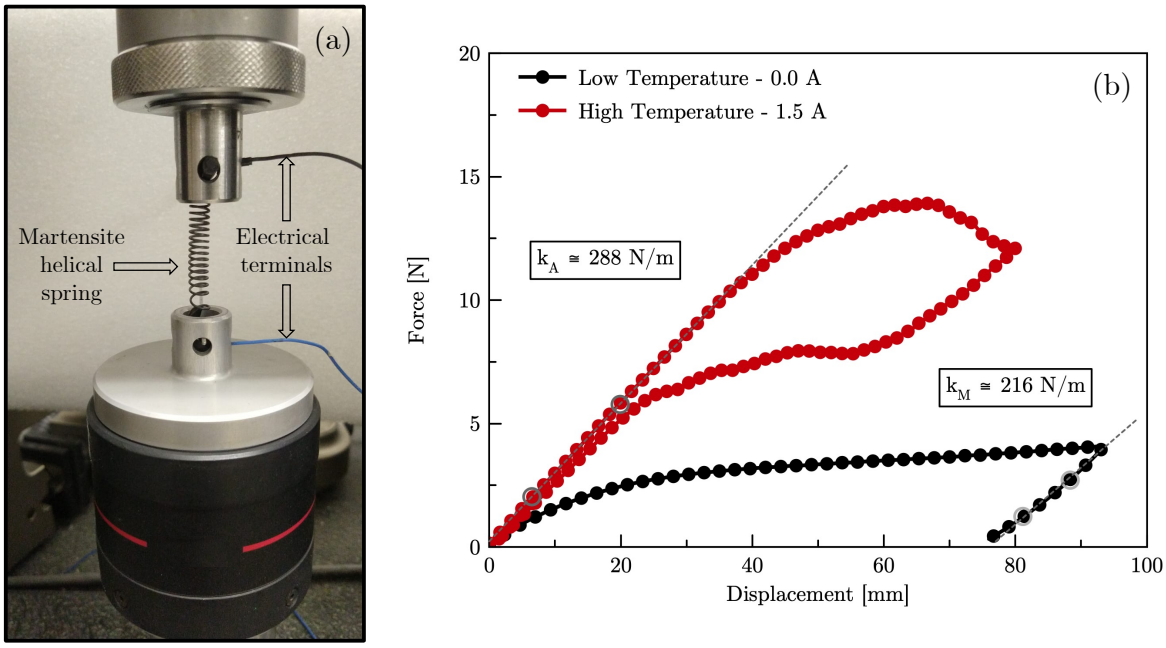


Fig. 4.10: Experimental quasi static load tests of the *SMA* mastensite helical spring. (a) Experimental apparatus. (b) Force × displacement curves considering different electrical currents. Ambient (low) temperature - without electrical current (0 A); and high temperature - with 1.5 A.

Table 5 deals with the martensite helical spring mechanical parameters found in its respective thermomechanical characterizations tests.

Table 5: *SMA* martensite helical spring experimental parameters.

M_s (K)	M_f (K)	A_s (K)	A_f (K)
314.65	304.75	299.10	323.4
i_{A_s} (A)	i_{A_f} (A)	k_M (N/m)	k_A (N/m)
0.25	1.37	216	288

4.1.1.3 Austenite SMA Helical Spring Characterization

Finally, the characterization of austenite *SMA* helical spring is in focus. A commercial shape memory alloy helical spring (*Moreli Ortodontia*) that presents a pseudoelastic effect at room temperature (298 K) is called an austenite helical spring in this work.

Fig. 4.11 present results obtained for *DSC* tests of a sample from *SMA* austenite helical spring. The procedures for test realization are the same as mentioned in the preview samples presented in this methodology.

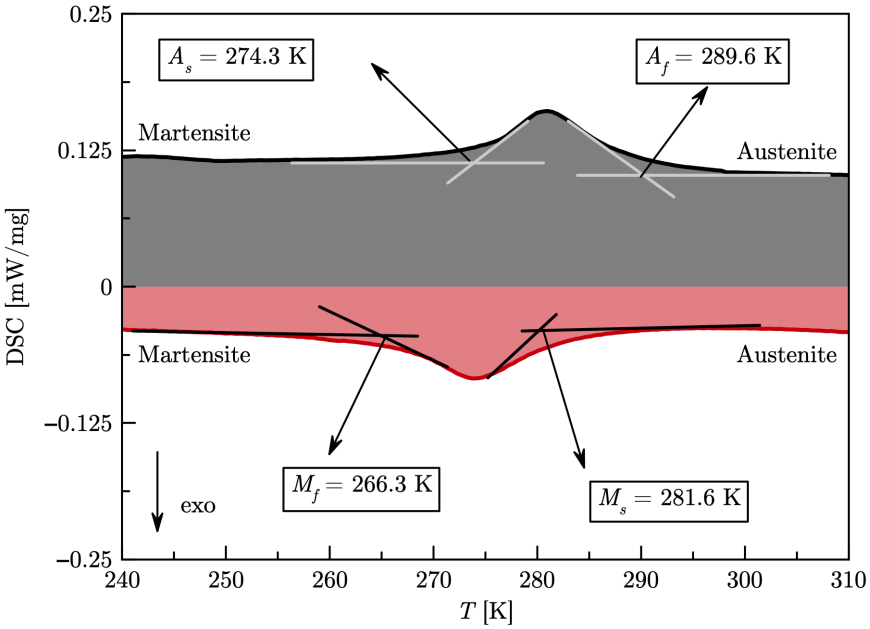


Fig. 4.11: Differential scanning calorimetry test of austenite helical spring.

In sequence, the characterization of a quasi-static mechanical gives Fig. 4.12 that shows a force-displacement diagram built using an Instron testing system (5966 model) with a controlled displacement rate of 4 mm/min. Tests are carried out at constant room temperature and different conditions of maximum prescribed displacement. Also, Fig. 4.12 shows attributed

stress and strain based on Eq. (94) and Eq. (95). A similar procedure as described in the previews sections is applied considering a linear fit in points between 20% and 50% of maximum displacement ($d_{SMA^{max}}$) for austenite Young's modulus determination.

Although in spring elements phase transformation is not fully complete at the cross-section, Young's modulus for martensite phase is considered as the result of a linear fit considering point between 80% and 90% of d_{SMA}^{max}.

Table 6 exposes constitutive parameters for polynomial model. Those parameters are applied in numerical simulations in section 5.3.

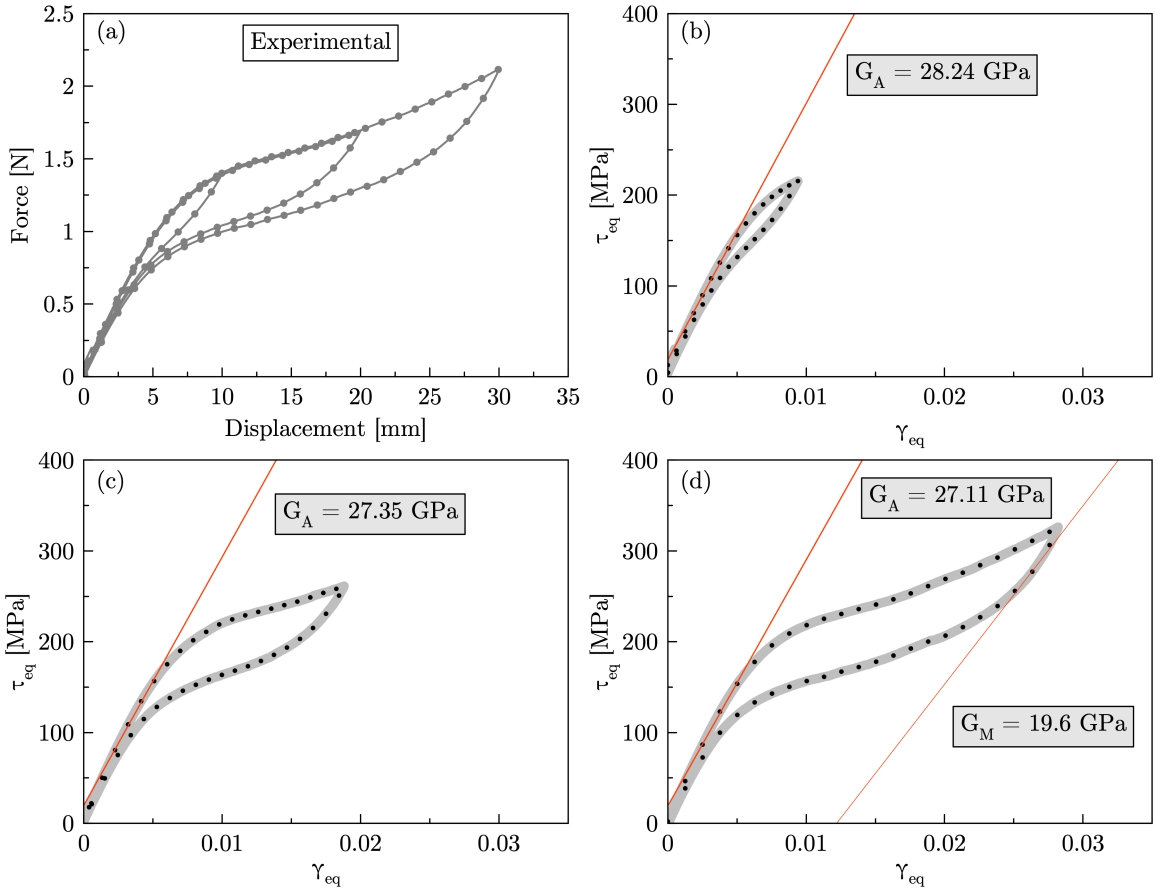


Fig. 4.12: Austenite helical spring quasi static tests. (a) Force × displacement diagram. Stress × strain diagrams: (b) $d_{SMA}^{max} = 10$ mm. (c) $d_{SMA}^{max} = 20$ mm. (d) $d_{SMA}^{max} = 30$ mm

Table 6: *SMA* austenite helical spring experimental constitutive parameters.

M_s (K)	M_f (K)	A_s (K)	A_f (K)	τ_s (MPa)	τ_f (MPa)
281.6	266.3	274.3	289.6	0	0
G_A (GPa)	G_M (GPa)	C_A (MPa)	C_M (MPa)	γ_R	
27.5	19.6	9	11	0.015	

4.1.2 Experimental Synergisctic Piezoelectric Energy Harvester with SMA

This subsection describes a vibration-based energy harvesting experimental approach that employs a synergistic use of piezoelectric and shape memory alloy elements. Methodology analysis is of concern. An experimental apparatus is built at CEFET/RJ in the LASEI laboratory (Laboratório de Sistemas e Estururas Inteligentes) with the objective to evaluate the performance of a real prototype of a SMA-piezoelectric energy harvester.

A piezoelectric element (PZT 5H - 40×10×0.5 mm - Mide Technology) is bonded with a double face tape to an aluminum cantilever beam with dimensions: 275×30×2 mm. The cantilever beam is clamped to an electrodynamics shaker (V350-DataPhysics Signal Force) that provides vibration to the system. A shape memory helical spring is attached to the free end of the aluminum cantilever beam with the other end fixed to a rigid support. It is considered that the martensite phase is stable at ambient temperatures, while austenite is stable at high temperatures ($T > A_f$). Temperature changes are induced through the Joule's effect by the application of electric current using a stabilized current source (TOE 8950). The geometrical properties of the *SMA* helical spring are presented in subsection 4.1.1. The energy harvesting electric circuit is represented by a simple external electric load resistance of 150 kΩ. A picture of the experimental setup is shown in Fig. 4.13. Note that the piezoelectric element is not clamped on the shaker support, it is coupled to the cantilever beam starting right after the clamp.

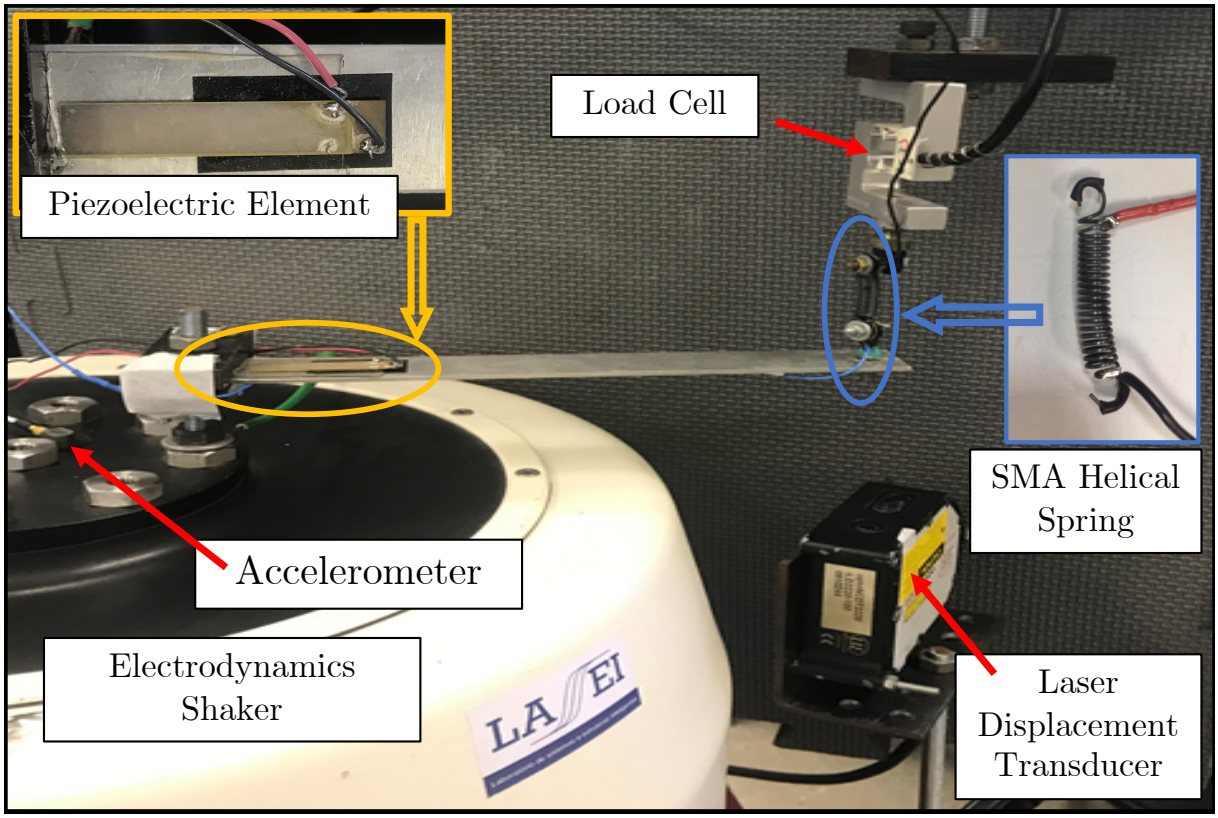


Fig. 4.13: Experimental apparatus of the energy harvester with synergistic use of piezoelectric and shape memory alloy elements. The system is composed of a cantilever beam with a piezoelectric element connected to a shape memory alloy spring, being excited in the vertical direction by an electrodynamics shaker

A laser displacement transducer (Micro-Epsilon $\mu\epsilon$ model optonNCDT2200) is employed to measure the free end displacement while the base acceleration is evaluated by an accelerometer (PCB 333B40) connected to the shaker. A load cell Leader CS-5 is employed to measure the restitution force provided by the *SMA* spring. A data acquisition system (CDAQ-9174 National Instruments) is employed. The system is subjected to a harmonic excitation with a maximum value of 9.81 m/s^2.

Energy harvesting capacity is evaluated by estimating the output and input powers. Output power is calculated by the square of electrical voltage measured in the piezoelectric element divided by the external electric resistance element. On the other hand, input power is estimated as the product of the applied force by the velocity measured at the cantilevered beam end connected to the *SMA* spring. Efficiency is estimated as the ratio between output and input powers. Fig. 4.14 shows the experimental workstation with auxiliary instruments mentioned.

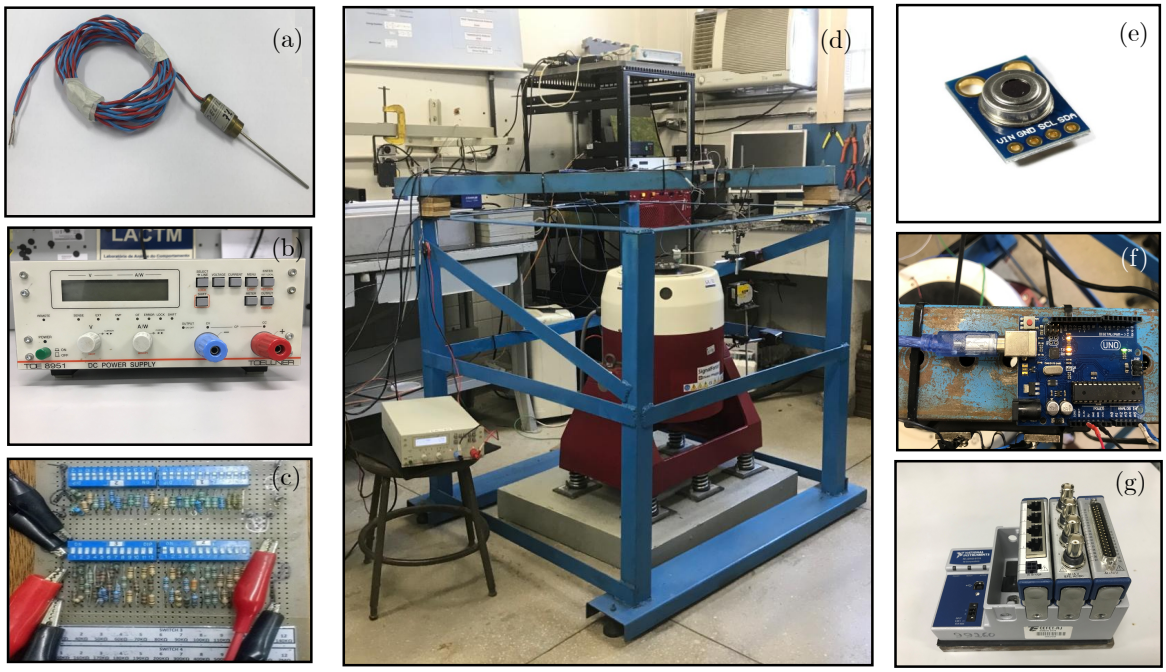


Fig. 4.14: Experimental setup for synergistic use of piezoelectric materials for energy harvesting. (a) Termocouple T type. (b) Electrical current font. (c) Electrical resistance board. (d) Work station. (e) Infrared temperature sensor. (f) Arduino board. (g) Data acquiring system.

To investigate the physical phenomenons involved in *SMA* piezoelectric energy harvesting a mathematical model is presented in the next subsection. The parameters obtained in the experimental approach are further used for numerical simulations.

4.2 Mathematical Modeling

This subsection describes the mathematical modeling methodology used for the numerical analyses developed in this thesis considering the archetypes presented in Fig. 4.2. First, the *SMA* constitutive model with assumed kinetic phase transformation proposed is tested for quasi-static and dynamical analyses. In sequence, the martensite *SMA* helical spring is connected to a piezoelectric energy harvester and modeled. The martensite *SMA* helical spring is heated by Joule's effect and the influence of phase transformation induced by temperature is evaluated. Finally, the austenite *SMA* helical spring is modeled with constant stress over the cross-section and connected to the piezoelectric energy harvester. The influence of phase transformation induced by the mechanical load is investigated by a quasi-static preload and base vibration.

4.2.1 SMA Polynomial Model with Assumed Kinetic Phase Transformation

The objective of this subsection is to develop a constitutive model to represent the constitutive behavior of *SMA* elements submitted to prescribed strain problems. The models with trans-

formation kinetics, previously discussed, have the characteristic that the kinetics function β is expressed as a function of stress and temperature. Hence, the stress driving case is directly evaluated but situations with strain driving cases need to be associated with a proper algorithm [33]. Beyond that, dynamical problems for discrete elements require the knowledge of the displacement attributed to each element to compute the respective forces. So, the proposed constitute model assumes analytical solutions for strain driving cases avoiding the use of iterative procedures to find the relation between stress, strain, temperature, and martensite volume fraction.

The same framework of the previous models is adopted, incorporating the improvements proposed by the Brinson [34] model. Therefore, it is possible to represent the martensite reorientation and the phase transformation induced by temperature and mechanical load considering different proprieties for each phase, austenite, and martensite. In this regard, the critical phase transformations stresses are defined as follows (Fig. 3.11 (b)):

$$\begin{aligned} \sigma_{fs} &= \sigma_1 + C_M(T - M_s) \quad \sigma_{rs} = C_A(T - A_s) \\ \sigma_{ff} &= \sigma_2 + C_M(T - M_s) \quad \sigma_{rf} = C_A(T - A_f) \end{aligned} \tag{45}$$

Martensite volume fraction (β) is expressed as follows:

$$\beta = \beta_0 + (1 - \beta_0) f_M(\tilde{\sigma}, \tilde{T}) \qquad A \rightarrow M/M^+ \;\; \& \;\; M \rightarrow M^+ \tag{46}$$

$$\beta = \beta_0 f_A(\tilde{\sigma}, \tilde{T}) \qquad M/M^+ \rightarrow A \tag{47}$$

where the hardening functions $f_M(\tilde{\sigma}, \tilde{T})$ and $f_A(\tilde{\sigma}, \tilde{T})$ are expressed by two successive second order polynomial equations each and β is expressed as:

$$\beta_S = \begin{cases} \beta_{S0} + (1 - \beta_{S0})(a_1 \tilde{\sigma}^2) & \text{if } \tilde{\sigma} \leq B_M \\ \beta_{S0} + (1 - \beta_{S0})(a_2 \tilde{\sigma}^2 + b_2 \tilde{\sigma} + c_2) & \text{if } \tilde{\sigma} > B_M \end{cases} \qquad A \rightarrow M^+ \;\; \& \;\; M \rightarrow M^+ \tag{48}$$

$$\beta_T = \beta_{T0} - \frac{\beta_{T0}}{1 - \beta_{S0}} (\beta_S - \beta_{S0}) \qquad M \rightarrow M^+ \tag{49}$$

$$\beta_T = \begin{cases} \beta_{T0} + (1 - \beta_{T0})(a_1 \tilde{T}^2) & \text{if } \tilde{T} \leq B_M \\ \beta_{T0} + (1 - \beta_{T0})(a_2 \tilde{T}^2 + b_2 \tilde{T} + c_2) & \text{if } \tilde{T} > B_M \end{cases} \qquad A \rightarrow M \tag{50}$$

$$\beta_S = \begin{cases} \beta_{S0}(a_3\tilde{\sigma}^2 + b_3\tilde{\sigma} + c_3) & \text{if } \tilde{\sigma} \geq B_A \\ \beta_{S0}(a_4\tilde{\sigma}^2) & \text{if } \tilde{\sigma} < B_A \end{cases} \qquad M^+ \rightarrow A \tag{51}$$

$$\beta_S = \begin{cases} \beta_{S0}(a_3\tilde{T}^2 + b_3\tilde{T} + c_3) & \text{if } \tilde{T} \geq B_A \\ \beta_{S0}(a_4\tilde{T}^2) & \text{if } \tilde{T} < B_A \end{cases} \qquad M^+ \rightarrow A \tag{52}$$

$$\beta_T = \begin{cases} \beta_{T0}(a_3\tilde{T}^2 + b_3\tilde{T} + c_3) & \text{if } \tilde{T} \geq B_A \\ \beta_{T0}(a_4\tilde{T}^2) & \text{if } \tilde{T} < B_A \end{cases} \qquad M \rightarrow A \tag{53}$$

The polynomial equation coefficients are defined with the aid of a variable λ to represent $\tilde{\sigma}$ and $\tilde{T}$:

$$f_M(\lambda) = \begin{cases} a_1\lambda^2 + b_1\lambda + c_1 & 0 \leqslant \lambda \leqslant B_M \\ a_2\lambda^2 + b_2\lambda + c_2 & B_M < \lambda \leqslant 1 \end{cases} \tag{54}$$

$$f_A(\lambda) = \begin{cases} a_3\lambda^2 + b_3\lambda + c_3 & 1 \leqslant \lambda \leqslant B_A \\ a_4\lambda^2 + b_4\lambda + c_4 & B_A < \lambda \leqslant 0 \end{cases} \tag{55}$$

where $0 < B_M < 1$ and $0 < B_A < 1$ are controlling parameters for forward and reverse transformations, respectively, defining start and finishes of the polynomial curve. These conditions are established as $f_M(0) = 0$ and $f_M(1) = 1$ and also considering that horizontal tangent at start and finish of the curve must be satisfied ($f'_M(0) = 0$ and $f'_M(1) = 0$). Continuity condition has to be considered in ($f_M(B_M)$) and also its derivatives in relation of λ, ($f'_M(B_M)$) at connection point.

Based on that, one can state $b_1 = 0$ and $c_1 = 0$ for martensite-austenite transformation using a system as follows, $[K]\{x\} = \{F\}$:

$$\begin{bmatrix} 0 & 1 & 1 & 1 \\ 0 & 2 & 1 & 0 \\ B_M^2 & -B_M^2 & -B_M & -1 \\ 2B_M & -2B_M & -1 & 0 \end{bmatrix} \begin{Bmatrix} a_1 \\ a_2 \\ b_2 \\ c_2 \end{Bmatrix} = \begin{Bmatrix} 1 \\ 0 \\ 0 \\ 0 \end{Bmatrix} \tag{56}$$

Inverting [K] matrix one can find the value of the coefficients as: $a_1 = \frac{1}{B_M}$, $a_2 = \frac{1}{B_M - 1}$, $b_2 = \frac{-2}{B_M - 1}$, $c_2 = \frac{B_M}{B_M - 1}$. Considering Eq. (21), one can achieve the analytical solution for σ according to:

For $\tilde{\sigma} < B_M$:

$$\sigma - \alpha[\beta_0 + (1-\beta_0)f_{M1}] - \sigma_0 - E\epsilon + E_0\epsilon_0 + \alpha_0\beta_0 = 0 \tag{57}$$

$$\sigma - \alpha\beta_0 - \alpha a_1\tilde{\sigma}^2 + \alpha\beta_0 a_1\tilde{\sigma}^2 - \sigma_0 - E\epsilon + E_0\epsilon_0 + \alpha_0\beta_0 = 0 \tag{58}$$

And, for $\tilde{\sigma} > B_M$:

$$\sigma - \alpha[\beta_0 + (1-\beta_0)f_{M2}] - \sigma_0 - E\epsilon + E_0\epsilon_0 + \alpha_0\beta_0 = 0 \tag{59}$$

$$\sigma - \alpha\beta_0 - \alpha a_2\tilde{\sigma}^2 - \alpha b_2\tilde{\sigma} - \alpha c_2 + \alpha\beta_0 a_2\tilde{\sigma}^2 + \alpha\beta_0 b_2\tilde{\sigma} + \alpha\beta_0 c_2 - \sigma_0 - E\epsilon + E_0\epsilon_0 + \alpha_0\beta_0 = 0 \tag{60}$$

For reverse transformation, $f_M(1) = 1$ and $f_A(0) = 0$. Horizontal tangent at start and finish of the curve must be satisfied ($f'_A(1) = 0$ and $f'_A(0) = 0$). And continuity has to be considered at the connection point B_A ($f_A(B_A)$ and $f'_A(B_A)$).

Since $b_4 = 0$ and $c_4 = 0$, the system is reduced to a $4X4$, $[K]\{x\} = \{F\}$, as follows:

$$\begin{bmatrix} 1 & 1 & 1 & 0 \\ 2 & 1 & 0 & 0 \\ B_A^2 & B_A^2 & 1 & -B_A^2 \\ 2B_A & 1 & 0 & -2B_A^2 \end{bmatrix} \begin{Bmatrix} a_3 \\ b_3 \\ c_4 \\ a_4 \end{Bmatrix} = \begin{Bmatrix} 1 \\ 0 \\ 0 \\ 0 \end{Bmatrix} \tag{61}$$

Inverting [K] matrix one finds the value of the coefficients as: $a_3 = \frac{1}{B_A - 1}$, $b_3 = \frac{-2}{B_A - 1}$, $c_3 = \frac{B_A}{B_A - 1}$, $a_4 = \frac{1}{B_A}$.

For $\tilde{\sigma} > B_A$:

$$\sigma - \alpha[\beta_0 f_{A1}] - \sigma_0 - E\epsilon + E_0\epsilon_0 + \alpha_0\beta_0 = 0 \tag{62}$$

$$\sigma - \alpha\beta_0 a_3\tilde{\sigma}^2 - \alpha\beta_0 b_3\tilde{\sigma} - \alpha\beta_0 c_3 - \sigma_0 - E\epsilon + E_0\epsilon_0 + \alpha_0\beta_0 = 0 \tag{63}$$

And, for $\tilde{\sigma} < B_A$:

$$\sigma - \alpha\beta_0[f_{A2}] - \sigma_0 - E\epsilon + E_0\epsilon_0 + \alpha_0\beta_0 = 0 \tag{64}$$

$$\sigma - \alpha\beta_0 a_4 \tilde{\sigma}^2 - \sigma_0 - E\epsilon + E_0\epsilon_0 + \alpha_0\beta_0 = 0 \tag{65}$$

The polynomial model presents an analytical solution for strain driving cases that avoids the iterative process. The traditional models with assumed phase transformation kinetics require an iterative algorithm to estimate stress values from the prescribed strain. Fig. 4.15 shows the iterative algorithm used to treat strain driving cases. The convergence is established by the difference $\epsilon_{n+1}^{trial} - \epsilon_{n+1} \leq p$, where p is a tolerance usually assumed to be (10^{-3}). In case of this condition is not satisfied, the algorithm return to process the trial variables again with different value of the initial stress-strain trial step.

1. Data Base at $x \in \mathfrak{P} : \{\epsilon_n, E_n, \alpha_n\}$
2. Given a strain filed at $x \in \mathfrak{p} : \epsilon_{n+1} = \epsilon_n + \Delta\epsilon_n$
3. Compute elastic trial stress and test for phase transformation:

$$\sigma_{n+1}^{\text{trial}} = \sigma_n + E_n\left[\epsilon_{n+1} - \epsilon_n\right]$$

$$\beta_{n+1}^{\text{trial}} = \begin{cases} \beta_0 + (1-\beta_0)\, f_{m(n+1)}^{\text{trial}} & \text{forward} \\ \beta_0 f_{a(n+1)}^{\text{trial}} & \text{reverse} \end{cases}$$

$$\epsilon_{n+1}^{\text{trial}} = \frac{1}{E}\left[\sigma_{n+1}^{\text{trial}} + \alpha\beta_{n+1}^{\text{trial}}\right]$$

4. IF $\epsilon_{n+1}^{\text{trial}} - \epsilon_{n+1} \leq p$ THEN Elastic Step: set $(\bullet)_{n+1} = (\bullet)_{n+1}^{\text{trial}}$ & EXIT

   ELSE

   Phase transformation step: IF $\epsilon_{n+1}^{\text{trial}} - \epsilon_{n+1} > 0$ THEN

   return to 3 . $\sigma_{n+1}^{\text{trial}} = \sigma_n + \frac{E_n[\epsilon_{n+1} - \epsilon_n]}{2}$

   ELSE

   return to 3 . $\sigma_{n+1}^{\text{trial}} = \sigma_n + 2\left(E_n\left[\epsilon_{n+1} - \epsilon_n\right]\right)$ &

   END IF

   END IF

Fig. 4.15: Iterative algorithm for convergence: *Prescribed* ϵ

On the other hand, Fig. 4.16 shows the analytical procedure to find stress by an incremental input of strain. The value of σ is obtained by the second-order polynomial constitutive equations. In sequence, $\beta(\tilde{T})$ is estimated and finally, find the value of E.

1. Data Base at $x \in \mathfrak{P} : \{\epsilon_n, E_n, \alpha_n\}$
2. Given a strain filed at $x \in \mathfrak{p} : \epsilon_{n+1} = \epsilon_n + \Delta\epsilon_n$
3. Compute elastic trial stress and test for phase transformation:

$$\sigma_{n+1}^{\text{trial}} = \sigma_n + E_n \left[\epsilon_{n+1} - \epsilon_n\right]$$

$$\beta_{n+1}^{\text{trial}} = \begin{cases} \beta_0 + (1 - \beta_0) f_{m(n+1)}^{\text{trial}} & \text{forward} \\ \beta_0 f_{a(n+1)}^{\text{trial}} & \text{reverse} \end{cases}$$

$$\epsilon_{n+1}^{\text{trial}} = \frac{1}{E}\left[\sigma_{n+1}^{\text{trial}} + \alpha\beta_{n+1}^{\text{trial}}\right]$$

4. IF $\epsilon_{n+1}^{\text{trial}} - \epsilon_{n+1} \leq p$ THEN

   Elastic Step: set $(\bullet)_{n+1} = (\bullet)_{n+1}^{\text{trial}}$ & EXIT

   ELSE

   Phase transformation step:

$$\sigma_{n+1} = \text{Polynomial solution}$$

$$\beta_{n+1} = \begin{cases} \beta_0 + (1 - \beta_0) f_{m(n+1)} & \text{forward} \\ \beta_0 f_{a(n+1)} & \text{reverse} \end{cases}$$

$$E_{n+1} = E_A + \beta_{n+1}\left(E_M - E_A\right)$$

   END IF

Fig. 4.16: Algorithm for analytical solution: *Prescribed* ϵ

4.2.1.1 Mechanical Oscillator with SMA element

The polynomial model is now applied to the *SMA* wire to evaluate model behavior in a dynamic system. Fig. 4.17(a) shows a mechanical system composed of a cantilever beam connected to a *SMA* unidimensional element and subjected to base excitation. Fig. 4.17(b) shows its representation in a single degree of freedom *SMA* oscillator.

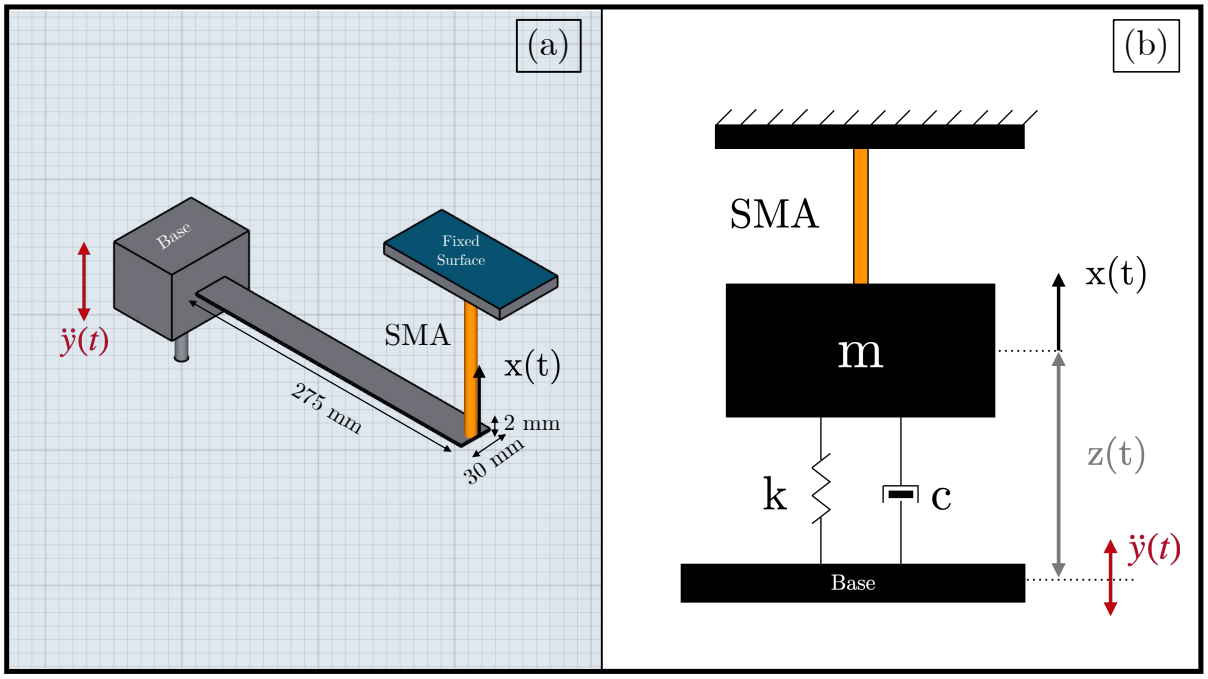


Fig. 4.17: A schematic illustration of a vibration based dynamical system with the addition of a *SMA* element. (a) Cantilever beam configuration and continuum elements. (b) Single degree of freedom and discrete parameters.

For a dynamical analysis, shape memory alloy element and cantilever beam shall assume near stiffness values. In this analysis, the cantilever beam is considered with the geometry described in subsection 4.1.2.

The beam characterization is based on *Euller-Bernoulli* assumptions allowing the estimation of an equivalent stiffness of the cantilevered beam. Therefore, the bending moment ($M(s)$) across the cantilever beam can be expressed by the second derivative of beam deflection ($w(s)$) times the bending coefficient (EI) as follows:

$$EI\frac{\partial^2 w}{\partial s^2} = M(s) \tag{66}$$

where s is a coordinate oriented from the clamp to the free end and varies from zero to L. E represents Young's modulus (70 GPa for aluminum), I is the cross section moment of inertia ($\frac{bh^3}{12}$) and L is the beam length. It is important to note that the piezoelectric element presents size and dimensions that can be neglected beside the aluminum beam in this configuration. For this reason, the modeling does not consider the structural properties of the piezoelectric element.

By considering a cantilever beam boundary conditions: ($w(s=0)=0$ and $w'(s=0)=0$) where [ ]' means the position derivative, it is possible to define the following stiffness by the equation

of static deflection of a cantilever beam under a concentrated load at the end [220]:

$$k = \frac{3EI}{L^3} = 213 \text{ N/m} \tag{67}$$

Since an *SMA* wire is connected to the end of the beam, the equivalent stiffness of the mechanical system can be calculated by the following expression

$$k_{eq} = k + k_{SMA} \tag{68}$$

where it is important to observe that, actually, k_{SMA} has possible values, depending on the phase (martensite or austenite), which is defined by the thermomechanical coupling.

The estimation of the equivalent mass has been treated by many authors [5, 18, 103]. Literature refers to models that consider a distributed mass along the beam and also a concentrated mass (tip mass) at the free end. In order to establish the equivalent mass, consider the kinetic energy of the beam and integrate a shape function. Considering the maximum beam kinetic energy:

$$K_{max} = \frac{1}{2}\int_0^L \frac{m}{L}\dot{w}(s)^2 ds \tag{69}$$

By considering the beam theory to express the velocity variation $\dot{w}(s)$, from elastic line theory [220] it can be written:

$$\dot{w}(s) = \frac{\dot{w}_{max}}{2L^3}(3s^2L - s^3) \tag{70}$$

consequently, Eq. (69) becomes:

$$K_{max} = \frac{1}{2L}(\frac{\dot{w}_{max}}{2L^3})^2 \int_0^L (3s^2L - s^3)^2 ds = \frac{1}{2}(\frac{33}{140}m)\dot{w}_{max}^2 \tag{71}$$

If m_{eq} represents the equivalent mass for a cantilever beam reduced to a single degree of freedom, the maximum kinetic energy can be expressed as:

$$K_{max} = \frac{1}{2}m_{eq}\dot{w}_{max}^2 \tag{72}$$

combining Eqs. (71) and (72), considering aluminum's density ($\rho_{Al} = 2700$ kg/m^3) and the beam dimensions, the equivalent mass is as follows,

$$m_{eq} = \frac{33}{140}\rho\Lambda + M_t = 10 \ \ g \tag{73}$$

where M_t represents the tip mass added on the free end of a cantilever beam. Here, no expressive tip mass is used in the experimental apparatus, and therefore, it is neglected. Hence, the equivalent mass of the mechanical system is the product of the material density (ρ) and its volume (Λ), times 33/140 coefficient.

SMA element is here treated as a unidimensional bar with an initial length of 150 mm is considered. Based on that and *SMA* Young's modulus listed in Table 4, *SMA* element stiffness is able to vary from 277 N/m to 121 N/m from austenite to martensite phase, respectively. So, it is possible to define natural frequency, $\omega = \frac{\Omega}{2\pi}$, attributed to *SMA* wire at austenite and martensite phases as $\omega_n^A = 35.25$ Hz and $\omega_n^M = 29.10$ Hz, respectively. It represents a variation of 21.13 % of system natural frequency.

Proceeding with free body diagram and second Newton's law, the equations of movement are found:

$$m_{eq}\ddot{z} + c\dot{z} + kz + F_{SMA} = -m_{eq}A_b\sin(\Omega t) \tag{74}$$

and can be solved by the following procedure and a Runge-Kutta 4th order algorithm:

$$\begin{cases} v = \dot{z} \\ \dot{v} = [m_{eq}^{-1}](-m_{eq}A_b\sin(\Omega t) - c\dot{z} - kz - F_{SMA}) \end{cases} \tag{75}$$

$$F_{SMA} = \frac{\sigma\pi d_W^2}{4}; \tag{76}$$

Table 7: Single degree of freedom mechanical oscillator with *SMA* element parameters.

m_{eq} (g)	c (Ns/m)	k (N/m)	$\frac{\pi d_W^2}{4}$ (m^2)
10	0.05	213	9.62×10^{-10}

Table 7 refers to parameters for dynamical simulations and solution of Eq. (74). m_{eq} represent the equivalent body mass (refer to Eq. (73)) and x the body displacement while k is the linear element stiffness and c the total damping coefficient. The damping coefficient is set as 0.05 in accord with experimental tests shown in section 5.2. Finally, the harmonic base vibration can

be set as $\ddot{y} = A_b \sin(\Omega t)$ where the magnitude and frequency are represented by A_b and Ω, respectively. $z = x - y$ is the relative displacement between base and body mass.

4.2.2 Piezoelectric Energy Harvester with SMA Martensite Helical Spring

This section is dedicated to establishing a mathematical model to describe the energy harvesting system based on the experimental apparatus of subsection 4.1.2. In essence, this system is a mechanical oscillator connected to an electric system by the piezoelectric element. Fig. 4.18 presents the experimental apparatus sketch and the equivalent electromechanical system.

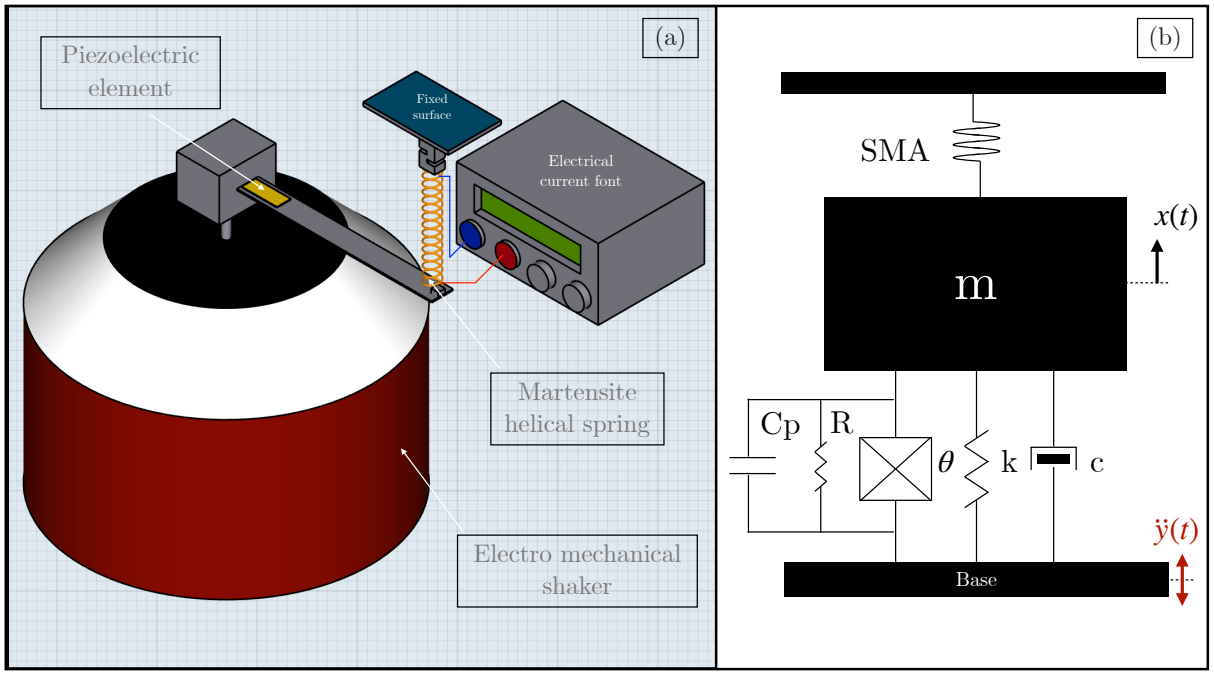


Fig. 4.18: Dynamical model of the energy harvester with synergistic use of piezoelectric and *SMA* martensite helical spring. (a) Cantilever beam. (b) Its representation as a single degree of freedom oscillator.

The dynamical system can be described by two coupled differential equations representing the mechanical and the electrical systems [18, 20, 103, 134].

$$m_{eq}\ddot{z} + c\dot{z} + kz + F_{SMA} - \theta V = -m_{eq}\ddot{y} \tag{77}$$

$$\theta\dot{z} + C_p\dot{V} + \frac{V}{R} = 0 \tag{78}$$

where $z(t)$ is the relative displacement between $x(t)$ - body displacement related to a inertial referential, and $y(t)$ - base displacement: $z(t) = x(t) - y(t)$; m is the equivalent mass, c is the total dissipation coefficient and k represents the beam stiffness; the eletro-mechanical coupling

provided by the piezoelectric element is represented by θ while C_p and R are the piezoelectric element capacitance and circuit resistance, respectively; $\ddot{y} = A_b \cos(\Omega t)$ where A_b is the maximum acceleration base-vibration amplitude, and F_{SMA} is the restitution force provided by the shape memory alloy element. Eqs. (77) and (78) are solved trough the fourth-order Runge-Kutta method implemented in a C programming language code. All simulation tests fot this configuration are performed considering null initial conditions for displacement, velocity and electrical voltage.

The energy harvesting performance is monitored by considering input power P_{in} that is essentially the mechanical power:

$$P_{in} = m\ddot{y}\dot{z} = m_{eq}A_b cos(\Omega t)\dot{z} \tag{79}$$

and the output power P_{out}, which is associated with the electrical power:

$$P_{out} = \frac{V^2}{R} \tag{80}$$

System efficiency can be evaluated by considering the ratio between output and input power.

$$\eta = \frac{P_{out}}{P_{in}} \tag{81}$$

Since the system responses are essentially linear for each phase, in this situation, it is possible to obtain analytical expressions for displacement and output power, that can be used for numerical simulation verification [20, 5]. Based on that, it is possible to define an expression for relative displacement, z^a, as a function of input acceleration $\ddot{y}$:

$$z^a = \ddot{y}\frac{\Omega_N^{-2}\sqrt{1+(r\nu)^2}}{\sqrt{(1-(1+2r\zeta)\nu^2)^2 + ((1+\kappa^2)r\nu + 2\zeta\nu - r\nu^3)^2}} \tag{82}$$

Concerning the output power, p^a_{out}, and the input power, p^a_{in}, the following expressions are written:

$$p^a_{out} = \ddot{y}^2\frac{m_{eq}(\Omega_N^{-1})r\kappa^2\nu^2}{(1-(1+2r\zeta)\nu^2)^2 + ((1+\kappa^2)r\nu + 2\zeta\nu - r\nu^3)^2} \tag{83}$$

$$p^a_{in} = m_{eq}\dot{z}^a\ddot{y} \tag{84}$$

These definitions allow one to present an analytical expression for the system efficiency η^a,

$$\eta^a = \frac{p^a_{out}}{p^a_{in}} \tag{85}$$

where $r = (\Omega_N R C_p)$, $\kappa^2 = \theta^2/(k_{eq} C_p)$, $\nu = \Omega/\Omega_N$ is the ratio between base vibration frequency and system natural frequency and $\zeta = c/(2m_{eq}\Omega_n)$.

For the considered situations, the martensite helical spring is subjected to stress levels that are below critical stresses, which means that stress-induced phase transformations are neglected. Therefore, only temperature-induced phase transformation is of concern, and the *SMA* martensite helical spring presents a linear response, but with different stiffness: martensite low-temperature behavior and austenite high-temperature behavior.

Based on that, k_{eq} assumes two different values: $k^M_{eq} = 429$ N/m for martensite phase; and $k^A_{eq} = 501$ N/m for austenite. Under these assumptions, the single degree of freedom equivalent mechanical system has two possible natural frequency: $\omega^M_N = 32.96\ Hz$ and $\omega^A_N = 35.61$ Hz. Therefore, it is expected a variation of resonance frequency peaks within a range of 2.65 Hz (35.61 - 32.96) which means 8.04% of variation with respect to low temperature resonance frequency value.

Based on the same assumptions, the shape memory alloy helical spring force can be expressed by

$$F_{SMA} = k_{SMA} \times z \tag{86}$$

where k_{SMA} alternates from martensite to austenite characteristics when temperature changes from low to high-temperature behaviors, according to the values presented in Fig. 4.10.

For the sake of simplicity, it is defined T_M as the temperature below which only the martensite phase is stable, being considered in such a way that $T_M \leq M_f$. Since $A_s < M_f$ it is also assumed that $T_M < A_s$. Therefore, it is adopted T_M =298 K, assumed to be the ambient temperature. The temperature above which only austenite is stable in a stress-free state needs to be $T_A \geq A_f$, being defined as $T_A = A_f$ =323.4 K. In terms of electric current, it is considered that the helical spring is in the martensite state for 0 A, while an austenite state is related to values greater than 1.37 A.

Damping coefficient associated with martensite, c_M, and austenite, c_A, phases are estimated in order to match experimental results. The same procedure is employed for the electromechanical

coupling, θ. Capacitance is defined in terms of constrained permittivity: $C_p = \frac{A_p \mu_{33}}{t_p}$ according to [19], where A_p and t_p are piezoelectric element surface area and thickness, respectively; μ_{33} is considered as the product of dimensionless piezo dielectric constant (3500, provided in data sheet) and the vacuum permittivity (8.85×10^{-12} F/m). Table 8 show parameters employed for numerical simulations.

Table 8: Single degree of freedom piezoelectric energy harvester with *SMA* martensite helical spring parameters.

m_{eq} (kg)	k (N/m)	θ (N/V)	C_p (F)	R (Ohm)
0.01	213	-3.1×10^{-5}	2.48×10^{-8}	150×10^{3}
T_M(K)	T_A(K)	c_M (Ns/m)	c_A (Ns/m)	A_b (m/s^2)
298	323.4	0.05	0.0335	9.81

Once temperature variation is induced by Joule's effect, it is possible to determine martensite helical spring temperature according to Eq. (44) as a function of applied electrical current. In addition, Eq. (53) defines $\beta(\tilde{T})$ for $M \rightarrow A$ and so, relations for k_{SMA} and c with temperature through $\beta(\tilde{T})$ can be established:

$$k_{SMA}(\beta) = k_A + \beta(\tilde{T})(k_M - k_A) \tag{87}$$

$$c(\beta) = c_A + \beta(\tilde{T})^2(c_M - c_A) \tag{88}$$

$$\Omega_N(\beta) = \sqrt{\frac{(k + k_{SMA}(\beta))}{m_{eq}}} \tag{89}$$

In this way, Eqs. (87) and (88) define the stiffness and damping associated to the martensite volume fraction $\beta(\tilde{T})$ and finally, Eq. (89) correlates the *SMA* piezoelectric energy harvester natural frequency as a function of $\beta(\tilde{T})$. Next sub section presents the mathematical modeling for the system coupled to the *SMA* austenite helical spring.

4.2.3 Piezoelectric Energy Harvester with SMA Austenite Helical Spring

The phase transformation induced by the mechanical load in the *SMA* piezoelectric energy harvester is under investigation now for the austenite helical spring.

A *SMA* helical spring that presents a pseudoelastic effect is becoming very common in engineering due to its capability to suffer larger displacements when compared to wires, bars, and rods for a specif restoring force. This ability can be addressed to the helical configuration which suffers shear stresses over spring wire cross-section for an axial load. The governing constitutive relation for a *SMA* helical springs can be written as:

$$\tau - \tau_0 = G\gamma - G_0\gamma_0 + \alpha_s\beta - \alpha_{s0}\beta_0 + \Theta T - \Theta_0 T_0 \tag{90}$$

where, τ, γ, β, Θ, and T represent shear stress, shear strain, martensite volume fraction, thermal dilatation coefficient, and temperature respectively. Subscripts zero means the variable value at the beginning of the load. G represents the shear Young's modulus and $\alpha_s = -G\gamma_R$ where γ_R is the maximum recoverable shear strain coefficient.

The polynomial models with kinetics transformation, previously discussed, have the characteristic that the kinetics function β is expressed as a function of stress as adopted in subsection 4.2.1.

Modeling of shape memory alloy helical springs are treated in several works [221, 217, 218]. The restoring force promoted by a pseudoelastic helical spring can be expressed considering the spire radius ($R_{AS} = D_{AS}/2$), the wire radius ($r_{AS} = d_{AS}/2$) and the number of active spires (N_{AS}). Shigley and Mischke [222] explains when a helical spring suffers an axial load or displacement, the wire coil cross-section is submitted to shear and normal stresses. Nevertheless, de Aguiar et al. [221], Enemark et al. [217, 218] neglect normal stresses besides shear ones due to their magnitude being way smaller than shear stresses for linear cases. Assuming torsional shear stress in a circular cross-section, total elongation ($d_{SMA} = L_{AS} - L_{AS0}$) and the shear stress at the periphery (γ_p) can be written as:

$$\gamma_p = \frac{r_{AS}}{2\pi N R_{AS}^2} d_{SMA} \tag{91}$$

Considering strain distribution as linear and a function of a radial coordinate a, $\gamma = \frac{a}{r_{AS}}\gamma_p$ for $0 < a \leq r_{AS}$, F_{SMA} become:

$$F_{SMA} = \frac{2\pi}{R_{AS}} \int_0^r \tau(a) a^2 \mathrm{d}a \tag{92}$$

For a *SMA* helical spring with phase transformation, de Aguiar et al. [221], Enemark et al. [217, 218] assume $\beta = \beta_{eq}$ constant over the cross-section and substituting it in governing equation (Eq. (90)) yields:

$$F_{SMA} = \frac{2\pi}{R_{AS}} \int_0^{r_{AS}} G\left(\frac{a}{r_{AS}}\gamma_p - \alpha_s\beta_{eq}\right) a^2 \mathrm{d}a = \frac{2\pi r_{AS}^3}{3R_{AS}} G\left(\frac{3}{4}\gamma_R - \alpha_s\beta_{eq}\right) \tag{93}$$

Beside of that, de Aguiar et al. [221], exposes different criterion for shear stress distribution in cross section. Authors considers a critical radius to border the region with to without phase transformation or even a constant value for γ and β through cross section. Enemark et al. [217] refers to de Aguiar et al. [221] and establish good results by considering constant strain $\gamma_{eq} = \frac{3}{4}\gamma_R$ and a constant equivalent stress $\tau_{eq} = G(\gamma_{eq} - \alpha_s\beta_{eq})$ as follow:

$$F_{SMA} = \frac{2\pi r_{AS}^3}{3R_{AS}} \tau_{eq} \tag{94}$$

and substituting γ_{eq} into Eq. (91), it becomes:

$$\gamma_{eq} = \frac{3r_{AS}}{8\pi N_{AS} R_{AS}^2} d_{SMA} \tag{95}$$

So, Eq. (94) defines the *SMA* helical spring relation between equivalent stress over the cross-section and axial force at spring extremities while Eq. (95) relates spring displacements with equivalent strains.

The *SMA* austenite helical spring is connected to the piezoelectric energy harvester as present in Fig. 4.19(a), which shows a representative illustration of the piezoelectric cantilever beam energy harvester now with the austenite helical spring. Fig. 4.19(b) presents in details the preload mechanism.

It is important to state that in this investigation, the load applied to the system is divided into two stages. The first stage deals with the initial quasi-static preload which is a prescribed force problem while the second stage deals with the dynamical load which is a prescribed displacement problem.

The preload mechanism was built considering a fixed surface connected by two parallel bolts to a rigid plate able to move. The load cell couples between the rigid plate and the austenite helical spring in order to measure the quasi-static load at the spring while the rigid plate slowly moves in a vertical direction according to screw nuts movement. Note that this is just a basic method to manually control the initial load and position in an austenite helical spring. For a more precise movement, electronic mechanical actuators could easily perform this task by prescribing loads and displacements.

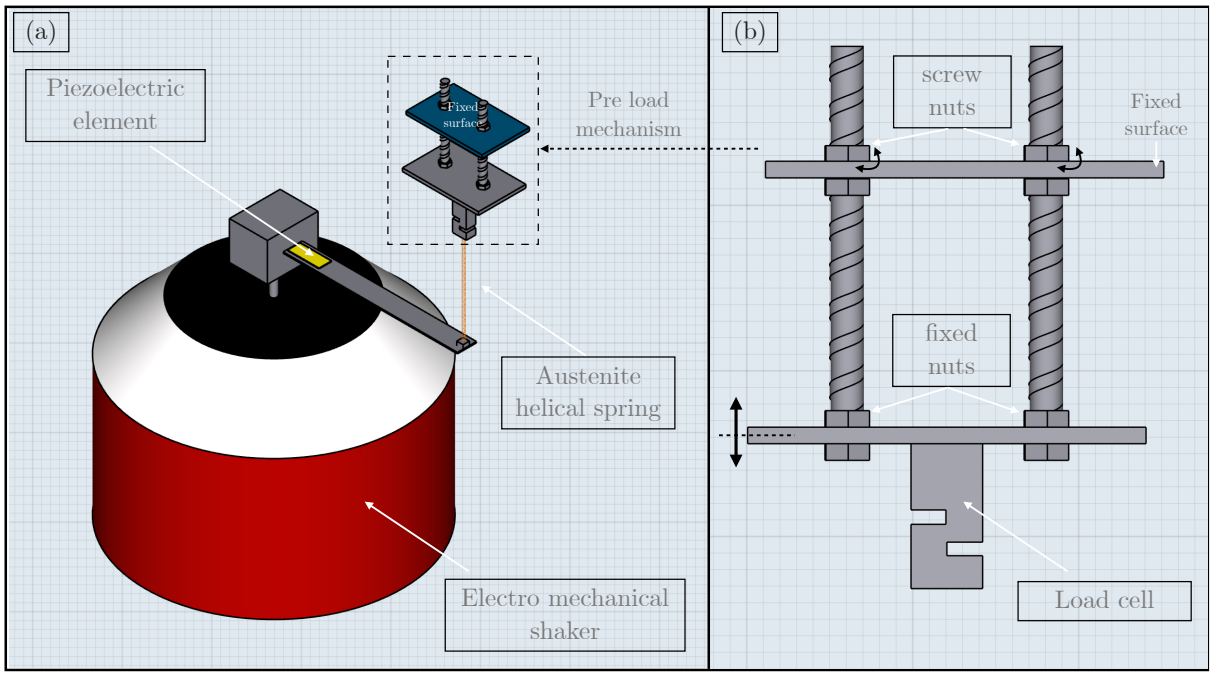


Fig. 4.19: Synergistic use of piezoelectric energy harvester coupled to *SMA* austenite helical spring. (a) Cantilever beam representative illustration. (b) Detail for electronic mechanical actuator to promote an initial preload variation.

The synergistic cantilever beam energy harvester is represented as a single degree of freedom system connected to an electrical circuit by a piezoelectric element as shown in Fig. 4.20.

As mentioned, the austenite helical spring is first submitted to a preload by the vertical movement of the rigid plate while the base remains fixed. This procedure promotes *SMA* helical spring phase transformation and consequently, Young‘s modulus variation. The preload is applied considering a quasi-static increase load in time steps. Before dynamical loads run out, the simulation hold for a few time steps to avoid any inertial transient effects in transition from quasi-static to dynamical base vibration movement.

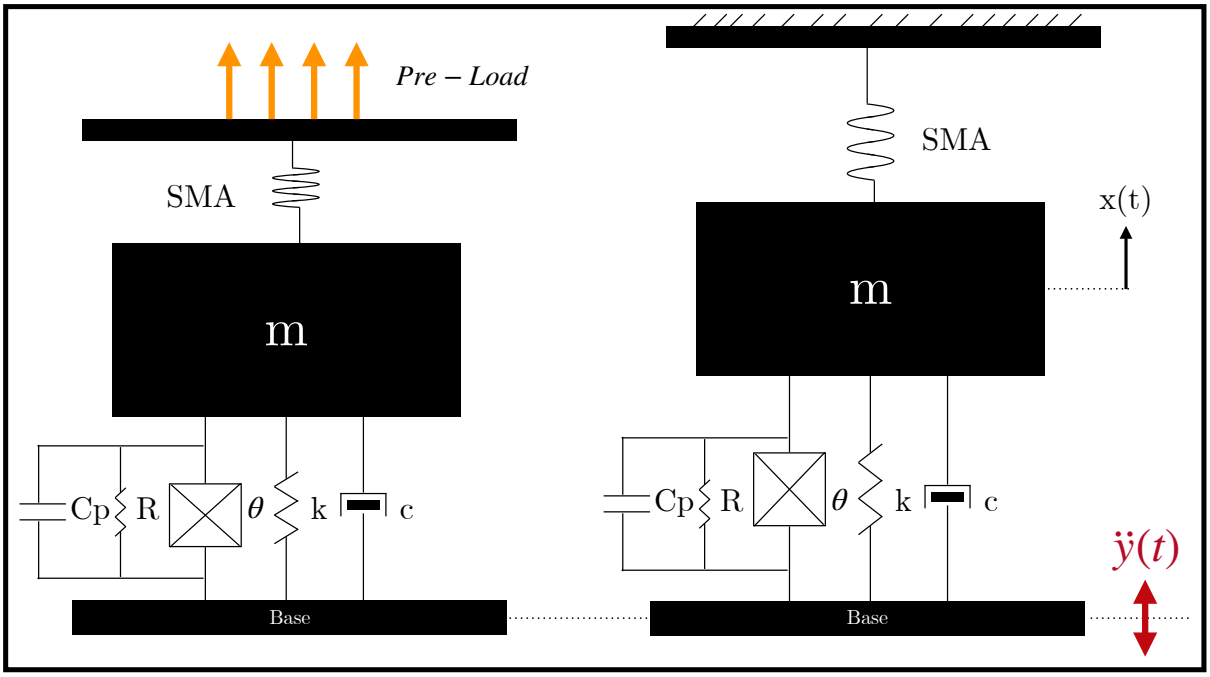


Fig. 4.20: Dynamical model of the energy harvester with synergistic use of piezoelectric and austenite *SMA* helical spring as a single degree of freedom and its preload stages.

Fig. 4.21(a) presents a representative diagram for body relative displacement while Fig. 4.21(b) deals with the representative body relative velocity. These diagrams show an application of a quasi-static preload able to promote a linear displacement between the body mass and the base. The hold moment is represented to avoid dynamical effects between the transition from quasi-static to dynamical load followed by an oscillatory motion promoted by base vibration. Note that Fig. 4.21 is just a qualitative representation of displacement and velocity.

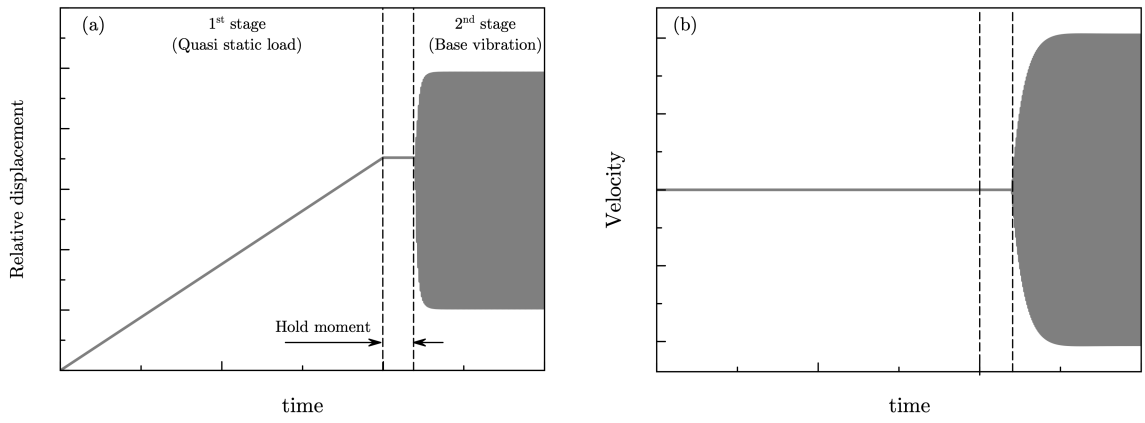


Fig. 4.21: Representative time evolution in the SMA-piezoelectric energy harvester. (a) Relative displacement. (c) Velocity

Proceeding with a free body diagram and Newton's second law, movement equations can be

expressed as two coupled differential equations represented by Eq. (96) and Eq. (97):

$$m_{eq}\ddot{z} + c\dot{z} + kz - F_{SMA} - \theta V = -m_{eq}\ddot{y} \tag{96}$$

$$\theta\dot{z} + C_p\dot{V} + \frac{V}{R} = 0 \tag{97}$$

where $z(t)$ is the relative displacement between $x(t)$ (body displacement related to a inertial referential), and y (base displacement): $z(t) = x(t) - y(x)$; m is the equivalent mass, c is the total dissipation coefficient and k represents a linear stiffness. The eletro-mechanical coupling provided by the piezoelectric element is represented by θ, while C_p and R_{eq} are the circuit equivalent capacitance and resistance, respectively.

Base vibration acceleration is given by $\ddot{y} = A_b \sin(\Omega t)$ where A_b is the maximum base vibration acceleration amplitude and F_{SMA} is the restitution force provided by the *SMA* helical spring. Movement differential equations Eqs. (96) and (97) are solved trough $4th$ order Runge-Kutta method. Helical spring elongation (d_{sma}) become the difference between the top fixed point displacement and the body mass displacement ($x(t)$). The *SMA* restitution force is evaluated considering Eq. (94) and Eq. (95), while the constitutive relation between τ_{eq} and γ_{eq} by the analytical solution provided in subsection 4.2.1. Table 9 show the values attributed to discrete parameters with concern of experimental apparatus.

Table 9: Single degree of freedom piezoelectric energy harvester with *SMA* austenite helical spring parameters.

m_{eq} (kg)	k (N/m)	θ (N/V)	C_p (F)	R (Ohm)
0.01	213	-3.1×10^{-5}	2.48×10^{-8}	150×10^{3}

The harvester efficiency (η) is investigated as a ratio between the total electrical power obtained (P_{out}) and the inputed mechanical energy (P_{in}). The relations can be established:

$$\eta = \frac{P_{out}}{P_{in}} \tag{98}$$

$$P_{in} = m\ddot{y}\dot{z} \longrightarrow m_{eq}A_b sin(\Omega t)\dot{z} \tag{99}$$

$$P_{out} = \frac{V^2}{R} \tag{100}$$

where V is the electrical voltage due to the direct piezoelectric effect. The next section presents results and discussion for a quasi-static load situation and a nonlinear dynamical approach for a piezoelectric energy harvester coupled to a pseudoelastic helical spring with preloaded.

The three problems which this methodology purposes to investigate are now modeled. The next section presents results for each case and compares numerical simulations with experimental results.

5 Results and Discussion

This section is dedicated to exposing results obtained via methodology presented in Chapter 4 to investigate the synergistic use of piezoelectric materials with shape memory alloys to increase operational range for energy harvesting. Results are divided into three sections. The first section explores results obtained with the SMA constitutive model proposed in this thesis. The second section presents numerical and experimental results associated with the energy harvesting device where the expansion of the operational range is obtained through phase transformation induced by temperature and the third section deals with numerical simulations for the SMA-piezoelectric energy harvester through phase transformation induced by mechanical load. Results involve experimental tests, numerical simulations, and analytical solutions.

5.1 SMA Polynomial Model with Assumed Kinetics Phase Transformation

This subsection presents results about the *SMA* polynomial constitutive model proposed in this thesis. Before applying the model proposed in a dynamical system, results for quasi-static load and unload with prescribed stress and strain are in discussion. It is important to remember that for dynamical problems, it is desired to obtain stress as a function of strain to solve numerically the equation of motion. In this way, considering Tanaka et al. [215], Liang and Rogers [216], Brinson [34], for prescribed stress load, no convergence method is need, once ϵ and β are explicit in stress relation. On the other hand, for strain prescribed load, a convergence algorithm must be employed to achieve the solution for the models in concern. Alternatively, the proposed model provides an analytical solution for prescribed strain load problems.

It is important to express that shape memory alloy element initial conditions are always considered as $\epsilon_0 = 0$, $\sigma_0 = 0$ and $\beta_0 = 0$ in analyses for phase transformation induced by mechanical load and $\epsilon_0 = 0$, $\sigma_0 = 0$ and $\beta_0 = 1$ for phase transformation induced by temperature.

Simulations of quasi-static tests are now of concern. The objective is to calibrate the proposed model and evaluate its capacity to represent *SMAs* phenomena and behavior in different conditions of thermomechanical load. Also, this subsection compares the proposed polynomial model with experimental data and with the traditional constitutive models with assumed kinetic phase transformation.

Initially, a comparison with experimental data is presented after the calibration process. Fig. 5.1 shows the proposed model with assumed kinetic transformation performance, comparing analytical solution with experimental results presented in previous subsections for different temperatures. Martensite reorientation, shape memory effect, and pseudoelastic effect are captured

by the model. Note that the critical stresses and hysteresis loop shifts up with the increase of temperature.

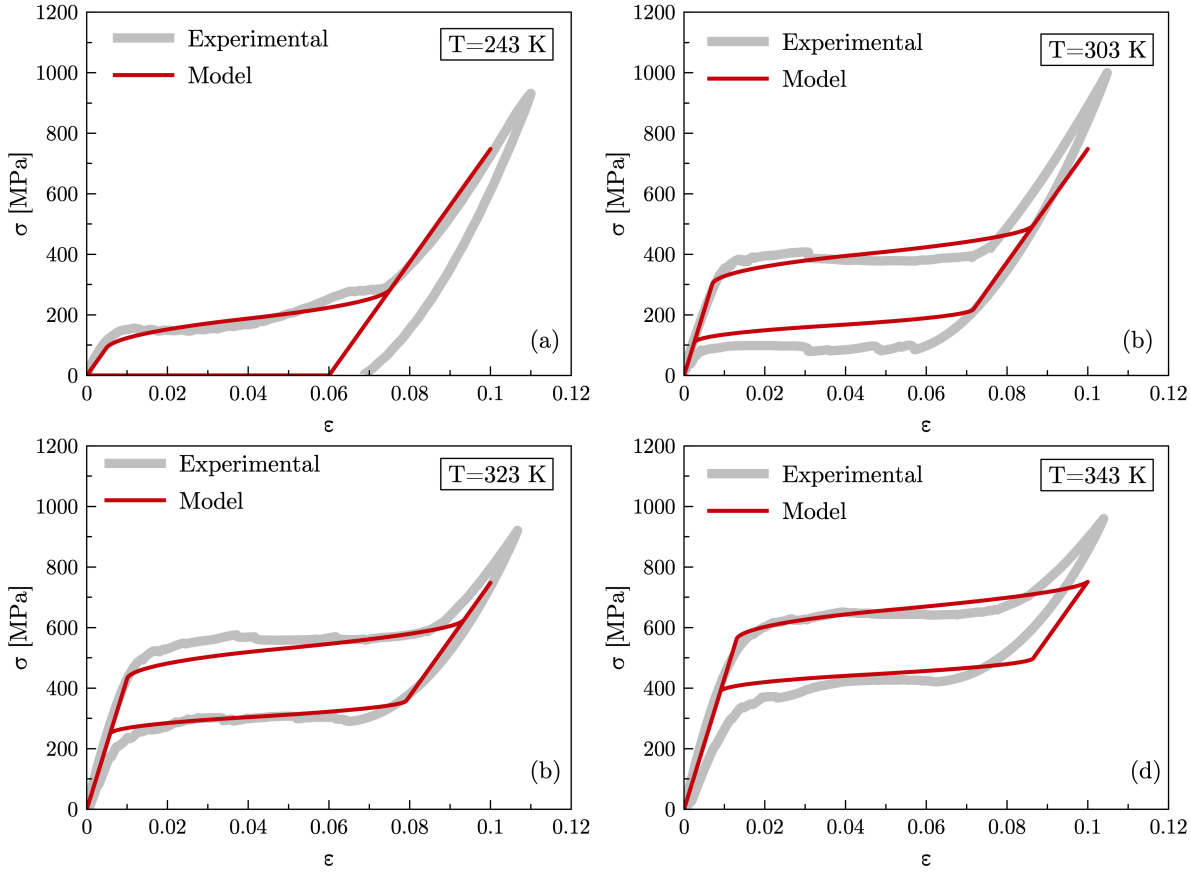


Fig. 5.1: Proposed assumed kinetic phase transformation model compared with experimental data for different temperature conditions: (a) T = 243 K. (b) T = 303 K. (c) T = 323 K. (d) T = 343 K.

A comparison with other constitutive models can now be established. Fig. 5.2 shows a comparison through pseudoelastic and shape memory effect for traditional models with assumed kinetic phase transformation and the formulation proposed, considering thermal and mechanical load. The formulation consist in rewrite the traditional equations into a radical times a hardening function as: $\beta = \beta_0 + (1 - \beta_0) f_M$ for forward transformation and $\beta = \beta_0 f_A$ for reverse phase transformation. In this way, it is possible to represent Tanaka et al. [215], Liang and Rogers [216], Brinson [34] by different hardening functions f_M and f_A.

Fig. 5.2 presents numerical results for all models considering a proposed unified formulation with hardening functions. This analysis considers prescribed stress for traditional models (gray curves) and prescribed strain load for the curves simulated with the proposed formulation (black and red curves). The objective of this analysis is to show that the proposed formulation is able to capture the same response as traditional models.

In Fig. 5.2, for prescribed strain responses, the iterative algorithm shown in subsection 4.2.1 is employed. The exponential curve is attributed to Eq. (31) and Eq. (32) while Tanaka is attributed to the original Tanaka et al. [215] model equations (Eq. (29) and Eq. (30)). Note that the exponential equations using $f_M = f_A$ lead to a similar result for the $A \rightarrow M$ forward transformation. Instead of that, for $M \rightarrow A$ reverse transformation, the concavity goes in a opposite path direction. This could be corrected by the use of $f_A = \exp\left[2\log(\tilde{T}, \tilde{\sigma})\right]$. However, do not maintain the pattern $f_M = f_A$.

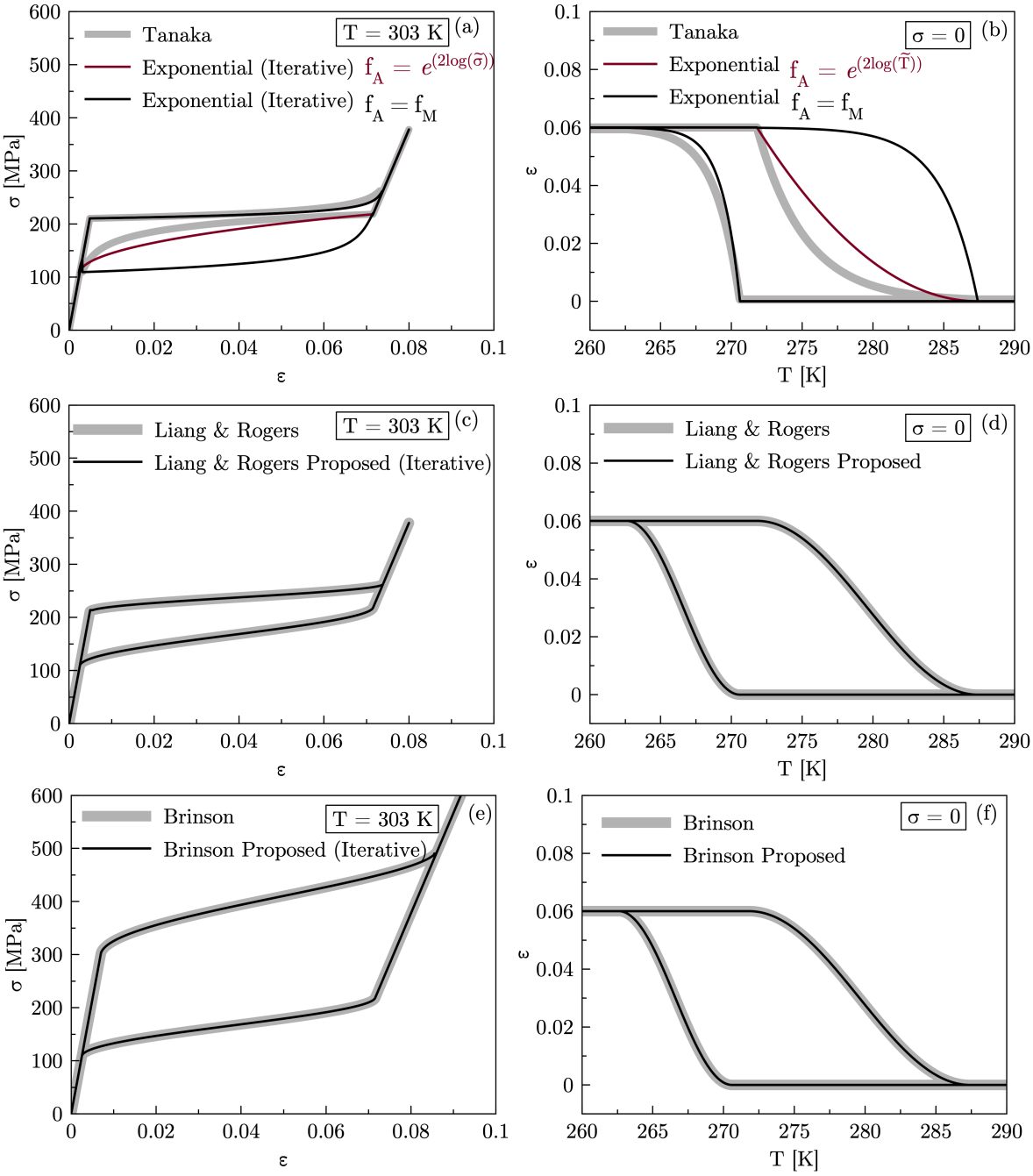


Fig. 5.2: Comparison of traditional models with assumed kinetics transformation and the formulation proposed. Tanaka: (a) Pseudoelastic effect, (b) Shape memory effect. Liang & Rogers: (c) Pseudoelastic effect, (d) Shape memory effect. Brinson: (f) Pseudoelastic effect, (f) Shape memory effect.

With exception of Fig. 5.2(a) and (b), the proposed formulation gives the same result as Liang and Rogers [216] and Brinson [34] models for the conditions simulated.

Fig. 5.3 compares in a prescribed strain problem an iterative solution of Brinson's model against the analytical solution provided by the proposed polynomial model with assumed kinetic phase transformation. The polynomial model presents a closed-form solution. Fig. 5.3(a) presents

results for phase transformation induced by temperature while Fig. 5.3(b) for phase transformation induced by mechanical load. Curves in Fig. 5.3(c) shows martensite reorientation process for $T < M_f$.

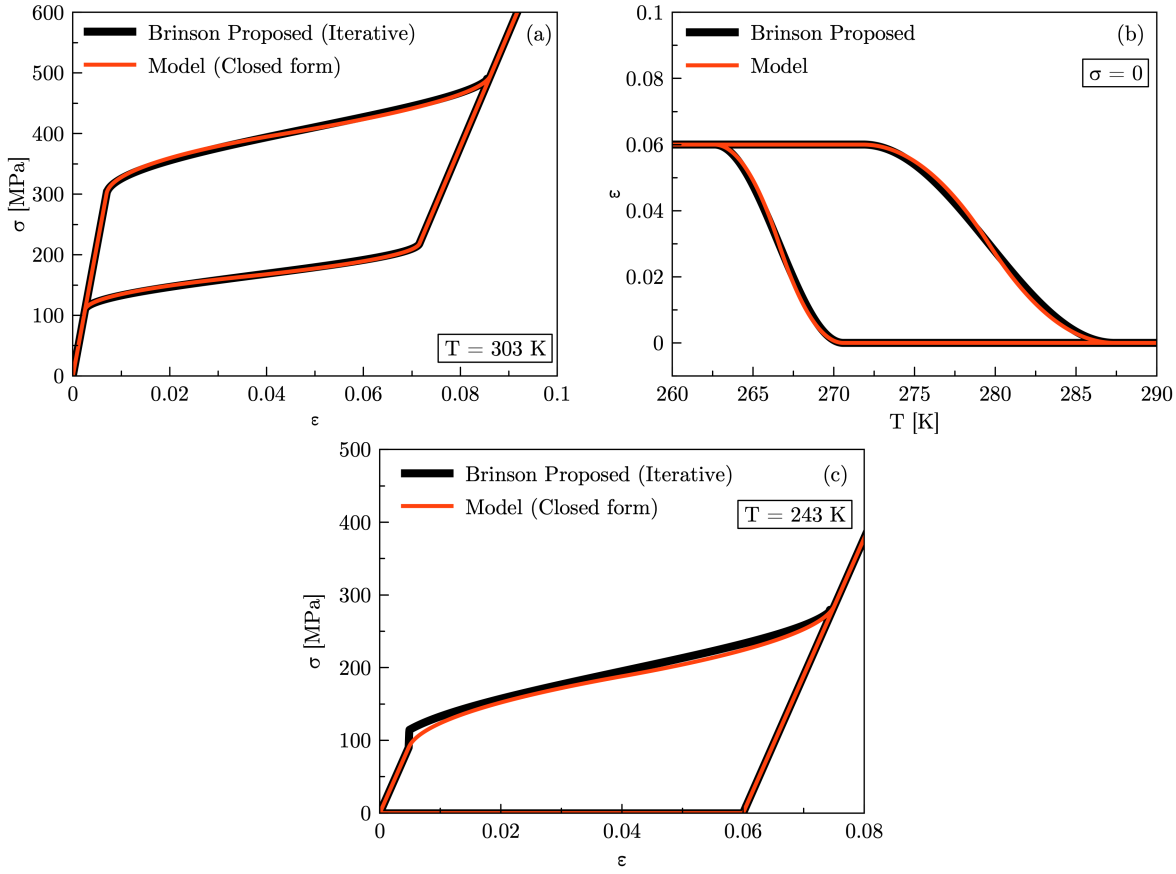


Fig. 5.3: Comparison of Brinson and proposed polynomial model for prescribed strain load. (a) Pseudoelastic effect. (b) Shape memory effect. (c) Martensite reorientation.

Simulations in Fig. 5.2 and Fig. 5.3 show that the proposed model is able to reproduce the iterative method for prescribed strain problems used for traditional models with kinetic phase transformation for phase transformations and also in the process of martensite reorientation.

Fig. 5.4(a) present the iterative number of steps performed by the algorithm during the process of load and unload at T=303 K (pseudoelastic effect) in Fig. 5.3(a). The process begins with 0 iterative steps while the *SMA* element behaves in the austenite elastic regime. When forward phase transformation begins, the algorithm requires 100 steps to reach a converged solution, followed by an average of 20 iterative steps for each step of time and finishing again with 100 iterative steps, where *SMA* enters in martensite elastic regime. It is important to state that the algorithm considers a maximum number of iterative steps as 100 steps, stopping the process after that. For reverse phase transformation, the algorithms perform an average of 30 steps for

each time step.

Fig. 5.4(b) deals with the number of iterative steps for T=243 K (martensite reorientation) in Fig. 5.3(c). Again, the algorithm begins with 0 iterative steps until the martensite reorientation process starts. The algorithms reach 100 iterative steps at the first moment, followed by an average of 3 iterative steps for each step of time, finishing with 100 steps to converge the solution.

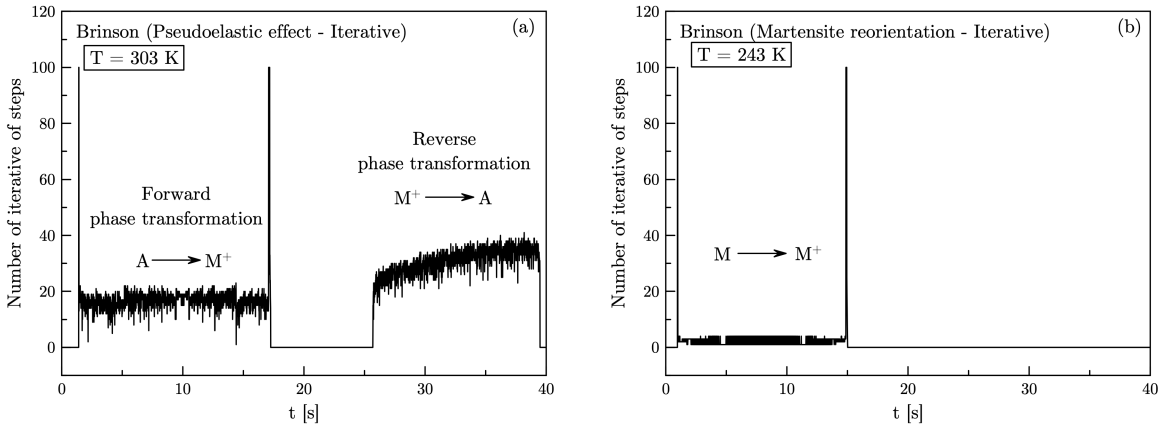


Fig. 5.4: Iterative number of steps for Brinson [34] model in prescribed strain load and phase transformation induced by mechanical load.

Table 10 provides information about the time needed for simulations contained in Fig. 5.3 and Fig. 5.4. Brinson [34] model and the proposed model are compared for load and unload in pseudoelastic and martensite reorientation phenomena. Brinson [34] model using the algorithm for convergence requires a total of 70079 iterative steps and 0.014 seconds to run while for martensite reorientation a total of 3659 iterative steps are performed and 0.013 seconds to run.

The proposed polynomial model does not require the algorithm for solution convergence due to providing an analytical solution for prescribed strain problems. For this reason, the computer registered 0.012 and 0.011 seconds for pseudoelastic and martensite reorientation processes, respectively. This represents a small difference when compared with the traditional method to use the convergence algorithm but it is important to remember these results deal with just one cycle of load and unload. In dynamical analyses, the total number of cycles to be evaluated can significantly increase.

Table 10: Time simulation for strain prescribed load in Brinson [34] model and the proposed polynomial model wish assumed kinetic phase transformation

Model		dt	Iterative steps	Time of simulation [s]
Brinson				
	Pseudoelastic	0.01	70079	0.014
	Martensite reorientation	0.01	3659	0.013
Polynomial				
	Psudoelastic	0.01	-	0.012
	Martensite reorientation	0.01	-	0.011

Considering now the purposed polynomial model, Fig. 5.5 present results to explore the capability to adjust phase transformation curves according to specific situations. Fig. 5.5(a) deals with load and unload at $T = 303$ K while Fig. 5.5(b) shows phase transformation is induced by temperature variation for different values of control parameters B_M and B_A. Note that is possible to adjust the curve concavity for forward and reverse transformation by the addition of two extra parameters than Brinson [34] model.

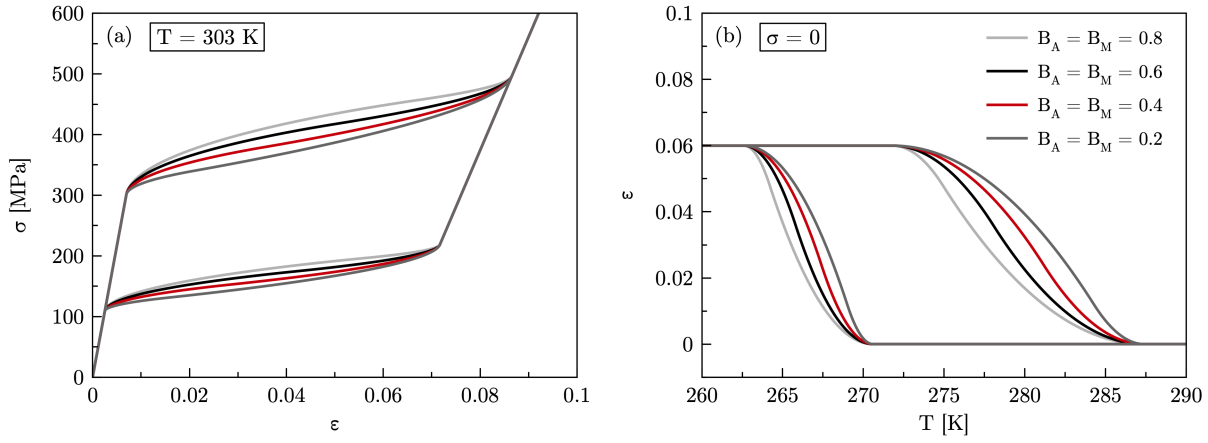


Fig. 5.5: Control parameters B_M and B_A analysis for polynomial model with assumed kinetic transformation. (a) Stress × strain diagram: Phase transformation induced by temperature. (b) Strain × temperature diagram: Phase transformation induced by mechanical load.

The ability of the proposed model to describe *SMA* thermomechanical behavior for different loading characteristics is now of concern considering internal subloops. Fig. 5.6 presents results for $T = 303$ K representing a high-temperature condition. Fig. 5.6(a) shows stress-strain curves associated with pseudoelastic effect considering both tensile and compression values for

prescribed strain with internal subloops. Fig. 5.6(b) shows prescribed strain while Fig. 5.6(c) shows Young's modulus and Fig. 5.6(d) presents the evolution of martensite volume fraction.

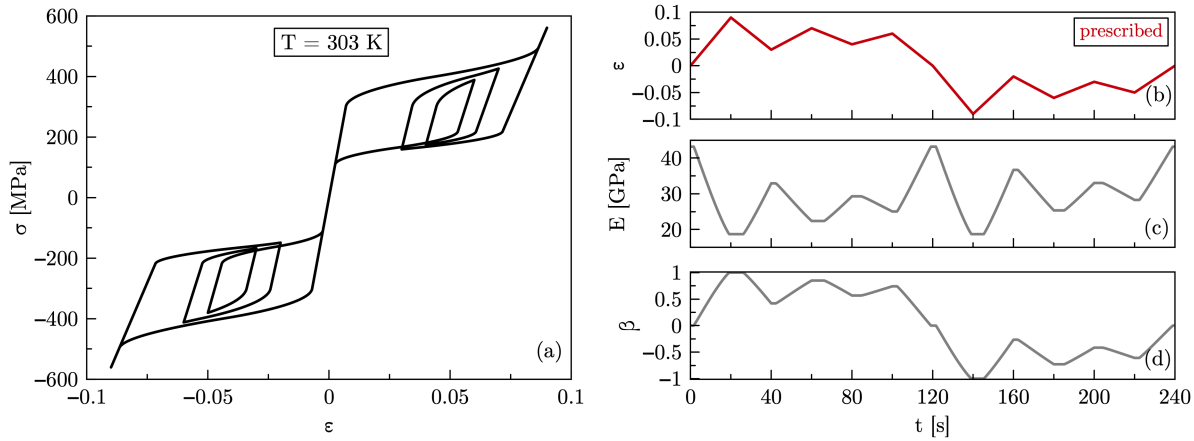


Fig. 5.6: Subloop analysis for the polynomial model with assumed kinetic phase transformation for $T > A_f$. (a) Stress × Strain diagram. (b) Prescribed strain. (c) Young's modulus. (d) Martensite volume fraction variation.

Fig. 5.7(a) presents strain-temperature curves for an *SMA* sample that is subjected to temperature variations with a null-stress state. Fig. 5.7(b) presents the prescribed temperature, Fig. 5.7(c) presents the strain evolution while Fig. 5.7(d) shows the evolution of the martensite volume fraction.

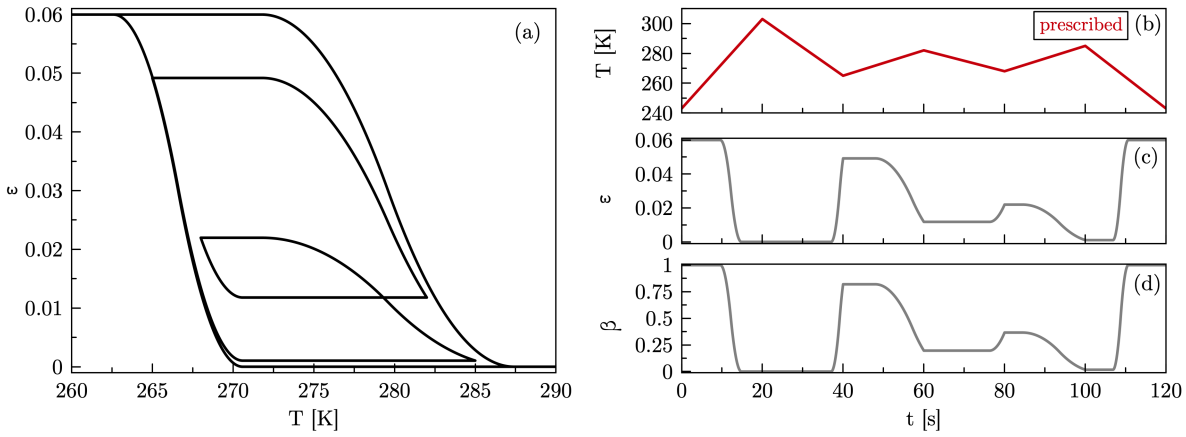


Fig. 5.7: Subloop analysis of polynomial model for $\sigma = 0$. (a) Strain × temperature diagram. (b) Prescribed temperature. (c) Strain and (d) martensite volume fraction time evolution.

5.1.1 Mechanical Oscillator with SMA element

The objective of this section is to evaluate the proposed *SMA* model (subsection 4.2.1) with an analytical solution for prescribed strain problems in a dynamical system. Dynamical simulations

for a single degree of freedom base vibration system connected to the *SMA* austenite wire element are divided into three sections: free vibrations, sweep response, and stationary forcing frequency.

5.1.1.1 Free Vibration

Free vibrations analysis is performed by assuming $A_b = 0$. Different values of temperature and initial conditions are treated to evaluate three scenarios: low temperature ($T < M_f$) without stress-induced phase transformations; high temperature ($T > A_f$) without stress-induced phase transformations and high temperature with stress-induced phase transformations.

For low temperature, it is assumed the SMA element was pre-strained to induce martensite reorientation from twinned to detwinned. This pre-strain procedure can be considered for practical analysis because it happens just on the first load cycle and induces a residual strain, which can be recovered by the thermal cycle and the focus of this investigation are mechanical loads.

Fig. 5.8 shows results for high temperature behavior ($T > A_f$) considering initial displacement $z_0 = 0$ and three different values of initial velocity ($\dot{z}$) equal to 0.1 m/s, 1 m/s and 3 m/s. Note that the increase of velocity introduces more energy to the system, inducing higher levels of phase transformations. It should be pointed out that the first case is an elastic response where the dissipation is only related to the linear viscous damper. On the other hand, the increase of the initial condition level, induces stress-induced phase transformations, being expressed by hysteretic responses and the variation of the martensite volume fraction.

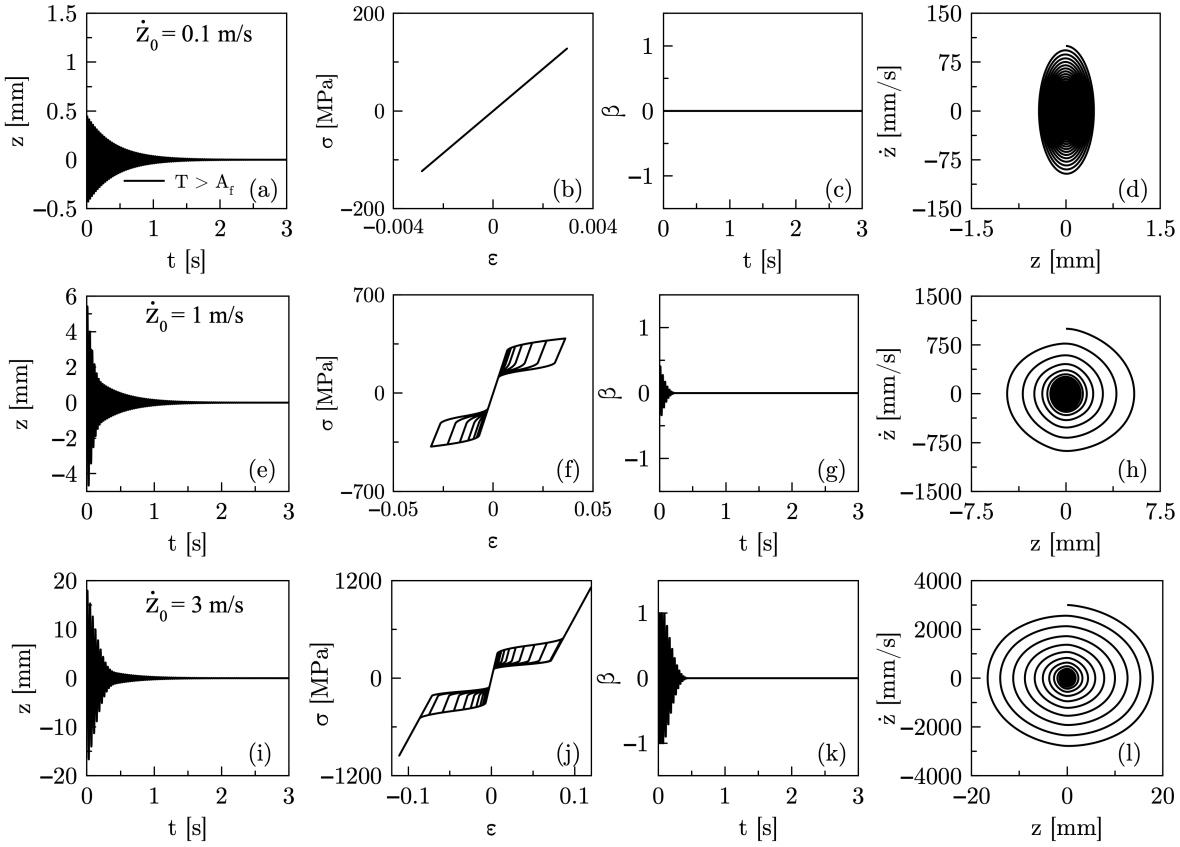


Fig. 5.8: High temperature free vibration for different initial conditions in free vibration analysis: (a), (e) and (i) present displacement time history. (b), (f) and (g) show stress-strain curves. (c), (g) and (k) show the martensite volume fraction. (d), (h) and (l) present the phase spaces.

Fig. 5.9 presents the low-temperature behavior ($T < M_f$), showing situations related to martensite behavior. Under these assumptions, initial conditions are assumed to be a displacement associated with the residual strain and the same three values of initial velocity ($\dot{z}$) equal to 0.1 m/s, 1 m/s, and 3 m/s. Results are now associated with different equilibrium points associated with the martensite phase. All cases do not present a phase transformation, presenting an elastic response around the equilibrium point. It is also noticeable that volume fractions are martensite for the whole process. The equilibrium point shift is experimentally confirmed by de Aguiar et al. [180] where the system oscillates around the residual pre-strain value.

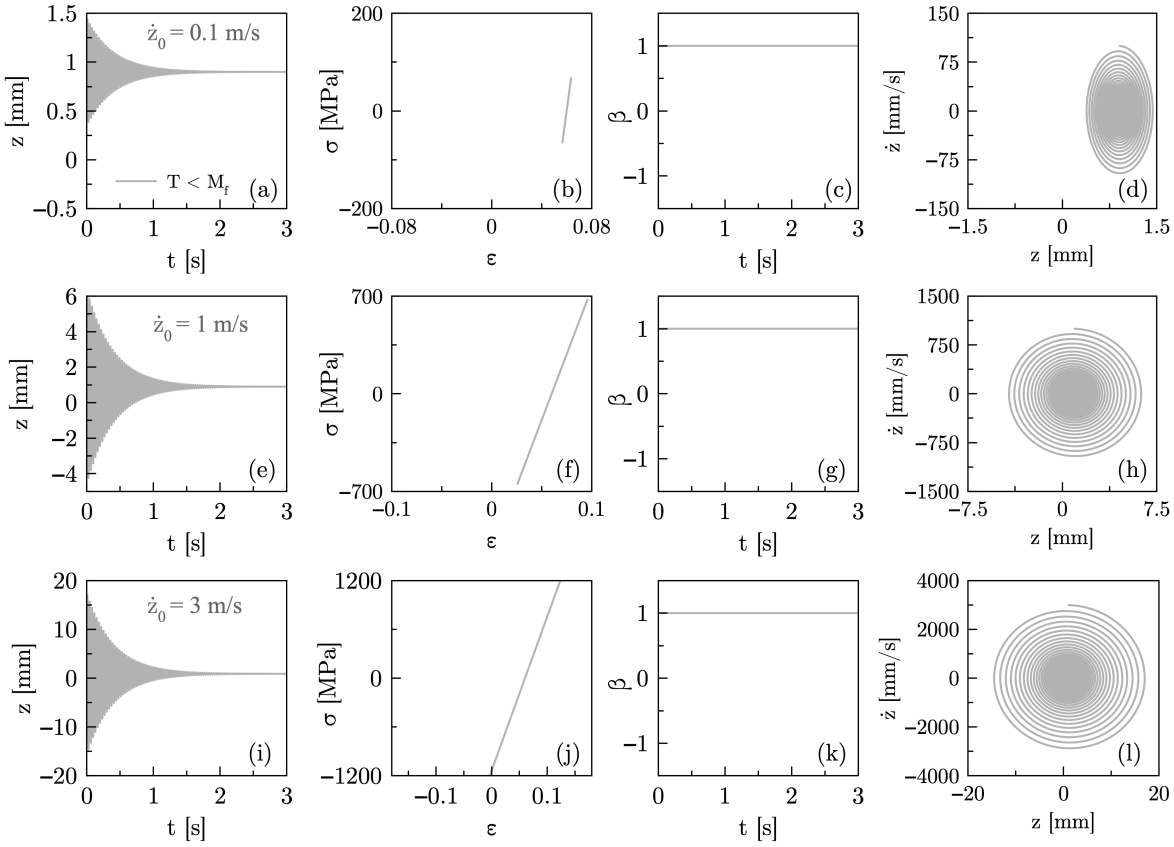


Fig. 5.9: Low temperature free vibration for different initial conditions in free vibration analysis: (a), (e) and (i) present displacement time history. (b), (f) and (g) show stress-strain curves. (c), (g) and (k) show the martensite volume fraction. (d), (h) and (l) present the phase spaces.

Also, free vibrations simulations are able to determine the damping capacity associated with the hysteresis between cycles. For this reason, simulations without the external damping element ($c = 0$) are performed. Fig. 5.10 present results that ensure that the model is able to dissipate energy even if the value of external damping assumes the value of zero.

Next subsection evaluates the system frequency responses for different *SMA* temperature conditions, system base vibration frequency, and amplitude.

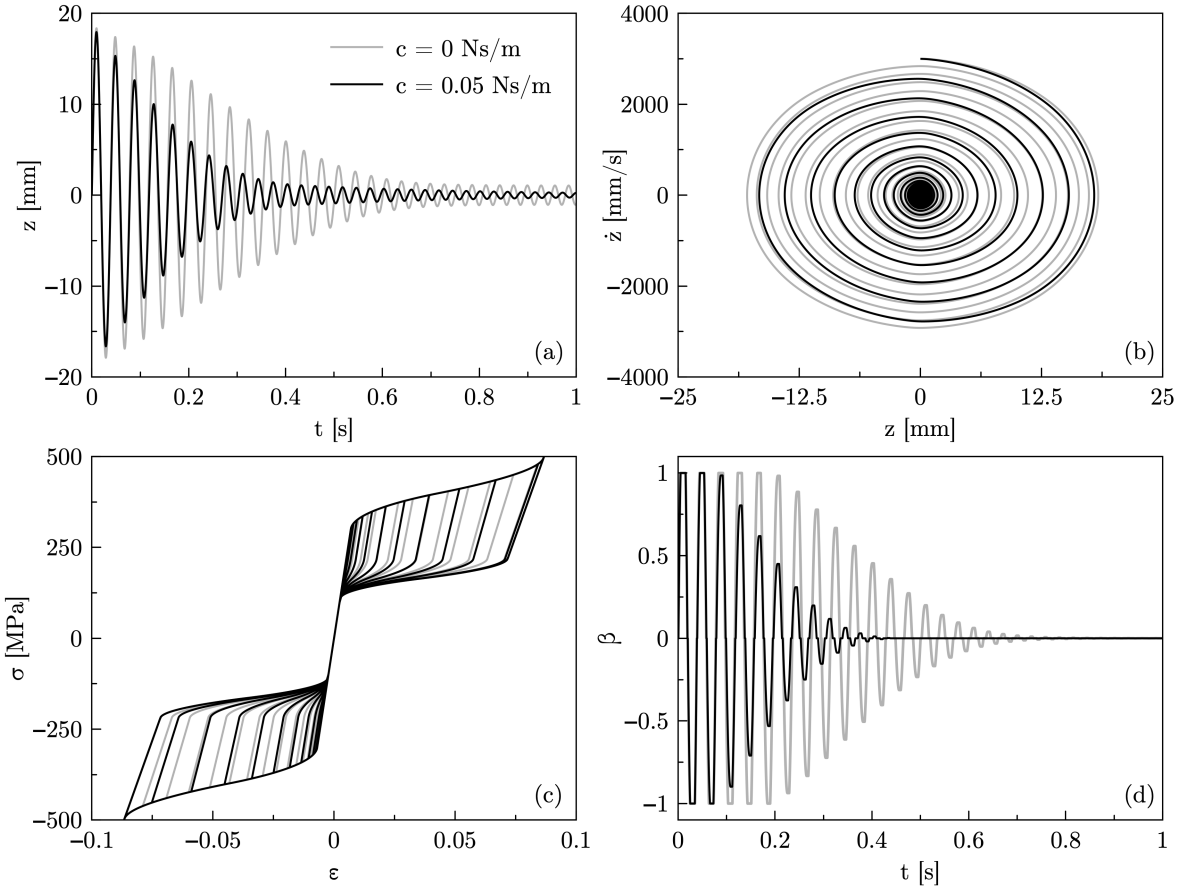


Fig. 5.10: External undamped ($c = 0$) damped system ($c = 0.05Ns/m$) free vibration analysis. (a) Displacement time evolution. (b) Phase space. (c) Stress × strain diagram. (d) Martensite time evolution.

5.1.1.2 Sweep Response

This subsection deals with sweep response diagrams for the mechanical oscillator considered in this work. Three important variables for shape memory alloy oscillatory devices are: temperature, forcing amplitude, and forcing frequency. Frequency sweep diagrams are evaluated in a forward direction considering one hundred forcing periods and, to ensure the solution has already achieved steady state response, it is considered response data for the last 20% of total periods. A series of analyses are performed after the convergence has been achieved for a time step $dt = \Gamma/100$, where Γ represents the forcing frequency period in order to evaluate the model performance varying the three mentioned parameters.

Fig. 5.11(a) evaluates the temperature influence where a small base vibration amplitude ($A_b = 0.1$ m/s^2) is applied in order to keep the system response at linear elastic range as shown in Fig. 5.11(b). The increase of *SMA* temperature promotes an increase in the total system stiffness and consequently shifts to right the curves and peaks in Fig. 5.11(a). Once the value of damping is the same for all simulations in Fig. 5.11(a), the increase in system stiffness promotes

also a decrease in the maximum relative displacement achieved. These characteristics are further explored for SMA-piezoelectric energy harvesting investigations in section 5.2.

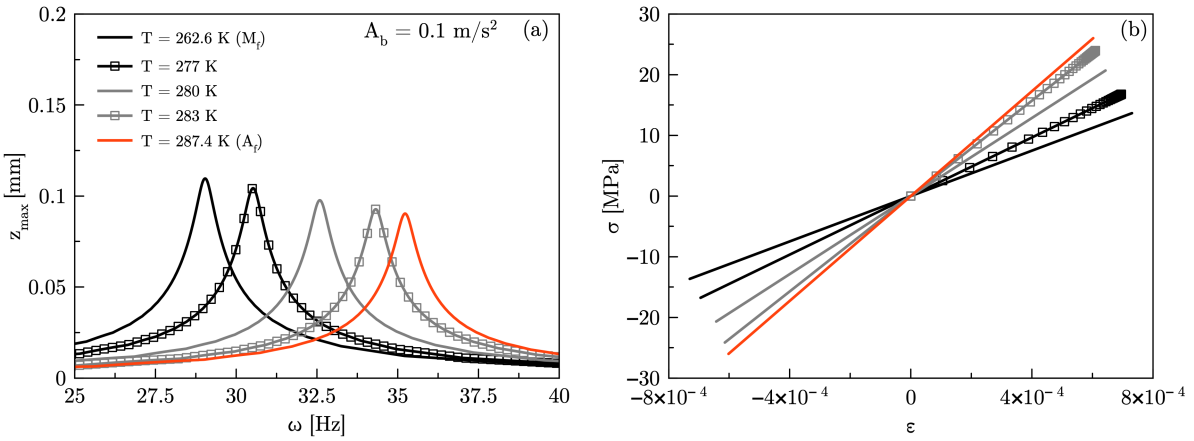


Fig. 5.11: Temperature influence analysis $A_b = 0.1$ m/s^2. (a) Frequency response. (b) Stress × strain diagrams.

Considering now a condition of high and constant temperature ($T = 303$ K), Fig. 5.12(a) shows results obtained for maximum displacement and maximum *SMA* stress for small values of base amplitude (A_b) where no phase transformation occurs. Note that the maximum values obtained for σ do not reach the first critical stress level for $T = 303$ K to begin phase transformation according to Table 4.

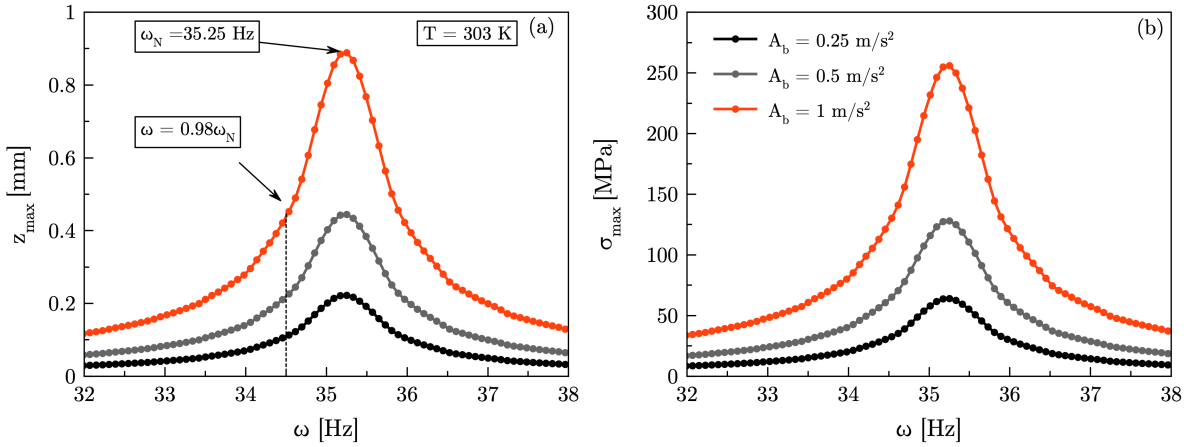


Fig. 5.12: Frequency response for different values of base amplitude for *SMA* linear elastic behavior. (a) Maximum displacement. (b) Maximum stress.

Fig. 5.12 shows the frequency attributed to the maximum displacement ($\omega_N = 35.25$ Hz) for linear response in the austenite range (T =303 K) and highlights a specific value of forcing frequency as $0.98\omega_N$ to investigate in stationary frequency response subsection, where $\omega_N = \frac{\Omega_N}{2\pi}$.

Fig. 5.13 present results where short amount of β (around 1%) is formed. It is possible to note

a discontinuity in correspondent curves when compared to linear behavior (dashed lines) where no phase transformation would happen. Linear behavior is simulated considering stress (σ) into Eq. (94) as a function of shape memory alloy element strain (ϵ) and directly proportional to austenite Young's modulus ($\beta = 0$ and constant). More severe nonlinear conditions are investigated in Fig. 5.14, and Fig. 5.15 considering larger values of base excitation amplitude. The time step is now: $dt = \Gamma/10^5$, and the number of periods simulated increases by two hundred. Analyses still consider response data for the last 20% of total periods.

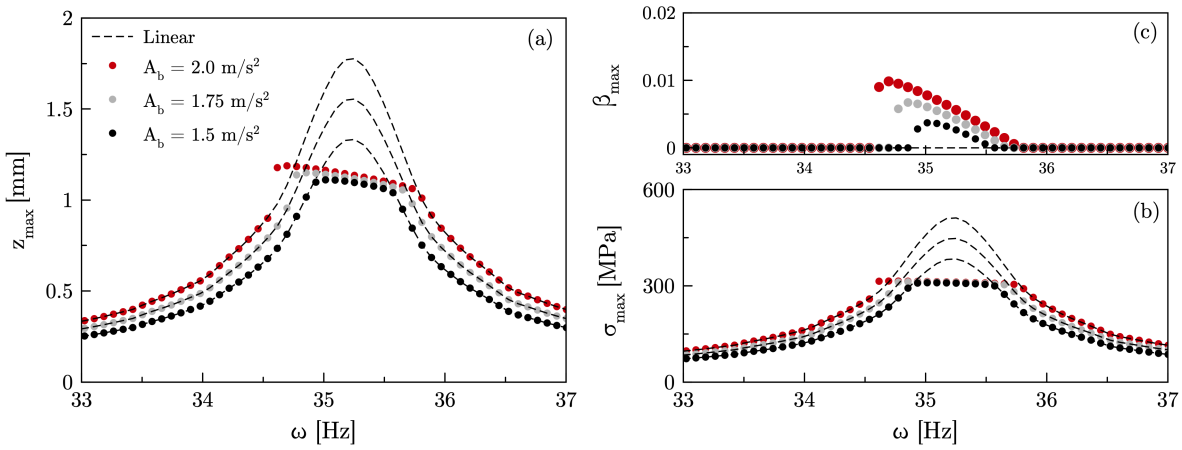


Fig. 5.13: Nonlinear frequency response for conditions with small values of *SMA* phase transformation. (a) Maximum displacement. (b) Maximum stress. (c) Maximum martensite volume fraction formed.

As the base excitation amplitude increases, the maximum martensite volume fraction increases, and relevant nonlinear behavior is observed in Fig. 5.14. Dynamical jumps and significant shifts in frequency values where maximum displacement occurs can be attributed to rapid change in *SMA* Young's modulus from austenite to martensite. The *SMA* softening due to martensite phase transformation promotes the rapid increase in maximum displacement which can be further explored for SMA-piezoelectric energy harvesting in section 5.3.

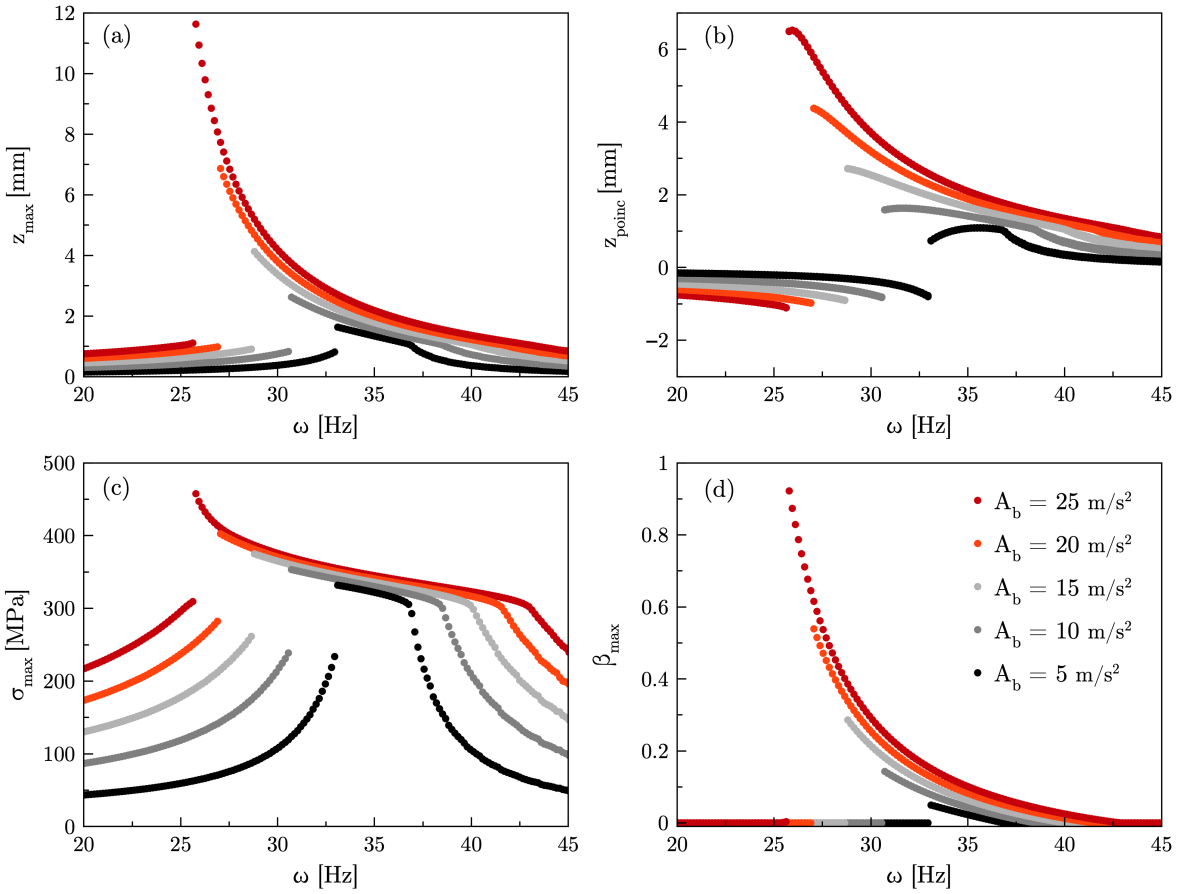


Fig. 5.14: Nonlinear frequency response for incomplete phase transformation. (a) Maximum displacement. (b) Displacement Poincaré section. (c) Maximum strain. (d) Maximum martensite volume fraction formed.

Fig. 5.14(a) shows the maximum displacement obtained for different values of force amplitude. Fig. 5.14(b) shows the Poincaré section collecting the value of the variable at the same position within the forcing period. Fig. 5.14(c) presents the maximum stress in *SMA* wire and a plateau is observed in the diagram. Finally, Fig. 5.14(d) shows the maximum amount of martensite volume fraction induced by base vibration for each value of forcing amplitude (A_b).

Full transformation occurs for relatively high levels of force amplitude and a different pattern can be observed comparing Fig. 5.14 with Fig. 5.15. In Fig. 5.14 is observed one dynamical jump and asymptotic curve behavior. In Fig. 5.15, the displacement diagram presents two dynamical jumps meaning the *SMA* wire assumes full martensite phase for a range of frequencies. Fig. 5.15(b) presents the Poincaré section enhancing the system periodicity remains the same as periodic with one period for all conditions treated in Fig. 5.15. Fig. 5.15(c) and (d) shows maximum levels of stress and β are present, respectively.

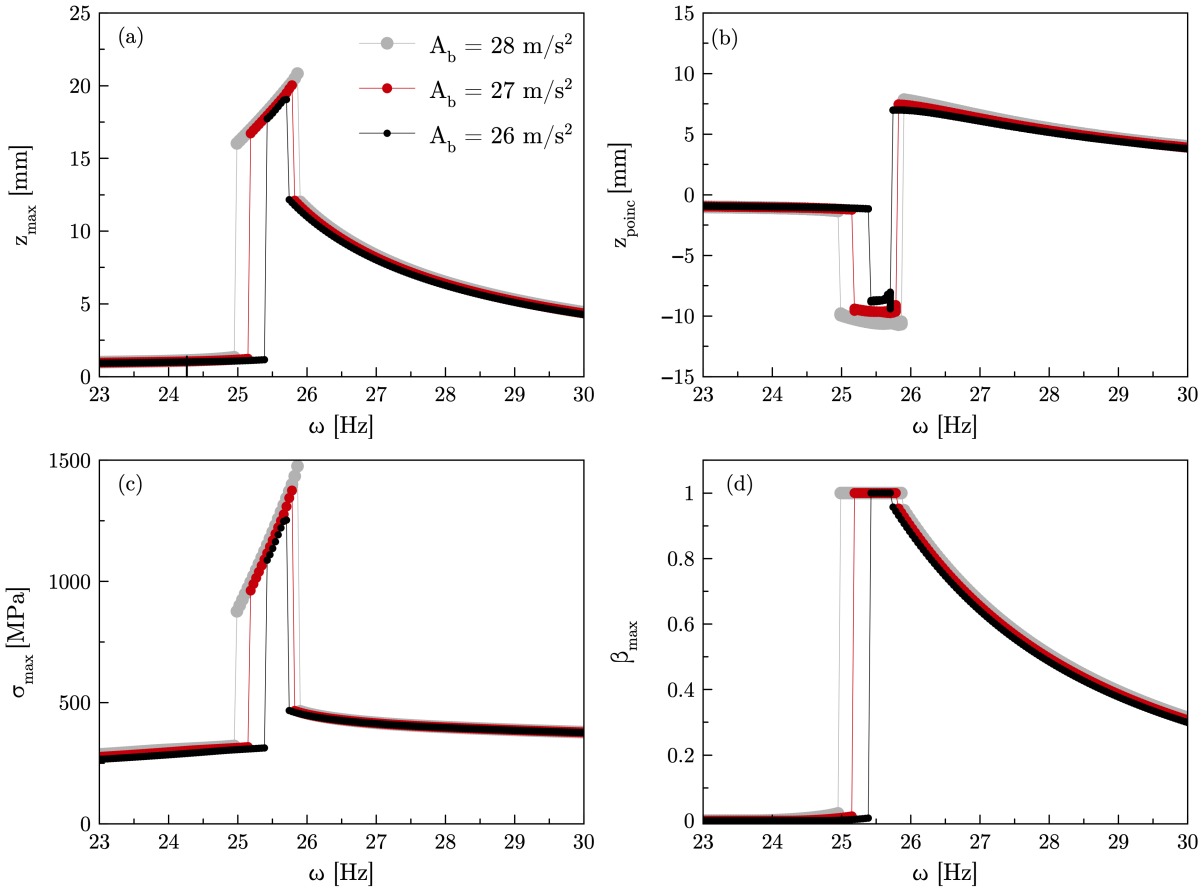


Fig. 5.15: Nonlinear frequency response with complete phase transformation. (a) Maximum displacement. (b) Displacement Poincaré section. (c) Maximum strain. (d) Maximum martensite volume fraction formed.

5.1.1.3 Stationary Forcing Frequency Response

This subsection show results for the SMA-oscillator operating in stationary forcing frequency. The objective is to investigate the time evolution and steady state response of the system associated with proper conditions evaluated in the previous subsection.

In a first stationary base frequency investigation, the selected forcing frequency ($0.98\omega_N$ =34.64 Hz) for a *SMA* element working in austenite linear elastic range is set according to Fig. 5.12. Thus, Fig. 5.16 shows system response for stationary frequency of base vibration through displacement time evolution and phase spaces diagrams. Base excitation amplitude increase from 1 m/s^2 (Fig. 5.16(a) to (c)) to 5 m/s^2 (Fig. 5.16(d) to (f)) and 25 m/s^2 (Fig. 5.16(g) to (i)) with the objective to promote phase transformation and nonlinear behavior. Phase spaces are shown with respect to the total simulation and highlighted in red lines are the steady state responses. Results indicate periodic response in the steady state region. The transient region and phase spaces diagrams alter due to the increase in base vibration amplitude promoted by the *SMA* phase transformation.

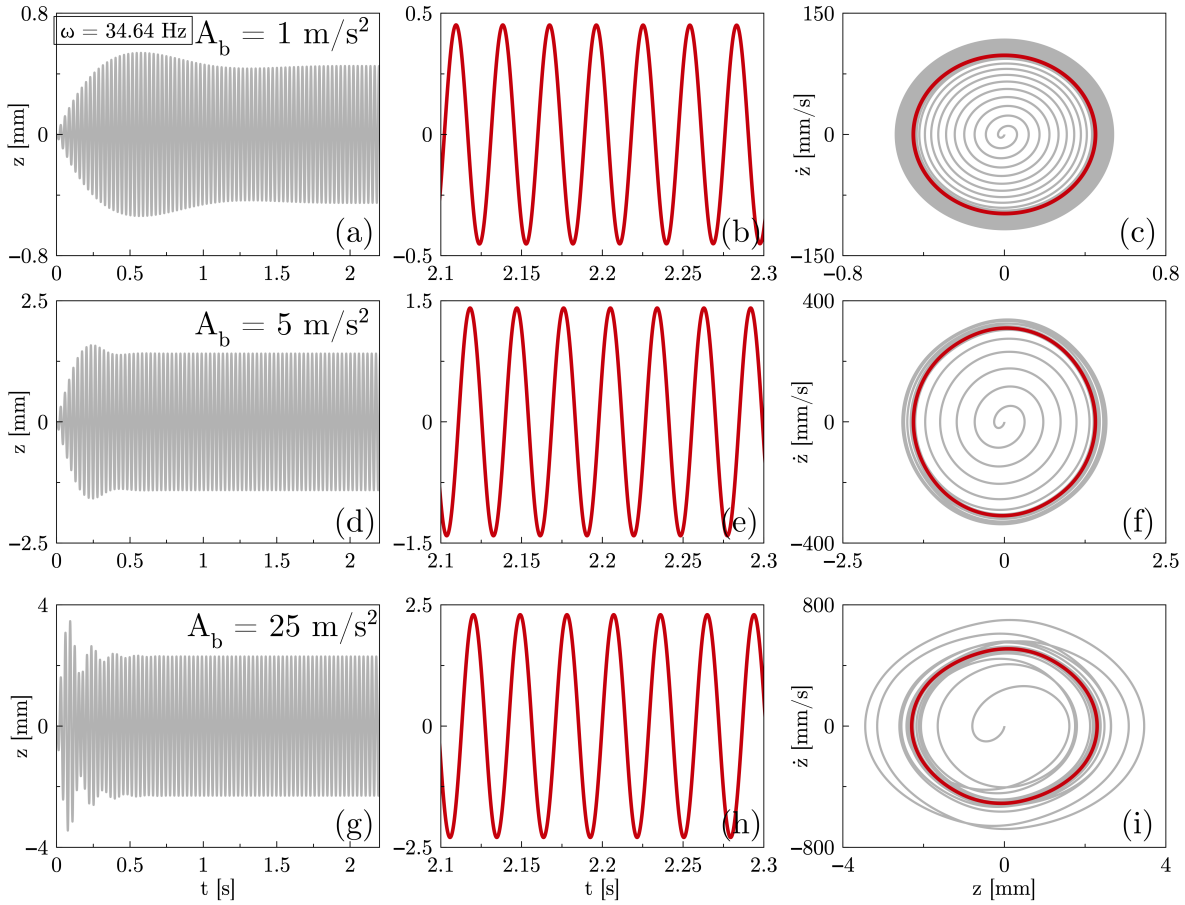


Fig. 5.16: System time domain responses in stationary forcing frequency for different levels of base amplitude. $A_b = 1$ m/s^2 from (a) to (c). $A_b = 5$ m/s^2 from (d) to (f) and $A_b = 25$ m/s^2 from (g) to (i).

Fig. 5.17 shows stress × strain diagrams and martensite volume fraction associated with each base amplitudes in concern. For $A_b = 1$ m/s^2, linear behavior is observed and no phase transformation occurs as expected. As soon as forcing amplitude increases, different amounts of phase transformation can be achieved. Again, gray lines indicate the total simulation while red lines highlight the steady-state response.

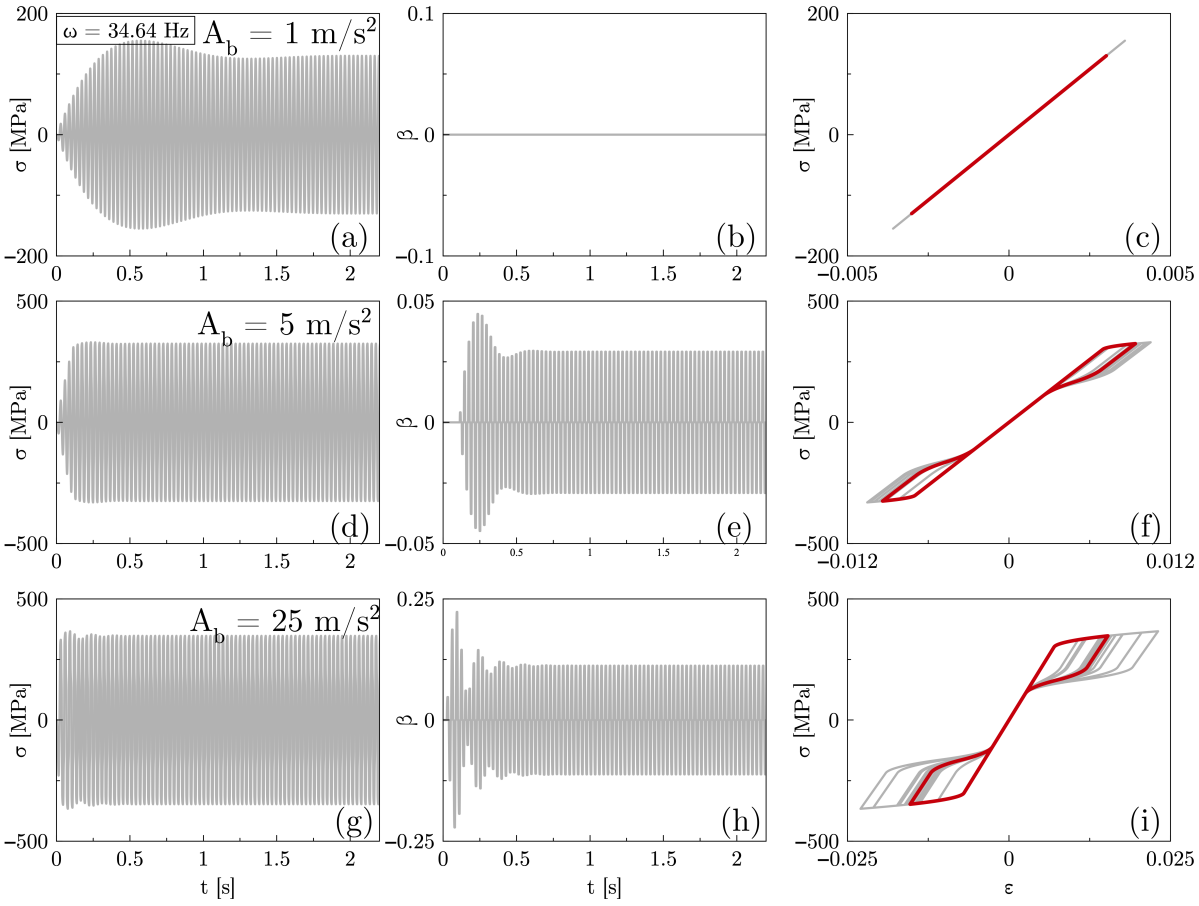


Fig. 5.17: *SMA* element time domain responses in stationary forcing frequency for different levels of base acceleration. $A_b = 1$ m/s^2 from (a) to (c). $A_b = 5$ m/s^2 from (d) to (f) and $A_b = 25$ m/s^2 from (g) to (i).

The frequency response curve in Fig. 5.14(a) is reproduced in Fig. 5.18(a), where $A_b = 25$ m/s^2 and highlights three different regions in diagram for stationary forcing frequency investigation. Fig. 5.18(b)-(d), show phase spaces related to the selected driven frequencies. In addition, Fig. 5.18(e)-(g) show martensite volume fraction and Fig. 5.18(h)-(j) deals with stress × strain diagrams.

It is possible to note a significant difference in system performance in a range between 20 and 33 Hz in Fig. 5.18. The dynamical jump is due to the change in *SMA* stiffness and damping capacity from an austenite linear elastic range (Fig. 5.18(b),(e) and (h)) to a nonlinear response oscillating between martensite and austenite phases. These characteristics can be explored in SMA-piezoelectric energy harvesting investigation.

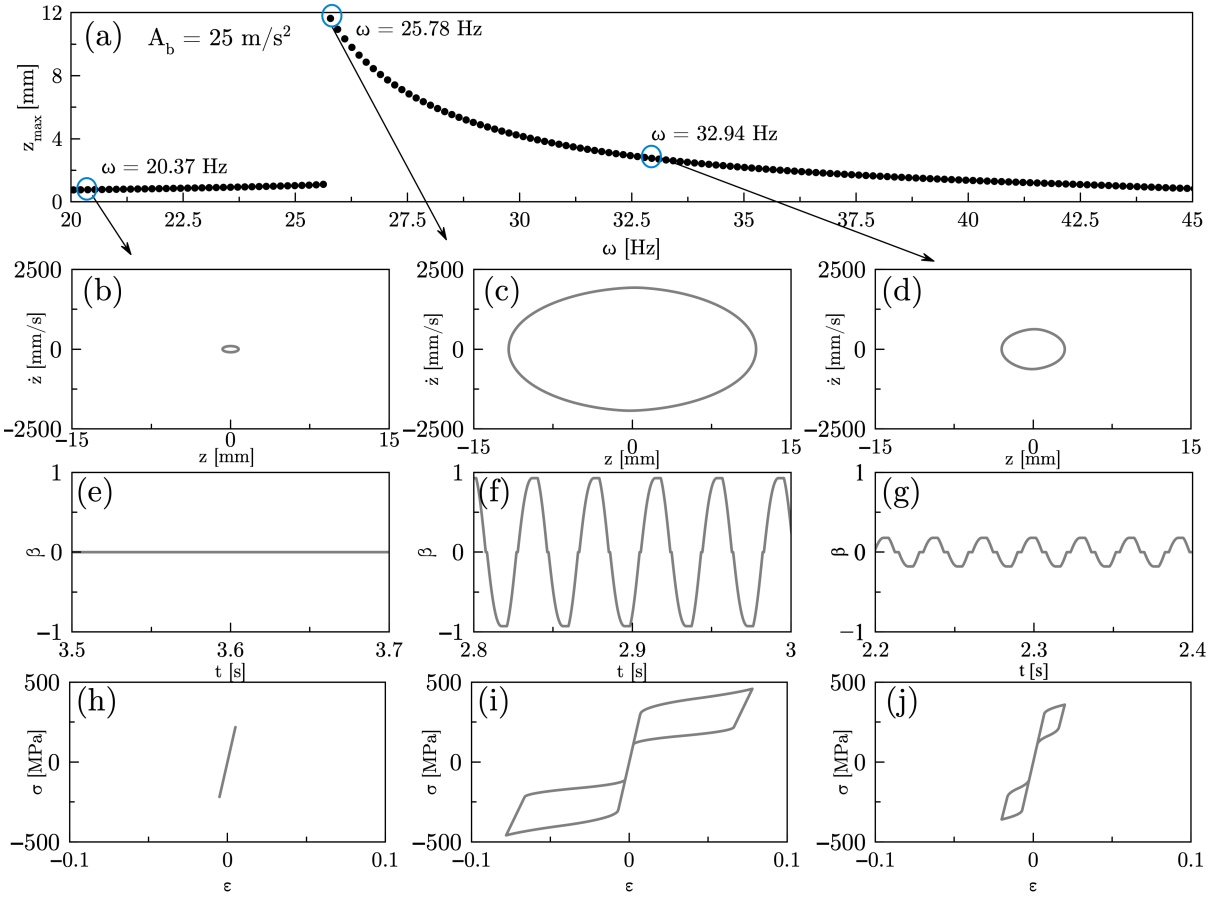


Fig. 5.18: Stationary forcing frequency analysis for $A_b = 25$ m/s^2. (a) Frequency response. From (b) to (c) phase spaces. From (e) to (g) martensite time evolution. From (h) to (j) stress × Strain diagrams.

Finally, Figure Fig. 5.19(a) investigates the response for $A_b = 26$ m/s^2 where two dynamical jumps can be observed. Again, three regions in diagram are selected to stationary frequency analysis. Fig. 5.19(b)-(d) show stress × strain diagrams related to selected frequency values while Fig. 5.19(e) shows martensite volume fraction in steady state response and Fig. 5.19(f) phase space diagram. Even more significant difference in system performance can be observed between a range of around 2 Hz (26.85-25.38) where *SMA* element present incomplete and complete phase transformation.

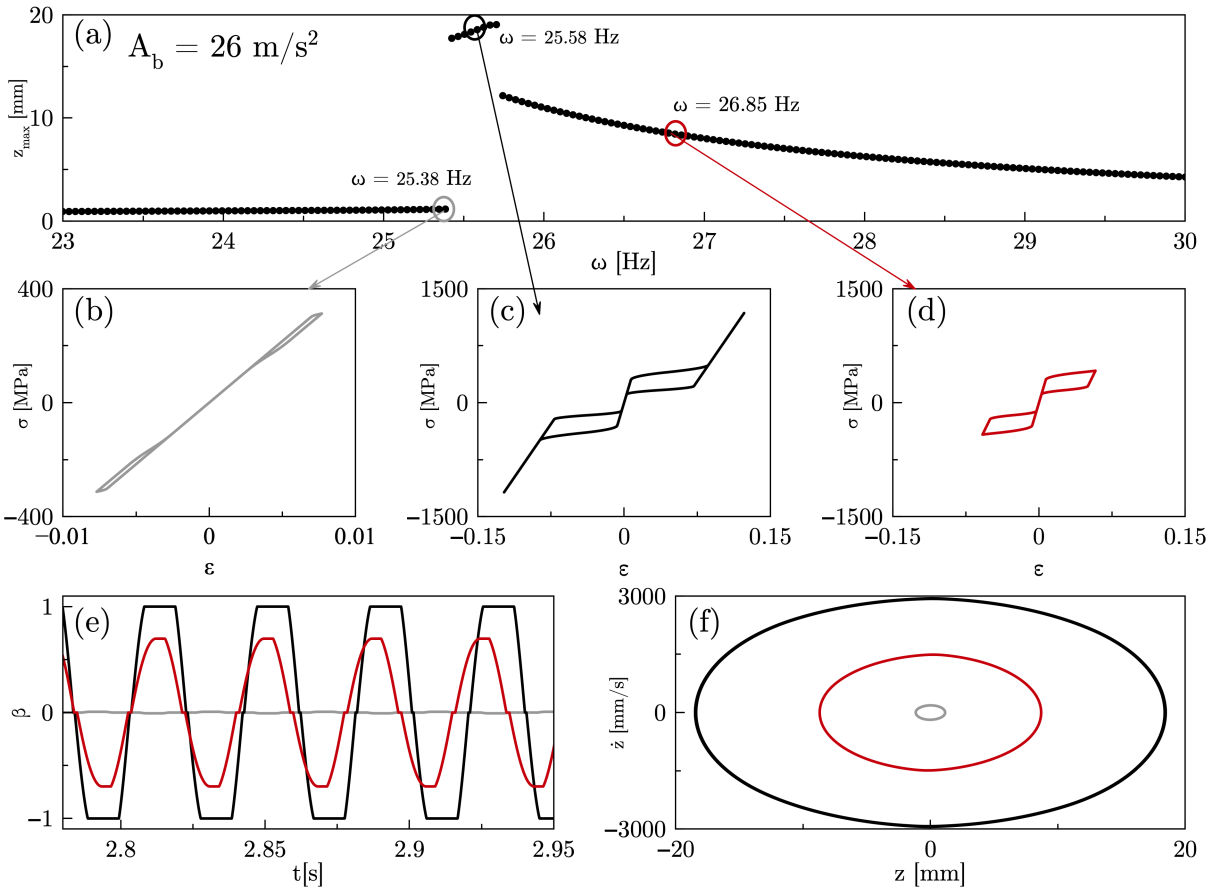


Fig. 5.19: Stationary forcing frequency analysis $b_b = 26$ m/s^2. (a) Frequency response diagram. From (b) to (d): Stress × Strain diagrams. (e) Martensite time evolution. (f) Phase space.

5.2 Piezoelectric Energy Harvester with SMA Martensite Helical Spring

Numerical simulations are performed employing the fourth-order Runge-Kutta method. Parameters presented in Table 8 and (subsection 4.2.2) are employed for all simulations and compared with experimental data. Convergence analysis is performed by defining a time step $dt = \Gamma/200$, where Γ represents the forcing frequency period.

5.2.1 Sweep Response

Initially, a diagram is built with an up-sweep test from 0 to 1000 kΩ by increments of 10 kΩ and evaluating the maximal power obtained as a function of electrical resistance. Fig. 5.20 shows this diagram for two different temperatures: low temperature, where the martensite phase is stable; and high temperature, where austenite is stable. The excitation force amplitude is $A_b = 9.81$ m/s^2 while excitation frequency is $\omega = \omega_N^M$, for low temperature, and $\omega = \omega_N^A$ for high temperature. Based on these results, it is possible to identify load resistance associated with the maximum output power values for both temperatures, representing the optimal operational

conditions for energy harvesting purposes. It is noticeable that the optimal resistances are 190 kΩ for low temperatures with a maximum output power of 0.35 mW. For high temperatures, an optimal resistance of 180 kΩ is identified and is associated with an output power of 0.73 mW. Despite these values, the experimental apparatus considers an electrical resistance of 150 kΩ. For this reason, 150 kΩ is adopted for numerical simulations and it is expected a maximum value of 0.34 and 0.72 mW for each case, respectively.

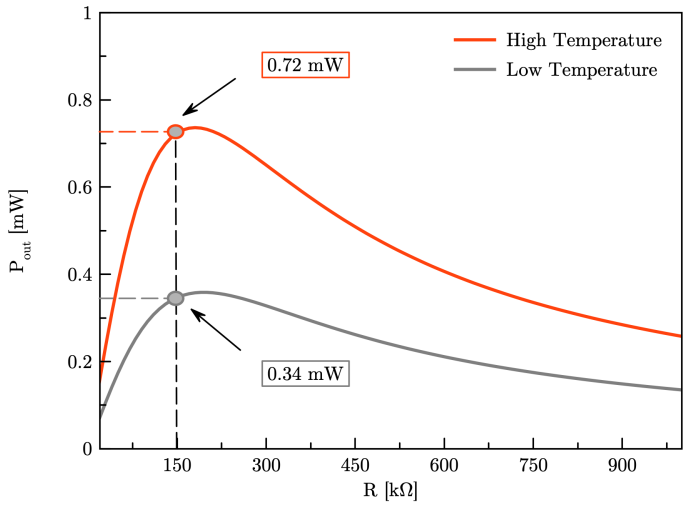


Fig. 5.20: Analysis of the energy harvester maximum output power as a function of external resistance load for low and high *SMA* temperature conditions.

Frequency response diagrams are now of concern, varying frequency in a forward direction with a value of maximum acceleration amplitude equal to 9.81 m/s^2, and capturing the maximum value of each variable - displacement, output power, input power, and efficiency. Numerical simulations consider one hundred cycles for each value of frequency. Two different temperatures are treated, considering two currents: 0 A and 2.5 A. Numerical simulations (Eq. (77) to Eq. (81)) and analytical analyses (Eq. (82) to Eq. (85)) are compared with experimental data, showing a good agreement as shown in Fig. 5.21. It is noticeable that the system presents two resonant conditions, one for each temperature, showing the adaptability conferred by the *SMA*. Experimental results presented a 2.49 Hz, (35.35–32.86) between maximum peaks representing a variation of 7.5% with respect to the resonance frequency related to low temperature.

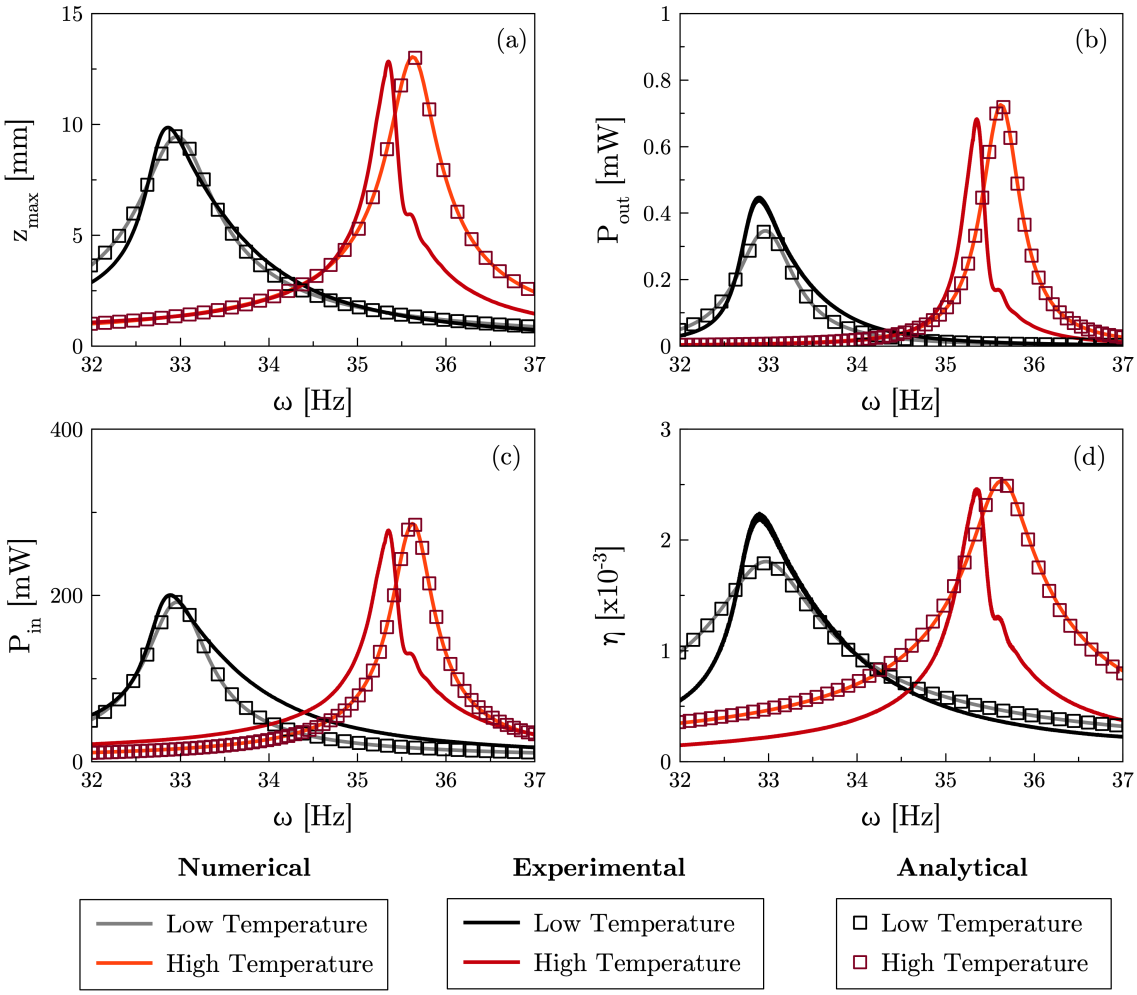


Fig. 5.21: Experimental, analytical and numerical results of the energy harvester frequency response. System adaptability is represented by the temperature dependent resonant conditions. (a) Maximum Displacement. (b) Maximum Output Power. (c) Maximum Input Power. (d) Maximum Efficiency.

Fig. 5.22 shows a different perspective of the adaptive behavior of the energy harvester, highlighting the peaks where maximum output power occurs. Also, system bandwidth is measured from peak to peak. In this regard, Δ_f becomes the difference between frequency peaks and Δ_{power} the increase of the output power.

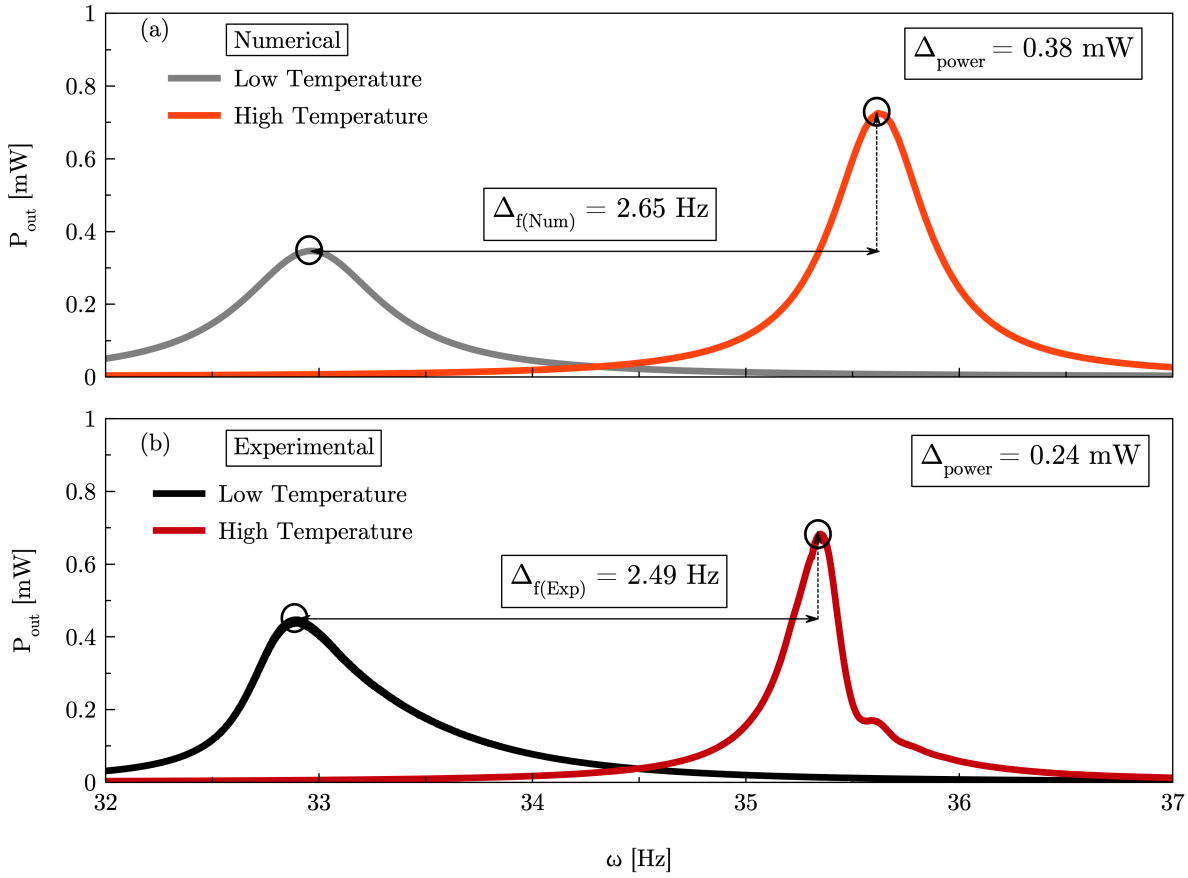


Fig. 5.22: Energy harvester bandwidth analysis highlighting the adaptive capacity provided by shape memory alloys, increasing of the output power. (a) Numerical simulations. (b) Experimental data.

In summary, results show that the adaptive behavior can change resonant conditions for two different levels, considering different temperatures promoted by the electric current applied. Therefore, the combination of piezoelectric and *SMA* defines a two-peak resonant system that can be adjusted based on the excitation conditions. This allows a broad bandwidth system and this behavior helps to enhance energy harvesting capacity. Numerical-analytical and experimental results are in close agreement and the discrepancies can be related to thermal variations, fixation conditions, and geometric parameters.

Fig. 5.23 shows the *SMA* martensite helical spring temperature measurements by thermal sensors (infrared and thermocouple) during the frequency sweep. It is possible to note an perturbation in temperature measured by both sensors for the high-temperature condition in the resonance region. These effects can be associated with the forced convection phenomena that are more significant in the high-temperature condition and even more in a high amplitude of vibration. Nonetheless, temperatures attributed to the 2.5 A condition, do not trespass the below limit of A_s to initiate reverse transformation.

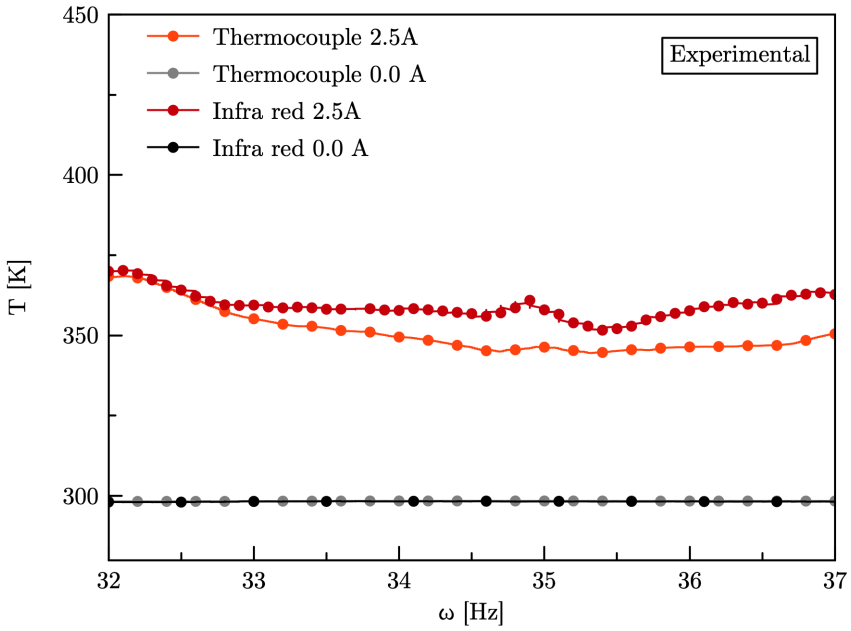


Fig. 5.23: *SMA* martensite helical spring temperature measurement by infra red sensor and thermocouple during frequency sweep.

In order to extend the numerical-experimental correlation about the SMA-piezoelectric energy harvester, experimental tests, and numerical simulations are also conducted for temperature values between low and high temperatures. Fig. 5.24 shows numerical simulations for low (0.0 A), high (1.37 A) temperatures and intermediate values of electrical current (0.5 A and 1.0 A). Fig. 5.24 also includes a curve (rendered in orange color) attributed to a simulation varying base vibration frequency and *SMA* temperature, simultaneously.

The objective of this analysis is to establish maximum output power values attributed to each specific value of ω between the interval of resonance frequency attributed to *SMA* low and high-temperature conditions. In this way, between this interval, the temperature increase keeps the system response in resonance condition. The orange curve is built considering Eq. (87), Eq. (88) and Eq. (89).

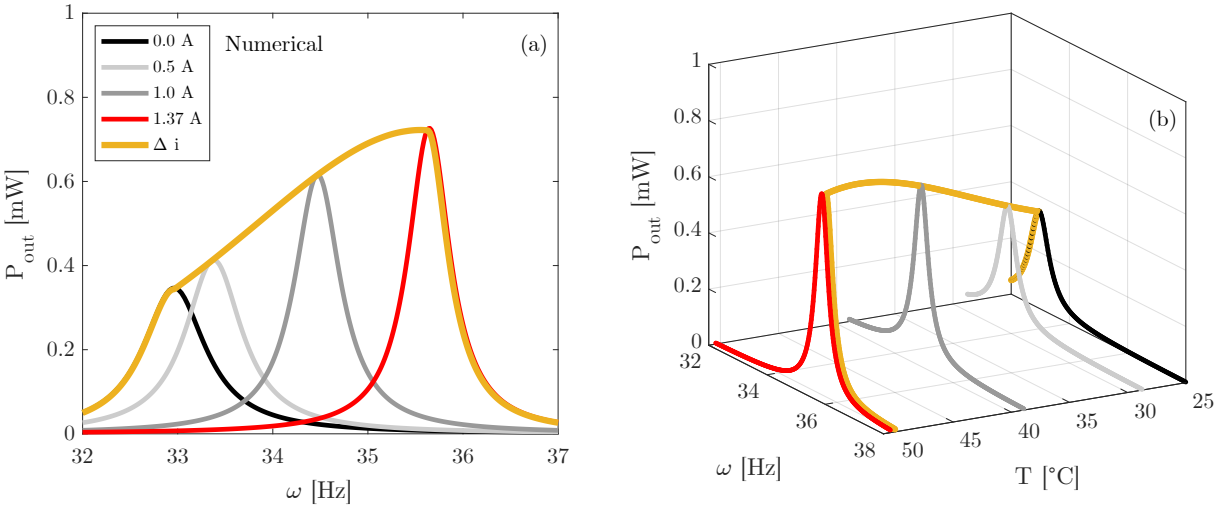


Fig. 5.24: Numerical output power frequency response for *SMA* piezoelectric energy harvester and phase transformation induced by temperature. (a) 2D diagram view. (b) 3D diagram view.

Once resonance frequencies for low and high temperature are established as 32.96 and 35.61 Hz from numerical simulations and analytical solution, when ω reaches 32.96 Hz, the temperature starts to increase from 298 K until 323.4 K (35.61 Hz) promoting $M \rightarrow A$ phase transformation. Given the base vibration frequency (ω) and knowing that $\omega_N = \omega$ to satisfy the resonance condition, it is possible to rearrange the Eq. (89) as: $(\Omega^2 m_{eq} - k - k_A)/(k_M - k_A) = \beta(\tilde{T})$ and estimate the values of $\beta(\tilde{T}) = f_A(\tilde{T})$ and solve for T.

Fig. 5.25 presents the comparison between numerical simulations in Fig. 5.24 and experimental test including now intermediate values of electrical current (0.5 A and 1.5 A). The maximum output power attributed to each case simulated in Fig. 5.24 is marked in Fig. 5.25 with their respective value of electrical current. By experimental curves in Fig. 5.25 it is possible to note good correlation with model predictions shown in Fig. 5.24.

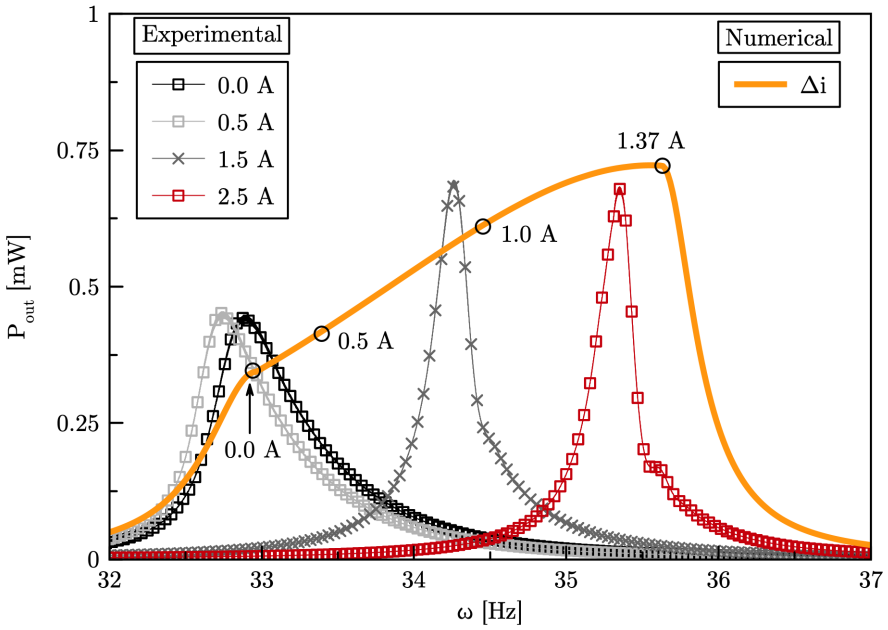


Fig. 5.25: Numerical-experimental correlation output power frequency response for *SMA* piezoelectric energy harvester and phase transformation induced by temperature.

The temperature variation is shown in Fig. 5.26(a) while (b) express ω_N and β temperature dependency according to polynomial model in Eq. (52).

Fig. 5.26(b) can be useful in indicating the temperature to be applied for each driven frequency condition between the mentioned interval and obtaining maximum displacements and output power responses. It also correlates with the estimated martensite volume fraction associated with temperature.

The harvester performance at stationary forcing frequency and in the steady-state condition is investigated in the next subsection. Adaptability characteristics are also explored for *SMA* low and high-temperature conditions.

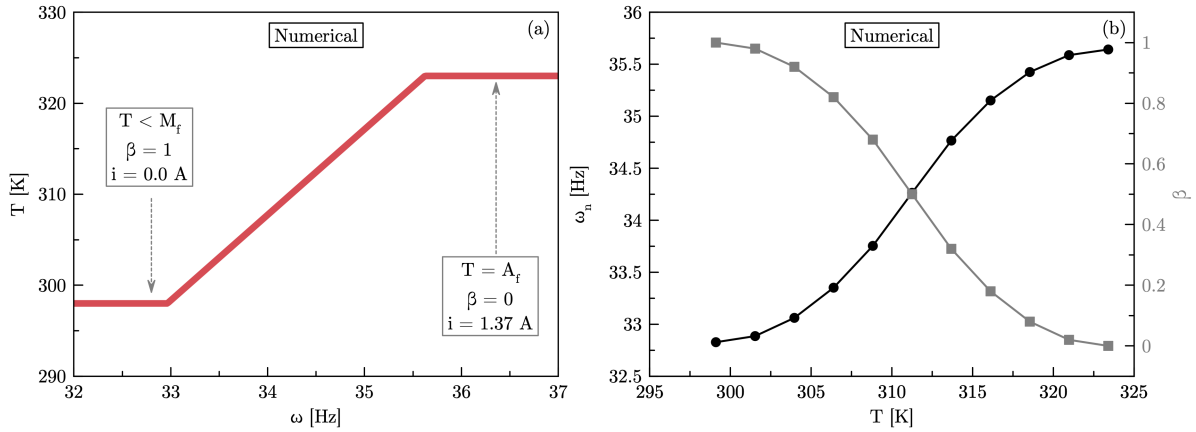


Fig. 5.26: Numerical simulation varying ω and T. (a) Applied temperature variation. (b) Harvester natural frequency and *SMA* martensite volume fraction temperature dependency.

5.2.2 Stationary Forcing Frequency Response

In order to evaluate the different behaviors related to each resonant condition, steady-state responses are now of concern for the low and high-temperature resonant conditions. Fig. 5.27 (a) presents force-displacement curves and (b) phase spaces for each temperature, showing the stiffness changes and the different amplitudes for each case. Note that numerical, analytical, and experimental approaches are presented, showing a good agreement. Numerical maximum displacements present a range of 3.11 mm (from 8.68 to 11.81 mm) while experimental maximum displacements present a range of 3.04 mm (from 9.8 to 12.84 mm). It means an increase of 26.5% for the numerical case while 23.6% for the experimental when the martensite helical spring is heated.

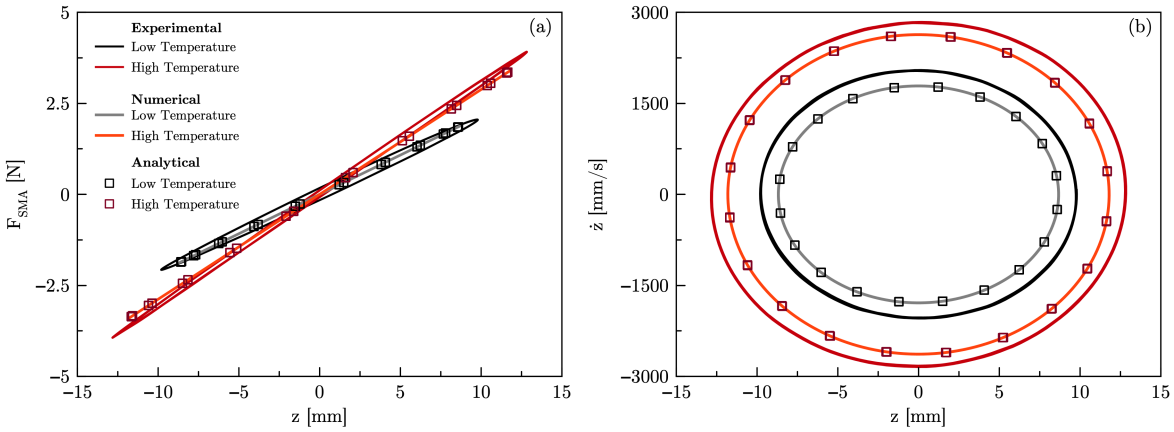


Fig. 5.27: Energy harvester steady state response comparing low and high temperature resonant stationary conditions. (a) Force-displacement curve. (b) Phase space.

Fig. 5.28 shows details of the force-displacement curve employed to assess the stiffness variation of the *SMA* helical spring for low and high-temperature conditions. Numerical simulations, Fig. 5.28 (a), show only a stiffness variation since the *SMA* element behaves in the linear elastic regime of martensite (low temperature) and austenite (high temperature). Experimentally, Fig. 5.28 (b), it is observed, that small hysteresis is responsible for an additional dissipation with the temperature increase. This hysteretic behavior alters the dissipation and consequently, the maximum amplitude of the system response.

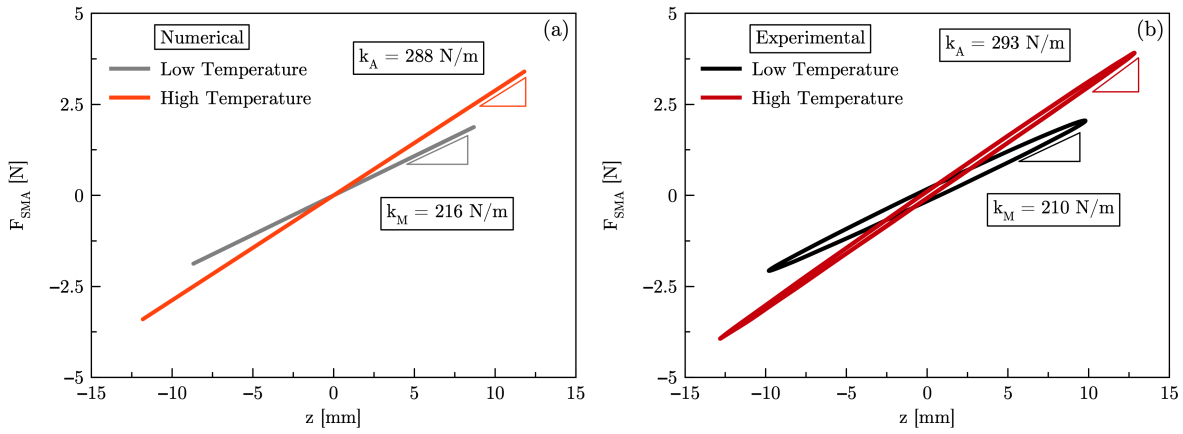


Fig. 5.28: Energy harvester force-displacement curves comparing low and high temperature resonant stationary conditions. (a) Numerical simulations. (b) Experimental data.

During the stationary forcing frequency experimental tests, the maximum values of displacement (z), F_{SMA} and the area inside curves in $F_{SMA} \times z$ diagram were registered for different base amplitude ratios, A_b/A_b^{max}, where $A_b^{max} = 9.81$ m/s^2. Once the linear elastic range for both martensite and austenite phases is considered, the value of maximum F_{SMA} divided by the maximum relative displacement, z, gives the angular coefficient associated with an instantaneous stiffness (k_{SMA}^{med}). In parallel, the internal area of $F_{SMA} \times z$ diagram is associated with the *SMA* viscous dissipation. Fig. 5.29 exposes these values when the system is operating in a steady state response.

In Fig. 5.29(a), it is possible to note a small increase in *SMA* stiffness followed by a significant decrease for low and high temperature conditions when the base amplitude reaches $A_b = A_b^{max}$. This phenomena can be attributed to air convection and heat losses that increases when the motion vibration increases. In addition, Fig. 5.28(b) shows that, in this experiment, the *SMA* dissipation energy is higher for 0.0 A condition than for 2.5 A when $A_b = 9.81$ m/s^2. This enhance the fact for $c_A < c_M$.

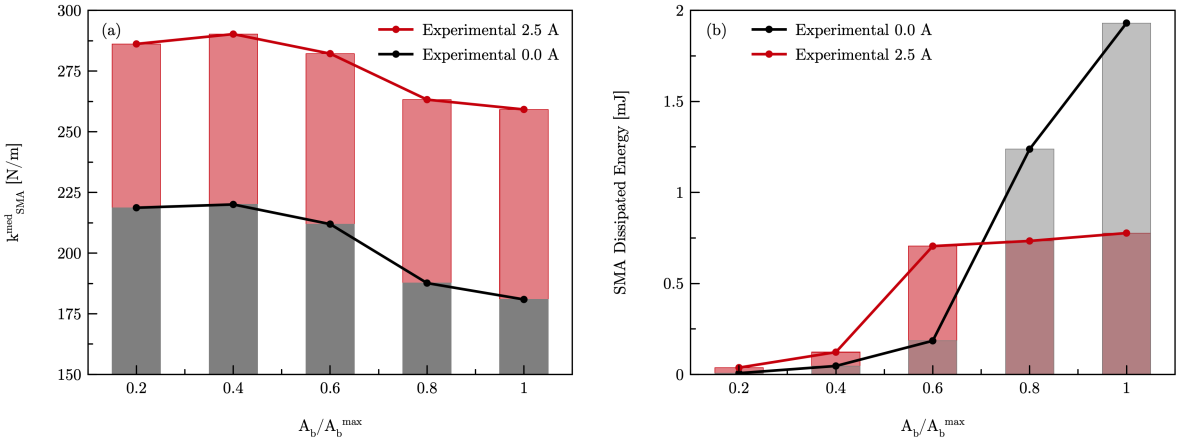


Fig. 5.29: Force-displacement analysis for low and high temperature resonant stationary conditions. (a) Mean stiffness. (b) Dissipated energy.

Fig. 5.30 shows steady state time history of the output power for each specific resonance stationary excitation frequency. Fig. 5.30 (a) presents numerical results while Fig. 5.30 (b) presents experimental results. Both cases have the output power trend with maximum values that are in agreement with the values expected from Fig. 5.20 and Fig. 5.22.

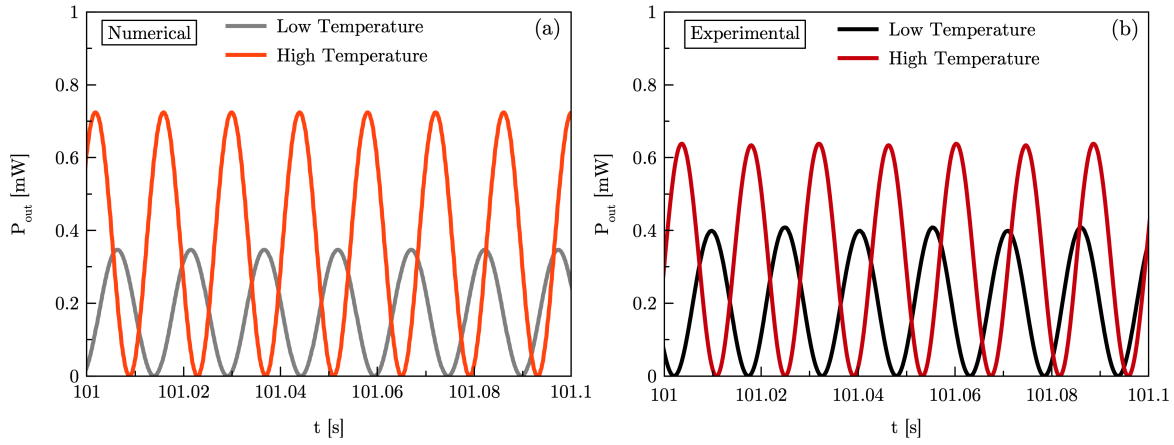


Fig. 5.30: Energy harvester output power time history for a fixed forcing frequency, comparing low and high temperature responses. (a) Numerical output power ($\omega = 32.96$ Hz for low temperature and $\omega = 35.61$ Hz for high temperature). (b) Experimental output power ($\omega = 32.86$ Hz for low temperature and $\omega = 35.35$ Hz for high temperature).

The adaptive characteristic of the energy harvesting system is now of concern showing an emblematic numerical simulation associated with the synergistic use of smart materials. Consider a situation where the forcing frequency is 35.61 Hz at room temperature, where the system is at the martensite phase. Under this condition, the system presents a small amplitude response, associated with low output power. In order to alter this condition, the temperature is increased

by applying an electric current of 1.37 A, which promotes a phase transformation from martensite to austenite, causing the *SMA* stiffness change. Under the new condition, the system's high-temperature natural frequency matches the excitation frequency, promoting higher levels of amplitude and, consequently, higher levels of converted output power. Fig. 5.31 presents numerical simulations of this case while Fig. 5.32 presents details about the steady-state system response for each one of the regions presented. This change represents an increase from 1.34 to 13.02 mm (around 10 times) on system maximum amplitude and from 0.008 to 0.72 mW (around 100 times) on the maximum output power. It should be pointed out that this test is a proof of concept simulation where the energy cost is not of concern. A proper system design should be analyzed in order to evaluate the net energy but, it is possible to imagine the use of some available external source to provide the necessary energy.

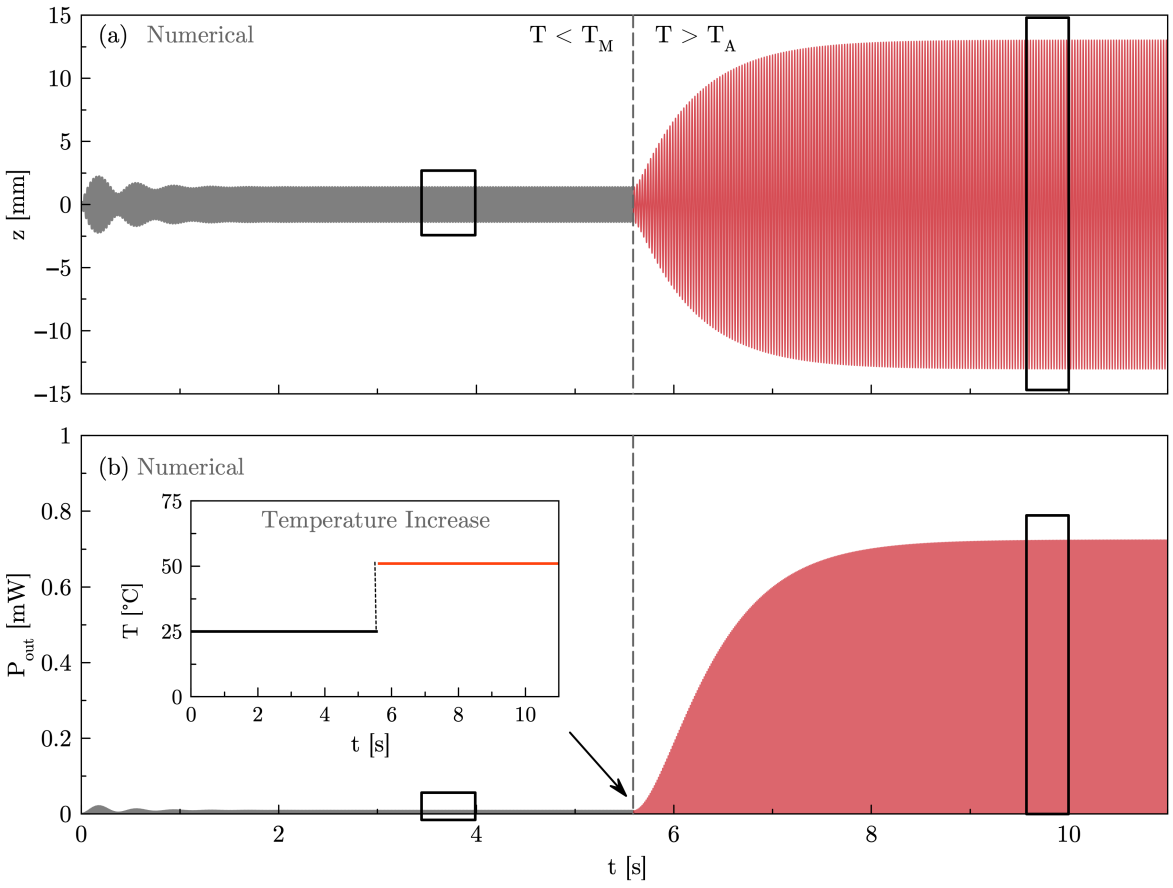


Fig. 5.31: Time evolution of the energy harvester response considering the temperature increase and a forcing frequency of 35.61 Hz. (a) Displacement. (b) Output Power.

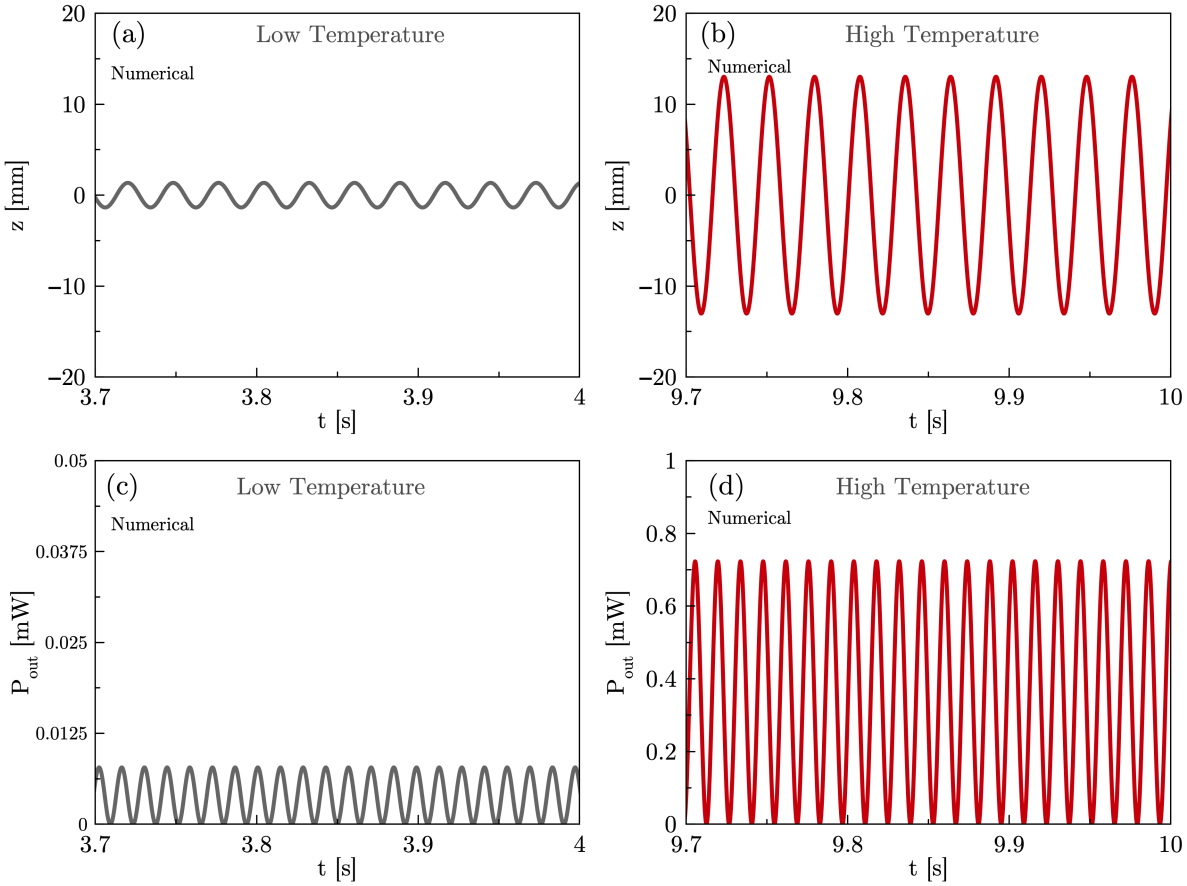


Fig. 5.32: Details about the energy harvester steady state responses for $\omega = 35.61$ Hz and different temperatures. (a) Low temperature displacement: $T < T_M$. (b) High temperature displacement: $T > T_A$. (c) Low temperature output power: $T < T_M$. (d) High temperature output power: $T > T_A$.

Fig. 5.33 shows the experimental situation for the *SMA* martensite helical spring at low temperature, 0.0 A, and base frequency, $\omega = 35$ Hz, where the system performs in low amplitude condition. Fig. 5.30(b) shows the condition of high amplitude associated with 2.5 A at this base frequency. The amplitude increase is attributed to the *SMA* martensite helical spring temperature increase which changes its mechanical stiffness and system natural frequency matches with external base vibration frequency. Consequently, the cantilever beam and the piezoelectric element are submitted to higher levels of strain, and the output power increase. In this sense, the control of *SMA* temperature can be used to give adaptability characteristics to the SMA-piezoelectric energy harvester.

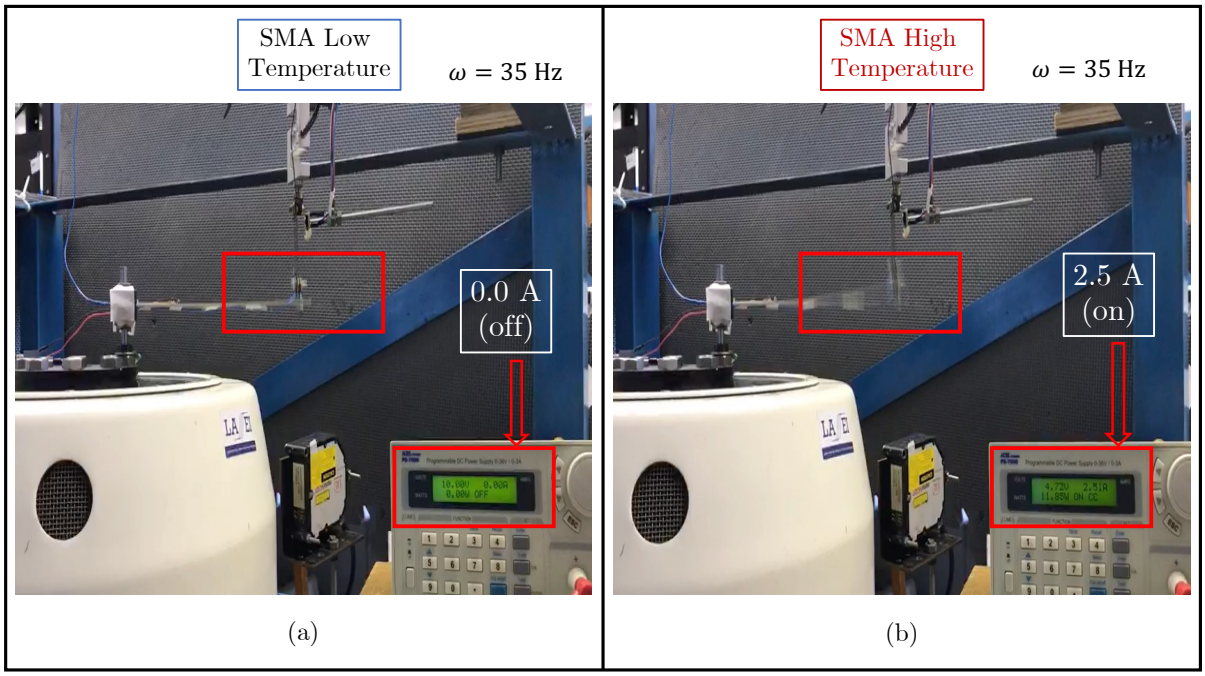


Fig. 5.33: SMA-piezoelectric energy harvester response considering the temperature increase and a forcing frequency of 35 Hz. (a) Low temperature (0.0 A). (b) High temperature (2.5 A).

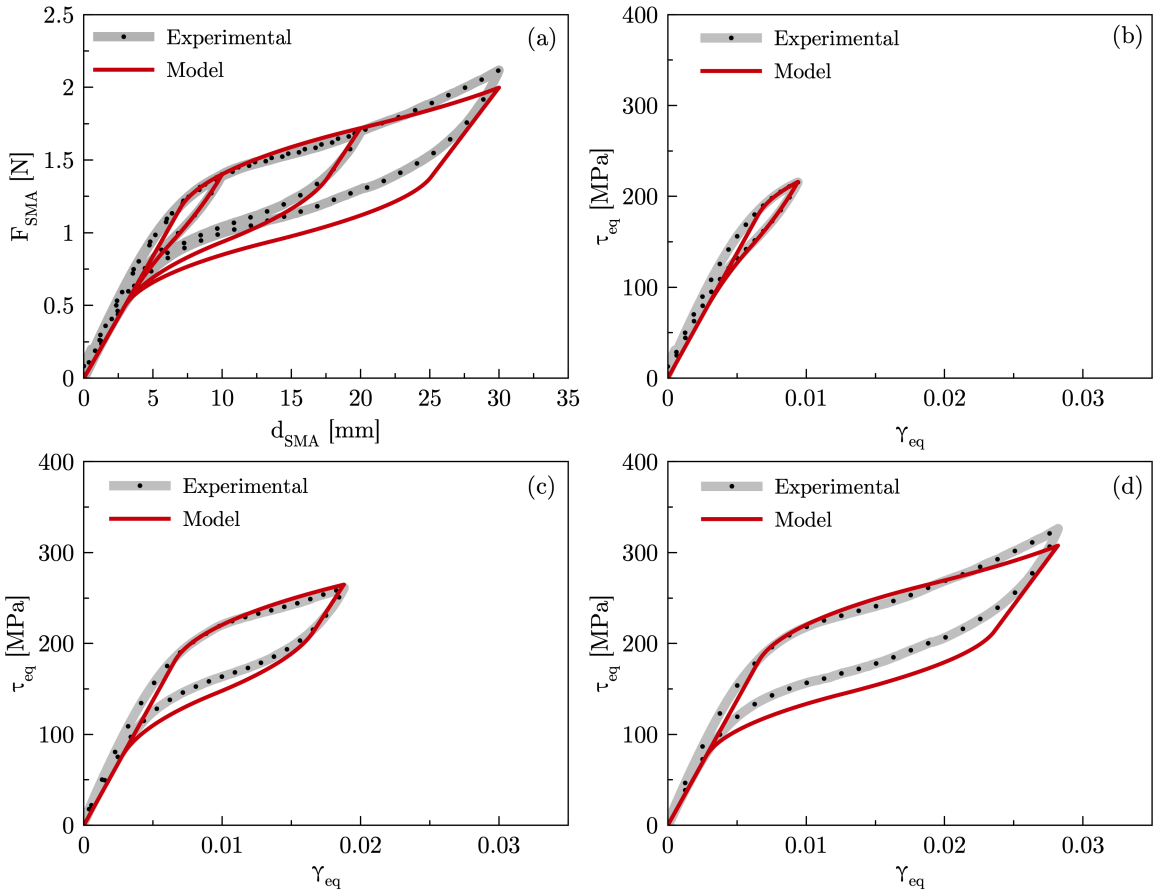
5.3 Piezoelectric Energy Harvester with SMA Austenite Helical Spring

This section investigates the system response with the *SMA* austenite helical spring connected to the harvester. Once the spring presents the austenite phase in ambient temperature, phase transformation occurs, initially, by an initial load (preload) and further also for base vibration motion. Analyses consider quasi-static results for helical spring model validation (referred in subsection 4.2.3) and dynamical results of SMA-piezoelectric energy harvester with phase transformation induced by mechanical load.

5.3.1 Quasi Static Analysis

The polynomial model is employed with the helical spring model and quasi-static simulations performed considering, experimental characterization, in section 4.1.1.3. Curves are built for the pseudoelastic helical spring submitted to axial quasi-static load and unload according to Eq. (94) and Eq. (95).

Fig. 5.34 compare the experimental curves with the polynomial model predictions. Fig. 5.34(a) shows Force × Displacement diagram while Fig. 5.34(b)-(d) deals with attributed equivalent Stress × Strain diagrams. For instance, results show that the model is able to represent the austenite helical spring mechanical behavior in described conditions.



. (3) ϵ_{max} =0.03.

Fig. 5.34: Austenite *SMA* helical spring polynomial model and experimental quasi static comparison. (a) Force × Displacement diagram for different maximum load amplitude. Associated equivalent Stress × Strain diagram for: (a) ϵ_{max} =0.01. (b) ϵ_{max} =0.02

The analysis starts by selecting a preload (PL value according to Fig. 5.34. The choice of PL = 1.5 N as a maximum preload to evaluate considers a safe condition to *SMA* austenite helical spring operate even for high levels of vibration base amplitude and do not exceed the quasi-static tested load levels. It is important to point out that shape memory alloys present functional and structural fatigue which strongly depends on the number and amplitude of phase transformation cycles. Intermediate values of PL = 0.5 N and 1.5 N are also in consideration.

For a harvesting investigation, the amount of energy required to promote a change in system configuration is a crucial parameter. In this way, Fig. 5.35(a) and (b) simulate and evaluates the work required in a quasi-static condition to promote forward and reverse phase transformation, respectively, until the load reaches PL = 1.5 N. The area under curve reveals that 10.83 mJ is necessary to change the *SMA* helical spring from null stress condition to PL = 1.5 N while just 9.5 mJ would be required to return to the initial state and restart the process. A total of

20.33 mJ is involved in the quasi-static load and unload cycle for $PL = 1.5$ N and 1.33 mJ is dissipated by the phase transformation hysteresis loop. The points attributed to $PL = 0.5$ and 1.0 N are also highlighted and indicate no martensite phase transformation for those levels of preload.

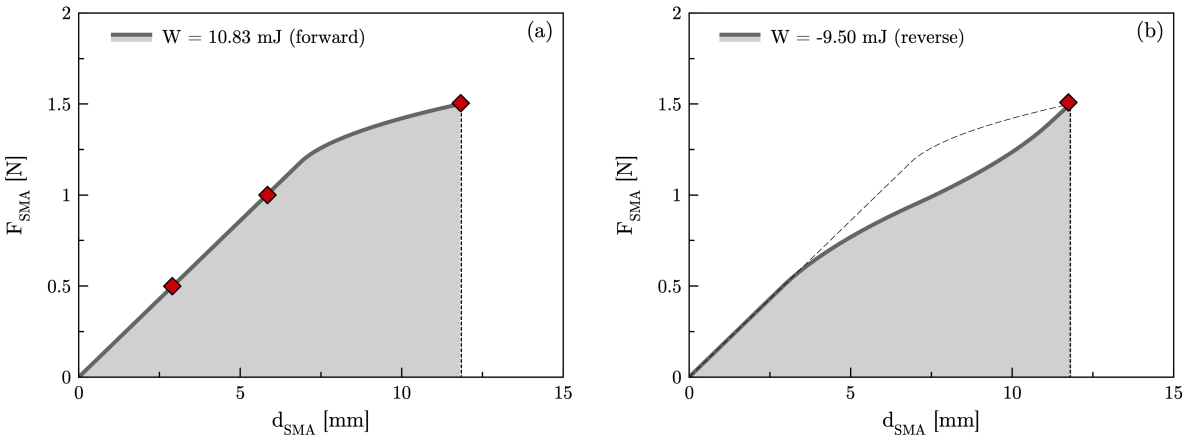


Fig. 5.35: Expended work estimation via Force × Displacement diagram for $PL = 1.5$ N. (a) Forward phase transformation (b) Reverse phase transformation.

Considering that the unloading work is done by the helical spring, Fig. 5.36 presents a diagram containing the total work need to load the austenite helical spring until the maximum preload of $PL = 0.5$, 1.0, and 1.5 N.

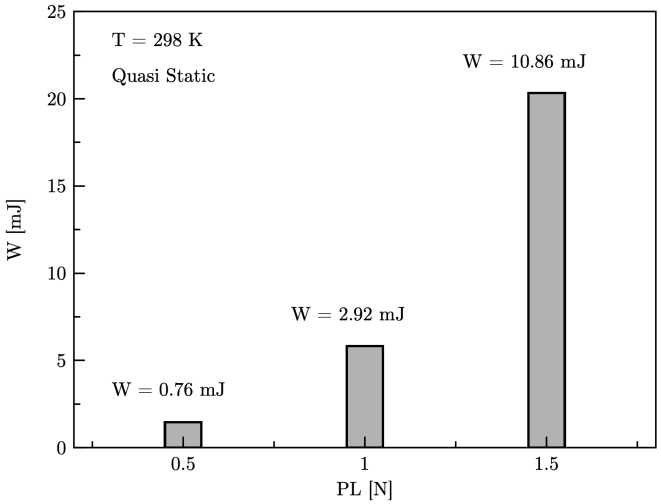


Fig. 5.36: Expended work estimation attributed to preload values in concern.

Fig. 5.37 show results assuming different conditions of temperature for the same maximum displacement attributed to $PL = 1.5$ N found in Fig. 5.35 (12 mm). Fig. 5.37(a) shows Force × Displacement diagram and the influence of temperature in critical stresses and damping capacity

(hysteresis loop). Fig. 5.37(b) and (c) shows equivalent stress and martensite volume fraction, respectively.

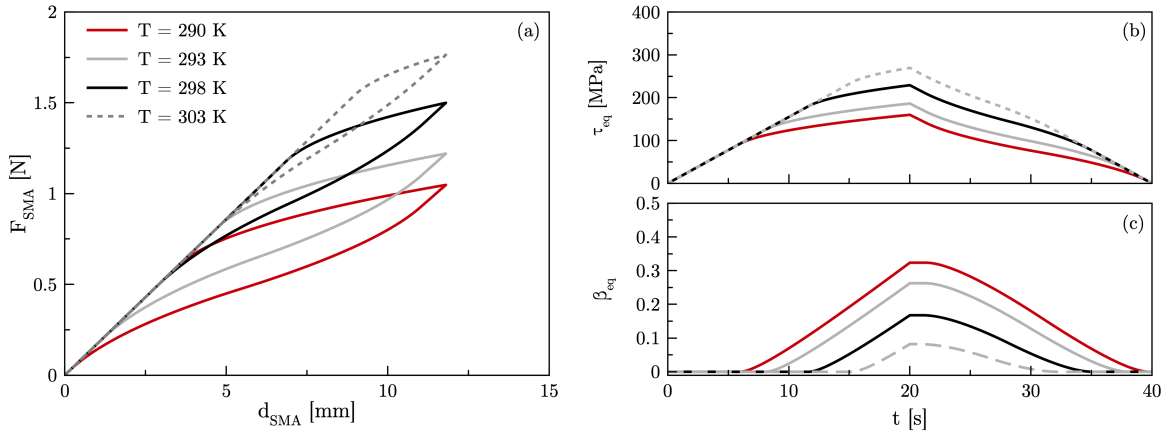


Fig. 5.37: *SMA* different temperature conditions. (a) Force × Displacement. (b) Equivalent shear stress. (c) Equivalent martensite volume fraction time evolution.

Finally, Fig. 5.38 illustrates a condition of load in order to evaluate the model performance to represent internal sub loops. Fig. 5.38(a) deals with Force × Displacement diagram at constant temperature. Fig. 5.38(b) present the *SMA* austenite helical spring prescribed shear strain while Fig. 5.38(c) shows equivalent shear stress. Fig. 5.38(d) shows martensite volume fraction time variation during the loading process.

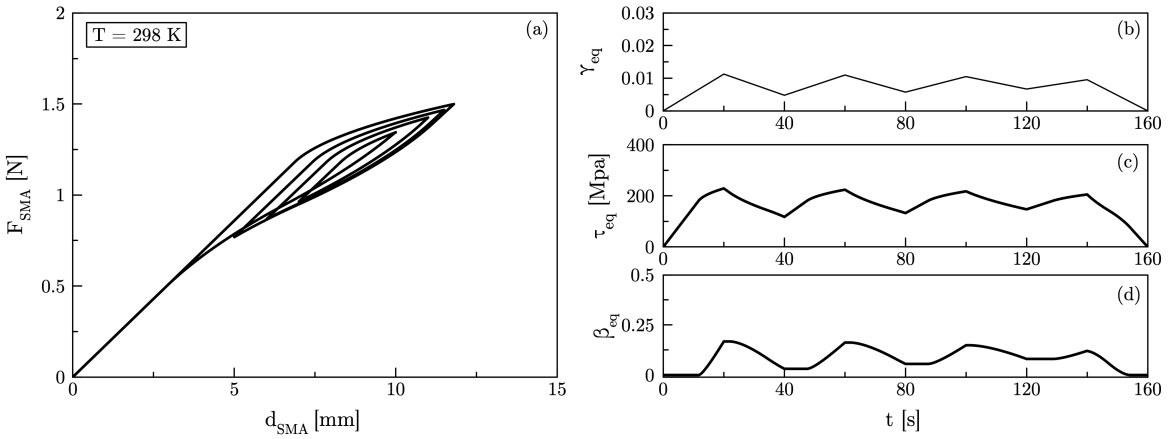


Fig. 5.38: Incomplete *SMA* phase transformation and subloops. (a) *SMA* helical spring axial Force × Displacement. (b) Prescribed shear strain. Equivalent shear stress. (d) Equivalent martensite volume fraction time evolution.

Next subsection investigates the *SMA* helical spring under dynamical load and the energy harvesting properties of a piezoelectric energy harvester connected to the *SMA* austenite helical spring. The phase transformation induced by the mechanical load is investigated for different

levels of preloads and base vibration amplitude.

5.3.2 Dynamical Analysis

This section investigates the influence of *SMA* phase transformation induced by the mechanical load in order to increase a piezoelectric energy harvester operational range. Phase transformation induced by the mechanical load can be promoted by preload (quasi-static) and also by the load provided by base vibration motion. The constitutive model presented in subsection 4.2.3 is employed for dynamical analyses. Numerical simulations are performed employing the fourth-order Runge-Kutta method. Convergence analysis is performed by defining a time step $dt = \Gamma \times 10^{-4}$, where Γ represents the forcing frequency period.

The influence of *SMA* preload in system behavior can be first evaluated in a condition where base vibration is not able to promote significant phase transformation. So, martensite phase transformation remains basically restricted to the quasi-static preloads. Fig. 5.39 shows *SMA* piezoelectric energy harvester frequency response where curves are built varying forcing frequency in a forward direction. The initial conditions are null at the beginning of the simulation. The base vibration amplitude (A_b) is set as 10 m/s^2 and different values of preload are PL = 0, 0.5, 1 and 1.5 N. Also, a case considering no phase transformation is evaluated. It represents a linear elastic traditional piezoelectric harvester where *SMA* austenite helical spring assumes constant Young's modulus ($E = E_A$) and no preload is applied.

Maximum relative displacement, output power, input power, and efficiency frequency responses are shown in Fig. 5.39(a), (b), (c), and (d), respectively, and indicate that the preload is able to alter *SMA* helical spring stiffness and as a consequence, shifting the resonance peak. Fig. 5.39(e) and (f) show maximum equivalent shear stress and martensite volume fraction in spring wire cross section. Note that the martensite volume fraction is not significantly altered by the dynamical load.

The diagrams in Fig. 5.39 show a dynamical jump for the case of PL = 1.0 N. According to Fig. 5.39(b) and (c), the output power and efficiency curves distribution shows an improvement in energy conversion for the case of PL = 1 N and PL = 1.5. Those conditions show a region between 26 to 28 Hz where the harvester can operate with more output power and efficiency than the other conditions simulated for A_b = 10 m/s^2.

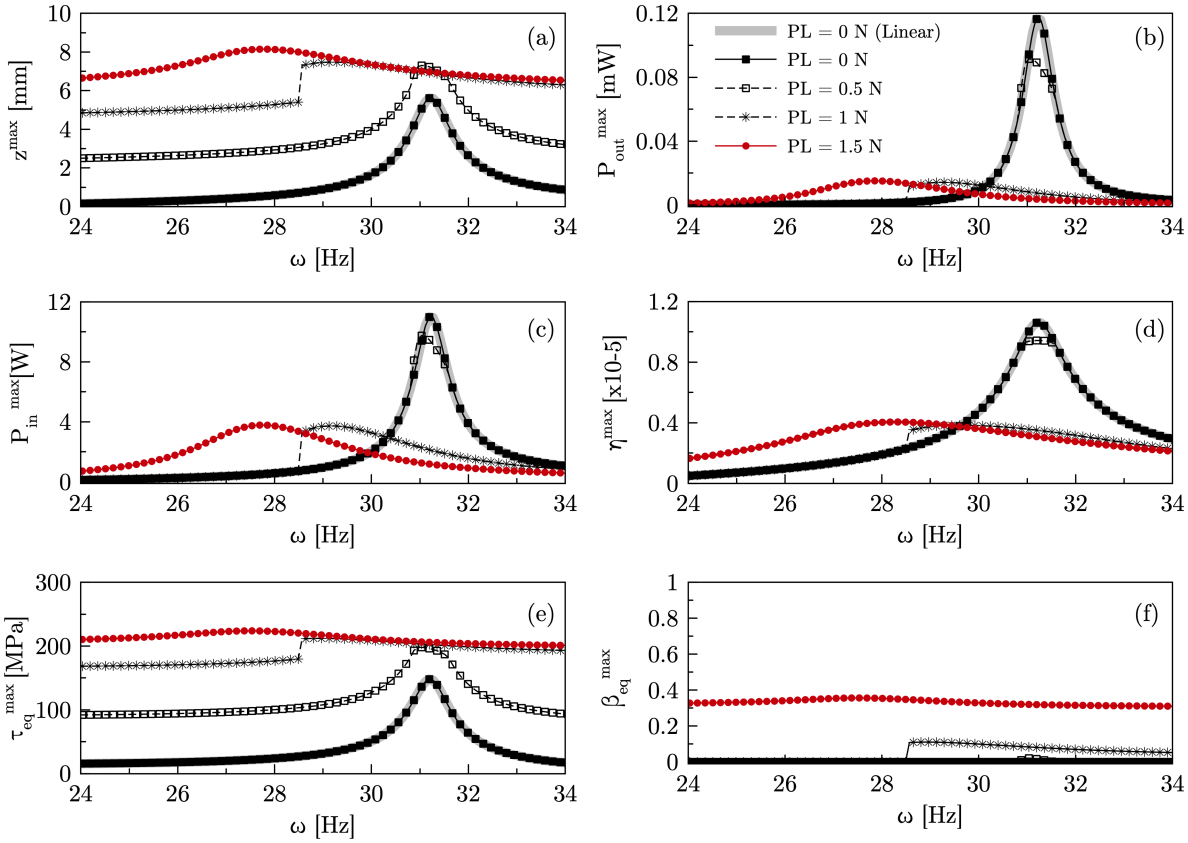


Fig. 5.39: Maximum values in frequency response analysis for $A_b = 10m/s^2$. (a) Relative displacement. (b) Output power. (c) Input mechanical power. (d) Efficiency. (e) Equivalent *SMA* shear stress. (f) Equivalent *SMA* martensite volume fraction.

Fig. 5.40(a) shows output power frequency response in detail. For the case of no preload (PL = 0 N), the energy harvested matches the linear case when $A_b = 10m/s^2$. The curve attributed to PL = 1.5 N indicates a shift $\Delta_f = 3.34$ Hz (31.19 - 27.85) in resonance peak when compared to $PL = 0$ N and the linear case. It represents a difference of 10.7% from the initial natural frequency value (31.19 Hz).

Output power is also investigated by observing system performance at a stationary forcing frequency for $\omega = 27.85$ Hz attributed to the resonance condition for $PL = 1.5$ N. Fig. 5.40 (b) compare the linear case and the case of $PL = 1.5$ N and shows a total amount of $\Delta_{power} = 0.014$ mW indicating an increase around 1540% for the mentioned conditions.

From the analysis shown in Fig. 5.35, the total amount of energy required to change *SMA* austenite helical spring from $PL = 0$ N to $PL = 1.5$ N is 10.86 mJ. So, it suggests, for the mentioned conditions, that the harvester should work for 722 seconds (or 12.02 minutes) to compensate for the quasi-static change in *SMA* austenite helical spring load.

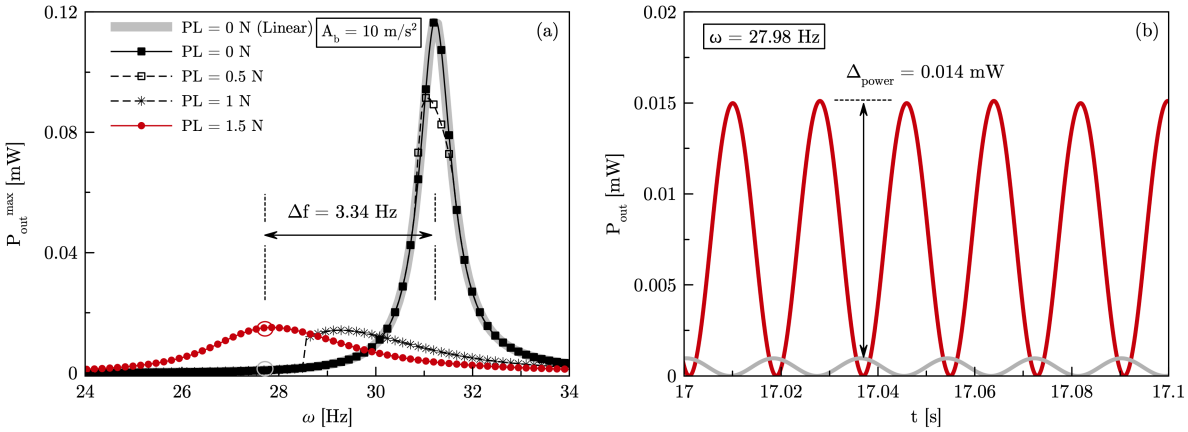


Fig. 5.40: (a) Maximum output power frequency response analysis for $A_b = 10m/s^2$. (b) Output power comparison in steady state response for stationary forcing frequency.

The investigation proceeds by the increase of the base vibration amplitude with the aim to promote phase transformation through base vibration combined with preload. Fig. 5.41 show output power frequency response for $A_b = 30$ m/s^2 for the selected preload values. Note that the increase from 10 to 30 m/s^2 in base vibration amplitude also promotes a shift in resonance peak in addition to the occurrence of the quasi-static load. It can be attributed to larger amount of martensite volume fraction present in helical spring induced by vibration load (see Fig. 5.40(f) and Fig. 5.41(f)).

Fig. 5.41(b) and (d) show a region between 25 to 31 Hz where the change in *SMA* austenite helical spring mechanical properties is able to increase the total output power and efficiency. Dynamical jumps are observed for the cases of $PL = 0$ and 0.5 N and the change in *SMA* quasi-static load promotes a significant increase in the harvester operational range. A significant amount of martensite volume fraction is obtained in the resonance region now for A_b =30 m/s^2.

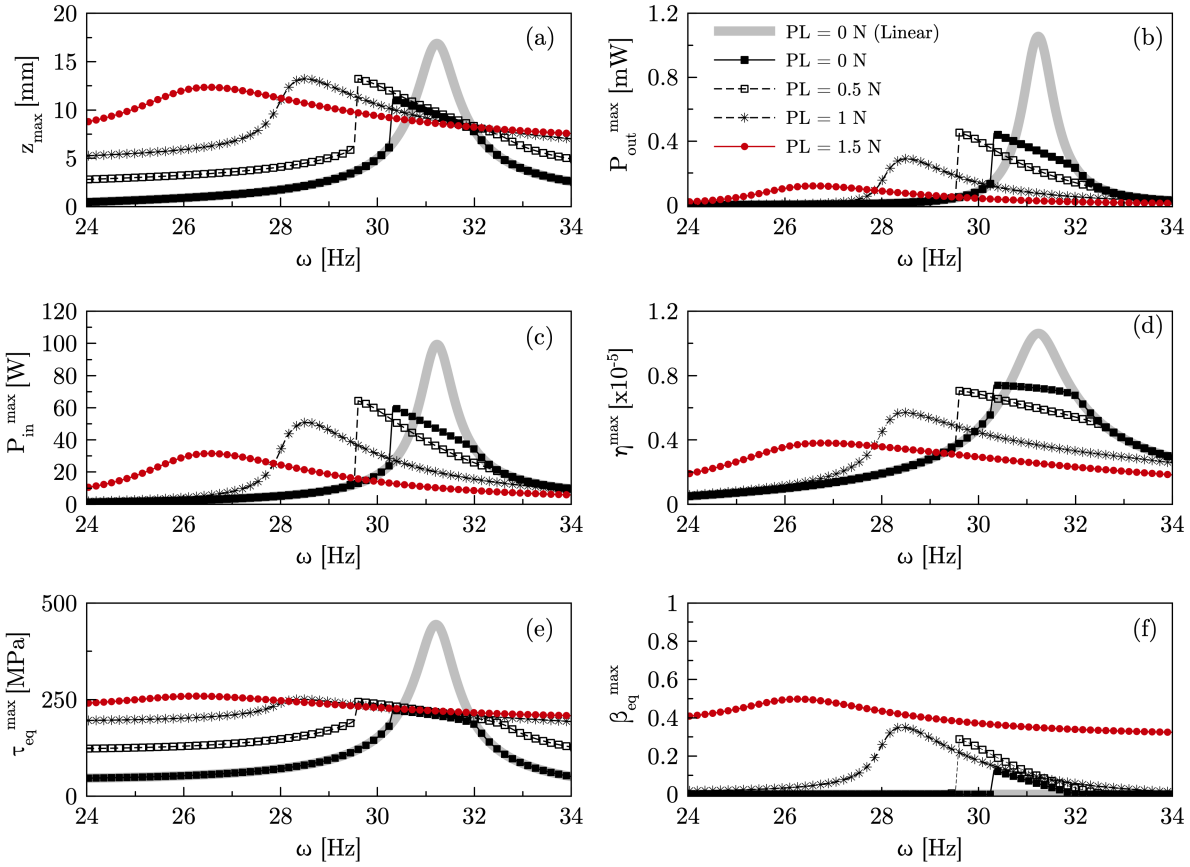


Fig. 5.41: Maximum values in frequency response analysis for $A_b = 30$ m/s^2. (a) Relative displacement. (b) Output power. (c) Input mechanical power. (d) Efficiency. (e) Equivalent *SMA* shear stress. (f) Equivalent *SMA* martensite volume fraction.

Following the same procedure as in Fig. 5.40, the system operational range is evaluated by observing the output power frequency response. Fig. 5.42(a) shows maximum output power for $A_b = 30$ m/s^2. The difference in resonance peak is also highlighted enhancing an ability to shift the resonance frequency $\Delta_f = 4.62$ (31.19 - 26.57) Hz. This value represents an increase of 14.81% in relation to the linear case natural frequency. Fig. 5.40(b) shows a comparative condition of steady state response for $PL = 1.5$ N and and the linear case when $\omega = 26.57$ Hz. It indicates a difference of $\Delta_{power} = 0.11$ mW between both conditions which means an increase near 3210%.

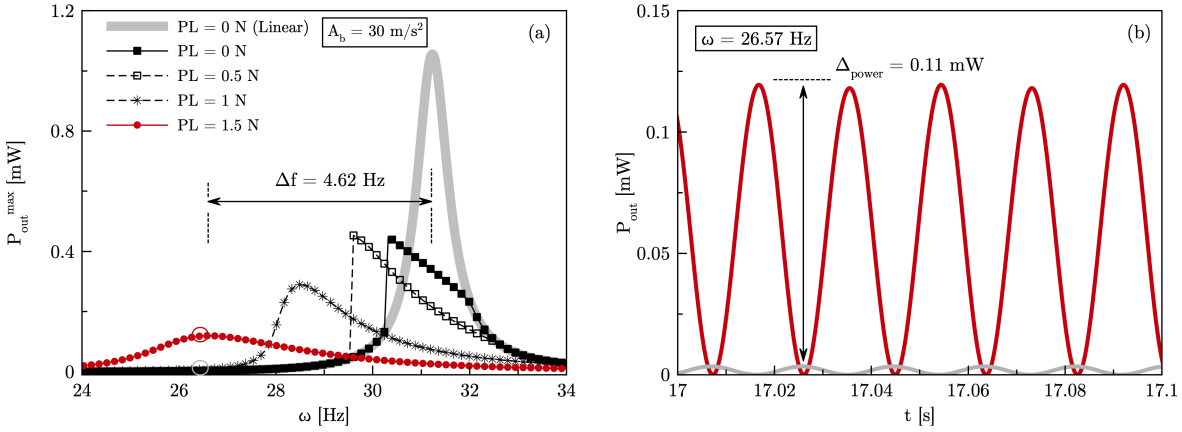


Fig. 5.42: Output power analysis. (a) Maximum output power frequency response for $A_b = 30$ m/s^2. (b) Output power comparison in steady state response for stationary forcing frequency $\omega = 26.67$ Hz.

In this way, considering the analysis shown in Fig. 5.35, it is possible to state that, for mentioned conditions, the harvester system needs to work 90.5 seconds (or 1.5 minutes) to compensate for the change in *SMA* austenite helical spring quasi-static load for $A_b = 30$ m/s^2.

Fig. 5.43 present an investigation of stationary forcing frequency for $\omega = 26.57$ Hz attributed to resonance peak for $PL = 1.5$ N and $A_b = 30$ m/s^2. Fig. 5.43(a) shows axial Force $\times$ Displacement diagram for *SMA* helical spring while Fig. 5.43(b) shows equivalent shear stress in *SMA* helical spring wire cross-section time evolution. The steady state response is highlighted in red. Fig. 5.43(c) deals with equivalent martensite volume fraction time evolution. The preload promotes an initial phase transformation and, in addition, base vibration motion promotes an oscillatory phase transformation. The damping capacity is considerably altered due to internal area in hysteresis loop.

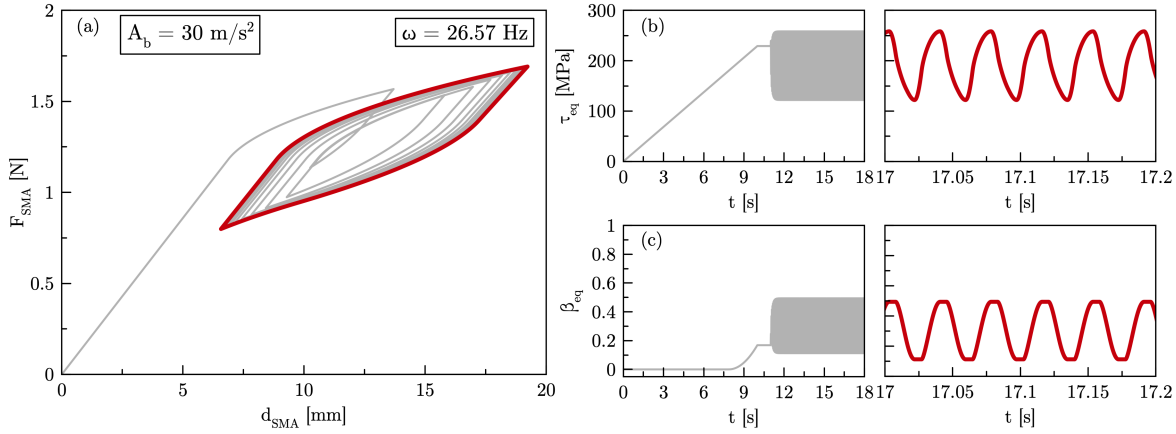


Fig. 5.43: Stationary forcing frequency analysis. (a) *SMA* spring axial Force $\times$ displacement. (b) Equivalent shear Stress $\times$ Strain time evolution. (c) Equivalent martensite volume fraction time evolution.

The body mass relative displacement is represented in Fig. 5.44(a) that deals with phase space diagram while Fig. 5.44(b) and (c) shows relative displacement during preload, transient and steady state regimes. Again, the steady state response is rendered in red. It is possible to note how the dynamical load provided by base vibration is able to influence equilibrium conditions by *SMA* phase transformation and changes in mechanical properties.

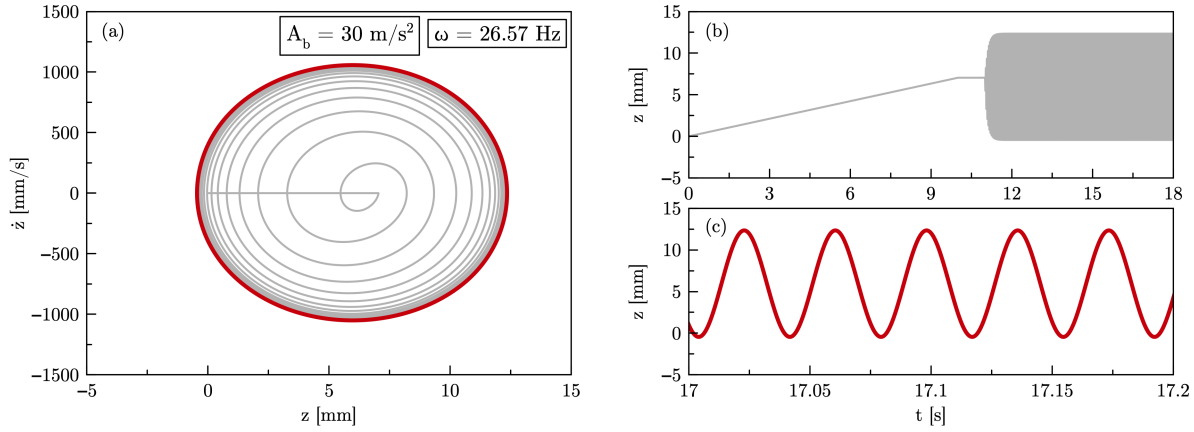


Fig. 5.44: Stationary forcing frequency analysis. (a) Phase space diagram. (b) Relative displacement time evolution. (c) Relative displacement steady state response.

Fig. 5.45 deals with an intermediate case of $PL = 0.5$ N which has presented the maximum output power for conditions simulated in this section with the *SMA* helical spring. Fig. 5.45(a) compares the output power frequency response with the linear case for $A_b = 30$ m/s^2 and it is possible to measure a $\Delta_f = 1.59$ Hz. Fig. 5.45(b)-(d) deals with Force $\times$ Displacement, phase space and output power for stationary forcing frequency $\omega = 29.6$ Hz, respectively, while Fig. 5.45(e)-(g) for $\omega = 29.4$ Hz.

The result in Fig. 5.45(a) indicates a dynamical jump and the sensibility of the system in the forcing frequency parameter at this region. Between $\omega = 29.4$ and $\omega = 29.6$ Hz, an increase around 100 times (0.453 - 0.00426 mW) is observed for the output power at steady state response. By the analysis of Fig. 5.45(b) and Fig. 5.45(e) it is possible to note that even with a higher area of the hysteresis loop, the system performs a higher amplitude resulting in a high level of energy converted.

Note that the work required to establish the helical spring at $PL = 0.5$ N is lower than to $PL = 1.5$ N and the total amount of power converted is even higher than presented in Fig. 5.42. It suggests a shorter time needed to compensate for the shift in the resonant frequency.

In addition, considering an extreme condition, temperature effects could be used to permit alter-

ing the *SMA* austenite helical spring critical phase transformations stresses (refer to Fig. 5.37) and make the harvester operate in a linear elastic range.

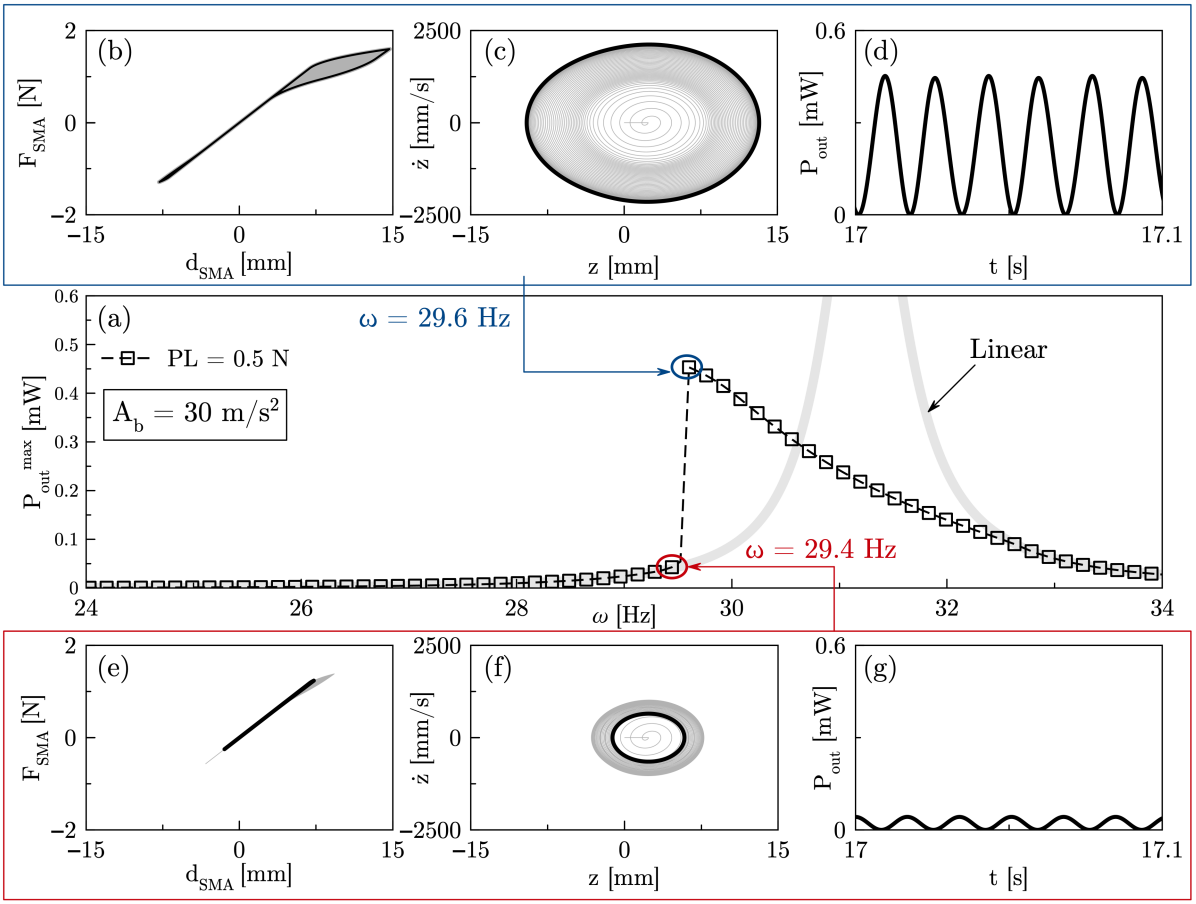


Fig. 5.45: Analysis of $PL = 0.5$ N. (a) Output power frequency response for $A_b = 30$ m/s^2. For stationary forcing frequency and $\omega = 29.6$ Hz: (b) Force × Displacement, (c) phase space and (d) output power. For $\omega = 29.4$ Hz, (e) Force × Displacement, (f) phase space and (g) output power.

Fig. 5.46 establishes the maximum output power for each value for preload and base vibration in Fig. 5.40 and Fig. 5.42.

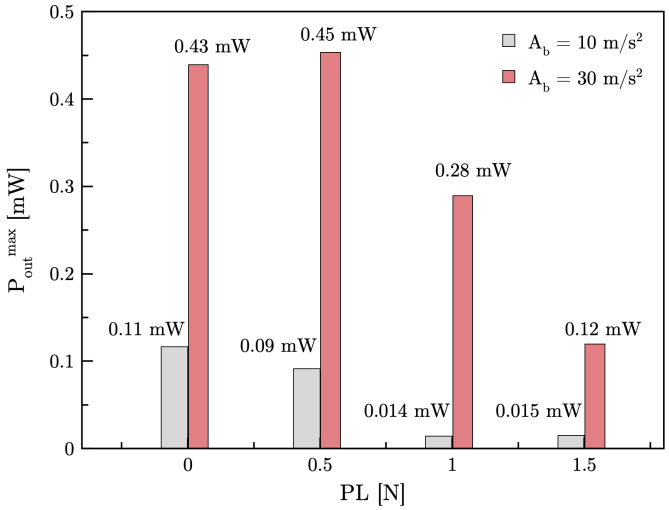


Fig. 5.46: Maximum output power diagram for preloads and base vibration amplitudes.

Finally, Fig. 5.47 present a comparative diagram for the time required to compensate for the quasi-static work in *SMA* austenite helical spring in situations where preload is applied. Note that the condition of $PL = 0.5$ N for $A_b = 10$ m/s^2 makes no sense accord to Fig. 5.40, once it decrease the maximum output power and do not increase the operation range.

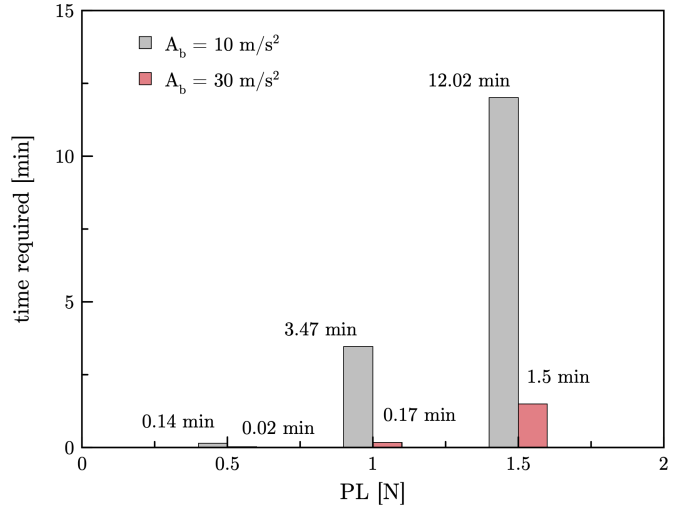


Fig. 5.47: Required time to compensate static load condition in *SMA* austenite helical spring.

Adaptive characteristic of phase transformation induced by the mechanical load in *SMA* energy harvesting system can be widely explored in terms of increasing the operational range and also the power converted. The results enhance diverse possibilities to deal with frequency response curves by controlling the preload applied in the *SMA* element. The use of higher levels of preload would be able to increase even the operation range but needs to be carefully evaluated due to

the increase of dissipation. Also, improvements in piezoelectric and *SMA* materials properties could address a higher electromechanical coupling and increase the rate of energy converted by the same amount of load. In shape memory alloys, an alloy with a higher difference in Young's modulus of austenite and martensite could increase the stiffness change during the preload and also the shift in resonance peaks.

6 Conclusions and Future Perspective

Piezoelectric energy harvesters have experimented with an increased development over the last 20 years with significant improvements. Harvester's hybridization presents a future tendency in a way to make the best of each energy source and convert it into usable electrical power. This thesis purposes the concept to use thermomechanical energy combined with mechanical vibration by the synergistic use of piezoelectric materials and shape memory alloys for energy harvesting. Once in real situations oscillatory sources of vibration present significant variation in driven frequency and amplitude, this work proposes a methodology to increase the range where piezoelectric harvesters work close to resonance condition through *SMA* thermomechanical state control.

Shape memory alloys present micromechanical solid phase transformation between austenite and martensite phases that are able to promote variation on mechanical properties as Young's modulus and damping capacity. This thesis presented a methodology that allowed to explore, separately, phase transformation induced by mechanical load and temperature in *SMA* elements connected to a piezoelectric energy harvester. Methodology procedures were based on *SMA* thermomechanical characterization, an experimental apparatus for dynamical tests and mathematical modeling of vibration-based systems connected to a *SMA* element.

SMA thermomechanical characterization was performed considering differential scanning calorimetry tests (DSC) to determine critical phase transformations at null stress conditions. In addition, critical phase transformation stresses were determined by tensile load and unload tests at different temperature conditions. It was possible to evaluate constitutive parameters for three *SMA* commercial elements being them a wire, a helical spring presenting a martensite phase, and a second helical spring presenting an austenite phase at room temperature, respectively.

An experimental apparatus was built in order to provide transverse base vibration to a mechanical system composed of a piezoelectric sheet element (PZT-5A) coupled to an aluminum beam in a cantilever beam configuration. The *SMA* helical spring presenting the martensite phase at room temperature was connected at a cantilever's free end integrating the harvester system. *SMA* Phase transformation was induced by temperature variation via Joule's effect promoting a shift in resonance peak around 8% of the original configuration.

For mathematical modeling, a constitutive polynomial model was developed in order to represent *SMA* constitutive behavior in dynamical problems where strain is a prescribed variable. The model assumed kinetics phase transformation and presented an analytical solution for the prescribed strain. Results showed that the model was able to represent *SMA* behavior for quasi-

static load submitted to different thermomechanical conditions. Dynamical results enhance the *SMA* thermomechanical nonlinear behavior promoting in the system the ability to shift its frequency response and resonance peak according to temperature or mechanical load stimulus.

The *SMA* polynomial model was employed in the mathematical modeling of a piezoelectric energy harvester connected to a martensite helical spring where phase transformation occurred by temperature variation. Results allow to investigate the temperature influence in a *SMA* piezoelectric energy harvester and show that numerical and experimental results are in close agreement. Temperature changes cause a shift of the system resonance frequency close to 10% that can be exploited for energy harvesting purposes. An improvement of the harvester performance in frequency response around 0.3 mW (0.38 mW for numerical simulations and 0.24 mW for experimental case) due to *SMA* temperature increase of the *SMA* element was observed. The required energy to promote phase transformation by temperature increase was not of concern and these tests were considered a proof of concept. A proper design is mentioned as a further work.

Adaptive behavior is highlighted from a stationary forcing frequency case, where the temperature increase is able to promote phase transformation and, as a consequence, frequency matches the system's high-temperature natural frequency. Results show an increase of 0.71 mW (around 100 times) at maximum output power and 11.68 mm (around 10 times) for maximum displacement. In this regard, *SMA* provides a useful adaptive frequency tuning that can be desirable to deal with external source fluctuations. This general idea can extend the operational range of energy harvesting systems, increasing the frequency of broadband.

Last approach focused on *SMA* phase transformation induced by mechanical load. The SMA helical spring presenting austenite phase stable at room temperature was connected to the piezoelectric energy harvester system and submitted to quasi-static preloads in order to modify the system's overall stiffness and damping characteristic. The required energy to promote the phase transformation via mechanical load was evaluated for different preloads amplitudes. In sequence, numerical simulations were performed to evaluate the harvester at different conditions of base vibration frequency and amplitude. Results show that the polynomial model with force-stress assumptions for helical spring was able to represent the quasi-static behavior of *SMA* austenite helical spring. Moreover, numerical simulations enhanced that preload and base vibration motion are able to promote phase transformation and shift in harvester frequency response by around 15% of natural frequency. In addition, it was possible to estimate an increase of around 30 times at maximum output power in the case of a stationary forcing frequency where

preload changes in order to tune the harvester on resonance condition.

By comparing both methods used to promote the *SMA* phase transformation, temperature, and mechanical load, it was possible to conclude that the mechanical load presented itself as a better option due to the necessary energy to promote phase transformation. The heat exchange between the *SMA* helical spring and the environment was not the focus of this work as well as the use of Joule's effect to heat the spring consumes a lot of energy. The use of mechanical load seems more efficient once you give the energy to promote the change in the helical spring stress state and after that hold the surface where it is fixed. In this way, the flow of energy to promote the phase transformation is stooped, different from the Joule's effect that requires a constant energy flow to keep the spring at high temperatures, otherwise it would suffer the cooling process returning to the ambient temperature. In this sense, the configuration using the austenite helical spring and mechanical load to promote the phase transformation requires less efforts to change the harvester's parameters.

The synergistic use of shape memory alloys and piezoelectric materials is an innovative and widespread theme with wide possibilities for development. Based on analyses performed in this thesis, it was found a good capability to increase harvester operational range via *SMA* phase transformation induced by temperature and mechanical load.

For a more accurate mathematical modeling of *SMA* piezoelectric energy harvesters, the *SMA* constitutive model can progress to assume strain rate dependence to represent the loss of *SMA* smart properties in dynamical systems. Beyond that, thermomechanical coupling representation can improve by considering thermal expansion contributions and even the use of thermal and mechanical load simultaneously.

As recommendations, further works can be developed by using different nonlinear characteristics mentioned in this thesis with the objective to increase even more the harvester's operational range. The combination of piezoelectric materials, shape memory alloys and magneto tip masses is an interesting field with plenty potential for research. Also, the use of piezoelectric materials with a *SMA* stop-ends for impact systems is a promissory approach with adaptability characteristics able to reach more frequencies with considerable output power. Finally, a configuration using more degree of freedom connected to shape memory elements can be explored, and consequently, significantly intensify the nonlinear effects in the dynamical response leading to larger bandwidths.

Future improvements in harvester design shall also consider the heat exchange between *SMA* sample and environment. The harvester efficiency can significant be optimized by reducing heat

losses or using different methods for temperature variation instead of Joule's effect. Future works can explore the harvester's capacity to recharge a battery under different conditions. The development of a prototype for real engineering applications would be a superior level of the synergistic use of smart materials for energy harvesting.

References

[1] A. B. de Magalhães, dos Santos A. D., and J. F. e Cunha. *Introdução À Engenharia Mecânica - Sua Relevância Na Sociedade E Na Vida Contemporânea*. Publindústria, 2015.

[2] J. R. S. Moreira. *Energias Renováveis, Geração Distribuída e Eficiência Energetica*. LTC, 2017.

[3] V. Quaschning. *Understanding renewable energy systems*. Routledge, 2016.

[4] R. U. Ayres and E. H. Ayres. *Crossing the energy divide: moving from fossil fuel dependence to a clean-energy future*. Pearson Prentice Hall, 2009.

[5] A. Erturk and D. J. Inman. *Piezoelectric Energy Harvesting*. John Wiley - Sons, Inc, 2011.

[6] C. V. de Souza and C. de Marqui. Airfoil-based piezoelectric energy harvesting by exploiting the pseudoelastic hysteresis of shape memory alloy springs. *Journal of Intelligent Material Systems and Structures*, 24(12):125014, 2015. URL https://doi.org/10.1088%2F0964-1726%2F24%2F12%2F125014.

[7] D. Li, Y. Wu, A. da Ronch, and J. Xiang. Energy harvesting by means of flow-induced vibrations on aerospace vehicles. *Progress in Aerospace Sciences*, 86:28–62, 2016. URL https://doi.org/10.1016/j.paerosci.2016.08.001.

[8] H. Elahi, K. Munir, M. Eugeni, M. Abrar, A. Khan, A. Arshad, and P. Gaudenzi. A review on applications of piezoelectric materials in aerospace industry. *Integrated Ferroelectrics*, 211(1):25–44, 2020. URL https://doi.org/10.1080/10584587.2020.1803672.

[9] H. J. Lee, S. Sherrit, L. P. Tosi, P. Walkemeyer, and T. Colonius. Piezoelectric energy harvesting in internal fluid flow. *Sensors*, 15(10):26039–26062, 2015. URL http://dx.doi.org/10.3390/s151026039.

[10] P. Musgrave, W. Zhou, and L. Zuo. Piezoelectric energy harvesting from torsional vibration. *ASME 2015 International Design Engineering Technical Conferences*, 8(27), 2015. URL https://doi.org/10.1115/DETC2015-47574.

[11] J. Zheng, B. Dou, Z. Li, T. Wu, H. Tian, and G. Cui. Design and analysis of a while-drilling energy-harvesting device based on piezoelectric effect. *Energies*, 14(5), 2021. URL https://doi.org/10.3390/en14051266.

[12] D. Y. Park, D. J. Joe, D. H. Kim, H. Park, J. H. Han, C. K. Jeong, H. Park, J. G.

Park, B. Joung, and K. J. Lee. Self-powered real-time arterial pulse monitoring using ultrathin epidermal piezoelectric sensors. *Advanced Materials*, 29(37):1702308, 2017. URL https://doi.org/10.1002/adma.201702308.

[13] F. Gao, G. Liu, B. L. H. Chung, H. H. Chan, and W. H. Liao. Macro fiber composite-based energy harvester for human knee. *Applied Physics Letters*, 115(3):033901, 2019. URL https://doi.org/10.1063/1.5098962.

[14] C. Dagdeviren, B. D. Yang, Y. Su, P. L. Tran, P. Joe, E. Anderson, J. Xia, V. Doraiswamy, B. Dedashti, X. Feng, B. Lu, R. Poston, Z. Khalpey, R. Ghaffari, Y. Huang, J. Slepian, and J. A. Rogers. Conformal piezoelectric energy harvesting and storage from motions of the heart, lung, and diaphragm. *Proceedings of the National Academy of Sciences*, 111(5): 1927–1932, 2014. URL https://doi.org/10.1073/pnas.1317233111.

[15] F. Ali, W. Raza, X. Li, H. Gul, and K. Kim. Piezoelectric energy harvesters for biomedical applications. *Nano Energy*, 19:879–902, 2019. URL https://doi.org/10.1016/j.nanoen.2019.01.012.

[16] H. A. Sodano, G. Park, and D. J. Inaman. Estimation of electric charge output for piezoelectric energy harvesting. *Strain*, 40(2):49–58, 2004. URL https://doi.org/10.1111/j.1475-1305.2004.00120.x.

[17] H. A. Sodano, D. J. Inaman, and G. Park. Comparison of piezoelectric energy harvesting devices for recharging batteries. *Journal of Intelligent Material Systems and Structures*, 16(10):799–807, 2005. URL https://doi.org/10.1177/1045389X05056681.

[18] N. E. Du Toit, Brian L. Wardle, and S. Kim. Design considerations for mems-scale piezoelectric mechanical vibration energy harvesters. *Integrated ferroelectrics*, 71(1):121–160, 2005. URL https://doi.org/10.1080/10584580590964574.

[19] M. Kim, M. Hoegen, J. Dugundji, and B. L. Wardle. Modeling and experimental verification of proof mass effects on vibration energy harvester performance. *Smart Materials and Structures*, 91(4):45023, 2010. URL https://doi.org/10.1088/0964-1726/19/4/045023.

[20] D. J. Leo. *Engineering Analysis of Smart Materials and Structures*. John Wiley and Sons, Inc., 2007.

[21] H. Maiua. *Piezoelectric Energy Harvesting*. IntechOpen, 2016.

[22] C. B. Williams and R. B. Yates. Analysis of a micro-electric generator for microsys-

tems. *Sensor and Actuators, a Physical*, 52(1-3):8–11, 1996. URL https://doi.org/10.1016/0924-4247(96)80118-X.

[23] A. Erturk. *Electromechanical Modeling of Piezoelectric Energy Harvesters*. PhD thesis, Virginia Polytechnic Institute and State University, 2009.

[24] A. Erturk and D. J. Inman. On mechanical modeling of cantilevered piezoelectric vibration energy harvesters. *Journal of Intelligent Material Systems and Structures*, 19(11):1311–1325, 2008. URL https://doi.org/10.1177/1045389X07085639.

[25] A. Erturk and D. J. Inman. An experimentally validated bimorph cantilever model for piezoelectric energy harvesting from base excitations. *Smart Materials and Structures*, 18 (25009):25009, 2009. URL https://doi.org/10.1088/0964-1726/18/2/025009.

[26] C. V. Karadag and N. Topaloglu. A self-sufficient and frequency tunable piezoelectric vibration energy harvester. *Journal of Vibration and Acoustics*, 139(1):11013, 2017. URL https://doi.org/10.1115/1.4034775.

[27] H. F. Tiersten. *Linear Piezoelectric Plate Vibrations: Elements of the Linear Theory of Piezoelectricity and the Vibrations Piezoelectric Plates*. Springer, 2013.

[28] N. Tran, M. H. Ghayesh, and M. Arjomandi. Ambient vibration energy harvesters: A review on nonlinear techniques for performance enhancement. *International Journal of Engineering Science*, 127:162–185, 2018. URL https://doi.org/10.1016/j.ijengsci.2018.02.003.

[29] A. Adeodato, B. T. Duarte, L. L. S. Monteiro, P. M. C. L. Pacheco, and M. A. Savi. Synergistic use of piezoelectric and shape memory alloy elements for vibration-based energy harvesting. *International Journal of Mechanical Sciences*, 194:106206, 2021. URL http://www.sciencedirect.com/science/article/pii/S0020740320343113.

[30] A. Rao, A. R. Srinivasa, and J. N. Reddy. *Design of Shape Memory Alloy (SMA) Actuators*. Springer International Publishing, 2015.

[31] D. Lagoudas. *Shape Memory Alloys*. Springer, 2008.

[32] M. H. Elahinia. *Shape Memory Alloy Actuators*. Wiley, 2016.

[33] M. A. Savi. Nonlinear dynamics and chaos in shape memory alloy systems. *International Journal of Non-Linear Mechanics*, 70, 2015. URL https://doi.org/10.1016/j.ijnonlinmec.2014.06.001.

[34] L. C. Brinson. One-dimensional constitutive behavior of shape memory alloys: Thermomechanical derivation with non-constant material functions and redefined martensite internal variable. *Journal of Intelligent Material Systems and Structures*, 4(2):229–242, 1993. URL https://doi.org/10.1177/1045389X9300400213.

[35] Kathy L. *Materials in Energy Conversion, Harvesting, and Storage*. John Wiley & Sons Inc, 2014.

[36] Wikipidia, 2021. URL https://en.wikipedia.org/wiki/Three_Gorges_Dam.

[37] Wikipidia, 2021. URL https://en.wikipedia.org/wiki/Solar_Energy_Generating_Systems.

[38] Istockphoto, 2021. URL Istockphoto.com.

[39] Offshore oil extraction at brazil (p58), 2014. URL https://petrobras.com.br/fatos-e-dados/plataforma-p-58-entra-em-operacao-no-parque-das-baleias.htm.

[40] Beatriciwind, 2021. URL https://www.beatricewind.com/.

[41] The Green Age, 2021. URL https://www.thegreenage.co.uk/.

[42] Think Geoenergy, 2021. URL https://www.thinkgeoenergy.com/.

[43] Casa Abril, 2021. URL https://casa.abril.com.br/sustentabilidade/ceara-planeja-transformar-onda-do-mar-em-energia-a-partir-de-2020/.

[44] D. Infield and L. Freris. *Renewable energy in power systems*. John Wiley & Sons, 2020.

[45] IEA International Energy Agency, 2020. URL https://www.iea.org/reports/key-world-energy-statistics-2020.

[46] S. J. Zinkle and G.S. Was. Materials challenges in nuclear energy. *Acta Materialia*, 61(3):735–758, 2013. URL http://www.sciencedirect.com/science/article/pii/S1359645412007987.

[47] A. Khaligh and O. C. Onar. *Energy harvesting: solar, wind, and ocean energy conversion systems*. CRC press, 2017.

[48] S. Beeby and N. White. *Energy Harvesting for Autonomous Systems*. Artech House Series, 2010.

[49] Y. K. Tan. *Energy harvesting autonomous sensor systems: design, analysis, and practical implementation*. CRC Press, 2013.

[50] V. Leonov. *Energy harvesting for self-powered wearable devices*. Springer, 2011.

[51] S. Roundy, V. Sundararajan, E. S. Leland, J. Baker, E. Carleton, E. Reilly, E. Lai, B. Otis, J. M. Rabaey, and P. K. Wright. Improving power output for vibration-based energy scavengers. *Energy Harvesting and Conservation*, 4(1):26–36, 2005. URL https://doi.org/10.1109/MPRV.2005.14.

[52] M. Bhaskaran, S. Sriram, and K. Iniewski. *Energy Harvesting with Functional Materials and Microsystems*. CRC Press, 2013.

[53] K. Uchino. Piezoelectric energy harvesting systems—essentials to successful developments. *Energy Technology*, 6, December 2018.

[54] F. U. Khan and M. U. Qadir. State-of-the-art in vibration-based electrostatic energy harvesting. *Journal of Micromechanics and Microengineering*, 26(10):103001, 2016. URL https://doi.org/10.1088/0960-1317/26/10/103001.

[55] R. Gao and Y. Cui. Vibration-based sensor powering for manufacturing process monitoring. *Transactions of the North American Manufacturing Research Institution*, 33:335–342, 2005.

[56] S. Roundy, P. K. Wright, and J. Rabaey. A study of low level vibrations as a power source for wireless sensor nodes. *Computer Communications*, 26(11):1131–1144, 2003. URL https://doi.org/10.1016/S0140-3664(02)00248-7.

[57] K. T. Palmer and M. J. Griffin. Prevalence and pattern of occupational exposure to whole body vibration in great britain: findings from a national survey. *BMJ Journals*, 57(4): 229–236, 2000. URL http://dx.doi.org/10.1136/oem.57.4.229.

[58] G. Despesse, T. Jager, C. Jean-Jacques, J. M. Léger, A. Vassilev, S. Basrour, and B. Charlot. Fabrication and characterization of high damping electrostatic micro devices for vibration energy scavenging. *Proc. Design, Test, Integration and Packaging of MEMS and MOEMS*, pages 386–390, 2005. URL https://www.researchgate.net/publication/237840904_Fabrication_and_characterization_of_high_damping_electrostatic_micro_devices_for_vibration_energy_scavenging.

[59] P. V. Malaji and S. F. Ali. Analysis of energy harvesting from multiple pendulums with and without mechanical coupling. *The European Physical Journal Special Topics*, 224(14): 2823–2838, 2015. URL https://doi.org/10.1140/epjst/e2015-02591-7.

[60] B. Yang, C. Lee, R. K. Kotlanka, J. Xie, and S. P. Lim. A mems rotary comb mechanism

for harvesting the kinetic energy of planar vibrations. *Journal of Micromechanics and Microengineering*, 20(6):65017, 2010. URL https://doi.org/10.1088/0960-1317/20/6/065017.

[61] Miyazaki M., Tanaka H., Ono G., Nagano T., Ohkubo N., Kawahara T., and Yano K. Electric-energy generation using variable-capacitive resonator for power-free lsi: efficiency analysis and fundamental experiment. *Proceedings of the 2003 International Symposium on Low Power Electronics and Design*, page 193–198, 2003. URL https://doi.org/10.1145/871506.871555.

[62] P. Basset, D. Galayko, A. M. Paracha, F. Marty, A. Dudka, and T. Bourouina. A batch-fabricated and electret-free silicon electrostatic vibration energy harvester. *Journal of Micromechanics and Microengineering*, 19(11):115025, 2009. URL https://doi.org/10.1088/0960-1317/19/11/115025.

[63] V. P. E. Wowk. A brief tutorial on machine vibration, 2005. URL https://www.machinedyn.com/docs/machine_vibration_tutorial.pdf.

[64] C. Ge, K. Dunno, M. A. Singh, L. Yuan, and L. Lu. Development of a drone's vibration, shock, and atmospheric profiles. *Applied Sciences*, 11(11), 2021. URL https://doi.org/10.3390/app11115176.

[65] P. Böröcz. Vibration and acceleration levels of multimodal container shipping physical environment. *Packaging Technology and Science*, 32(6):269–277, 2019. URL https://doi.org/10.1002/pts.2434.

[66] A. Toprak and O. Tigli. Piezoelectric energy harvesting: State-of-the-art and challenges. *Applied Physics Reviews,*, 1(3):31104, 2014. URL https://doi.org/10.1063/1.4896166.

[67] J. Palosaari. *Energy Harvesting from walking using piezoelectric cymbal and diaphragm type structures*. ACTA University of Oulu, 2017.

[68] Google.Scholar, January 2021. URL https://scholar.google.com.br.

[69] Lens.org, May 2021. URL https://www.lens.org/.

[70] M. T. Todaro, F. Guido, L. Algieri, V. M. Mastronardi, D. Desmaële, G. Epifani, and M. De Vittorio. Biocompatible, flexible, and compliant energy harvesters based on piezoelectric thin films. *IEEE Transactions on Nanotechnology*, 17(2):220–230, 2018. URL https://doi.org/10.1109/TNANO.2017.2789300.

[71] Y. Yang, J. Yeo, and S. Priya. Harvesting energy from the counterbalancing (weaving)

movement in bicycle riding. *Sensors*, 12(8):10248–10258, 2012. URL https://doi.org/10.3390/s120810248.

[72] J. Yun, S. Patel, M. Reynolds, and G. Aboudy. A quantitative investigation of inertial power harvesting for human-powered devices. *Proceedings of the 10th international conference on Ubiquitous computing*, page 74–83, 2008. URL https://doi.org/10.1145/1409635.1409646.

[73] A. Sadat, Hongwei Q., Chuanzhao Y., J. S. Yuan, and X. Huikai. Low-power cmos wireless mems motion sensor for physiological activity monitoring. *IEEE Transactions on Circuits and Systems I: Regular Papers*, 52(12):2539–2551, 2005. URL https://doi.org/10.1109/TCSI.2005.857772.

[74] C. Alippi, G. Anastasi, M. Di Francesco, and M. Roveri. An adaptive sampling algorithm for effective energy management in wireless sensor networks with energy-hungry sensors. *IEEE Transactions on Instrumentation and Measurement*, 59(2):335–344, 2010. URL https://doi.org/10.1109/TIM.2009.2023818.

[75] D. V. Sachan, S. Imam, and M. Beg. Energy-efficient communication methods in wireless sensor networks: A critical review. *International Journal of Computer Applications*, 39: 35–48, 2012. URL https://doi.org/10.5120/4915-7484.

[76] Ndir co2 sensor, -. URL https://www.envirotech-online.com/news/air-monitoring/6/gas-sensing-solutions/the-worldrsquos-lowest-power-consumption-ndir-co2-sensor/12745.

[77] Adxl330 3-axis accelerometer, -. URL http://www.analog.com/en/prod/0,2877,ADXL330,00.html.

[78] Hih-3610-001 humidity sensor, -. URL https://br.mouser.com/ProductDetail/Honeywell/HIH-3610-001?qs=djRoAdQKA8%2FpHxL5mEaq%2Fg%3D%3D.

[79] C. Hierold, B. Clasbrummel, D. Behrend, T. Scheiter, M. Steger, K. Oppermann, H. Kapels, E. Landgraf, D. Wenzel, and D. Etzrodt. Low power integrated pressure sensor system for medical applications. *Sensors and Actuators A: Physical*, 73(1):58–67, 1999. URL https://doi.org/10.1016/S0924-4247(98)00255-6.

[80] M. Niroomand and H. Foroughi. A rotary electromagnetic microgenerator for energy harvesting from human motions. *Journal of Applied Research and Technology*, 14(4), 2016. URL https://doi.org/10.22201/icat.16656423.2016.14.4.32.

[81] J. Sauerbrey, D. Schmitt-Landsiedel, and R. Thewes. A 0.5-v 1-μw successive ap-

proximation adc. *IEEE Journal of Solid-State Circuits*, 38(7):1261–1265, 2003. URL https://doi.org/10.1109/JSSC.2003.813217.

[82] K. A. Cook-Chennault, N. Thambi, and A. M. Sastry. Powering mems portable devices — a review of non-regenerative and regenerative power supply systems with special emphasis on piezoelectric energy harvesting systems. *Smart Materials and Structures*, 17(4):43001, 2008. URL https://doi.org/10.1088/0964-1726/17/4/043001.

[83] S. P. Beeby and T. O'donnell. Electromagnetic energy harvesting. *Energy Harvesting Technologies*, pages 129–161, 2005.

[84] N. E. du Toit. *Modeling and Design of a MEMS Piezoelectric Vibration Energy Harvester*. Phd, Massachusetts Institute of Technology, 2005.

[85] Chongfeng Wei and Xingjian Jing. A comprehensive review on vibration energy harvesting: Modelling and realization. *Renewable and Sustainable Energy Reviews*, 74: 1 – 18, 2017. ISSN 1364-0321. doi: https://doi.org/10.1016/j.rser.2017.01.073. URL http://www.sciencedirect.com/science/article/pii/S1364032117300837.

[86] Y. Zhang, T. Wang, A. Zhang, Z. Peng, D. Luo, R. Chen, and F. Wang. Electrostatic energy harvesting device with dual resonant structure for wideband random vibration sources at low frequency. *Review of Scientific Instruments*, 87(12):125001, 2016. URL https://doi.org/10.1063/1.4968811.

[87] K. Tao, J. Wu, L. Tang, L. Hu, S. L. Woh, and J. Miao. Enhanced electrostatic vibrational energy harvesting using integrated opposite-charged electrets. *Journal of Micromechanics and Microengineering*, 27(4):44002, 2017. URL https://doi.org/10.1088/1361-6439/aa5e73.

[88] N. Miljkovic, D. J. Preston, R. Enright, and E. N. Wang. Jumping-droplet electrostatic energy harvesting. *Applied Physics Letters*, 105(1):13111, 2014. URL https://doi.org/10.1063/1.4886798.

[89] P. D. Mitcheson, T. C. Green, E. M. Yeatman, and A. S. Holmes. Architectures for vibration-driven micropower generators. *Journal of microelectromechanical systems*, 13 (3):429–440, 2004. URL https://doi.org/10.1109/JMEMS.2004.830151.

[90] D. A. Wang and Chang K. H. Electromagnetic energy harvesting from flow induced vibration. *Microelectronics Journal*, 41(6):356–364, 2010. URL https://doi.org/10.1016/j.mejo.2010.04.005.

[91] P. Carneiro, M. P. S. dos Santos, A. Rodrigues, J. A. F. Ferreira, J. A. O. Simões, A. T. Marques, and A. L. Kholkin. Electromagnetic energy harvesting using magnetic levitation architectures: A review. *Applied Energy*, 260:114191, 2020. URL https://doi.org/10.1016/j.apenergy.2019.114191.

[92] M. R. Jolly, J. W. Bender, and J. D. Carlson. Properties and applications of commercial magnetorheological fluids. *Journal of Intelligent Material Systems and Structures*, 10(1): 5–13, 1999. URL https://doi.org/10.1177/1045389X9901000102.

[93] J. de Vicente, D. J. Klingenberg, and R. Hidalgo-Alvarez. Magnetorheological fluids: a review. *Soft Matter*, 7(8):3701–3710, 2011. URL https://doi.org/10.1039/C0SM01221A.

[94] L. Wang and F. G. Yuan. Vibration energy harvesting by magnetostrictive material. *Smart Materials and Structures*, 17:045009, 2008.

[95] F. Narita and M. Fox. A review on piezoelectric, magnetostrictive, and magnetoelectric materials and device technologies for energy harvesting applications. *Advanced Engineering Materials*, 20(5):1700743, 2018. URL https://doi.org/10.1002/adem.201700743.

[96] C. S. Clemente, D. Davino, G. Maddaloni, M. R. Pecce, and C. Visone. A magnetostrictive energy harvesting system for bridge structural health monitoring. *Advances in Science and Technology*, 101:20–25, 2017. URL https://doi.org/10.4028/www.scientific.net/AST.101.20.

[97] S. Pryia and D. J. Inman. *Piezoelectric Energy Harvesting*. Springer, 2009.

[98] H. G. Yeo, T. Xue, S. Roundy, X. Ma, C. Rahn, and S. Trolier-McKinstry. Strongly (001) oriented bimorph pzt film on metal foils grown by rf-sputtering for wrist-worn piezoelectric energy harvesters. *Advanced Functional Materials*, 28(36):1801327, 2018. URL https://doi.org/10.1002/adfm.201801327.

[99] S. R. Anton and H. A. Sodano. A review of power harvesting using piezoelectric materials (2003–2006). *Smart Materials and Structures*, 16(3):R1, 2007. URL https://doi.org/10.1088/0964-1726/16/3/R01.

[100] J. Davidson and C. Mo. Recent advances in energy harvesting technologies for structural health monitoring applications. *Smart Materials Research*, 2014, 2014.

[101] S. Priya, H. C. Song, Y. Zhou, R. Varghese, A. Chopra, S. G. Kim, I. Kanno, L. Wu, D. S. Ha, J. Ryu, and R. G. Polcawich. A review on piezoelectric energy harvesting:

Materials, methods, and circuits. *Energy Harvesting and Systems*, 4(1):3–39, 2017. URL https://doi.org/10.1515/ehs-2016-0028.

[102] Z. Yang, A. Erturk, and J. Zu. On the efficiency of piezoelectric energy harvesters. *Extreme Mechanics Letters*, 15:26–37, 2017. URL https://doi.org/10.1016/j.eml.2017.05.002.

[103] A. Erturk and D. J. Inman. Issues in mathematical modeling of piezoelectric energy harvesters. *Smart Materials and Structures*, 17(6):65016, 2008. URL https://doi.org/10.1088%2F0964-1726%2F17%2F6%2F065016.

[104] C. de Marqui, A. Erturk, and D. J. Inman. An electromechanical finite element model for piezoelectric energy harvester plates. *Journal of Sound and Vibration*, 327:9–25, 2009. URL https://doi.org/10.1016/j.jsv.2009.05.015.

[105] A. Kumar, A. Sharma, R. Kumar, R. Vaish, and V. S. Chauhan. Finite element analysis of vibration energy harvesting using lead-free piezoelectric materials: A comparative study. *Journal of Asian Ceramic Societies*, 2(2):138–143, 2014. URL https://doi.org/10.1016/j.jascer.2014.02.001.

[106] S. Ravi and A. Zilian. Simultaneous finite element analysis of circuit-integrated piezoelectric energy harvesting from fluid-structure interaction. *Mechanical Systems and Signal Processing*, 114:259–274, 2019. ISSN 888-3270. URL https://doi.org/10.1016/j.ymssp.2018.05.016.

[107] D. A. Wang and H. H. Ko. Piezoelectric energy harvesting from flow-induced vibration. *Journal of Micromechanics and Microengineering*, 20(2):25019, 2010. URL https://doi.org/10.1088/0960-1317/20/2/025019.

[108] P. Gambier, S. R. Anton, N. Kong, A. Erturk, and D. J. Inman. Piezoelectric, solar and thermal energy harvesting for hybrid low-power generator systems with thin-film batteries. *Measurement Science and Technology*, 23(1):15101, 2011. URL https://doi.org/10.1088%2F0957-0233%2F23%2F1%2F015101.

[109] Y. Bouzelata, E. Kurt, Y. Uzun, and R. Chenni. Mitigation of high harmonicity and design of a battery charger for a new piezoelectric wind energy harvester. *Sensors and Actuators*, 273:72–83, 2018. URL https://doi.org/10.1016/j.sna.2018.02.023.

[110] A. Kumar, R. Kiran, V. S. Chauhan, R. Kumar, and R. Vaish. Piezoelectric energy harvester for pacemaker application: a comparative study. *Materials Research Express*, 5 (7):75701, 2018. URL https://orcid.org/0000-0001-7510-7302.

[111] T. Zhao, Y. Fu, H. He, C. Dong, L. Zhang, H. Zeng, L. Xing, and X. Xue. Self-powered gustation electronic skin for mimicking taste buds based on piezoelectric–enzymatic reaction coupling process. *Nanotechnology*, 29(7):075501, 2018. URL https://orcid.org/0000-0003-1379-6813.

[112] J. Granstorm, J. Feenstra, and H. A. Sodano. Energy harvesting from a backpack instrumented with piezoelectric shoulder straps. *Smart Materials and Structures*, 16(5):1810, 2007. URL https://doi.org/10.1088/0964-1726/16/5/036.

[113] Y. Bai, P. Tofel, Z. Hadas, J. Smilek, P. Losak, and P. Skarvada. Investigation of a cantilever structured piezoelectric energy harvester used for wearable devices with random vibration input. *Mechanical Systems and Signal Processing*, 106:303–318, 2018. URL https://doi.org/10.1016/j.ymssp.2018.01.006.

[114] J. Kim, J. Lee, J. Lee, Y. Yamauchi, C. H. Choi, and J. H. Kim. Research update: Hybrid energy devices combining nanogenerators and energy storage systems for self-charging capability. *Apl Materials*, 5(7):073804, 2017. URL https://doi.org/10.1063/1.4979718.

[115] NewAtlas, 2013. URL https://newatlas.com/panasonic-power-loader-light-exoskeleton/25682/.

[116] M. A. Ilyas and J. Swingler. Piezoelectric energy harvesting from raindrop impacts. *Energy*, 90:796–806, 2015. URL https://doi.org/10.1016/j.energy.2015.07.114.

[117] J. Zhang, Z. Fang, C. Shu, J. Zhang, Q. Zhang, and C. Li. A rotational piezoelectric energy harvester for efficient wind energy harvesting. *Sensors and Actuators A: Physical*, 262:123–129, 2017. URL https://doi.org/10.1016/j.sna.2017.05.027.

[118] S. Orrego, K. Shoele, A. Ruas, K. Doran, B. Caggiano, R. Mittal, and S. H. Kang. Harvesting ambient wind energy with an inverted piezoelectric flag. *Applied Energy*, 194: 212–222, 2017. URL https://doi.org/10.1016/j.apenergy.2017.03.016.

[119] F. Petrini and K. Gkoumas. Piezoelectric energy harvesting from vortex shedding and galloping induced vibrations inside hvac ducts. *Energy and Buildings*, 2158:371–383, 2018. URL https://doi.org/10.1016/j.enbuild.2017.09.099.

[120] H. Wang, A. Jasim, and X. Chen. Energy harvesting technologies in roadway and bridge for different applications – a comprehensive review. *Applied Energy*, 212:1083–1094, 2018. URL https://doi.org/10.1016/j.apenergy.2017.12.125.

[121] S. W. Arms, C. P. Townsend, D. L. Churchill, J. H. Galbreath, and S. W. Mundell. Power

management for energy harvesting wireless sensors. *Smart Structures and Materials*, 5763: 267–275, 2005.

[122] X. Zhao, H. Xiang, and Z. Shi. Piezoelectric energy harvesting from vehicles induced bending deformation in pavements considering the arrangement of harvesters. *Applied Mathematical Modelling*, 77:327 – 340, 2020. URL https://doi.org/10.1016/j.apm.2019.07.048.

[123] N. Makki and R. P. Iliev. Pneumatic tire-based piezoelectric power generation. *International Society for Optics and Photonics*, 7977:186–198, 2011. URL https://doi.org/10.1117/12.880636.

[124] N. Makki and R. P. Iliev. Piezoelectric power generation for sensor applications: design of a battery-less wireless tire pressure sensor. *International Society for Optics and Photonics*, 8066:373–382, 2011. URL https://doi.org/10.1117/12.887112.

[125] N. Makki and R. P. Iliev. Battery-and wire-less tire pressure measurement systems (tpms) sensor. *Microsystem technologies*, 18(7):1201–1212, 2012. URL https://doi.org/10.1117/12.887112.

[126] G. Yesner, A. Jasim, H. Wang, B. Basily, A. Maher, and A. Safari. Energy harvesting and evaluation of a novel piezoelectric bridge transducer. *Sensors and Actuators A: physical*, 285:348–354, 2019. URL https://doi.org/10.1016/j.sna.2018.11.013.

[127] A. Jasim, G. Yesner, H. Wang, A. Safari, and B. Basily. Laboratory testing and numerical simulation of piezoelectric energy harvester for roadway applications. *Applied Energy*, 224: 438–447, 2018. URL https://doi.org/10.1016/j.apenergy.2018.05.040.

[128] Japan uses energy-generating floor to help power subway, 2008. URL https://www.dailymail.co.uk/news/article-1094248/The-power-commuter--Japan-uses-energy-generating-floor-help-power-subway.html.

[129] Wearable device- smart shoe generate power from walking, 2015. URL https://www.mepits.com/project/257/techno-innovations/wearable-device-smart-shoe-generate-power-from-walking.

[130] E. A. Ethem, K. Hanseup, and N. Khalil. Energy scavenging from insect flight. *Journal of Micromechanics and Microengineering*, 21(9):095016, aug 2011. URL https://doi.org/10.1088/0960-1317/21/9/095016.

[131] M. W. Shafer, R. MacCurdy, E. Garcia, and D. Winkler. Harvestable vibrational energy

from an avian source: theoretical predictions vs. measured values. *International Society for Optics and Photonics*, 8341:26–36, 2012. URL https://doi.org/10.1117/12.915370.

[132] H. Liu, J. Zhong, C. Lee, S-W. Lee, and L. Lin. A comprehensive review on piezoelectric energy harvesting technology: Materials, mechanisms, and applications. *Applied Physics Reviews*, 5(4):041306, 2018. URL https://doi.org/10.1063/1.5074184.

[133] M. A. Savi. *Dinâmica Não-Linear e Caos*. e-papers, 2nd edition, 2017.

[134] A. S. de Paula, D. J. Inman, and M. A. Savi. Energy harvesting in a nonlinear piezomagnetoelastic beam subjected to random excitation. *Mechanical Systems and Signal Processing*, 54:405–416, 2015. URL https://doi.org/10.1016/j.ymssp.2014.08.020.

[135] B. Maaer, A. Boughamoura, A. M. R. F. El-Bab, L. A. Francis, and F. Tounsi. A review on design improvements and techniques for mechanical energy harvesting using piezoelectric and electromagnetic schemes. *Energy Conversion and Management*, 199:111973, 2019. URL https://doi.org/10.1016/j.enconman.2019.111973.

[136] D. Younesian and M. R. Alam. Multi-stable mechanisms for high-efficiency and broadband ocean wave energy harvesting. *Applied Energy*, 197:292 – 302, 2017. URL https://doi.org/10.1016/j.apenergy.2017.04.019.

[137] Huaxia Deng, Yu Du, Zhemin Wang, Jingchang Ye, Jin Zhang, Mengchao Ma, and Xiang Zhong. Poly-stable energy harvesting based on synergetic multistable vibration. *Communications Physics*, 2(1):1–10, 2019. URL https://doi.org/10.1038/s42005-019-0117-9.

[138] W. Wang, J. Cao, C. Bowen, S. Zhou, and J. Lin. Optimum resistance analysis and experimental verification of nonlinear piezoelectric energy harvesting from human motions. *Energy*, 118:221–230, 2017. URL https://doi.org/10.1016/j.energy.2016.12.035.

[139] S. Dhote, Z. Yang, K. Behdinan, and Zu. J. Enhanced broadband multi-mode compliant orthoplanar spring piezoelectric vibration energy harvester using magnetic force. *International Journal of Mechanical Sciences*, 135:63–71, 2018. URL https://doi.org/10.1016/j.ijmecsci.2017.11.012.

[140] M. S. Woo, J. H. Ahn, J. H. Eom, W. S. Hwang, J. H. Kim, C. H. Yanf, G. J. Song, S. D. Hong, J. P. Jhun, and T. H. Sung. Study on increasing output current of piezoelectric energy harvester by fabrication of multilayer thick film. *Sensors and Actuators A: Physical*, 269:524–534, 2018. URL https://doi.org/10.1016/j.sna.2017.12.025.

[141] R. Ai, L. L. S. Monteiro, P. C. C. Monteiro Jr, P. M. C. L. Pacheco, and M. A. Savi.

Piezoelectric vibration-based energy harvesting enhancement exploiting nonsmoothness. *Actuators*, 1:25, 2019. URL https://doi.org/10.3390/act8010025.

[142] H. Liu, C. Lee, T. Kobayashi, C. j. Tai, and C. Quan. Investigation of a mems piezoelectric energy harvester system with a frequency-widened-bandwidth mechanism introduced by mechanical stoppers. *Smart Materials and Structures*, 21(3):035005, 2012. URL https://doi.org/10.1088/0964-1726/21/3/035005.

[143] H. Liu, C. Lee, T. Kobayashi, C. j. Tai, and C. Quan. Piezoelectric mems-based wideband energy harvesting systems using a frequency-up-conversion cantilever stopper. *Sensors and Actuators A: Physical*, 186:242–248, 2012. URL https://doi.org/10.1016/j.sna.2012.01.033.

[144] S. Liu, Q. Cheng, D. Zhao, and L. Feng. Theoretical modeling and analysis of two-degree-of-freedom piezoelectric energy harvester with stopper. *Sensors and Actuators A: Physical*, 245:97–105, 2016. URL https://doi.org/10.1016/j.sna.2016.04.060.

[145] W. J. Su. Impact-driven broadband piezoelectric energy harvesting using a two-degrees-of-freedom structure. *Microsystem Technologies*, pages 1–10, 2020.

[146] S. Zhou, W. Chen, M. H. Malakooti, J. Cao, and D. J. Inman. Design and modeling of a flexible longitudinal zigzag structure for enhanced vibration energy harvesting. *Journal of Intelligent Material Systems and Structures*, 28(3):367–380, 2017. URL https://doi.org/10.1177/1045389X16645862.

[147] Z. Zhou, J. D. Hobeck, J. Cao, and D. J. Inman. Analytical and experimental investigation of flexible longitudinal zigzag structures for enhanced multi-directional energy harvesting. *Smart Materials and Structures*, 26(3):035008, 2017. URL https://doi.org/10.1088/1361-665X/26/3/035008.

[148] A. J. Leem, A. Moosavian, and D. J. Inman. A piezoelectrically generated bistable laminate for morphing. *Materials Letters*, 190:123–126, 2017. URL https://doi.org/10.1016/j.matlet.2017.01.005.

[149] A. J. Lee and D. J. Inman. A multifunctional bistable laminate:snap-through morphing enabled by broadband energy harvesting. *Journal of Intelligent Material Systems and Structures*, 29(11):2528–2543, 2018. URL https://doi.org/10.1177/1045389X18770895.

[150] S. A. Emam, J. Hobeck, and D. J. Inman. Experimental investigation into the nonlinear dynamics of a bistable laminate. *Nonlinear Dynamics*, 25(4):3019–3039, 2019. URL https://doi.org/10.1007/s11071-018-04738-0.

[151] A. G. Moura and A. Erturk. Varying cross-section and axial strain-gradient effects in flexoelectric cantilevers at submicron thickness levels. *Active and Passive Smart Structures and Integrated Systems XII International Society for Optics and Photonics*, page 105951C, 2018. URL https://doi.org/10.1117/12.2300997.

[152] X. Wang, C. Chen, N. Wang, H. San, Y. Yu, E. Halvorsen, and X. Chen. A frequency and bandwidth tunable piezoelectric vibration energy harvester using multiple nonlinear techniques. *Applied Energy*, 190:368–375, 2017. URL https://doi.org/10.1016/j.apenergy.2016.12.168.

[153] R. Sun, S. C. Carreira, Y. Chen, C. Xiang, L. Xu, B. Zhang, M. Chen, I. Farrow, F. Scarpa, and J. Rossiter. Stretchable piezoelectric sensing systems for self-powered and wireless health monitoring. *Advanced Materials Technologies*, 4(5):1900100, 2019. URL https://doi.org/10.1002/admt.201900100.

[154] H. Güleç, M. Gurbuz, A. G. Toktas, M. Gul, B. Koc, and A. Dogan. A new design to improve bandwidth of piezoelectric energy harvester. *Journal of the Australian Ceramic Society*, 56(1):117–126, 2020. URL https://doi.org/10.1007/s41779-019-00425-4.

[155] D. Avirovik, A. Kumar, R. J. Bodnar, and S. Priya. Remote light energy harvesting and actuation using shape memory alloy—piezoelectric hybrid transducer. *Smart Materials and Structures*, 22(5):52001, 2013. URL https://doi.org/10.1088/0964-1726/22/5/052001.

[156] L. L. Silva, S. A. Oliveira, P. M. C. L. Pacheco, and M. A. Savi. Synergistic use of smart materials for vibration-based energy harvesting. *The European Physical Journal Special Topics*, 224(14):3005–3021, 2015. URL https://doi.org/10.1140/epjst/e2015-02603-8.

[157] A. Adeodato, L. L. S. Monteiro, P. C. C. M. Junior, F. M. Viola, S. O. Almeida, P. M. C. L. Pacheco, and M. A. Savi. Nonlinear dynamics of a vibration-based energy harvesting system using piezoelectric and shape memory alloy elements. *CILAMCE 2016*, 2016.

[158] A. Adeodato, B. T. Duarte, R. A. A. de Aguiar, L. L. S. Monteiro, , M. A. Savi, and P. M. C. L. Pacheco. Experimental analysis of an energy harvesting system with piezoelectric and shape memory alloy. *COBEM 2017*, 2017.

[159] A. Adeodato, G. X. G. Borges, B. T. Duarte, R. A. A. de Aguiar, L. L. S. Monteiro, , M. A. Savi, and P. M. C. L. Pacheco. Experimental investigation of piezoelectric vibrationbased energy harvesting with shape memory alloy elements. *COBEM 2019*, 2019.

[160] V. Chiaverini. *Tecnologia Mecânica*, volume I e II. McGraw-Hill, 1998.

[161] W. D. Jr. Callister. *Materials Science and Engineering an Introduction*. John Wiley and Sons, Inc., 2007.

[162] J. Lemaitre and J. L. Chaboche. *Mechanics of Solid Materials*. Cambridge University Press, 1990.

[163] P. M. C. L. Pacheco. *Análise do Acoplamento Termomecânico em Materiais Elasto-Viscoplásticos*. Dsc, Pontifícia Universidade Catótilica do Rio de Janeiro, 1994.

[164] K. Otsuka and C. M. Wayman. *Shape Memory Materials*. Cambrige University Press, 1998.

[165] A. Paiva and M. A. Savi. An overview of constitutive models for shape memory alloys. *Mathematical problems in engineering*, 2006, 2006. URL https://doi.org/10.1155/MPE/2006/56876.

[166] P. C. C. Monteiro, L. L. S. Monteiro, M. A. Savi, T. A. Netto, P. M. C. L. Pacheco, and T. de Paiva. A comparative analysis of different shape memory alloy actuator configurations. *Journal of Intelligent Material Systems and Structures*, 28(11):1415–1427, 2017. URL https://doi.org/10.1177/1045389X16672571.

[167] M. J. Jani, M. Leary, and A. Subic. Designing shape memory alloy linear actuators: A review. *Journal of Intelligent Material Systems and Structures*, 28(13):1699–1718, 2017. URL https://doi.org/10.1177/1045389X16679296.

[168] P. C. C. Monteiro, L. L. S. Monteiro, T. A. Netto, and M. A. Savi. Experimental investigation of the influence of the heating rate in an sma actuator performance. *Sensors and Actuators A: Physical*, 199(1):254 – 259, 2013. URL https://doi.org/10.1016/j.sna.2013.05.016.

[169] S. de Oliveira, S. A. Silva, C. R. Souto, and A. Ries. Experimental characterization and control of a force actuator based on shape memory alloy wire. *Journal of Control, Automation and Electrical Systems*, 29(6):670–676, 2018. URL https://doi.org/10.1007/s40313-018-0416-5.

[170] R. Vaidyanathan and R. D. Chiel, H. J.and Quinn. A hydrostatic robot for marine applications. *Robotics and Autonomous Systems*, 30(1-2):26103–113, 2000. URL https://doi.org/10.1016/S0921-8890(99)00067-6.

[171] D. Y. Lee, J. S. Kim, S. R. Kim, J. S. Koh, and K. J. Cho. The deformable wheel robot using magic-ball origami structure. *ASME 2013 international design engineering*

technical conferences and computers and information in engineering conference, 2014. URL https://doi.org/10.1115/DETC2013-13016.

[172] D. S. Copaci, Blanco. D., A. M. Clemente, and L. Moreno. Flexible shape memory alloy actuators for soft robotics: Modelling and control. *International Journal of Advanced Robotic Systems*, 17(1):1729881419886747, 2020. URL https://doi.org/10.1177/1729881419886747.

[173] C. Bil, K. Massey, and E. J. Abdullah. Wing morphing control with shape memory alloy actuators. *Journal of Intelligent Material Systems and Structures*, 24(7):879–898, 2013. URL https://doi.org/10.1177/1045389X12471866.

[174] P. B. C. Leal and M. A. Savi. Shape memory alloy-based mechanism for aeronautical application: Theory, optimization and experiment. *Aerospace Science and Technology*, 76:155–163, 2018. URL http://www.sciencedirect.com/science/article/pii/S1270963817316954.

[175] D. J. Hartl, J. T. Mooney, D. C. Lagoudas, F. T. Calkins, and J. H. Mabe. Use of a ni60ti shape memory alloy for active jet engine chevron application: I. thermomechanical characterization. *Smart Materials and Structures*, 19(1):15020, 2009. URL https://doi.org/10.1088/0964-1726/19/1/015020.

[176] D. J. Hartl, J. T. Mooney, D. C. Lagoudas, F. T. Calkins, and J. H. Mabe. Use of a ni60ti shape memory alloy for active jet engine chevron application: II. experimentally validated numerical analysis. *Smart Materials and Structures*, 19(1):15021, 2009. URL https://doi.org/10.1088/0964-1726/19/1/015021.

[177] A. M. Pankonien, C. T. Faria, and D. J. Inman. Synergistic smart morphing aileron. *54th AIAA/ASME/ASCE/AHS/ASC structures, structural dynamics, and materials conference*, page 1512, 2013.

[178] M. W. Han, R. Rodrigue, H. I. Kim, S. K. Song, and S. H. Ahn. Shape memory alloy/glass fiber woven composite for soft morphing winglets of unmanned aerial vehicles. *Composite Structures*, 140:202–212, 2016. URL http://www.sciencedirect.com/science/article/pii/S0263822315011411.

[179] D. Z. Li and Z. C. Feng. Dynamic properties of pseudoelastic shape memory alloys. *Smart Materials and Structures*, 3041:715–725, 1997. URL https://doi.org/10.1117/12.275696.

[180] R. A. A. de Aguiar, M. A. Savi, and P. M. C. L. Pacheco. Experimental investigation of

vibration reduction using shape memory alloys. *Journal of Intelligent Material Systems and Structures*, 24(2):247–261, 2013. URL https://doi.org/10.1177/1045389X12461696.

[181] S. C. Kwon, S. H. Jeon, and H. U. Oh. Performance investigation of a novel pseudoelastic SMA mesh washer gear wheel with micro-jitter attenuation capability. *Smart Materials and Structures*, 25(5):55004, 2016. URL https://doi.org/10.1088/0964-1726/25/5/055004.

[182] F. A. Nae, T. Ikeda, and Y. Matsuzaki. The active tuning of a shape memory alloy pseudoelastic property. *Smart Materials and Structures*, 13(3):503–511, 2004. URL https://doi.org/10.1088/0964-1726/13/3/008.

[183] Y. Y. He, S. Oi, F. L. Chu, and H. X. Li. Vibration control of a rotor bearing system using shape memory alloy: *i*. theory. *Smart Materials and Structures*, 16(1):114–121, 2006. URL https://doi.org/10.1088/0964-1726/16/1/014.

[184] Y. Y. He, S. Oi, F. L. Chu, and H. X. Li. Vibration control of a rotor–bearing system using shape memory alloy: *ii*. experimental study. *Smart Materials and Structures*, 16(1): 122–127, 2006. URL https://doi.org/10.1088/0964-1726/16/1/014.

[185] Y. Zhang, Y. You, G. Anlas, J. Zhu, and W. Zhang. Experimental and theoretical investigation of the frequency effect on low cycle fatigue of shape memory alloys. *International Journal of Plasticity*, 90:1–30, 2016. URL https://doi.org/10.1016/j.ijplas.2016.11.012.

[186] G. Eggeler, E. Hornbogen, A. Yawny, A. Heckmann, and M. Wagner. Structural and functional fatigue of niti shape memory alloys. *Materials Science and Engineering: A*, 378 (1):24–33, 2004. URL https://doi.org/10.1016/j.msea.2003.10.327.

[187] V. M. Dornelas, S. A. de Oliveira, and M. A. Savi. A macroscopic description of shape memory alloy functional fatigue. *International Journal of Mechanical Sciences*, 170: 105345, 2020. URL https://doi.org/10.1016/j.ijmecsci.2019.105345.

[188] V. M. Dornelas, S. A. de Oliveira, M. A. Savi, P. M. C. L. Pacheco, and L. F. G. de Souza. Fatigue on shape memory alloys: Experimental observations and constitutive modeling. *International Journal of Solids and Structures*, 213:1 – 24, 2021. URL https://doi.org/10.1016/j.ijsolstr.2020.11.023.

[189] C. Cismasiu and F. P. A. Santos. Numerical simulation of a semi-active vibration control device based on superelastic shape memory alloy wires. *Shape Memory Alloys*, 2010.

[190] S. Saadat, J. Salichs, M. Noori, Z. Hou, H. Davoodi, I. Bar-on, Y. Suzuki, and A. Masuda. An overview of vibration and seismic applications of niti shape memory alloy. *Smart*

Materials and Structures, 11(2):218, 2002. URL https://doi.org/10.1088%2F0964-1726%2F11%2F2%2F305.

[191] Y. L. Han, Q. S. Li, A. Q. Li, A. Y. T. Leung, and P. H. Lin. Structural vibration control by shape memory alloy damper. *Earthquake engineering and structural dynamics*, 97(4): 483–494, 2003. URL https://doi.org/10.1002/eqe.243.

[192] W. Wang, C. Fang, and J. Liu. Large size superelastic sma bars: heat treatment strategy, mechanical property and seismic application. *Smart Materials and Structures*, 25(7): 075001, 2016. URL https://doi.org/10.1088%2F0964-1726%2F25%2F7%2F075001.

[193] S. Varela and M. Saiddi. A bridge column with superelastic niti sma and replaceable rubber hinge for earthquake damage mitigation. *Smart Materials and Structures*, 25(7): 075012, 2016. URL https://doi.org/10.1088%2F0964-1726%2F25%2F7%2F075012.

[194] L. L. Vignoli, M. A. Savi, and S. El-Borgi. Nonlinear dynamics of earthquakeresistant structures using shape memory alloy composites. *Journal of Intelligent Material Systems and Structures*, 31(5):771–787, 2020. URL https://doi.org/10.1177/1045389X19898269.

[195] L. Casagrande, E. Villa, A. Nespoli, A. Occhiuzzi, A. Bonati, and F. Auricchio. Innovative dampers as floor isolation systems for seismically-retrofit multi-storey critical facilities. *Engineering Structures*, 201:109772, 2019. URL https://doi.org/10.1016/j.engstruct.2019.109772.

[196] M. H. Enferadi, M. R. Ghasemi, and N. Shabakhty. Wave-induced vibration control of offshore jacket platforms through sma dampers. *Applied Ocean Research*, 90:101848, 2019. URL https://www.sciencedirect.com/science/article/pii/S0141118718308976.

[197] M. R. Ghasemi, N. Shabakhty, and M. H. Enferadi. Vibration control of offshore jacket platforms through shape memory alloy pounding tuned mass damper (sma-ptmd). *Ocean Engineering*, 191:106348, 2019. URL https://doi.org/10.1016/j.oceaneng.2019.106348.

[198] S. Das, M. M. Sajeer, and A. Chakraborty. Vibration control of horizontal axis offshore wind turbine blade using SMA stiffener. *Smart Materials and Structures*, 28(9):095025, 2019. URL https://doi.org/10.1088/1361-665x/ab1174.

[199] D. Bernardini and F. Vestroni. Non-isothermal oscillations of pseudoelastic devices. *International Journal of Non-Linear Mechanics*, 38(9):1297–1313, 2003. URL https://doi.org/10.1016/S0020-7462(02)00065-3.

[200] D. Bernardini and G. Rega. Chaos robustness and strength in thermomechanical shape

memory alloy oscillators. part I: A predictive theoretical framework for the peseudoelastic behavior. *International Journal of Bifurcation and Chaos*, 21(10):2769–2782, 2011. URL https://doi.org/10.1142/S0218127411030131.

[201] D. Bernardini and G. Rega. Chaos robustness and strength in thermomechanical shape memory alloy oscillators. part II: Numerical and theoretical evaluation. *International Journal of Bifurcation and Chaos*, 21(10):2783–2800, 2011. URL https://doi.org/10.1142/S0218127411030143.

[202] O. Doaré, A. Sbarra, Touzé C., M. O. Moussa, and Z. Moumni. Experimental analysis of the quasi-static and dynamic torsional behaviour of shape memory alloys. *International Journal of Solids and Structures*, 49(1):32–42, 2012. URL https://doi.org/10.1016/j.ijsolstr.2011.09.009.

[203] C. V. de Souza and C. de Marqui. Experimental study on the aeroelastic behavior of a typical airfoil section with superelastic shape memory alloy springs. *Journal of Intelligent Material Systems and Structures*, 29:623–635, 2018. URL ttps://doi.org/10.1177/1045389X17721024.

[204] M. J. Borges, A. A. Silva, C. J. Araujo, R. L. Pimentel, A. S. Aquino, R. Senko, and R. P. B. Reis. On the active control of a rotor-bearing system using shape memory alloy actuators: an experimental analysis. *Journal of the Brazilian Society of Mechanical Sciences and Engineering*, 40(5):269, 2018. URL https://doi.org/10.1007/s40430-018-1175-8.

[205] Y. Matsuzaki and H. Naito. Macroscopic and microscopic constitutive models of shape memory alloys based on phase interaction energy function: A review. *Journal of Intelligent Material Systems and Structures*, 15(2):141–155, 2004. URL https://doi.org/10.1177/1045389X04039953.

[206] F. Auricchio, R. L. Taylor, and J. Lubliner. Shape-memory alloys: macromodelling and numerical simulations of the superelastic behavior. *Computer methods in applied mechanics and engineering*, 146(3-4):281–312, 1997.

[207] C. Cisse, W. Zaki, and T. B. Zineb. A review of constitutive models and modeling techniques for shape memory alloys. *International Journal of Plasticity*, 76:244–284, 2016. URL https://doi.org/10.1016/j.ijplas.2015.08.006.

[208] F. Falk. Model free energy, mechanics, and thermodynamics of shape memory alloys. *Acta Metallurgica*, 28:1773–1780, 1980.

[209] M. Fremond. Matériaux à mémoire de forme. *Comptes Rendus Mathematique*, 2(7): 239–244, 1987.

[210] M. Fremond. Shape memory alloy: a thermomechanical macroscopic theory. *CISM Courses and Lectures*, -(351):3–68, 1996.

[211] J. G. Boyd and D. C. Lagoudas. A thermodynamical constitutive model for shape memory materials. part i. the monolithic shape memory alloy. *International Journal of Plasticity*, 12(6):805–842, 1996. URL https://doi.org/10.1016/S0749-6419(96)00030-7.

[212] A. C. Souza, E. N. Mamiya, and N. Zouain. Three-dimensional model for solids undergoing stress-induced phase transformations. *European Journal of Mechanics - A/Solids*, 17(5): 789–806, 1998. URL https://doi.org/10.1016/S0997-7538(98)80005-3.

[213] A. Bhattacharyya and D. C. Lagoudas. A stochastic thermodynamic model for the gradual thermal transformation of SMA polycrystals. *Smart Materials and Structures*, 6(3):235–250, 1997. URL https://doi.org/10.1088/0964-1726/6/3/003.

[214] M. Fischlschweiger and E. R. Oberaigner. Kinetics and rates of martensitic phase transformation based on statistical physics. *Computational Materials Science*, 52(1):189–192, 2012. URL https://doi.org/10.1016/j.commatsci.2011.03.038. Proceedings of the 20th International Workshop on Computational Mechanics of Materials - IWCMM 20.

[215] K. Tanaka, F. Nishimura, M. Matsui, H. Tobushi, and P. Lin. Phenomenological analysis of plateaus on stress-strain hysteresis in tini shape memory alloy wires. *Mechanics of Materials*, 24(1):1930, 1986. URL https://doi.org/10.1016/0167-6636(96)00030-0.

[216] C. Liang and C. A. Rogers. One-dimensional thermomechanical constitutive relations for shape memory materials. *Journal of intelligent material systems and structures*, 8(4): 285–302, 1990. URL https://doi.org/10.1177/1045389X9700800402.

[217] S. Enemark, M. A. Savi, and I. F. Santos. Nonlinear dynamics of a pseudoelastic shape memory alloy system — theory and experiment. *Smart Materials and Structures*, 23(8): 085018, 2014. URL https://doi.org/10.1088%2F0964-1726%2F23%2F8%2F085018.

[218] S. Enemark, I. F. Santos, and M. A. Savi. Modelling, characterisation and uncertainties of stabilised pseudoelastic shape memory alloy helical springs. *Intelligent Material Systems and Structures*, 27(20):2721–2743, 2016. URL https://doi.org/10.1177/1045389X16635845.

[219] M. A. Savi, P. M. C. L. Pacheco, M. S. Garcia, L. F. G. Aguiar, R. A. A. Souza, and R. B.

da Hora. Nonlinear geometric influence on the mechanical behavior of shape memory alloy helical springs. *Smart Materials and Structures*, 24:035012, 2015. URL https://doi.org/10.1088%2F0964-1726%2F24%2F3%2F035012.

[220] Russell Charles Hibbeler. *Resistência dos Materiais 7ª Edição*. Pearson Education, 2010.

[221] R. A. A. de Aguiar, M. A. Savi, and P. M. C. L. Pacheco. Experimental and numerical investigations of shape memory alloy helical springs. *Smart Materials and Structures*, 19 (2):25008, 2010. URL https://doi.org/10.1088%2F0964-1726%2F19%2F2%2F025008.

[222] J. E. Shigley and C. R. Mischke. *Mechanical Engineering Design*. McGraw-Hil, 2001.